

Formation of morphogen gradients

Dissertation

zur Erlangung des akademischen Grades

Doctor rerum naturalium (Dr. rer. nat.)

vorgelegt

der Fakultät Mathematik und Naturwissenschaften
der Technischen Universität Dresden

von

Tobias Bollenbach

geboren am 13.9.1978 in Göttingen

Gutachter:

1. _____

2. _____

3. _____

Eingereicht am: _____

Tag der Verteidigung: _____

Acknowledgments

Most of all, I would like to thank Prof. Dr. Frank Jülicher for giving me the opportunity to work in his group at the Max Planck Institute for the Physics of Complex Systems and for many fruitful discussions about this project.

I would further like to thank Dr. Karsten Kruse for his interest in this work and his continuing support during the course of this project.

Moreover, I thank Dr. Periklis Pantazis and Dr. Marcos González-Gaitán at the Max Planck Institute for Molecular Cell Biology and Genetics for an outstanding and productive collaboration. The countless discussions with them and their experiments were the bedrock of this work.

Finally, I would like to thank the many people at both institutes who have helped me with the innumerable little problems that have occurred in the last years.

Abstract

Morphogens are signaling molecules that play a key role in animal development. They spread from a restricted source into an adjacent target tissue forming a concentration gradient. The fate of cells in the target tissue is determined by the local concentration of such morphogens. Morphogen transport through the tissue has been studied in experiments which lead to the suggestion of several transport mechanisms. While diffusion in the extracellular space contributes to transport, recent experiments on the morphogen Decapentaplegic (Dpp) in the fruit fly *Drosophila* provide evidence for the importance of a cellular transport mechanism that was termed “planar transcytosis”. In this mechanism, morphogens are transported through cells by repeated rounds of internalization and externalization.

Starting from a microscopic theoretical description of these processes, we derive systems of nonlinear transport equations which describe the interplay of transcytosis and passive diffusion. We compare the results of numerical calculations based on this theoretical description of morphogen transport to recent experimental data on the morphogen Dpp in the *Drosophila* wing disk. Agreement with the experimental data is only achieved if the parameters entering the theoretical description are chosen such that transcytosis contributes strongly to transport.

Analyzing the derived transport equations, we find that transcytosis leads to an increased robustness of the created gradients with respect to morphogen over-expression. Indications for this kind of robustness have been found in experiments. Furthermore, we theoretically investigate morphogen gradient formation in disordered systems. Here, an important question is how the position of concentration thresholds can be defined with high precision in the noisy environment present in typical developing tissues. Among other things, we find that the dimensionality of the system in which the gradient is formed plays an important role for the precision. Comparing gradients formed by transcytosis to those formed by extracellular diffusion, we find substantial differences that may result in a higher precision of gradients formed by transcytosis. Finally, we suggest several experiments to test the theoretical predictions of this work.

Contents

1	Introduction	9
1.1	Morphogens and cell differentiation	9
1.2	Dpp in the Drosophila wing disk	11
1.3	Open questions	15
1.4	Morphogen transport and gradient formation	16
1.5	Robustness and precision of morphogen gradients	18
1.6	Overview of this work	19
2	Dpp transport in the Drosophila wing disk	21
2.1	Parameters and boundary conditions	22
2.2	Transcytosis regime	25
2.2.1	Gradient formation in wild type	25
2.2.2	Shibire rescue assay	28
2.2.3	Shibire clone assay	31
2.3	Extracellular diffusion dominated regime (DBTS model)	33
2.3.1	Gradient formation in wild type	36
2.3.2	Shibire rescue assay	36
2.3.3	Shibire clone assay	37
2.4	Interpretation of clone experiments	39
2.5	FRAP experiments	43
3	Theoretical description of morphogen transport	47
3.1	One dimensional description	48
3.1.1	Microscopic one dimensional description	48
3.1.2	Transport equations for transcytosis	51
3.2	Two dimensional description	57
3.2.1	Microscopic two dimensional description	57
3.2.2	Transport equations for transcytosis	59
3.3	Analysis of the effective transport equations	61
3.3.1	Properties of transcytosis	61
3.3.2	Simple limits	62
3.3.3	Analytical steady state solution	63
3.4	Extracellular diffusion dominated limit and DBTS model	64
4	Robustness and precision of morphogen gradients	67
4.1	Robustness of morphogen gradients	67
4.1.1	Robustness of gradients formed by transcytosis	68
4.1.2	Robustness with extracellular diffusion	68
4.2	Precision of morphogen gradients	69

4.2.1	Microscopic origin of fluctuations	72
4.2.2	Definition of precision	74
4.2.3	Effects of disorder on the precision of gradients	76
5	Gradient formation in disordered systems	83
5.1	Diffusion with particle decay	83
5.1.1	Diffusion with frozen disorder	84
5.1.2	Effects of the disorder on the steady state	86
5.1.3	Generalization to two and three space dimensions	91
5.2	Detailed description of transport with disorder	97
5.2.1	One dimensional description with receptor kinetics	97
5.2.2	One dimensional description with constant surface receptor approximation	100
5.2.3	Fluctuations of microscopic quantities	104
5.2.4	Two dimensional description	104
6	Summary and outlook	107
A	Generalizations of the description	113
A.1	Two ligand species	113
A.2	Directional bias in transcytosis	117
A.3	The glypican model	120
B	DBT model of morphogen transport	121
B.1	Shibire clone assay	121
B.2	Description of two ligand species in the DBT model	127
B.3	Receptor production in the diffusion regime	127
C	Indirect assays on Dpp	131
D	Explicit expressions for coefficients	135
D.1	Coefficients in the transport equations (3.12, 3.13)	135
D.2	Explicit expressions for the $F_\alpha(\lambda)$ in (5.33)	136
D.3	Normalized standard deviation for transcytosis	136
E	Supplementary analytic calculations	137
E.1	Derivation of continuous equations for the diffusion model with disorder	137
E.2	Green's functions of $D\Delta - k$	137
E.2.1	Derivation of Green's function in three dimensions	137
E.2.2	Properties at the boundary in two dimensions	138
E.3	Normalized standard deviation	138
E.3.1	Two dimensions	138
E.3.2	Three dimensions	139
F	Numerical methods	141
F.1	Diffusion dominated limit	141
F.2	Discrete description of transcytosis	142
F.3	Effective transport equation for transcytosis	142
F.4	Ensemble averages for frozen disorder	143

Chapter 1

Introduction

The development of higher organisms is a fascinating process. Amazingly, a single nearly uniform fertilized egg cell develops into a complex organism consisting of cells that perform a great variety of different functions. This enormous increase in complexity during development has intrigued scientists for ages [74].

Over the last century, many general processes that play a significant role in the development of all organisms were identified in experiments. Among these key mechanisms are cell division, morphogenesis, i.e. the emergence of the shape of the organism, cell migration, cell death and the growth of the organism by several orders of magnitude [103, 65]. A process of paramount importance for the emergence of complex organisms is cell differentiation. In this work, we will focus on issues related to this process.

1.1 Morphogens and cell differentiation

While all cells in an organism contain the same genetic information which is stored in their DNA, the functions they perform can be very different. Striking examples in Humans are the morphological and functional differences between nerve cells in the brain, liver cells, white and red blood cells, or skin cells.

All these different cells of the organism are descendants of the same fertilized egg cell and result from cell divisions. The process that leads to different cell functions or “fates” during the development of the organism is called “cell differentiation”. A cell fate is generally determined by a certain set of genes that are expressed in the cell [55]. Here, “expression” of a gene means that the information stored in the DNA that is present in all cells is actually used to produce corresponding RNA molecules which are usually used as a template for the subsequent production of proteins. RNA and protein production are called “transcription” and “translation” respectively [1, 103, 65].

As cells of certain types are located at very well-defined positions in the adult organism, cell differentiation must be precisely established in a manner that is insensitive to fluctuations and changes of the environmental conditions. In order to understand development, it is consequently a highly relevant question how the observed patterns of cell differentiation are established and maintained in a developing organism.

The idea that concentration gradients of certain molecules play a role in this process dates back over 100 years [69, 70, 35]. In the middle of the last century, Turing coined the term “morphogens” for certain diffusing molecules that self-organize into spatial patterns which are subsequently used to structure the organism [94]. In the wake of this seminal theoretical work, reaction-diffusion mechanisms of biological pattern formation were studied extensively, in particular by Meinhardt and his coworkers [38, 67, 19, 58, 76]. Such mechanisms may indeed

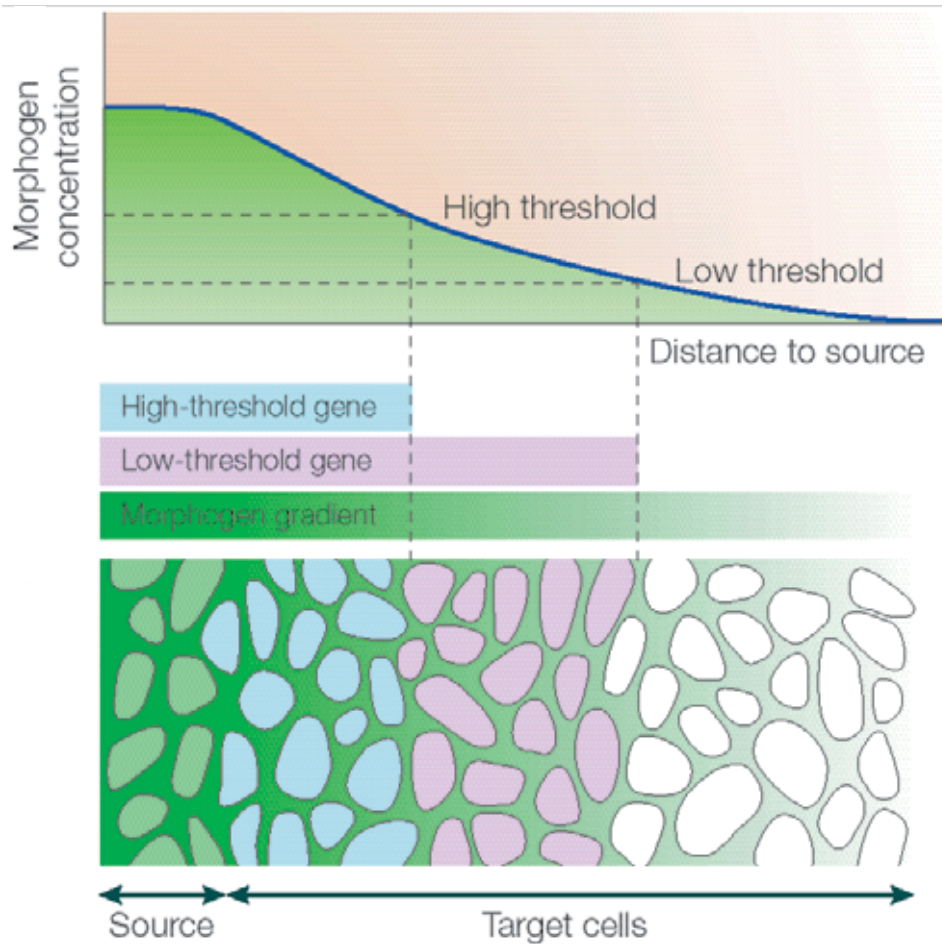


Figure 1.1: Schematic of a morphogen gradient controlling cell differentiation. The morphogens are produced in the source and spread into the adjacent target tissue where they are partly degraded so that a graded concentration profile is established. In the schematic, two different target genes of the morphogen are expressed in the target cells if the morphogen concentration exceeds two corresponding threshold values. These different cell responses are indicated in light blue and red respectively. Figure modified from [41].

underlie the pigmentation patterns seen in certain animal coats like the stripe patterns in the zebra or the angelfish [76, 103].

However, the modern concept of morphogens is different from Turing’s original idea. In 1969, Wolpert suggested that morphogens are produced in cells which are located in a spatially restricted source region [101]. From this source, they spread into the adjacent tissue which is called the “target tissue”. The morphogens are degraded throughout this tissue or possibly only in a “sink” region located at some distance to the source. This setup leads to the formation of a graded profile of morphogen concentration in the target tissue which is called “morphogen gradient”. The key concept is that the fates of the cells in the target tissue are determined by the local concentration of the morphogen which contains positional information about the distance to the morphogen source, see Fig. 1.1 for an illustration. According to their classical definition, morphogens induce the cell fates in a direct manner, i.e. cell differentiation is controlled by their concentration alone without intermediates [64]. Note, that there are other signaling molecules that affect cell differentiation but are not classified as morphogens because they do not match some of the criteria just pointed out [65, 64].

The cells in the target tissue detect the morphogen concentration via receptor molecules on their surface that the morphogens can bind to. They respond by adopting a certain cell fate that depends on the number of receptor molecules on their surface that are bound to morphogens [26, 86, 13]. The different fates are generally identified by the expression state of certain genes, the “target genes” of the morphogen. These genes are either strongly expressed or hardly expressed at all in the cells of the target tissue. Their expression switches discontinuously between these two states at certain threshold values of the morphogen concentration, see Fig. 1.1.

In principle, the local concentration of several different such morphogens distributed in gradients originating from spatially distinct sources provides sufficient information to determine cell fates at well-defined positions in the tissue.

To further clarify the role of morphogen gradients in animal development, it is important to mention that the cells of the organism differentiate progressively during development. This means that the cell fates become more and more precisely specified as development proceeds. The same morphogen molecule usually acts at different stages of the development of one organism and can trigger very different responses in cells depending on their differentiation history. In this sense, cells have a different competence to respond to the morphogen [103]. This is the reason why a very limited number of different morphogen molecules that are often used many times in the development of one organism and frequently even in several different species can lead to a much larger number of different cell fates.

There is growing experimental evidence for the existence of morphogens that act in agreement with the concept specified above [91, 45]. In the late 1980s, Driever and Nüsslein-Volhard experimentally demonstrated the existence of a gradient of the protein Bicoid that acts as a morphogen in the *Drosophila* embryo [22, 23, 24, 25]. More recently discovered morphogens are the molecules Hedgehog (Hh) [5] and Wingless (Wg) [105] both of which play a role in the development of the fruit fly *Drosophila*. Note however, that there are some doubts about the direct action of Wingless [64]. Several further examples are given by the members of the TGF- β superfamily, a class of structurally similar signaling molecules [66] like Activin, Bone Morphogenetic Proteins 2 and 4 (BMP2 and BMP4), Squint, and Sonic Hedgehog (Shh) which act in various contexts in vertebrates and amphibians [15, 21, 46, 12, 85, 64]. Another prominent member of the TGF- β superfamily is the morphogen Decapentaplegic (Dpp) which plays a role in several stages of *Drosophila* development [36, 37, 84, 98, 62, 73]. While, so far, most of the morphogens were identified in animals, there are signs that there are similar molecules affecting pattern formation in plants [8].

1.2 Dpp in the *Drosophila* wing disk

Development has been experimentally investigated in a variety of model organisms [44, 64, 45]. Here, we focus on a model system in which several morphogens have been identified and some of “the most sophisticated studies of morphogen properties and functions” [107] have been done — the “wing imaginal disk” or simply “wing disk” of the fruit fly *Drosophila melanogaster* [51]. The wing disk exists in the larvae stage of *Drosophila* development. This disk undergoes shape changes during later stages of development and ultimately develops into the wing of the adult animal, see Fig. 1.2 B. The wing disk is patterned by gradients of the morphogens Hh, Wg, and Dpp as shown schematically in Fig. 1.2 C. Note, that 19 similar imaginal disks exist in the *Drosophila* larvae which are precursors of the head, the legs, the antenna, and other parts of the adult fly, see Fig. 1.2 A.

Although much more generally applicable, the theoretical aspects of morphogen gradient formation investigated in this work are motivated by the situation of Dpp in the wing disk. It

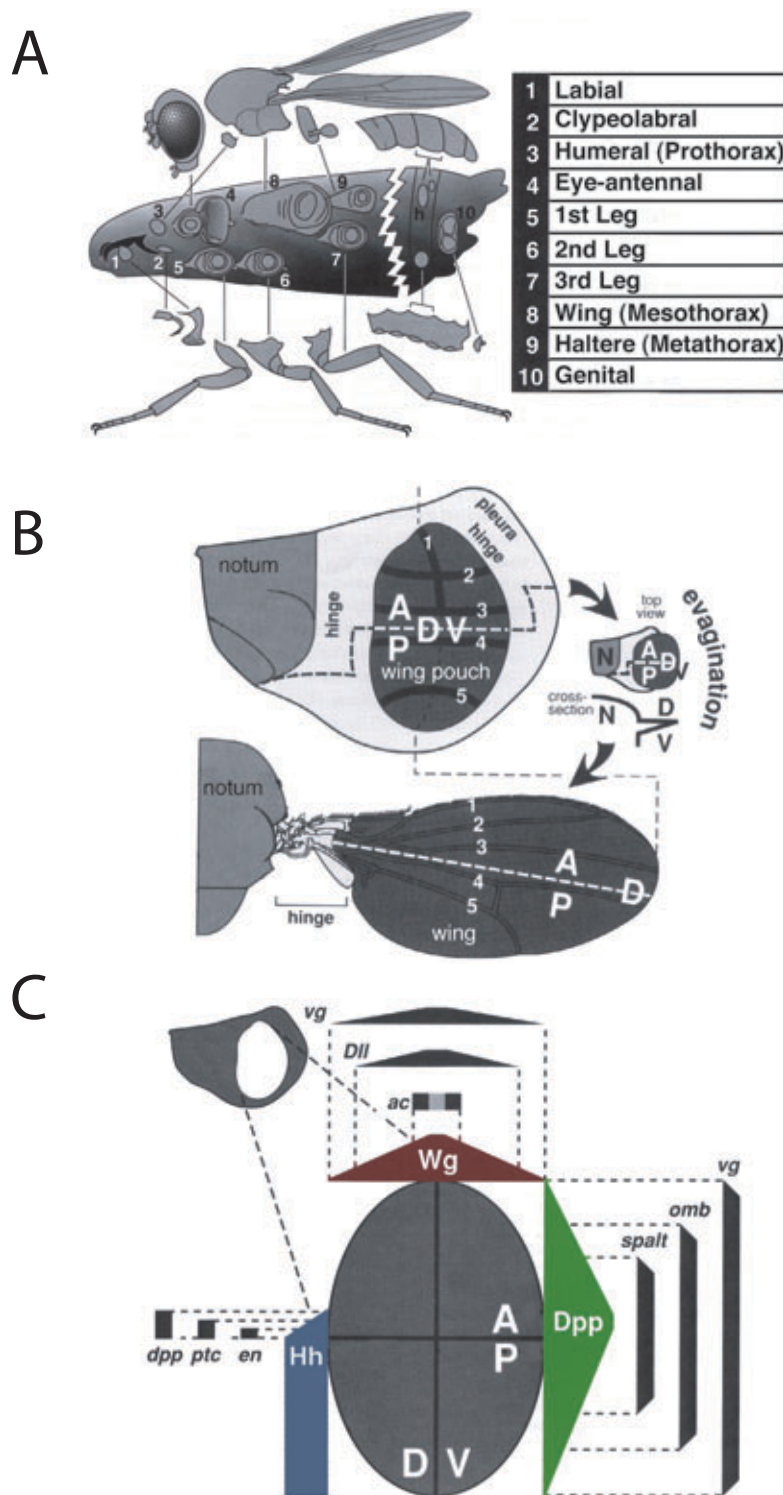


Figure 1.2: Imaginal disks in *Drosophila* development and the patterning of the wing disk. (A) Imaginal disks in the larvae stage of *Drosophila* development. The adult structures that are formed from these disks are indicated. (B) The patterning of the wing disk determines the structure of the wing in the adult animal. The dorsal, ventral, anterior, and posterior compartments of the wing disk and the adult structure are indicated by the initial letters of these terms respectively. The wing disk is folded along the dorsal-ventral compartment boundary line to form the adult wing as indicated. (C) Schematic of the gradients of the morphogens Dpp, Hh, and Wg and the expression domain of their respective target genes in the wing disk. Figure modified from [51, 78].

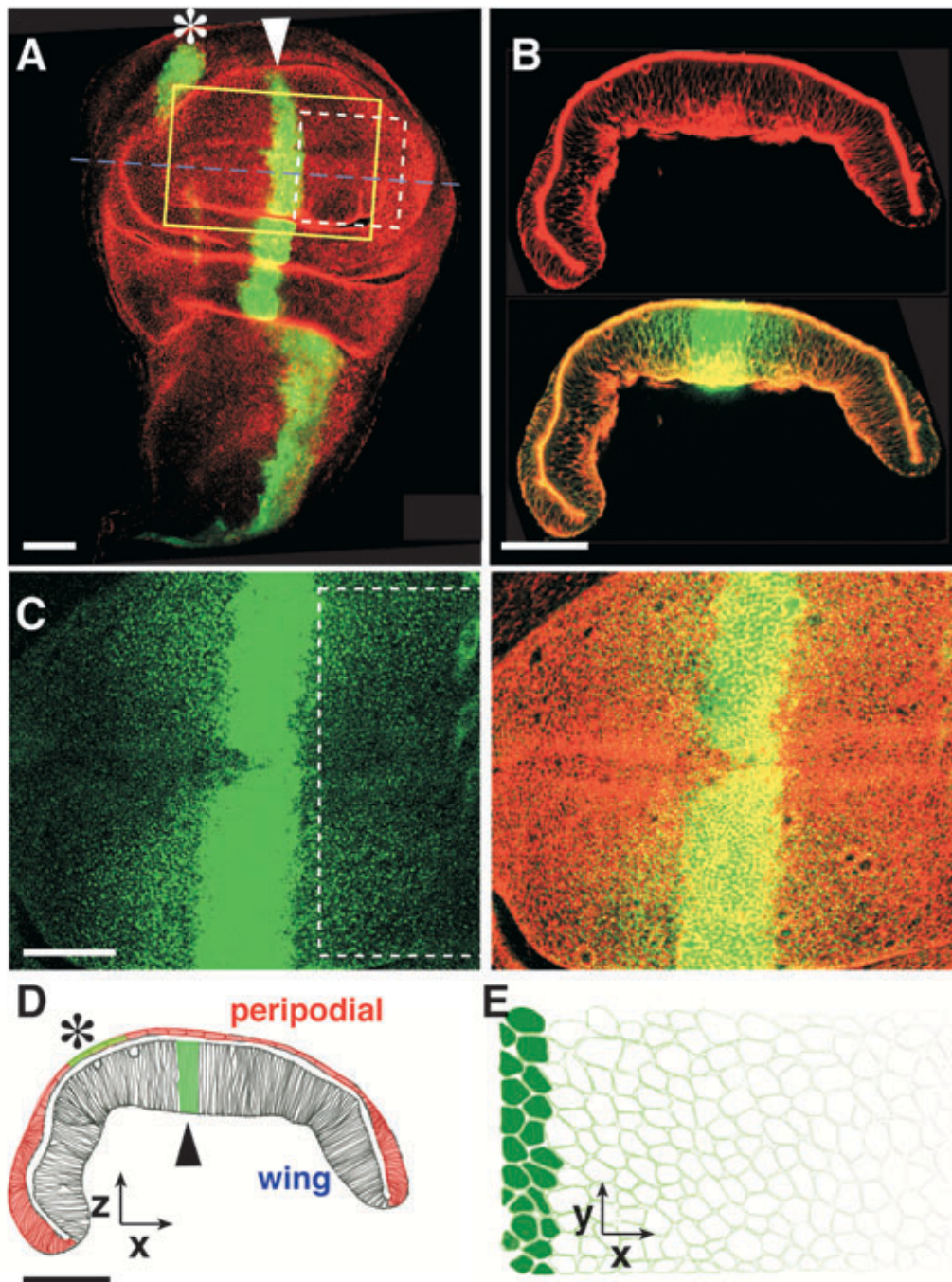


Figure 1.3: Dpp in the *Drosophila* wing disk. (A) Double staining of a developing wing showing the Dpp source labeled in green and the cell profiles labeled in red. The Dpp source in the wing primordium is indicated by the arrowhead, the one in the peripodial epithelium by the asterisk. (B) Double staining of a z -section of a developing wing at the level of the dashed blue line in A, showing cell profiles labeled in red, superimposed by GFP-Dpp expression shown in green in the lower panel. (C) Detail of GFP-Dpp localization (green) in the region of the developing wing corresponding to the yellow box in A. Cell profiles are labeled red in the right panel. (D,E) Schematic representation of the developing wing in a xz - (D) and xy -section (E). Note the position of the Dpp source (cells filled in green at the left in E) both in the wing primordium (arrowhead) and the peripodial epithelium (red in D; asterisk). Bars correspond to $50\ \mu\text{m}$. Anterior to the left, posterior to the right. Figure modified from [59].

is consequently important to get acquainted with a few details concerning this system.

The wing disk is a single layered epithelium which forms a flat pouch consisting of two cell layers, which are connected at the edges, see Fig. 1.3. One cell layer consists of columnar epithelial cells and includes the part of the tissue that will later develop into the wing blade. This epithelial cell layer is called the “wing primordium”. The other layer is called the “peripodial epithelium”. The wing disk is separated into an anterior and a posterior compartment. Cells which produce the morphogen Dpp are located within a narrow band, approximately five cell diameters wide, along the boundary between these two compartments. In the wing primordium, a gradient of the morphogen Dpp forms adjacent to this source in both compartments in a region that is shown by the yellow box indicated in Fig. 1.3 A. The measurements of this region are approximately 100 by 50 cell diameters where a typical cell diameter in this xy -plane of the wing disk is $4\mu\text{m}$. In the z -direction which is vertical to this plane, the cells are about $30\mu\text{m}$ high but Dpp is mostly confined to a sheet of only about $5\mu\text{m}$ height in the z -direction [34].

The target genes of Dpp which are called *spalt* (*sal*), *optomotor-blind* (*omb*), and *vestigial* (*vg*) are expressed in this region. Their respective expression domain is controlled by Dpp in a concentration-dependent manner [87, 62, 73] as illustrated in Fig. 1.2 C.

It is noteworthy that Dpp itself is a target gene of the morphogen Hh which is expressed in the posterior compartment of the wing disk and forms a gradient over up to ten cell diameters into the anterior compartment, see Fig. 1.2 C. Apart from Dpp and Hh, the morphogen Wg is expressed in a source stripe that is roughly orthogonal to the stripe of the Dpp source. The Wg source is located along the boundary between the dorsal and the ventral compartment of the wing disk and gradients of Wg form in these two compartments, see Fig. 1.2 C. In principle, the combination of the Dpp and Wg morphogen gradients can provide complete positional information about the location of a cell in the two dimensional epithelium.

Recently, the Dpp gradient has been visualized in the wing disk by using a GFP-Dpp fusion protein of a green fluorescent protein (GFP) and Dpp [34, 92]. This GFP-Dpp protein can be visualized by excitation with a laser of wavelength 488nm. It has been experimentally demonstrated that GFP-Dpp has a very similar functionality as endogenous Dpp, i.e. unmodified Dpp as it is present in wild type flies, and can consequently be assumed to behave almost identical. In a seminal series of semi-quantitative experiments, GFP-Dpp was found accumulated in structures inside the cells and could also be detected in the extracellular space surrounding the cells. It was detected up to 40 cell diameters away from the source [34]. While there is no evidence for a localized Dpp sink in the wing disk, it was found that GFP-Dpp is degraded throughout the target tissue on a time scale of a few hours. The time scale of gradient formation was estimated to be six to eight hours. Moreover, it was shown that Dpp spreading is nondirectional in the wing disk [34].

Furthermore, the role of endocytosis in Dpp gradient formation was studied [34]. Endocytosis is a process in which the cells internalize molecules from their surface. In this process, the plasma membrane on the cell surface invaginates and forms a vesicle that is pinched off the membrane with the help of a protein called Dynamin. This vesicle is subsequently transported through the interior of the cell [1]. Inside the cell, the contents of the vesicle can be separated and sorted in a specific way. For example, they can be degraded in a so-called “lysosome” or returned to the cell surface by a process termed exocytosis.

Endocytosis can be blocked in the wing disk by the use of “shibire”, a thermo-sensitive mutation of the dynamin gene [14]. Cells carrying the shibire mutation can perform endocytosis at temperatures of about 25°C . At a higher temperature of 34°C endocytosis is almost completely blocked in these cells [34].

An experiment was performed in which endocytosis was blocked in the whole target tissue.

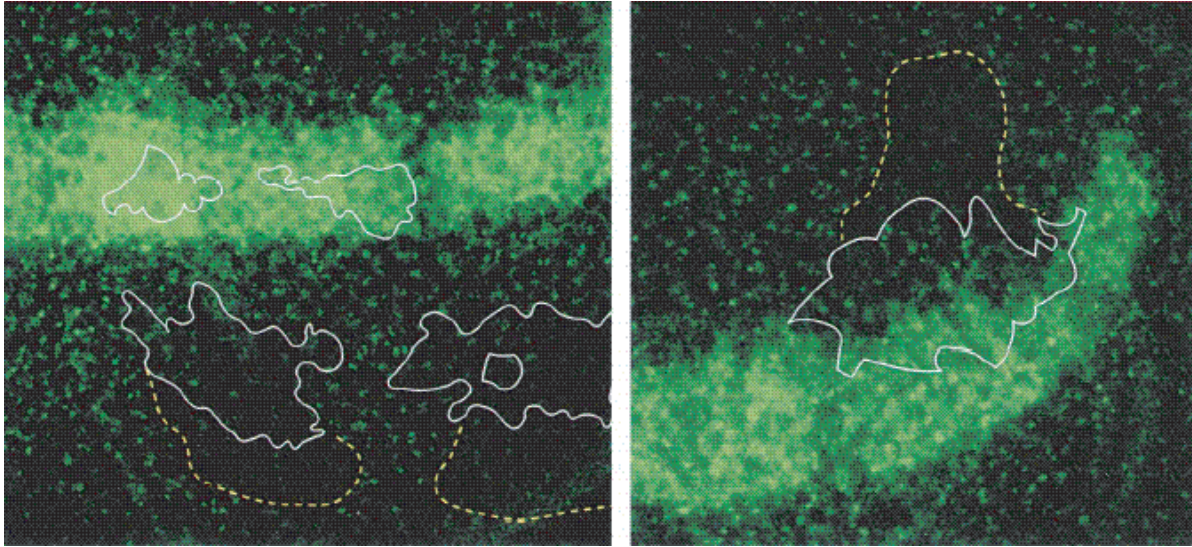


Figure 1.4: GFP-Dpp depletion behind shibire clones, i.e. patches of endocytosis defective cells. GFP-Dpp is shown in green, the bright green stripe constitutes the source of GFP-Dpp producing cells. The shibire clones are outlined in white. Note the depletion of GFP fluorescence in the region behind the clones indicated by the dashed yellow lines. See [34] and main text for details on the experiment. Figure modified from [34].

It was observed that the GFP-Dpp gradient, that is present in the target tissue before the block of endocytosis, vanishes in the following six hours [34]. In another experiment, endocytosis was only blocked in a relatively small patch of cells in the target tissue, called a “shibire clone”, after a front of GFP-Dpp molecules moving towards this patch of cells had been initiated from the Dpp source. A depletion of GFP-Dpp could be observed behind the shibire clone five hours after blocking endocytosis in this clone, see Fig. 1.4. At later times this depletion diminished [34]. Both experiments lead to the suggestion that endocytosis plays an important role in Dpp transport [34, 33, 41]. We will carefully analyze the implications of these experimental data in chapter 2.

1.3 Open questions

Over the last decades, substantial progress has been made in the understanding of various issues related to morphogen gradients and cell differentiation [102, 90, 35]. However, there is a considerable number of open questions remaining.

One of these is how the morphogen gradient, once established, is perceived by the cells, i.e. which are the molecular mechanisms inside the cell that lead to the control of gene expression [45]. It is well-established that the cells detect the local morphogen concentration via receptor molecules that change their conformation when bound to a morphogen molecule as compared to their unbound state [65]. The cell fate is then controlled by the absolute number of morphogen-bound receptor molecules [26, 86] or the ratio of bound and unbound receptor molecules [13].

When morphogen-bound receptors are present, a series of molecular interactions, called a “signaling pathway”, is triggered inside the cell. This pathway ultimately leads to the activation of proteins that control the transcription of the target genes [72, 65]. However, in the *Drosophila* wing disk as in most systems, only some of the molecular components participating in this process could so far be identified [72, 41]. It is consequently unclear how

the concentration-dependent response to the morphogen occurs [72]. While certain signaling pathways have been identified [65], the systematic quantitative study of these networks of many different interacting molecules and genes is an emerging field [3, 30, 95, 49, 53, 104, 75, 80].

A different but equally important question is how morphogen gradients are formed in developing organisms [90, 33, 96]. The morphogen molecules are secreted by the cells in the source region but how are they transported into the target tissue? And how is it possible that a precise pattern of gene expression is established there that is insensitive to perturbations? These are the main questions that we will address in this work.

1.4 Morphogen transport and gradient formation

Suggestions for mechanisms by which morphogen gradients can be formed were made shortly after Wolpert had introduced the concept [101]. In 1970, Crick suggested that these gradients could be established by passive diffusion of the morphogens [18]. He supported this proposal with theoretical arguments concerning the time scale needed for the formation of a gradient by passive diffusion. Notably, he suggested that the morphogens diffuse through the cells and not in the extracellular space surrounding them.

Similar to Crick's original idea, it is widely believed today that morphogens can passively diffuse in the extracellular space which surrounds the cells [89, 93], see Fig. 1.5 A. Experimental data indicating that extracellular diffusion is probably the dominant transport mechanism have been obtained for some morphogens like for example Wg [89]. Moreover, gradient formation based on passive extracellular diffusion has recently been investigated theoretically [28, 60, 29, 59]. While this is one possibility how these molecules could be transported, several other mechanisms have been suggested.

One of these mechanisms is called "planar transcytosis" [39, 6, 34]. In this mechanism, the morphogens are internalized into the cell after binding to a receptor molecule on the cell surface. They are subsequently transported through the cell interior by active mechanisms, and finally externalized at a different location on the cell surface. Repetition of this process results in transport of the morphogen over many cell diameters, see Fig. 1.5 B. Evidence for the importance of this mechanism is given by the results of the experiments studying the role of endocytosis in Dpp transported discussed in section 1.2 [34].

Another possibility is that the morphogens bind to large molecules called "glypicans" which are present on the cell surface and are subsequently transported by diffusion in the cell membrane, see Fig. 1.5 C. While this mechanism is vaguely defined and could not be clearly distinguished in experiments so far, recent data have shown a role of glypicans in morphogen transport [7, 47, 48]. Although apparently not appreciated by the authors of these articles, a very similar mechanism called "bucket brigade" in which morphogen transport is partly due to diffusion of the receptor-bound morphogen in the cell membrane has been suggested earlier as a result of theoretical considerations [56].

Morphogens could also be transported through long thin projections called "cytonemes" that have been shown to exist in the wing disk [83]. These cytonemes could connect cells in the target tissue to source cells, thus providing tubes through which the morphogens could move by diffusion, convection, or even active transport, see Fig. 1.5 D. However, the function of cytonemes is unclear and their role in morphogen transport is largely hypothetical.

Another possibility is that morphogens are carried along with the cells which are displaced during the growth of the tissue [81]. Here, repeated cell divisions in which the morphogens present inside the cell and on its membrane are divided on the two daughter cells and movement resulting from tissue growth leads to the formation of a gradient. As the completion of one cell division cycle typically occurs on a time scale of several hours, this mechanism leads to a

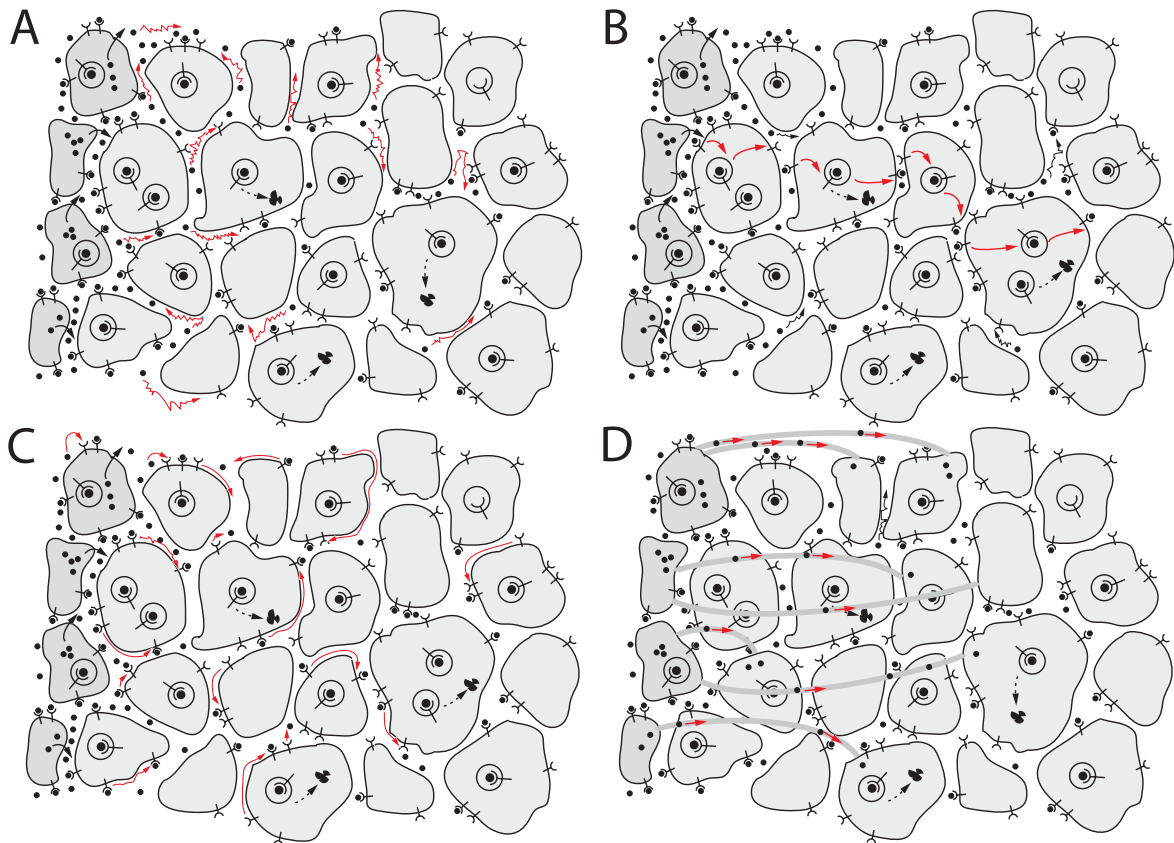


Figure 1.5: Schematic of possible morphogen transport mechanisms. (A) Transport by extracellular diffusion. The morphogens are produced and secreted by the source cells which are shown in darker gray. They move through the tissue by passive diffusion in the extracellular space surrounding the cells. (B) Transport by transcytosis. The morphogens bind to receptor molecules on the cell surface. These complexes are then internalized into the cell and can subsequently be externalized at a random location on the cell surface. The morphogens can then detach from the receptor molecule. Repetition of this process leads to transport over many cell diameters as shown. (C) Transport by diffusion in the cell membrane. The morphogen molecules bind to a molecule that is attached to the cell membrane, e.g. a glypican or a receptor. These complexes then move around the cell surface by passive diffusion in the cell membrane. The morphogens can detach from the molecule in the cell membrane and subsequently bind to one that is located on the surface of a different cell. This results in transport over many cell diameters. (D) Transport via cytonemes which are membrane tubes that connect the source cells to the cells in the target tissue. The morphogens could move through these tubes by passive diffusion, active transport or convection.

slow formation of gradients. Due to this fact, this mechanism is unlikely to be the dominant contribution to the transport of morphogens like Dpp [93].

Independently of the transport mechanism, it has been suggested that morphogens are not transported as individual molecules but rather bundled in membrane vesicles called argosomes [43].

While a considerable amount of data concerning the transport of different morphogens has been obtained [34, 92, 89, 43, 7, 47, 68, 48], these data have so far not lead to the clear identification of a dominant transport mechanism. This is partly due to a lack of quantitative data. While the existence of the suggested morphogen transport mechanisms is often beyond doubt, the question is rather how much they contribute to transport.

For the formation of a stable morphogen gradient, not only transport but also degradation of the morphogen is needed. Degradation can occur inside the cells following the internalization of the morphogen or in the extracellular space where certain molecules, so-called proteases, can degrade the morphogens. While the rate of degradation is known to be position- or concentration-dependent for some morphogens, there are usually no localized morphogen sinks in the tissue [93, 33].

1.5 Robustness and precision of morphogen gradients

It is hard to imagine how reliable morphogen gradients with concentration thresholds located at well-defined positions can form in a developing organism where cells are constantly dividing and noise is ubiquitous. For this reason, many biologists have rejected the idea that these gradients play a role in the patterning of tissues for a long time [74]. Even now that the existence of morphogen gradients has been experimentally demonstrated, the question how they can reliably fulfill their task during development remains.

It has been shown experimentally for Dpp in the *Drosophila* wing disk that the morphogen production in the source cells can be strongly enhanced without affecting the development of the fly significantly [71]. This suggests that the Dpp gradient is robust to changes in the Dpp production rate. Such robustness to perturbations is anticipated to be present in many biological systems [3, 42, 57]. The remarkable robustness of morphogen gradients has recently been investigated theoretically and mechanisms that lead to robust gradients were suggested [28, 29, 9]. Moreover, it was found that time-dependent noise in the morphogen secretion rate of the source can disrupt the robustness of the gradient [32].

The presence of molecule number fluctuations and disorder due to cell-to-cell variability in developing tissues is generally anticipated to lead to relatively strong fluctuations of the local morphogen concentration in a gradient. A strong variability of the gradient of the morphogen Bicoid has indeed been observed in the *Drosophila* embryo [54]. As the concentration thresholds of the gradient must be located at well-defined positions in order to precisely pattern the tissue, such a variability is problematic. In the *Drosophila* embryo, it appears that interactions with other molecules that could not be clearly identified lead to a high precision of the resulting gene expression patterns [54]. In general, however, such backup mechanisms cannot be expected to be present in systems where morphogens act directly on the cells in the target tissue. Thus, it is a relevant question if a high precision of morphogen gradients can be achieved in disordered systems or if other mechanisms are generally needed to achieve a precise patterning of the tissue. While diffusion in disordered media has been studied extensively [50, 10], the presence of disorder has so far received little experimental and virtually no theoretical attention in connection with morphogen gradient formation.

1.6 Overview of this work

This work is a mainly theoretical investigation of morphogen transport and gradient formation. We focus on two transport mechanisms which are supported by considerable experimental evidence — diffusion in the extracellular space and transcytosis.

In chapter 2, we relate a theoretical description of morphogen transport which captures these two transport mechanisms to recent experimental data for the morphogen Dpp in the *Drosophila* wing disk. We investigate in how far two limits of our description in which morphogen transport is primarily due to extracellular diffusion and transcytosis respectively are in agreement with these data. It turns out that transcytosis is in semi-quantitative agreement with the experimental data whereas extracellular diffusion is inconsistent in some points.

In chapter 3, we present and analyze our theoretical description of morphogen transport and degradation in detail. The two limits of this description in which diffusion and transcytosis dominate transport are discussed. Effective nonlinear transport equations for both limits are derived. Chapter 3 is rather technical and focused on theoretical aspects.

In chapter 4, two key results which follow from the theoretical foundations developed in chapters 3 and 5 are discussed. Firstly, we show that morphogen gradients formed by transcytosis are robust, i.e. they do not depend sensitively on the morphogen production rate of the source cells. This robustness is lost if extracellular diffusion gives a significant contribution to transport. Secondly, the precision of morphogen gradients, i.e. their ability to define the position of concentration thresholds in the target tissue with high accuracy, is discussed. It is argued that high precision can only be achieved in systems that are at least two dimensional. Moreover, we reason that transcytosis and possibly also other active transport mechanisms can achieve a higher precision than passive diffusion. These are generic experimentally testable predictions of our theoretical investigation.

Chapter 5 deals with the effects of spatial disorder on steady state morphogen gradients. Among other things, it is shown that the uncertainty of the local morphogen concentration usually increases with increasing distance to the morphogen source in a way that is characteristic of the dimensionality of the system in which the morphogen gradient is formed. The chapter is very technical and strongly concentrates on the theoretical aspects of the effects of disorder.

In chapter 6, we conclude with a summary of the main results of this work. The biological relevance of these findings is discussed and experiments to test predictions of our theoretical investigation are suggested. In appendix A, we present potentially relevant generalizations of our theoretical description of transport. Among other things, we apply the method used in chapter 3 to develop a theoretical description of the glypican model of morphogen transport in section A.3. In appendix B, we discuss the shortcomings of a recently suggested model of morphogen transport by extracellular diffusion [60]. In appendix C, we compare results obtained from our description of morphogen transport to additional experimental data. In most of the remaining appendices, we show details of the calculations performed in this work.

A reader more interested in theoretical problems and technical aspects should concentrate on chapters 3 and 5 while those more interested in the biological relevance of this work should focus on chapters 2 and 4. Chapter 6 is recommended for everyone who would like to get briefly acquainted with the main results of this work.

Chapter 2

Dpp transport in the *Drosophila* wing disk

In this chapter, we present recent experimental data on morphogen gradient formation and apply a theoretical description of morphogen transport to the specific situation of Dpp in the *Drosophila* wing disk. We restrict ourselves to this system because it has been studied extensively in semi-quantitative experiments. Each experiment is compared to numerical calculations based on a theoretical description of morphogen transport which we will discuss and analyze in detail in chapter 3.

The description captures key processes like the diffusion of morphogens in the extracellular space with a diffusion coefficient D_0 , morphogen binding and un-binding to and from receptor molecules that are located on the cell surfaces which is characterized by rates k_{on} and k_{off} , internalization of these receptor-ligand complexes into the cell at rate b_{int} and their subsequent externalization at rate b_{ext} . Free morphogens are degraded by proteases in the extracellular space with rate e_{deg} and ligands bound to receptors are degraded inside the cells with rate b_{deg} . These processes are schematically shown in Fig. 2.1. Moreover, the production and intracellular trafficking of free receptor molecules by the cells is included in the description. These are internalized and externalized with rates f_{int} and f_{ext} respectively. In addition, each cell produces receptors at a rate f_{syn} and degrades them at a rate f_{deg} . The receptor production saturates at a maximal surface receptor concentration R_{max} . Finally, cells belonging to the morphogen source produce morphogens at rate ν .

In this description, morphogens can be transported over many cell diameters by diffusion in the extracellular space and transcytosis, see Fig. 1.5 A and B. Transcytosis occurs when a morphogen binds to a receptor, is internalized into a cell, transported through its interior, and subsequently externalized at a different location of the surface of the same cell. Repeating this process together with morphogens being passed from the cell surface to the surface of neighboring cells leads to long range transport.

The relative contributions of the two mechanisms to morphogen transport depend on the parameter values. In section 2.2, we will perform a comparison of experimental data to calculations using a parameter choice for which transcytosis contributes dominantly to morphogen transport. In section 2.3, we will carry out the same comparison using a different parameter choice for which extracellular diffusion dominates. We will refer to these theoretical descriptions with different parameter sets as the “transcytosis regime” and the “diffusion regime” respectively. We study these regimes in order to find out in how far they are in agreement with the experimental data. Note, that we have previously discussed the diffusion regime in [59] where we called this description the “diffusion, binding, and trafficking model with saturating surface receptor concentration” (DBTS model).

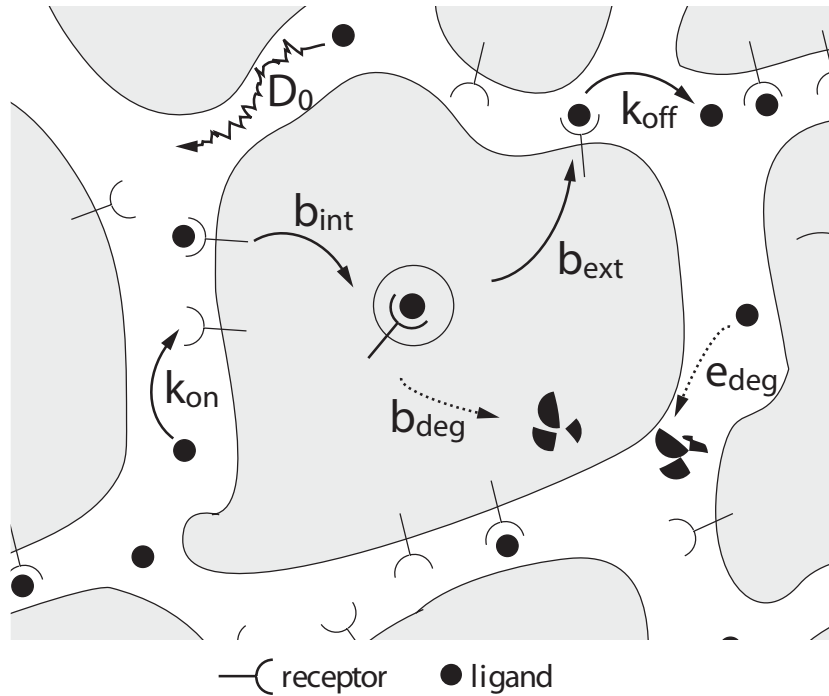


Figure 2.1: Schematic representation of the key processes captured by our theoretical description of morphogen transport. Cells are shown in light gray, the extracellular space in white. The rates of morphogen-receptor binding and un-binding, internalization and externalization of morphogen-receptor pairs are denoted k_{on} , k_{off} , b_{int} and b_{ext} . Degradation of morphogens occurs inside the cells with rate b_{deg} and in the extracellular space with rate e_{deg} . The diffusion of morphogens in the extracellular space is characterized by a diffusion coefficient D_0 . Moreover, free receptors are produced, internalized, and externalized by the cells at rates f_{syn} , f_{int} , and f_{ext} respectively (not shown). See chapter 3 for a more detailed discussion of our theoretical description of morphogen transport.

2.1 Parameters and boundary conditions

In Table 2.1, we show the two sets of parameters which are used throughout this chapter for the transcytosis regime and the diffusion regime and compare them to those used in a previous theoretical study of Dpp transport in the wing disk [60] and to values measured in cell cultures. Since these parameters have not yet been measured experimentally for Dpp and its receptor Thick-veins in the wing disk, we choose their values within plausible limits given by typical values measured for similar systems. For both the diffusion and the transcytosis regime, we have applied several different parameter sets in numerical calculations attempting to obtain the best possible agreement with the experimental data. The two parameter sets used here lead to a reproduction of the time scale of gradient formation and the length scale of the Dpp gradient in wild type wing disks. When we were unable to obtain good agreement with all experimental data discussed here, we tried to achieve the best consistency with the “shibire clone assay”, see below.

The extracellular diffusion coefficient D_0 is chosen much smaller in the transcytosis regime than in the diffusion regime in which D_0 corresponds approximately to the free diffusion coefficient for a particle with the size of a Dpp molecule in a watery liquid [60]. In a tissue, D_0 could be effectively reduced to a very low value if the morphogen molecules bind to cell membranes or components of the extracellular matrix because this would severely obstruct

	transcytosis	extracellular diffusion	Lander et al.	EGF/EGFR
$k_{\text{off}}[\text{min}^{-1}]$	4	6×10^{-4}	6×10^{-4}	0.34
$b_{\text{int}}[\text{min}^{-1}]$	4	0.6	0.036	0.3
$f_{\text{int}}[\text{min}^{-1}]$	1.2	0.36	0.036	0.03
$b_{\text{ext}}[\text{min}^{-1}]$	8	0.04	0.004	0.058
$f_{\text{ext}}[\text{min}^{-1}]$	8	0.03	0.003	0.058
$b_{\text{deg}}[\text{min}^{-1}]$	0.012	0.002	0.002	0.002
$f_{\text{deg}}[\text{min}^{-1}]$	0.004	0.006	0.006	0.002
$e_{\text{deg}}[\text{min}^{-1}]$	0.008	0	0	0.04
$k_{\text{on}}R_0[\text{min}^{-1}]$	6.7	2.4	0.72	(3.73)
$\nu/R_0[\text{min}^{-1}]$	0.053	0.48	0.032	-
$f_{\text{syn}}^0/R_0[\text{min}^{-1}]$	1.6×10^{-3}	0.072	0.072	-
$D_0[\mu\text{m}^2/\text{s}]$	1.5×10^{-3}	10	10	-
R_{max}/R_0	1.6	20	-	-
ψ	2.0	1.0	-	-

Table 2.1: Parameter values used in the numerical calculations in this chapter. The notation used here is extensively explained in section 3.1.1. R_0 denotes the steady state number of receptor molecules present on the surface of one cell in the absence of ligand. Values measured for the epidermal growth factor (EGF) and its receptor (EGFR) in B82 fibroblasts [52, 61, 88, 17] and those suggested by Lander et al. [60] are given for comparison. The value of k_{on} measured for the EGF/EGFR system has been converted to the units used here by assuming a volume of the extracellular space per cell of 3.2×10^{-14} liters and a surface receptor number per cell of $R_0 = 1,000$. The rates of ligand and receptor synthesis per cell are denoted ν and f_{syn}^0 respectively. In the calculations in the extracellular diffusion regime which are based on (3.28), the ligand current j_x across the source boundary of the area of interest (AOI) is obtained from the ligand production rate ν via $j_x = \nu d/2a^2$, where $d = 20\mu\text{m}$ is the width of the source and $a = 4\mu\text{m}$ is the cell diameter. In the calculations in the transcytosis regime, the rate of ligands appearing in the system at $x = 0$ is 3ν capturing the source of three cells width. Due to the discrete lattice structure used in the transcytosis regime, the extracellular diffusion coefficient D_0 had to be estimated using $a = 4\mu\text{m}$.

their free diffusion. The other rates in the transcytosis regime are mostly about an order of magnitude larger than in the diffusion regime. To estimate the contribution of transcytosis to transport for both parameter sets, we have calculated the effective diffusion coefficient D_{tc} in the absence of extracellular diffusion for a small morphogen concentration λ and with the receptor concentration ρ at its equilibrium value in the absence of morphogens ρ_0 . For the parameters in the transcytosis regime, we find $D_{\text{tc}} \approx 0.04\mu\text{m}^2/\text{s}$ and for those in the diffusion regime $D_{\text{tc}} \approx 1.7 \times 10^{-6}\mu\text{m}^2/\text{s}$. The analytic expression of $D_\lambda(\lambda, \rho)$ for a two dimensional triangular lattice as discussed in section 3.2.2 was used with $a = 4\mu\text{m}$ to calculate these values. Here, a denotes the average diameter of the cells in the plane in which transport occurs.

We use R_0 , the steady state number of receptor molecules present on the surface of one cell in the absence of ligands, as a molecule number scale in our description. We further define r_0 as a molecule number per unit area in two dimensions via $r_0 = R_0/a^2$. We do not specify an actual value for R_0 because we only need to compare relative molecule numbers or concentrations to interpret our results. The number of receptor molecules per cell in the wing disk which corresponds to R_0 is believed to be on the order of 10^3 [40, 60].

Geometry of the wing disk and boundary conditions Let us first discuss the geometry of the wing disk. In principle, we need to take the complete geometry of the wing disk described in 1.2 into account in a mathematical description of the ligand kinetics. However, we are only

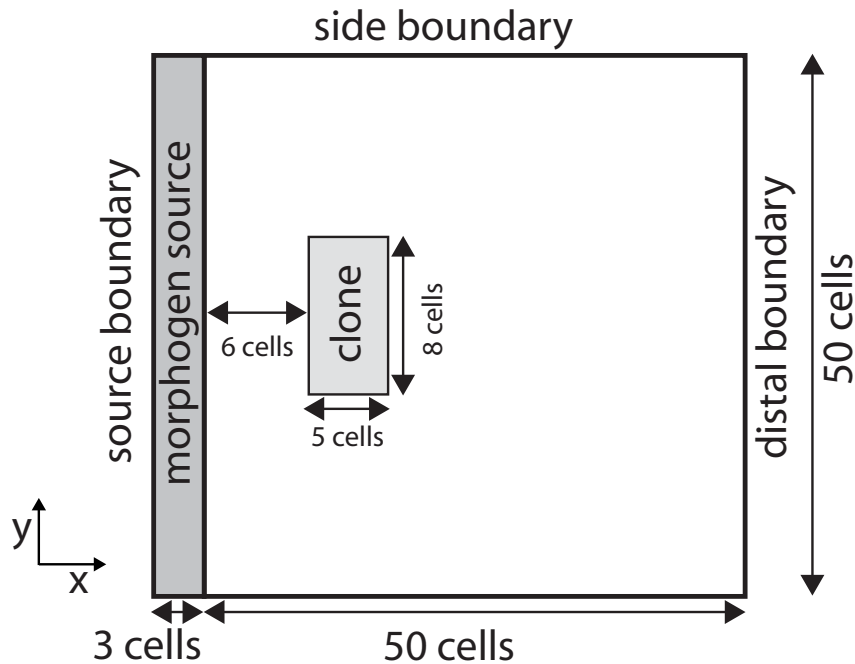


Figure 2.2: Schematic of the geometry and boundaries of the area of interest (AOI) used for the numerical calculations in the transcytosis regime in this chapter. The spatially extended morphogen source is only explicitly described in the calculations corresponding to the *shibire* rescue assay, see section 2.2.2, and the region labeled “clone” only plays a role in the calculations corresponding to the *shibire* clone assay, see section 2.2.3.

interested in the ligand kinetics inside an area of interest (AOI) that is given by the region in the posterior compartment of the wing primordium in which the Dpp gradient forms. This region is outlined by the dashed white lines in Fig. 1.3 A and C. The ligand kinetics inside this rectangular AOI should depend only weakly on the kinetics outside, if the size of the AOI is chosen sufficiently large and reasonable boundary conditions are specified at the edges of the AOI. We will now discuss our choice of boundary conditions at these edges which we refer to as “source boundary”, “distal boundary”, and “side boundaries”, see Fig. 2.2. For simplicity, it is assumed that the Dpp source is homogeneous in the y -direction and mirror symmetric about its center line which coincides with the source boundary of the AOI used here. As we are only interested in gradient formation in either the anterior or the posterior compartment of the wing disk, this symmetry allows us to describe the source by a three cell wide stripe next to the source boundary where ligand is injected into the extracellular space with no flux boundary conditions imposed at the source boundary. This corresponds to half the source diameter of approximately six cells in the wing disk.

Let us consider the distal boundary on the opposite side of the AOI with respect to the source. As the wing disk does not end there, an out-flux of ligand across this boundary is present which becomes small if the ligand concentration is small close to this distal boundary. This out-flux is possibly reduced by an inward current in the opposite direction stemming from secreting cells in the peripodial epithelium, see Fig. 1.3. The total current across this boundary is assumed to be negligible if the distal boundary is located sufficiently far away from the source. Thus, we impose zero flux at this boundary and choose the width of the AOI such that this choice of boundary condition does not affect the results near the source where

the gradient develops.

At the remaining side boundaries of the AOI, we impose periodic boundary conditions. This corresponds to the assumption that the whole system is translation invariant and extends infinitely in the y -direction. This is justified because, although certainly not infinite, the region of the wing disk where the Dpp gradient forms is approximately homogeneous in the y -direction over a considerable range, see Fig. 1.3. In principle, one could also choose no flux boundary conditions at these side boundaries. The specific choice does not affect the results for the situations studied in this chapter.

The initial conditions depend on the specific experimental setup and will be discussed for each experimental situation separately.

2.2 Comparison to our theoretical description in the transcytosis regime

We now compare experimental data to results from calculations based on the theoretical description of morphogen transport introduced in section 3.1.1 with the set of parameters for the transcytosis regime as shown in Table 2.1. All numerical calculations for the transcytosis regime in this section are based on the discrete microscopic description of morphogen transport with receptor kinetics. Specifically, the two dimensional description on a triangular lattice in which the cells are hexagons is used, see section 3.2.1. Since in most experiments discussed here, both endogenous Dpp and fluorescently labeled GFP-Dpp are present in the system, we account for the presence of two distinguishable but otherwise identical ligand species where appropriate, see section A.1 of the appendix for details.

2.2.1 Gradient formation in wild type

In this section, we discuss morphogen gradient formation in the wild type situation. To visualize the morphogen Dpp in these experiments, a green-fluorescent-protein-tagged chimera (GFP-Dpp) is used which fluoresces when excited with a 488nm laser beam. It has been demonstrated that the functionality of this GFP-Dpp is very similar to that of Dpp [34]. Using the UAS/Gal4 expression system that enables the expression of transgenic constructs like GFP-Dpp in well-defined regions of the tissue in *Drosophila* [11], GFP-Dpp is expressed in the same source region as endogenous Dpp. It has been demonstrated that these modifications have very little effect on the development of the flies [34]. Hence, these details can be neglected here and we can assume that the GFP-Dpp observed in these experiments behaves like endogenous Dpp in wild type flies. Details concerning the experimental methods used to obtain the data presented here can be found in [34, 59, 7, 78].

Experimental data Using the thermo-sensitivity of the UAS/Gal4 system, the production of GFP-Dpp in the source is suddenly started when the temperature is shifted from 16°C to 25°C. The following time development of GFP-Dpp gradient formation was studied [34]. It was found that the visible gradient is formed within approximately eight hours and extends more than 30 cell diameters into the target tissue which lies adjacent to the source [34]. After two hours, GFP-Dpp is detected up to twelve and after four hours up to 20 cell diameters away from the source [34]. GFP-Dpp fluorescence is visible in punctate structures inside the cells while less fluorescence can be detected in the extracellular space, see Fig. 2.3 E-K. Extracellular GFP-Dpp was observed by antibody staining against GFP using a specific protocol [59]. Note, that in this experiment even before the temperature shift, there is a gradient of endogenous Dpp which is not labeled with GFP present in the tissue.

Functional Dpp is over-expressed in these experiments because, in addition to the normal synthesis of endogenous Dpp, GFP-Dpp is produced in the source cells. The rate of GFP-Dpp production was experimentally estimated to be roughly five times larger than that of endogenous Dpp [40]. So, in these experiments, the source secretes approximately six times as many morphogen molecules per unit time as in a wild type fly in which only endogenous Dpp is produced. The findings that the flies still develop in a relatively normal way and that the expression patterns of the target genes of Dpp in the wing disk are hardly affected is remarkable. These observations suggest that the formation of the Dpp gradient is insensitive to the Dpp secretion rate of the source although they do not provide direct evidence for this. In section 4.1, we will study this feature in detail.

As a side note, it shall be mentioned that Dpp transport in the wing disk was shown to be nondirectional on length scales that are large compared to the cell diameter a . Patches of GFP-Dpp producing cells, so-called GFP-Dpp flip-out clones, were created and GFP-Dpp was found symmetrically in all directions around these clones in the surrounding tissue [34]. If transport were directional, one would expect to see an asymmetric distribution around these clones.

Apart from the GFP-Dpp profile, the receptor distribution was investigated. Using a specific antibody raised against the Dpp receptor Thick-veins (Tkv), it was found that the receptor is distributed in a “counter-gradient” with low receptor levels near the Dpp source and high levels far away from it [92, 59]. This observation suggests that the presence of Dpp causes the cells to reduce their receptor levels, e.g. by reducing receptor production or enhancing receptor degradation. It was further observed that the receptor mRNA is distributed in a similar counter-gradient as the actual receptor protein [63] which provides support for the view that the lower receptor concentrations near the Dpp source originate in a reduced receptor production that is triggered by the presence of Dpp in a concentration dependent manner. This phenomenon is called “receptor down-regulation”.

Calculation in the transcytosis regime We performed numerical calculations based on our description of morphogen transport in the transcytosis regime to check if these experimental data can be reproduced. As both endogenous Dpp and GFP-Dpp are present in the tissue in this experiment, we use the description for two ligand species, see chapter A.1 of the appendix. We first set the production rate of unlabeled ligand which corresponds to endogenous Dpp to $\nu^* = \nu/5$ and that of the labeled ligand corresponding to GFP-Dpp to zero. The system was then evolved until it was very near its steady state. This situation corresponds to the above experiment before the temperature shift. Mimicking the temperature shift at $t = 0$, the production rate for GFP-Dpp was then suddenly raised to the value ν shown in Table 2.1 while ν^* was left unmodified.

The following time development of the profiles of the receptor and labeled ligand concentrations is shown in Fig. 2.3 A-D. Due to our specific parameter choice, the labeled ligand forms a gradient over roughly 30 cell diameters. The system is very close to its steady state at $t = 8h$. The approach to this steady state is reminiscent of a front of ligands propagating away from the source with decreasing velocity. A counter-gradient of the receptor concentration is present at all times.

In summary, the numerical calculations for the transcytosis regime are able to reproduce the experimentally observed ligand and receptor profiles.

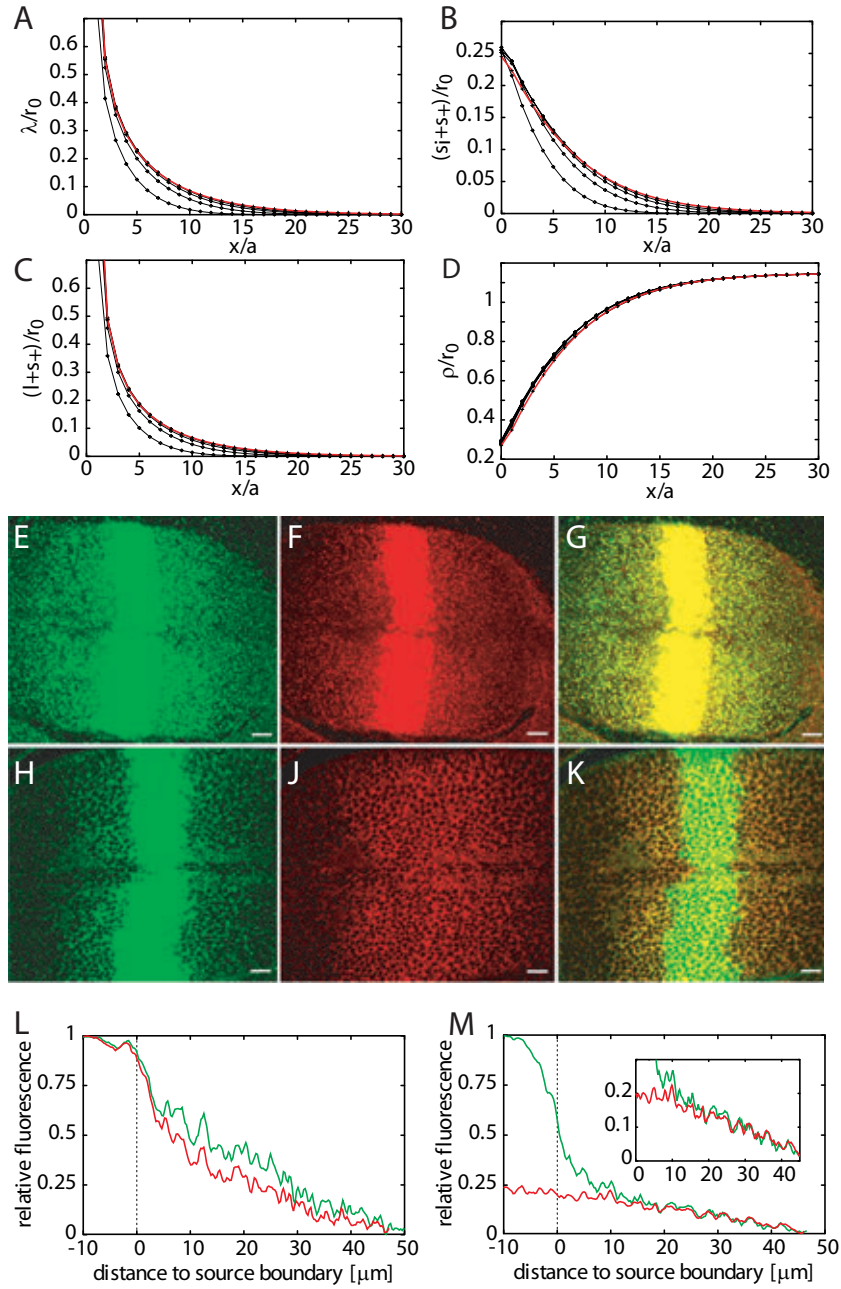


Figure 2.3: GFP-Dpp gradient formation under wild-type conditions. (A-D) Time development of gradient formation calculated using our theoretical description of morphogen transport in the transcytosis regime with parameters as shown in Table 2.1. The concentration profiles of the total ligand λ (A), the receptor-bound ligand $s_+ + s_i$ (B), the extracellular ligand $l + s_+$ (C), and the total receptor ρ (D) are shown at $t = 1\text{h}, 3\text{h}, 5\text{h}, 7\text{h}$ (solid black lines), and in steady state (red lines). All concentrations are normalized to the steady state cell surface receptor concentration in the absence of ligands r_0 . (E-G) Gradient of total GFP-Dpp in the wing disk measured by GFP fluorescence (E) and antibody staining against GFP (F), overlay of both (G). (H-K) Gradient of GFP-Dpp measured by GFP fluorescence after applying an extracellular staining protocol (H) and extracellular GFP-Dpp measured by antibody staining against GFP (J), overlay of both (K). (L) Quantified fluorescence as a function of the distance to the Dpp source of the gradient shown in E (green) and of that shown in F (red). (M) Quantified fluorescence as a function of the distance to the Dpp source of the gradient shown in H (green) and of that shown in J (red). Images (E-M) are taken from [59]. Scale bars in E-K correspond to $10\mu\text{m}$.

2.2.2 Shibire rescue assay

The *shibire* mutation in *Drosophila* is a thermo-sensitive mutation that affects the protein Dynamin which is needed to perform endocytosis [14]. In the “*shibire* rescue assay”, the role of Dynamin-dependent endocytosis in gradient formation is studied. Mutant flies are used that behave similarly to wild type flies at 25°C, the permissive temperature of the *shibire* mutation. If the temperature is raised to 34°C, the restrictive temperature of the *shibire* mutation, endocytosis is blocked in all cells of the wing disk except for those of the Dpp source which are rescued from the effects of the mutation and can be assumed to function normally, see [34] for details.

Experimental data In *shibire* rescue wing disks at 25°C, the observed GFP-Dpp gradients are similar to those in wild type flies. After shifting to the restrictive temperature of the *shibire* mutation, the GFP-Dpp gradient vanishes in the following hours [34]. Six hours after the temperature shift, the amount of GFP-Dpp found in the target tissue has strongly decreased and only very little GFP-Dpp is detectable in the extracellular space in a range of three cell diameters adjacent to the Dpp source. The extracellular, i.e. free and surface receptor bound, GFP-Dpp concentration profile was investigated separately by antibody staining against GFP. It was found that the extracellular GFP-Dpp concentration in the gradient region is strongly reduced six hours after the temperature shift [59], see Fig. 2.4 D-F. The total and extracellular GFP-Dpp levels in the source appear almost unchanged in these experiments. Moreover, the total and extracellular receptor concentrations were investigated by antibody-staining. No large changes of these concentrations in comparison to control experiments could be detected after six hours at the restrictive temperature [59], see Fig. 2.4 G-L.

In our theoretical description of morphogen transport, endocytosis corresponds to the internalization step, in which a receptor-ligand complex or a free receptor is transported from the surface of a cell into its interior. Hence, the effect of a temperature shift for a *shibire* rescue wing disk translates to the reduction of the internalization rates for the bound and free receptor, b_{int} and f_{int} , for all cells except for those in the source region. As experimental data indicate that endocytosis is almost completely blocked in *shibire* mutants, we could reduce these rates to zero. However, we consider it more realistic to assume that there is some residual endocytosis in *shibire* mutant cells which was previously suggested in [60]. Consequently, we strongly reduce b_{int} and f_{int} to 3% of their wild type values. The amount of this decrease is somewhat arbitrary. The rates can be reduced to another small fraction of their original values or zero without significantly changing the following results.

Calculation in the transcytosis regime We performed a numerical calculation corresponding to this experimental situation using the parameter set in the transcytosis regime. The morphogen source was explicitly described by a three cell wide stripe adjacent to the source boundary in which each cell feeds morphogen molecules into the extracellular space which surrounds it at rate ν . The boundary line between this source and the receiving cells is located at $x = 0$. We used a steady state gradient calculated for the wild type rates b_{int} and f_{int} as initial condition and reduced b_{int} and f_{int} as described above at $t = 0$. The following evolution of the ligand and receptor profiles is shown in Fig. 2.4. At $t = 6\text{h}$, the total and the extracellular ligand concentration in the region of the receiving cells have both roughly decreased by a factor of three, see Fig. 2.4 A and B. At that time, the surface receptor concentration in the immediate proximity of the source region has risen by a factor of up to three compared to its value at $t = 0$. Farther away from the source the surface receptor concentration has only slightly increased by a factor of around 1.5, see Fig. 2.4 C.

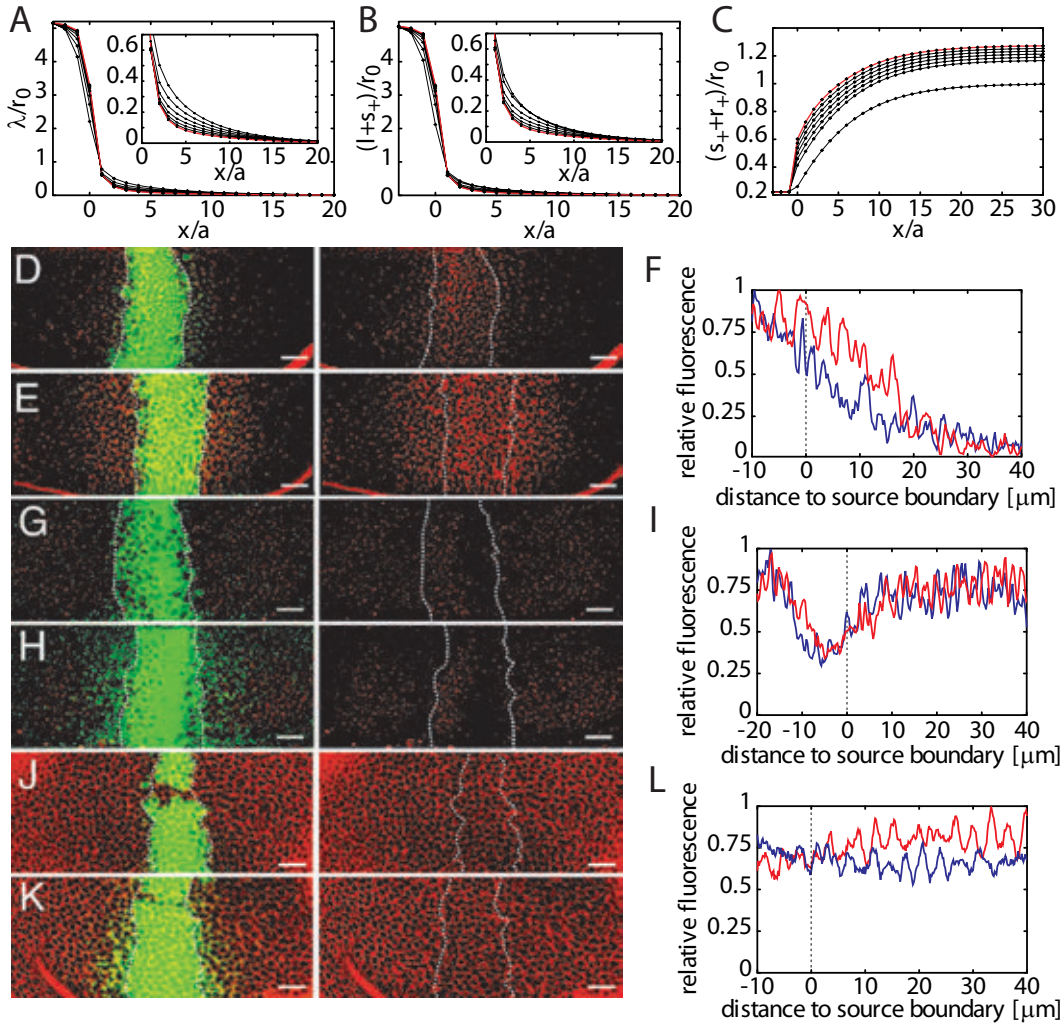


Figure 2.4: Shibire rescue assay for the conditions used in [34, 59] in comparison to results of calculations based on our theoretical description of morphogen transport in the transcytosis regime. A source region of three cell diameters width located at $x < 0$ was explicitly simulated, see main text for details. (A-C) Time development of the profiles of the total ligand concentration λ (A), the extracellular ligand concentration $l + s_+$ (B), and the surface receptor concentration $s_+ + r_+$ (C). Lines are separated by one hour. The profiles at $t = 6$ h, the time at which the experimental observations were made, are shown by the red lines. The insets in A-C show a magnified view of the region $0 \leq x \leq 20$. All concentrations are normalized to the steady state cell surface receptor concentration in the absence of ligands r_0 . (D,E) Double labeling showing GFP-Dpp (green) and immunostaining of extracellular GFP-Dpp (red) for a shibire rescue fly (D) and a heterozygous control (E) that were kept at 34°C for six hours. Note, that the range of the extracellular GFP-Dpp gradient is strongly reduced in D. (F) Normalized fluorescence intensity profiles of extracellular GFP-Dpp in the control (red line) and the shibire rescue fly (blue line). (G,H) Double labeling showing GFP-Dpp (green) and immunostaining of the Dpp-receptor Tkv (red) for a shibire rescue fly (G) and a heterozygous control (H) that were kept at 34°C for six hours. (I) Normalized fluorescence intensity profiles of Tkv immunostaining in the control (red line) and the shibire rescue fly (blue line). No significant change of the receptor levels in the receiving tissue is observed. (J,K) Double labeling showing GFP-Dpp (green) and immunostaining of surface Tkv (red) for a shibire rescue fly (J) and a heterozygous control (K) that were kept at 34°C for six hours. (L) Normalized fluorescence intensity profiles of surface Tkv in the control (red line) and the shibire rescue fly (blue line). No significant change of the surface receptor levels in the receiving tissue is observed. Scale bars $10 \mu\text{m}$. See [59] for more details on the experiments. D-L are taken from [59].

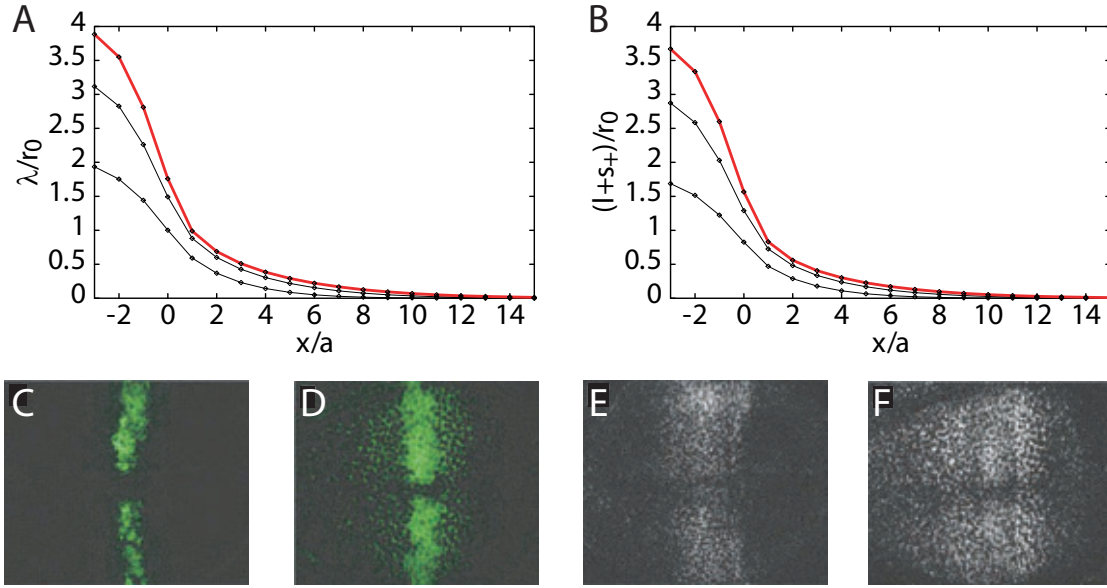


Figure 2.5: Modified shibire rescue assay [7] in comparison to the results of a corresponding calculation based on our theoretical description of morphogen transport in the transcytosis regime. (A,B) Time development of the total (A) and extracellular (B) ligand profiles obtained from the calculation, see main text for details. Lines are separated by one hour. The profiles at $t = 3$ h are shown in red. The concentrations are normalized to the steady state cell surface receptor concentration in the absence of ligands r_0 . (C,D) Total GFP-Dpp fluorescence in the wing disk of a shibire rescue fly kept at 16°C (C) and after three hours at 32°C (D). (E,F) Extracellular GFP-Dpp detected by antibody staining at 16°C (E) and after three hours at 32°C (F). (C-F) were taken from [7].

The calculation with parameters in the transcytosis regime leads to results that are consistent with the ligand profiles experimentally observed in the shibire rescue assay. The same statement holds for the receptor profiles. The slight increase of the receptor concentrations found in the calculation would be hard to detect by the relatively insensitive method of antibody-staining used to measure the receptor concentrations in the experiments. Note, that a sufficiently large extracellular ligand degradation rate e_{deg} is crucial for the rapid decrease of the ligand concentration in the region of the receiving cells because most of the ligand that is initially inside the cells is externalized after the reduction of the internalization rate b_{int} and f_{int} .

Modified shibire rescue assay A shibire rescue experiment was also performed under different conditions. Belenkaya et al. [7] first kept the flies at 16°C where endocytosis works but almost no GFP-Dpp is produced by the source cells. They then shifted the temperature to 32°C for 3 hours. At this temperature, endocytosis in shibire mutant cells is significantly reduced but not as strongly as at 34°C [34, 77]. The extracellular and total ligand profiles were then observed by antibody staining against GFP and measuring GFP fluorescence respectively. Extracellular and total GFP-Dpp was detected in a graded distribution that extended approximately ten cell diameters into the target tissue, see Fig. 2.5 C-F.

Calculation in the transcytosis regime We performed numerical calculations corresponding to this situation for the transcytosis regime. As initial condition, we used a tissue devoid

of ligand in steady state. Mimicking the temperature shift at $t = 0$, the ligand production rate in the source was increased to ν . Simultaneously, the internalization rates b_{int} and f_{int} were reduced by a factor of five to simulate a reduction of endocytosis that is less pronounced than in the previous simulation corresponding to the experiment done at 34°C. The resulting profiles of the total and extracellular ligand concentrations are shown in Fig. 2.5. The gradients of total and extracellular ligand reach approximately ten cell diameters away from the source at $t = 3\text{h}$.

The ligand and receptor profiles obtained from the numerical calculations with parameters in the transcytosis regime are thus consistent with those observed experimentally in the modified shibire rescue assay. However, we would like to point out that this modified shibire rescue experiment is only of limited value because it appears evident that the initiation of GFP-Dpp production in the source cells leads to some increase of total and extracellular GFP-Dpp in the receiving cells.

2.2.3 Shibire clone assay

The “shibire clone assay” is a more sophisticated means for studying the role of endocytosis in Dpp transport. Again, mutant flies are used that behave like wild type flies at 25°C, the permissive temperature of the shibire mutation. Upon heating the flies to the restrictive temperature 34°C, endocytosis is blocked, but only in small patches of cells in the wing disk which are called “shibire clones” [34]. The remaining tissue can perform endocytosis normally. Moreover, the Dpp source cells secrete GFP-Dpp in large amounts only after the temperature shift to 34°C, while endogenous Dpp is secreted by these cells independently of the temperature. This experiment is less invasive than the shibire rescue assay because only few cells in the tissue are affected by the shibire mutation. The remaining cells possess one functional copy of the dynamin gene and can be considered to behave similar to wild type cells. A detailed account of how this complicated experiment is performed and how shibire clones are created in developing flies is given in [34].

Experimental data Following the temperature shift, GFP-Dpp propagates from the source into the receiving tissue towards the clones. After a certain time, typically five hours, a transient GFP-Dpp depletion behind the clones is observed [34], see Fig. 1.4. Here, “behind” refers to the side of the clone that lies distal to the source. At twelve hours after the temperature shift, this depletion cannot be observed anymore. This suggests that the shadow has been filled by GFP-Dpp moving around or through the clone. Inside the clones, relatively small amounts of GFP-Dpp are observed during this whole time span.

The shibire clone assay has been repeated by Belenkaya et al. [7] who used essentially the same procedure as described above. Five hours after the temperature shift to 34°C, the extracellular ligand profiles were observed using antibody staining against GFP. An accumulation of extracellular GFP-Dpp was detected in shibire clones.

The Dpp receptor levels at the restrictive temperature were also experimentally investigated using shibire clones. In the experiments by Belenkaya et al., slightly increased total receptor levels were observed in shibire clones after five hours of endocytic block [7]. We, however, were not able to detect a significant change of the surface receptor levels as compared to the wild type situation [59]. Independent of these details, we would like to emphasize that there is no evidence for a reproducible rapid increase of the surface receptor concentration in shibire clones at the restrictive temperature.

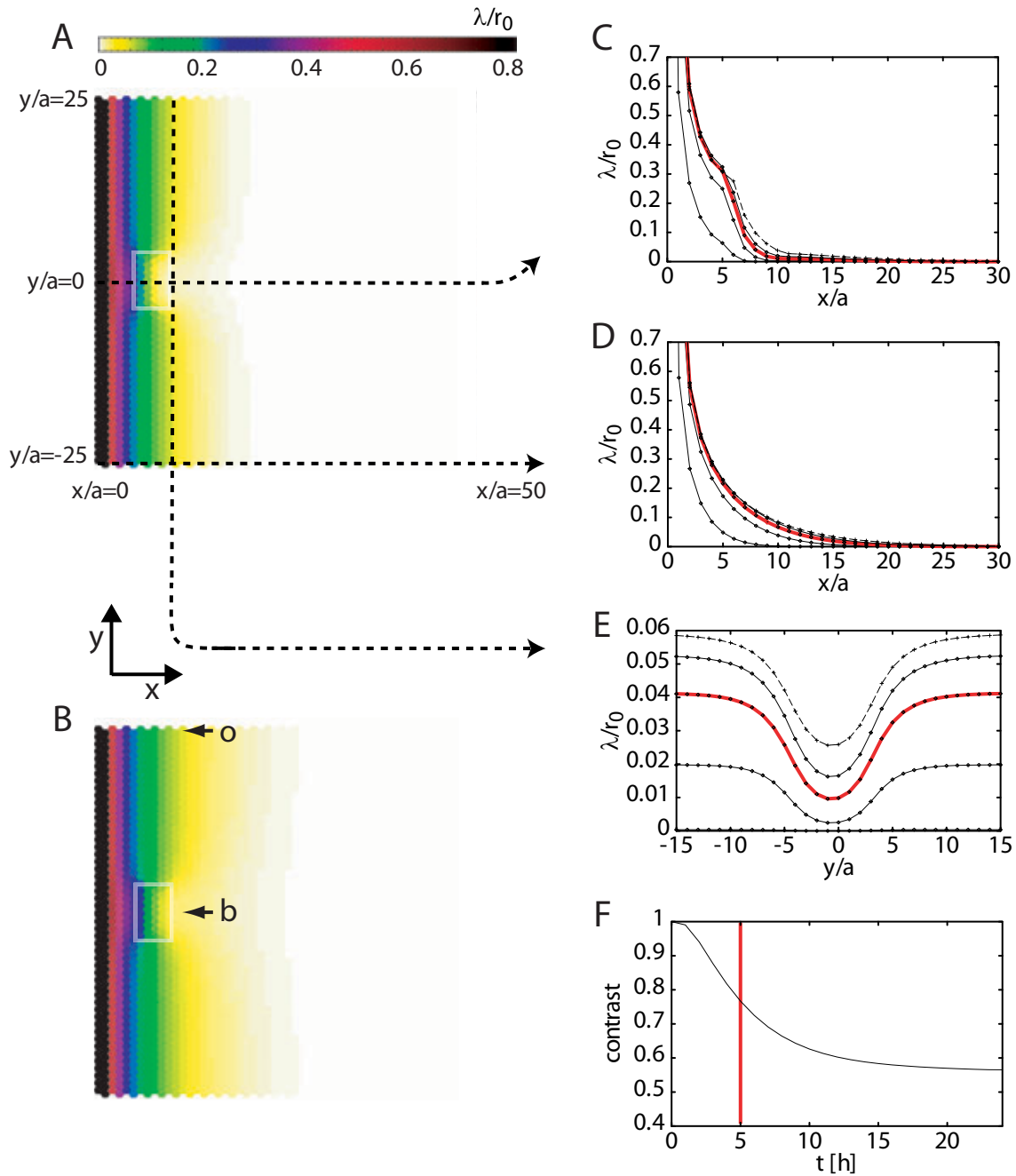


Figure 2.6: Profiles of the total ligand concentration λ in a calculation corresponding to the shibire clone assay based on our theoretical description of morphogen transport in the transcytosis regime. (A,B) Profiles of the total ligand concentration at $t = 5$ h (A) and at $t = 24$ h which is very close to the steady state (B). The region corresponding to the clone is indicated by the transparent white boxes, see also Fig. 2.2. (C-E) Time development of the total ligand concentration λ along slices in the x -direction through the clone (C), far away from the clone (D), and along a slice in the y -direction behind the clone (E) as indicated by the dashed lines in A. Profiles are shown at $t = 1$ h, 3h, 5h, 7h, and in steady state. The profiles at $t = 5$ h at which time the observations in the experiments were made [34] are shown in red and those in the steady state by broken lines. (F) Contrast of the ligand depletion behind the clone as defined in equation (2.1). The two positions at which the values of λ are compared to calculate the contrast are indicated by the arrows in B. All concentrations are normalized to the steady state cell surface receptor concentration in the absence of ligands r_0 .

Calculation in the transcytosis regime We performed numerical calculations in the transcytosis regime corresponding to this experimental setup. As initial condition, a steady state gradient of the unlabeled ligand as in the calculation corresponding to the wild type experiment described in section 2.2.1 was used. Mimicking the effects of the temperature shift, the production rate of the labeled ligand was raised from 0 to ν at $t = 0$. Simultaneously, the internalization rates b_{int} and f_{int} were reduced to 3% of their wild type values in a rectangular patch of 5×8 cells located at a distance of six cells from the source, see Fig. 2.2. This patch mimics a typical shibire clone. Note, that this is the same way the effect of the shibire mutation at 34°C was described in the calculation corresponding to the shibire rescue assay discussed in section 2.2.2.

The following time development of the obtained ligand and receptor profiles is shown in Fig. 2.6. A depletion of the total ligand concentration is seen behind the clone. A dimensionless measure for the strength of this “shadow” is given by the contrast c defined as

$$c(t) = 1 - \frac{\lambda_b(t)}{\lambda_o(t)}, \quad (2.1)$$

where $\lambda_b(t)$ denotes the total labeled ligand concentration directly behind the clone and $\lambda_o(t)$ that at a position of equal distance to the source but far away from the clone. The two locations used here are indicated by the arrows in Fig 2.6 B. The time development of the contrast is shown in Fig 2.6 F. It is apparent that the contrast is largest in the beginning and decreases with time.

There is no significant amount of intracellular ligand present inside the clone region at any time during this simulation. In Fig. 2.7, we show the corresponding distributions of extracellular ligands. In the part of the clone region facing the source, an accumulation of extracellular ligand is seen at five hours and later times, see Fig. 2.7 E.

While the exact shape of the two dimensional ligand profiles and the function $c(t)$ depend on the specifics of the somewhat arbitrarily chosen clone geometry, the qualitative behavior described here is independent of these details. Consequently, we find that the ligand profiles inside and outside of the clone region obtained from the numerical calculations for the transcytosis regime are consistent with those observed experimentally. The very large contrast in the first hours cannot be observed in the experiments because at these times, there is only very little GFP-Dpp near the clone, see Fig. 2.6 C and E. At $t = 5\text{h}$, detectable amounts of ligand are present around the clone and the contrast is still above 0.75 which explains why a shadow can be observed in the experiments at this time. After $t = 12\text{h}$, the contrast decays to values below 0.6 which is probably too small to be detectable in the experiments. Note, that the contrast $c(t)$ overestimates the intensity of shadows because only the ligand concentration at one point directly behind the clone enters whereas in the experiments, the fluorescence intensity in a larger region behind the clone is observed. Finally, we would like to mention that the accumulation of extracellular ligand inside the clone region does not occur if the internalization rates b_{int} and f_{int} are reduced to zero in the clone region.

In summary, we find that the transcytosis regime of our description is in semi-quantitative agreement with the key experiments on Dpp that were discussed in this section.

2.3 Comparison to our theoretical description in the extracellular diffusion dominated regime (DBTS model)

In this section, we compare the data of three key experiments — gradient formation in wild type, the shibire clone assay, and the shibire rescue assay — to calculations based on our

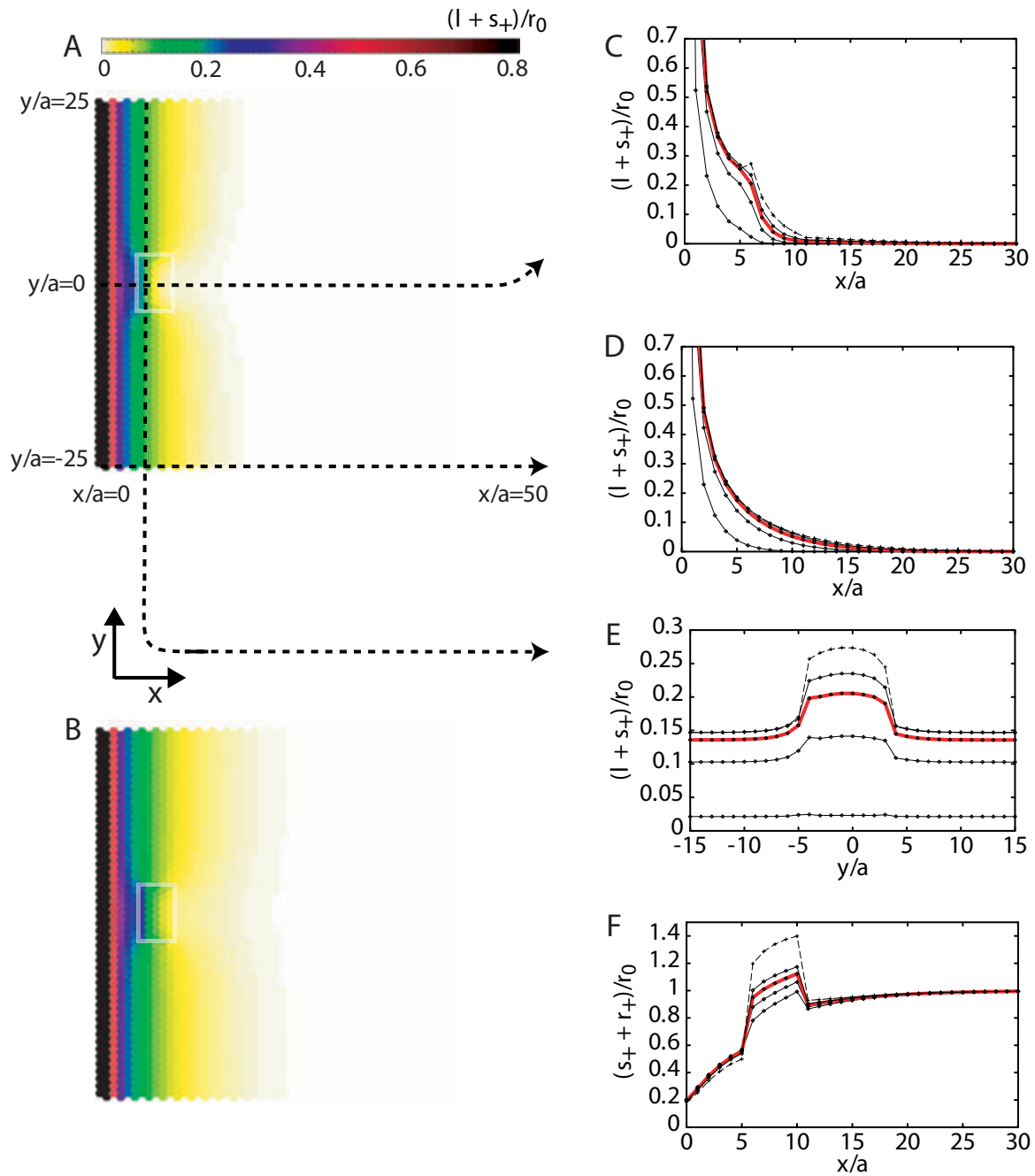


Figure 2.7: Profiles of the extracellular ligand concentration $l + s_+$ in a calculation corresponding to the shibire clone assay based on our theoretical description of morphogen transport in the transcytosis regime. (A,B) Profiles of the extracellular ligand concentration at $t = 5\text{h}$ (A) and at $t = 24\text{h}$ which is very close to the steady state (B). The region corresponding to the clone in which b_{int} and f_{int} are reduced to 3% of their wild-type values is indicated by the transparent white boxes, see also Fig. 2.2. (C-E) Time development of the extracellular ligand concentration $l + s_+$ along slices through the clone in the x -direction (C), far away from the clone in the x -direction (D), and through the clone in the y -direction (E) as indicated by the dashed lines in A. Profiles are shown at $t = 1\text{h}, 3\text{h}, 5\text{h}, 7\text{h}$, and in steady state. (F) Surface receptor concentration $s_+ + r_+$ along the same slice as in C. The profiles at $t = 5\text{h}$ at which time the observations in the experiments were made [7] are shown in red and those in the steady state by broken lines. All concentrations are normalized to the steady state cell surface receptor concentration in the absence of ligands r_0 .

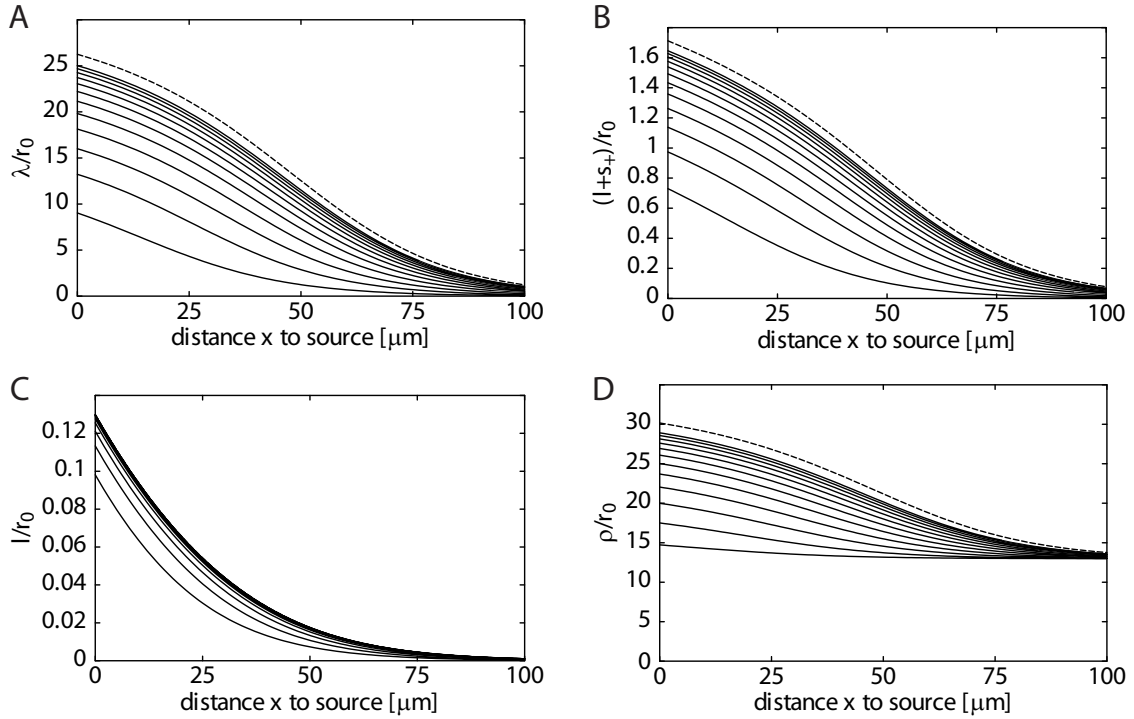


Figure 2.8: Gradient formation corresponding to wild-type conditions obtained from calculations based on the theoretical description of morphogen transport in the diffusion regime (3.28). (A-D) Time development of gradient formation. The concentration profiles of total ligand λ (A), extracellular ligand $l + s_+$ (B), free extracellular ligand l (C), and total receptor ρ (D) are shown during gradient formation. The lines are separated by two hours and the respective steady states are shown by the broken lines. The initial conditions imposed at $t = 0$ were $l = s_+ = s_i = 0$, $r_+ = r_0$, and $r_i = f_{\text{int}}/f_{\text{ext}}^0$, where $r_0 = f_{\text{syn}}^0 f_{\text{ext}}^0 / a^2 f_{\text{deg}} f_{\text{int}}$. All concentrations are normalized to r_0 . Parameters as shown in Table 2.1 with $r_{\text{max}} = R_{\text{max}}/a^2$. Figure modified from [59].

theoretical description in the diffusion regime. We previously presented these results in [59] where we called the diffusion regime of our description the “diffusion, binding, and trafficking model with saturating surface receptor concentration” (DBTS model).

For all calculations discussed here, the set of reaction-diffusion equations of the DBTS model (3.28) is solved for an AOI of $200\mu\text{m} \times 200\mu\text{m}$ with boundary conditions as introduced above. This AOI is equivalent to the one used in the calculations for the transcytosis regime as a typical cell diameter in the wing disk is $a = 4\mu\text{m}$. The set of parameters in the diffusion regime shown in Table 2.1 with $r_{\text{max}} = R_{\text{max}}/a^2$ is used. The use of equations (3.28) implies that we always neglect the presence of endogenous Dpp in the tissue and that we use a slightly different description of the receptor kinetics than in the transcytosis regime as will be discussed in section 3.4. The results presented here are not significantly affected by these details, see also chapter B of the appendix.

2.3.1 Gradient formation in wild type

We performed a numerical calculation corresponding to gradient formation in wild type as described in section 2.2.1 using the set of parameters in the diffusion regime. As initial condition, a tissue devoid of ligand in steady state was used. The resulting time development of the ligand and receptor profiles is shown in Fig. 2.8. The ligand profiles are consistent with the experimental observations. Note, however, that the ligand profiles exhibit differences compared to the results of the calculation with parameters in the transcytosis regime. The free extracellular ligand gradient is established over a considerable range after a short time of about two hours. The total ligand concentration increases over the whole gradient range during gradient formation, i.e. its time development does not resemble a front propagating away from the source. These differences between the diffusion regime and the transcytosis regime could so far not be distinguished in the experiments because there are no reliable data on the time development of the free extracellular morphogen concentration during gradient formation.

2.3.2 Shibire rescue assay

We repeated the calculation corresponding to the shibire rescue assay described in section 2.2.2 using the set of parameters in the diffusion regime. As before, we explicitly included the morphogen source in our description. The source is mimicked by a stripe of $10\mu\text{m}$ width located at $x < 0$ in which the free extracellular ligand concentration l is increased at a constant rate $\nu/2a^2$ with the remaining kinetics unaltered. As discussed above, zero flux boundary conditions are imposed at the edge of this stripe at $x = -10\mu\text{m}$. The block of endocytosis at the restrictive temperature 34°C is mimicked by setting the corresponding rates b_{int} and f_{int} to zero. In Fig. 2.9, we show the time development of the resulting profiles of ligand and receptor concentration. While the total ligand concentration λ slightly increases outside of the source region, a strong increase of the extracellular ligand concentration $l + s_+$ and the surface receptor concentration $s_+ + r_+$ is found there.

This is in contrast to the experimental data which show a strong decrease of the total and extracellular Dpp concentration and no significant increase in surface receptor levels [59]. The increase of the extracellular ligand concentration $l + s_+$ and the surface receptor concentration $s_+ + r_+$ occurs because the main effect of endocytosis in the diffusion regime of our description is to remove receptor bound ligands and free receptors from the cell surface and thus the extracellular space. Consequently, a reduction of endocytosis leads to an increase of the extracellular ligand and receptor concentrations.

One should ask the question if better agreement with the experimental data can be achieved for a different parameter choice in the diffusion regime. It appears impossible that the extracellular ligand concentration could decrease because blocking endocytosis effectively reduces ligand degradation and does not directly affect ligand transport as long as the set of parameters is in the diffusion regime. We have also numerically verified that a larger extracellular degradation rate e_{deg} does not change the behavior described above. Moreover, the results presented here do not change significantly if the effect of the shibire mutation is mimicked by strongly reducing the internalization rates b_{int} and f_{int} to a value that is still larger than zero. In principle, the increase of the surface receptor concentration could be suppressed by choosing a smaller value for R_{max} . However, as we will see below, a strong increase of the surface receptor concentration is needed to obtain results consistent with experimental data in the shibire clone assay.

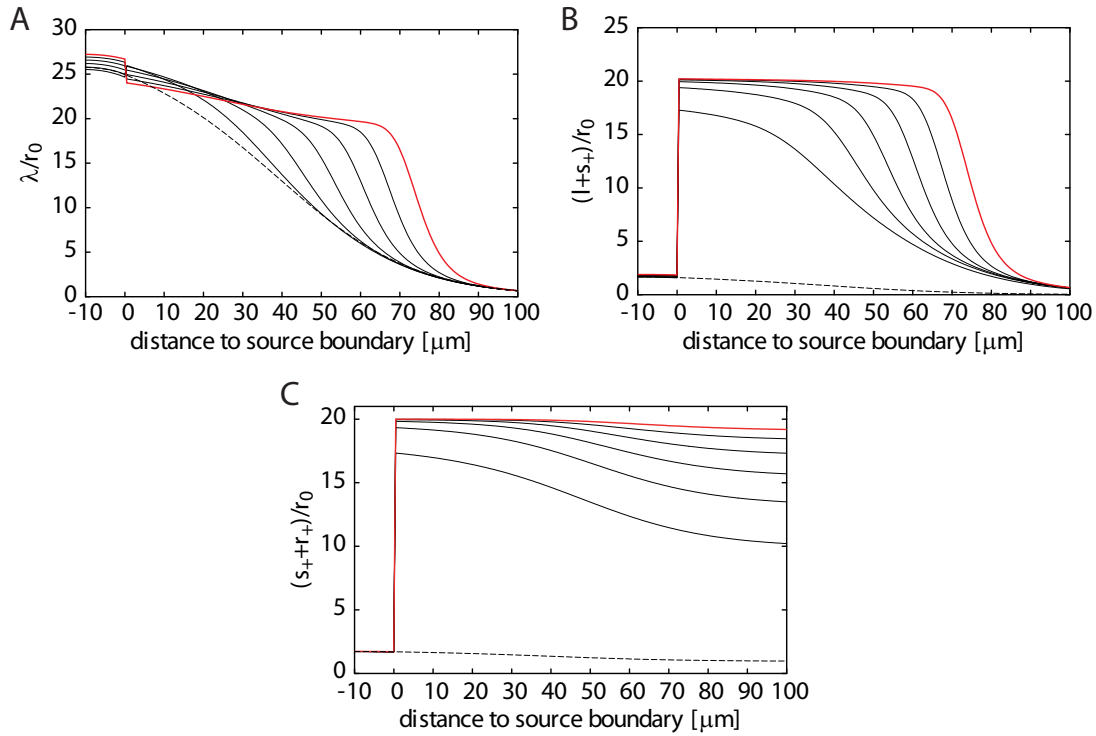


Figure 2.9: Results from a calculation corresponding to the shibire rescue assay. The ligand and receptor profiles were calculated using the theoretical description of morphogen transport in the diffusion regime (3.28). A source region of $10\mu\text{m}$ width located at $x < 0$ was explicitly simulated, see main text for details. (A) Time development of the total ligand concentration λ . Lines are separated by one hour. The initial profile is shown by the broken line. The red line corresponds to the time at which the experimental observations were made. (B) As in A but for the extracellular ligand concentration $l + s_+$. (C) As in A but for the surface receptor concentration $s_+ + r_+$. Note the strong increase of the extracellular ligand and surface receptor concentrations outside of the source region. All concentrations are normalized to $r_0 = f_{\text{syn}}^0 f_{\text{ext}}^0 / a^2 f_{\text{deg}} f_{\text{int}}$. Figure modified from [59].

2.3.3 Shibire clone assay

We performed two dimensional calculations corresponding to the shibire clone assay with essentially the same geometry as described in 2.2.3. We use a slightly different position of the clone in the AOI: it is located at $25\mu\text{m}$ distance to the source and extends $25\mu\text{m}$ in the x -direction and $50\mu\text{m}$ in the y -direction. The block of endocytosis at the restrictive temperature is mimicked by setting the corresponding rates b_{int} and f_{int} to zero in the clone region. The resulting ligand profiles and the time development of the contrast of the shadow behind the clone as defined in equation (2.1) are shown in Fig. 2.10. The contrast reveals that, consistent with the experiments, there is a strong shadow at $t = 5\text{h}$ which then decreases and actually turns into an “anti shadow”, an accumulation of ligand behind the clone, at later times. In the clone region a similar total ligand concentration as around it is observed at $t = 5\text{h}$. The extracellular ligand and receptor concentrations increase dramatically in the clone region, see Fig. B.1 F and G.

In this calculation, the appearance of a shadow has its origin in this strong, swift increase

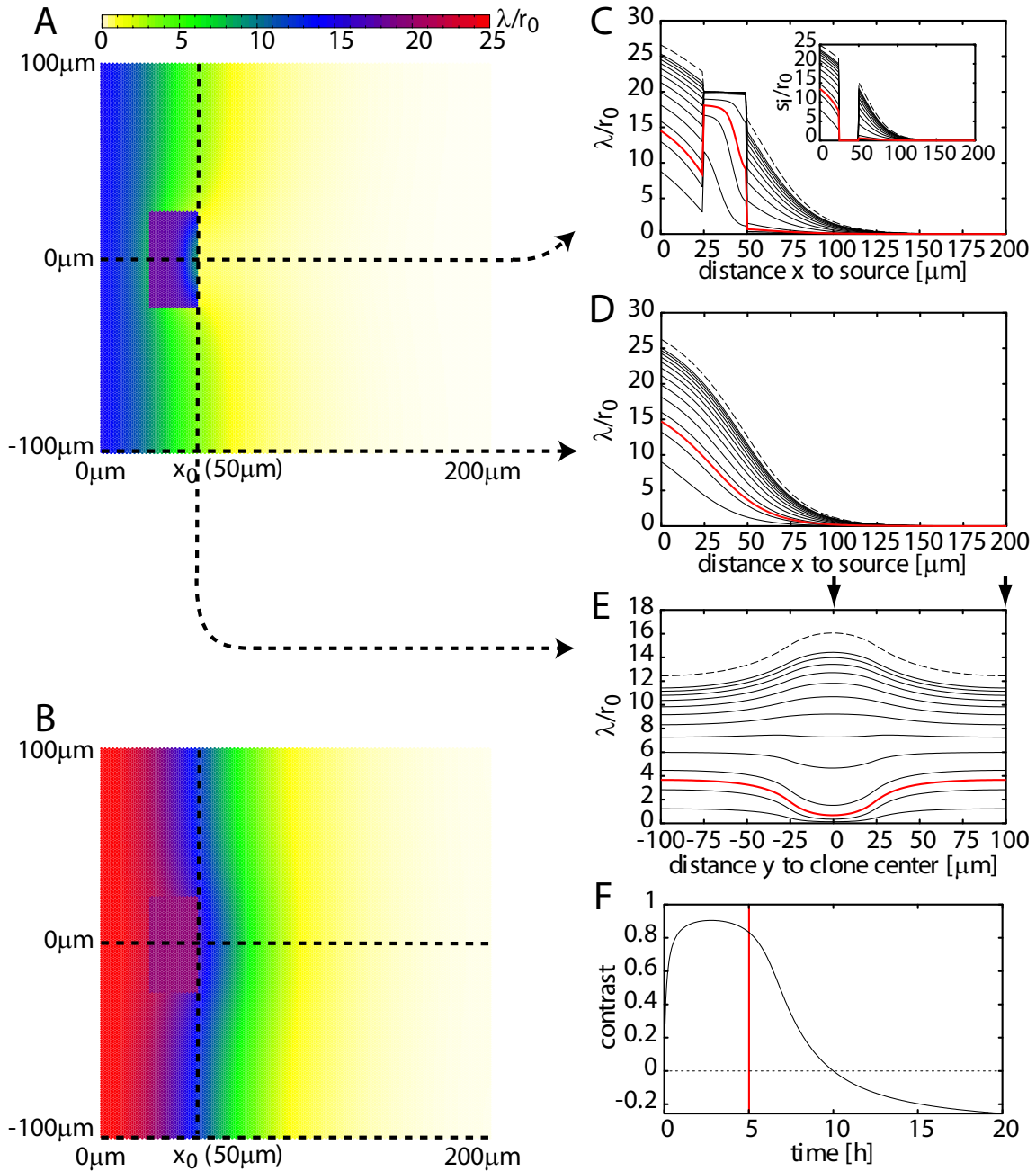


Figure 2.10: Profiles of the total ligand concentration λ in a calculation corresponding to the shibire clone assay based on our theoretical description of morphogen transport in the diffusion regime. (A,B) Profiles of the total ligand concentration at $t = 5$ h (A) and at $t = 48$ h which is very close to the steady state (B). (C-E) Time development of the total ligand concentration λ along slices through the clone (C), far away from the clone (D), and behind the clone (E) as indicated by the dashed lines in A. Unbroken black lines are separated by two hours. The broken lines represent the steady state distributions. The profiles at $t = 5$ h at which the observations in the experiments were made [34] are shown in red. (F) Contrast of the depletion of the total ligand concentration λ behind the clone as defined in equation (2.1). The two positions at which the values of λ are compared to calculate the contrast are indicated by the arrows in E. All concentrations are normalized to $r_0 = f_{\text{syn}}^0 f_{\text{ext}}^0 / a^2 f_{\text{deg}} f_{\text{int}}$. Figure modified from [59].

of the free surface receptor concentration in the clone region. This increase is achieved by a choice of sufficiently large values for R_{\max} and f_{ext} , see Table 2.1. The shadow arises because a large amount of ligand binds to free receptors on the surface of cells in the clone region and is thus immobilized. It disappears when the surface receptors in that region are mostly occupied by ligands so that the extracellular diffusion of ligands through the clone is no longer obstructed. Thus, a rapid increase of the surface receptor levels and a strong accumulation of extracellular ligands are necessary for the formation of a shadow in the diffusion regime. To verify this, we have performed numerical calculations in which lower values of R_{\max} and f_{ext}^0 were used. The contrast of the shadow at $t = 5\text{h}$ was strongly reduced for significantly smaller values of these parameters. It should also be mentioned that setting the internalization rates b_{int} and f_{int} to a strongly reduced value in the clone region instead of setting them to zero does not change our results significantly.

While the ligand profiles found outside of the clone region are consistent with the experimental data, neither a strong accumulation of extracellular ligand nor of cell surface receptor was detected in shibire clones after five hours at the restrictive temperature [59, 34]. Slight increases of the total receptor and extracellular Dpp levels could be detected in shibire clones [7]. However, the speed and the magnitude of the accumulation are not in agreement with those found in the numerical calculation.

In summary, we have illustrated in this section that a parameter choice for which transport is dominated by extracellular diffusion leads to results that are inconsistent with some of the experimental data available for the shibire clone and rescue experiments. This is of key importance because it suggests that transcytosis is the dominant transport mechanism used in morphogen gradient formation for Dpp in the wing disk. However, one should keep in mind that unknown processes which are not included in our theoretical description might alter these results.

2.4 Interpretation of morphogen profiles in clone experiments

In the experimental study of morphogen transport in *Drosophila*, it is a frequently used technique to create patches of mutant cells, i.e. clones, which have different properties than the cells in the remaining tissue. An example of such an experiment was discussed in section 2.2.3. One then tries to extract information about the effects of the mutation in the clone cells by observing how the ligand profiles are affected by the presence of the clone. For example, a depletion of ligand behind a clone suggests that ligand transport through the clone is obstructed and the investigated mutation thus plays a role in transport. In this section, we discuss the effects of clones on the ligand profiles to put such conclusions drawn from experimental data on a stronger basis. A mainly numerical investigation of this problem was performed in [27].

Distortion of steady state profiles We study a simple linear system capable of gradient formation in two space dimensions. Ligand transport is described by the diffusion equation with degradation term $\partial_t c = D\Delta c - kc$. Here, $c(\vec{x}, t)$ denotes the ligand concentration, D the effective diffusion coefficient, and k the effective degradation rate. Motivated by the geometry of the wing disk, a typical tissue in which morphogen gradients are formed, we study the steady state solutions of this equation in the half-space $x \geq 0$ with a ligand source located at $x < 0$. The boundary conditions are $D\partial_x c|_{x=0} = -j_0$ and $c(\infty, y) = 0$. This system gives a rough linear approximation to more detailed descriptions of gradient formation like those discussed in chapter 3. We assume that inside the clone, the values for D and k are different than in the

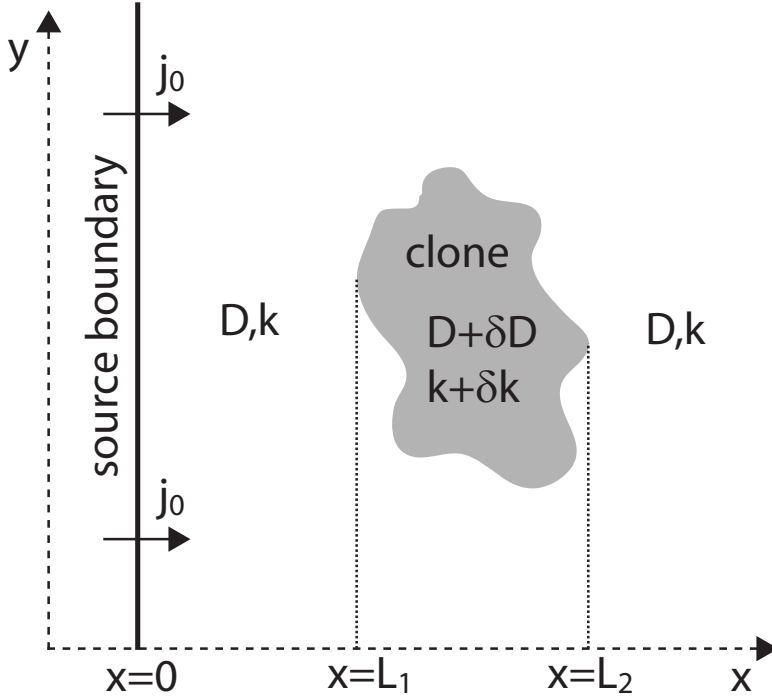


Figure 2.11: Schematic of the geometry used in section 2.4 with a clone region \mathcal{C} in which D and k have different values than outside of it.

remaining tissue, see Fig. 2.11. The equation describing this scenario in two dimensions is

$$\partial_t c(\vec{x}, t) = \nabla \cdot (D + \delta D(\vec{x})) \nabla c(\vec{x}, t) - (k + \delta k(\vec{x})) c(\vec{x}, t), \quad (2.2)$$

with $\delta D(\vec{x}) = \delta D \chi_{\mathcal{C}}(\vec{x})$ and $\delta k(\vec{x}) = \delta k \chi_{\mathcal{C}}(\vec{x})$. Here, δD and δk are constants quantifying the difference of the effective diffusion coefficient and degradation rate inside the clone region compared to the outside and $\chi_{\mathcal{C}}$ is the characteristic function of the clone region \mathcal{C} with $\chi_{\mathcal{C}}(\vec{x}) = 1$ if $\vec{x} \in \mathcal{C}$ and $\chi_{\mathcal{C}}(\vec{x}) = 0$ if $\vec{x} \notin \mathcal{C}$.

Assuming that $|\delta D| \ll D$ and $|\delta k| \ll k$, we can perturbatively calculate the steady state solution of equation (2.2). We formally introduce a small parameter ϵ and use the ansatz $c(x) = c_0(x) + \epsilon c_1(x) + \dots$ to solve the equation

$$\nabla \cdot (D + \epsilon \delta D(\vec{x})) \nabla c(\vec{x}) - (k + \epsilon \delta k(\vec{x})) c(\vec{x}) = 0,$$

to each order in ϵ . The unperturbed solution for $\epsilon = 0$ is $c_0(\vec{x}) = c_0(x) = c_0^0 e^{-x/\xi_D}$, where $\xi_D = \sqrt{D/k}$ is the diffusion length. To first order in ϵ , we have

$$D \Delta c_1(\vec{x}) - k c_1(\vec{x}) = -\nabla \cdot \delta D(\vec{x}) \nabla c_0(\vec{x}) + \delta k(\vec{x}) c_0(\vec{x})$$

with the boundary condition $\partial_x c_1(\vec{x}) = 0$ at $x = 0$. The free Green's function of the operator $(D(\partial_x^2 + \partial_y^2) - k)$ is

$$G_0(\vec{x}, \vec{x}') = \frac{-1}{2\pi D} K_0(|\vec{x} - \vec{x}'|/\xi_D),$$

where K_0 is a modified Bessel function of the second kind [97]. From this, we can construct the Green's function G_+ satisfying $\partial_x G_+(\vec{x}, \vec{x}')|_{x=0} = 0$ using a mirror image technique:

$$G_+(x, y, x', y') = G_0(x, y, x', y') + G_0(x, y, -x', y').$$

behind	$\delta D > 0$	$\delta D < 0$	$\delta D = 0$
$\delta k > 0$?	–	–
$\delta k < 0$	+	?	+
$\delta k = 0$	+	–	0
in front	$\delta D > 0$	$\delta D < 0$	$\delta D = 0$
$\delta k > 0$	–	?	–
$\delta k < 0$?	+	+
$\delta k = 0$	–	+	0

Table 2.2: Effects of a clone on the concentration profile in front of and behind the clone, i.e. for $x < L_1$ and $x > L_2$ respectively. Here, “+” denotes an accumulation, “–” a depletion, “0” no effect, and for “?” no general statement can be made because the effect depends on the absolute values of δD and δk .

Using this, we find for the first order correction $c_1(\vec{x})$:

$$\begin{aligned}
c_1(\vec{x}) &= \int_0^\infty dx' \int_{-\infty}^\infty dy' G_+(\vec{x}, \vec{x}') [-\nabla_{\vec{x}'} \cdot (\delta D(\vec{x}') \nabla_{\vec{x}'} c_0(x')) + \delta k(\vec{x}') c_0(x')] \\
&= \int_{\mathcal{C}} dx' dy' [\delta D c_0'(x') \partial_{x'} G_+(\vec{x}, \vec{x}') + \delta k c_0(x') G_+(\vec{x}, \vec{x}')] \quad (2.3)
\end{aligned}$$

where we have used $\nabla_{\vec{x}'} \cdot (\delta D(\vec{x}') \nabla_{\vec{x}'} c_0(x')) = \partial_{x'}(\delta D(\vec{x}') \partial_{x'} c_0(x'))$ and integrated by parts once. Higher order corrections can be calculated iteratively. Note, that this perturbative approach is only valid if $|\delta D|$ and $|\delta k|$ are sufficiently small for this iteration to converge.

It is not possible to express the integral in (2.3) in terms of elementary functions. Nevertheless, we can identify important properties of the solution. Since the integration extends only over the clone region \mathcal{C} and $G_+(\vec{x}, \vec{x}')$ rapidly decays for increasing $|\vec{x} - \vec{x}'|$ on a length scale given by ξ_D , we see that the ligand profile is only affected in the clone region and its vicinity. We further have $G_+(\vec{x}, \vec{x}') < 0$ and sufficiently far away from the source boundary located at $x = 0$, $\partial_{x'} G_+(\vec{x}, \vec{x}') > 0$ if $x < x'$ and $\partial_{x'} G_+(\vec{x}, \vec{x}') < 0$ if $x > x'$. In many cases, this enables us to identify the sign of $c_1(\vec{x})$ for $x < L_1$ and $x > L_2$, with $L_1 = \inf\{x | \vec{x} \in \mathcal{C}\}$ and $L_2 = \sup\{x | \vec{x} \in \mathcal{C}\}$, see also Fig. 2.11. This means that we can identify if there is a depletion or an accumulation of ligands in front of and behind the clone respectively. The results of these considerations are summarized in Table 2.2.

We have also evaluated (2.3) numerically to get a better impression of how the ligand profiles are distorted by the clone. The resulting distortions $c_1(\vec{x})$ of the steady state profile are shown in Fig. 2.12 for several different cases. They illustrate the results summarized in Table 2.2.

In the light of these results, we understand the steady state ligand profiles observed in the clone experiments and the corresponding numerical calculations better. The shibire clone in the calculations for a parameter choice in the extracellular diffusion dominated regime discussed in 2.3.3 leads to an enlarged effective diffusion coefficient in the clone region and to a reduced effective degradation rate. This is why an accumulation of ligand both in front of and behind the clone is observed in steady state. Note that without a reduction of the degradation rate, a ligand depletion should be observed in front of the clone. In the corresponding calculation in the transcytosis regime discussed in 2.2.3, we found a ligand accumulation in front of the clone and a depletion behind it. This is consistent with a reduced effective diffusion coefficient in the clone region. Indeed, morphogen transport by transcytosis can be characterized by an effective diffusion coefficient that becomes small if the internalization rate b_{int} is reduced to small values as we will show in section 3.1.2.

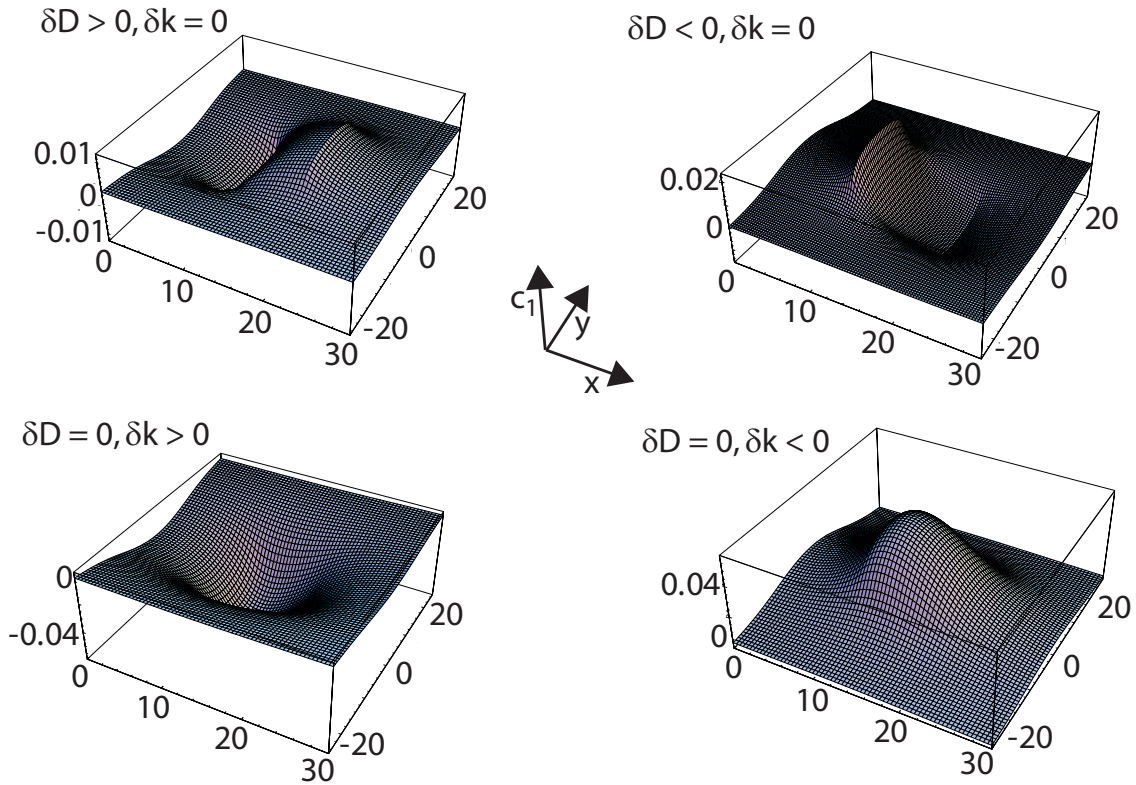


Figure 2.12: First order correction $c_1(\vec{x})$ of the two dimensional steady state concentration profiles in the presence of a rectangular clone located in the region $10 \leq x \leq 20$ and $-10 \leq y \leq 10$. The morphogen source is located at $x < 0$. For simplicity, we use the dimensionless parameters $D = 5$, $k = .1$ $\delta D/D = \pm .4$, and $\delta k/k = \pm 1$. The zeroth order solution of the steady state profile is $c_0(x) = \exp(-x/\xi_D)$.

Approach to the steady state So far, we have discussed the effects of clones in the steady state. However, one should also consider the time development of the ligand profiles in and around clones during the approach to the steady state. This is relevant because in the shibire clone experiment, a transient ligand depletion behind the clone is observed that is not apparent when the system is close to its steady state.

Let us revisit the results of the calculation in the transcytosis regime discussed in 2.2.3. There, a ligand depletion with decreasing contrast was found behind the clone region. This is consistent with the experimental data because, for a certain time span, the contrast could be sufficiently large to be detected in experiments and then fall below detectable values. The behavior found in the numerical calculation can be understood if we go to the extreme situation of vanishing diffusion coefficient in the clone region. This situation is described by imposing zero-flux boundary conditions along the border of the clone region. Ligands can only reach the region behind the clone by moving around it. This takes longer than reaching a region of equal distance to the source boundary located away from the clone because a larger distance has to be covered by the ligands. This is the origin of the decreasing contrast of the shadow shown in Fig. 2.6 F.

The time development found in the calculations in the diffusion regime discussed in 2.3.3 can also be explained. There, a complicated kinetics in the clone region leads to the formation of a ligand depletion behind the clone that changes into an accumulation during the approach

to the steady state, see Fig. 2.10 F. In the beginning, the effective diffusion coefficient in the clone region is reduced because large numbers of ligands get trapped by binding to free surface receptors. This leads to a ligand depletion behind the clone because the ligand flow through the clone region is reduced. The surface receptors in the clone region then become more and more occupied allowing ligands to diffuse freely through this region. This causes an increase of the effective diffusion coefficient with time which in turn results in a rapid padding of the region behind the clone with ligands moving from the source through the clone region. Note, that the effective degradation rate for ligands is zero in the clone region at all times in this calculation because the extracellular degradation rate is zero and internalization of receptor-bound ligands does not occur.

2.5 Fluorescence recovery after photo-bleaching experiments

We measured the apparent diffusion coefficient D for GFP-Dpp in the wing disk using fluorescence recovery after photo-bleaching (FRAP). In our particular application of this method, the fluorescent GFP molecules are photo-bleached in a $10\mu\text{m}$ wide stripe near the the Dpp source and parallel to it by irradiation with a laser beam of wavelength 488nm. In the following hour, the fluorescence intensity in the photo-bleached region is recorded and quantified [78, 77]. Since the transport mechanism on hand is unknown but nondirectional, it is a reasonable null hypothesis that the transport phenomenon observed obeys the linear diffusion equation. For simplicity, we neglect the degradation and production of GFP-Dpp molecules. Preliminary experimental data indicate that both processes have only a small influence on the observed fluorescence during the time span of about one hour in which the FRAP experiments are done, so that their negligence should lead to a relatively small error [40].

As we discuss in more detail below, one can extract the apparent diffusion coefficient D from the fluorescence recovery curve. The relation between GFP-Dpp concentration and detected fluorescence is assumed to be linear for this. This is reasonable if one operates in a regime where the maximum fluorescence is well below the saturation threshold of the photon detector. Control experiments indicate that this is indeed the case [40]. Both wild type wing disks and shibire rescue wing disks were investigated at 34°C and 25°C [78, 77]. These temperatures correspond to a restrictive and a permissive temperature of the shibire mutation respectively.

We have solved the one dimensional linear diffusion equation $\partial_t c(t, x) = D\partial_x^2 c(t, x)$ for the initial condition $c(0, x) = c_b$ for $-w/2 \leq x \leq w/2$ and $c(0, x) = c_u$ otherwise. This corresponds to a photo-bleached stripe of width w in which the concentration of fluorescent molecules is reduced to a value c_b which is smaller than the value c_u present in the un-bleached region. By assuming a homogenous concentration c_u outside of the photo-bleached region, we make a small error since in the experiments a stripe in a graded concentration profile is bleached. From the solution $c(t, x)$, we have calculated the time development of the average concentration $f(t)$ in the region $-w/2 \leq x \leq w/2$:

$$f(t) = w^{-1} \int_{-w/2}^{w/2} dx c(t, x) = (c_u - c_b) \left[1 - \left(2\sqrt{\frac{Dt}{\pi w^2}} \left(e^{\frac{-w^2}{4Dt}} - 1 \right) + \text{erf} \left(\frac{w}{2\sqrt{Dt}} \right) \right) \right] + c_b, \quad (2.4)$$

where $\text{erf}(z) = 2\pi^{-1/2} \int_0^z dq \exp(-q^2)$ is the error function [97]. The time evolution of the average fluorescence in the photo-bleached stripe was extracted from the experimental data by quantifying the fluorescence intensity using Zeiss image analysis software. Finally, the parameters D , c_b , and c_u were optimized to obtain the best possible agreement of $f(t)$ with the experimental fluorescence recovery curve. The nonlinear least-squares Marquardt-Levenberg algorithm as implemented in gnuplot [99] was used for this procedure. Exemplary recovery

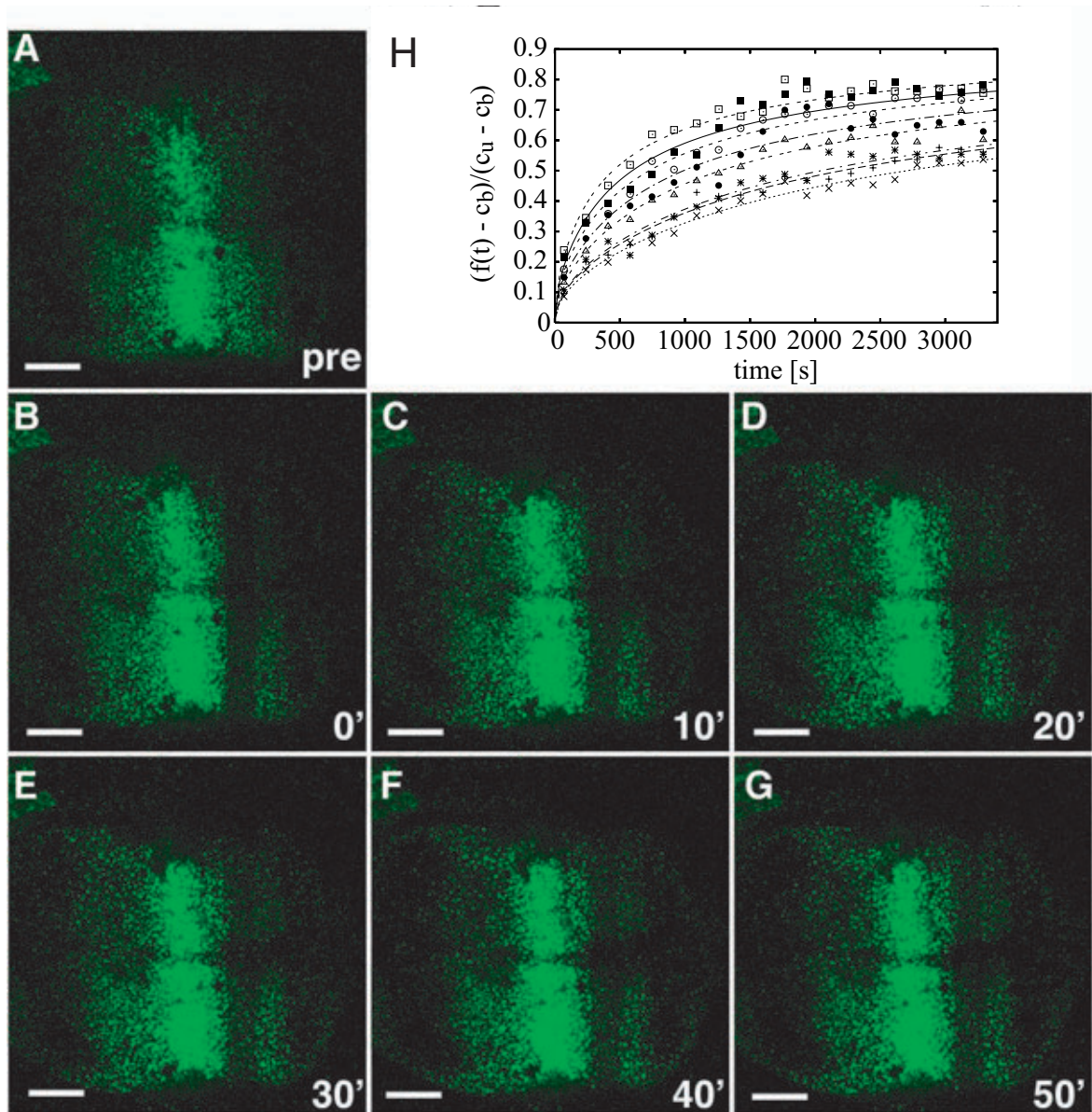


Figure 2.13: Experimental fluorescence data and exemplary fit curves for fluorescence recovery after photo-bleaching (FRAP) experiments on GFP-Dpp in the *Drosophila* wing disk. (A-G) Projection of the GFP fluorescence in five individual sections measured by confocal time-lapse microscopy [78] before photo-bleaching (A) and 0 (B), 10 (C), 20 (D), 30 (E), 40 (F), and 50 (G) minutes after photo-bleaching a $10\mu\text{m}$ wide stripe near the GFP-Dpp source. (H) The fitted fluorescence recovery curves $(f(t) - c_b)/(c_u - c_b)$ which are shown by lines are compared to the corresponding data obtained from eight experiments in wild type wing disks at 25°C which are shown by different symbols. Scale bars correspond to $10\mu\text{m}$. Experimental data courtesy of P. Pantazis [78, 77]. Figure modified from [78].

	25°C	34°C
wt	0.03 ± 0.02 (n=8)	0.008 ± 0.002 (n=3)
shi	0.006 ± 0.002 (n=3)	0 (n=3)

Table 2.3: Apparent diffusion coefficient of GFP-Dpp in the wing disk measured using FRAP in wild type (wt) and in shibire (shi) mutant animals at different temperatures as indicated. The units are $\mu\text{m}^2/\text{s}$. The values are averages of n repetitions of each experiment under identical conditions [78, 77]. For the shibire mutant at 34°C, the fluorescence recovery in the photo-bleached region was very weak corresponding to a diffusion coefficient $D \approx 0$. Experimental data courtesy of P. Pantazis [78, 77].

curves with the corresponding fit curves $f(t)$ and the original experimental data are shown in Fig. 2.13. Note, that due to technical difficulties, the recovery in the photo-bleached region can only be followed for approximately one hour after photo-bleaching. This time span is insufficient to obtain complete fluorescence recovery in the photo-bleached region which would simplify the analysis of these data [4] and presumably lead to a smaller variability of the apparent diffusion coefficients extracted from individual experiments.

The apparent Diffusion coefficients D thus extracted from the recovery curves are shown in Table 2.3. The values found in wild type at the higher temperature 34°C are slightly lower than at 25°C. In the shibire rescue disks at the permissive temperature the apparent diffusion coefficient is comparable to that found in wild type. At the restrictive temperature 34°C, no significant fluorescence recovery can be observed in the photo-bleached stripe in shibire rescue wing disks which corresponds to $D \approx 0$. These quantitative data provide further evidence for a role of endocytosis in Dpp transport.

Chapter 3

Theoretical description of morphogen transport

In this chapter, we develop a theoretical description of morphogen transport and gradient formation. The description is motivated by the formation of the gradient of the morphogen Dpp in the *Drosophila* wing disk as introduced in sections 1.2 and 2.2.1. This is a typical setting for morphogen gradient formation. The contributions to morphogen transport taken into account are passive diffusion in the extracellular space and transcytosis, see section 1.4. In section A.3 of the appendix, we also investigate transport of morphogens by diffusion in the cell membrane. Further generalizations of the description are discussed in the remainder of appendix A.

The wing disk is an epithelium that consists of a single cell layer, see Fig. 1.3. Moreover, Dpp in the wing primordium is mostly observed in a sheet that extends over about $200 \times 100 \mu\text{m}$ in the xy -plane but only about $5 \mu\text{m}$ in the z -direction [34], see section 1.2. These observations show that the transport of Dpp occurs essentially in two dimensions. It is also a reasonable approximation to neglect the folding of the wing disk in the three dimensional space and thus to assume it to be planar.

We will first develop a description of morphogen transport and degradation in one space dimension and later generalize it to two space dimensions. This description reflects the symmetries of the system on length scales that are large compared to one cell diameter. The non-directionality of Dpp transport that has been experimentally observed on such a length scale [34] suggests that the mathematical description should be invariant under rotations and space inversion. Our description has these symmetries which are only violated by boundary effects. Note, that this is an idealization of the situation present in a tissue like the wing disk. Strictly speaking, the two dimensional arrangement of the cells breaks rotational invariance. However, due to the disordered nature of this arrangement, no distinguished direction is defined in the tissue, so that the assumption of rotational symmetry should give a very good approximation to the real situation. A one dimensional description is of interest because the geometry of the region of the wing disk in which the Dpp gradient forms is approximately translation invariant in the direction parallel to the Dpp source over a considerable range, see Fig. 1.3 C.

While we discuss boundary conditions in general here, one must keep in mind that the correct boundary and initial conditions depend on the specific system and experimental setup on hand. We gave a detailed specification of these boundary and initial conditions for several experiments performed in the wing disk in chapter 2. If appropriate parameters and boundary conditions are applied, the theoretical description developed here is, in fact, very general and applicable to many systems in which molecules are transported by passive diffusion and

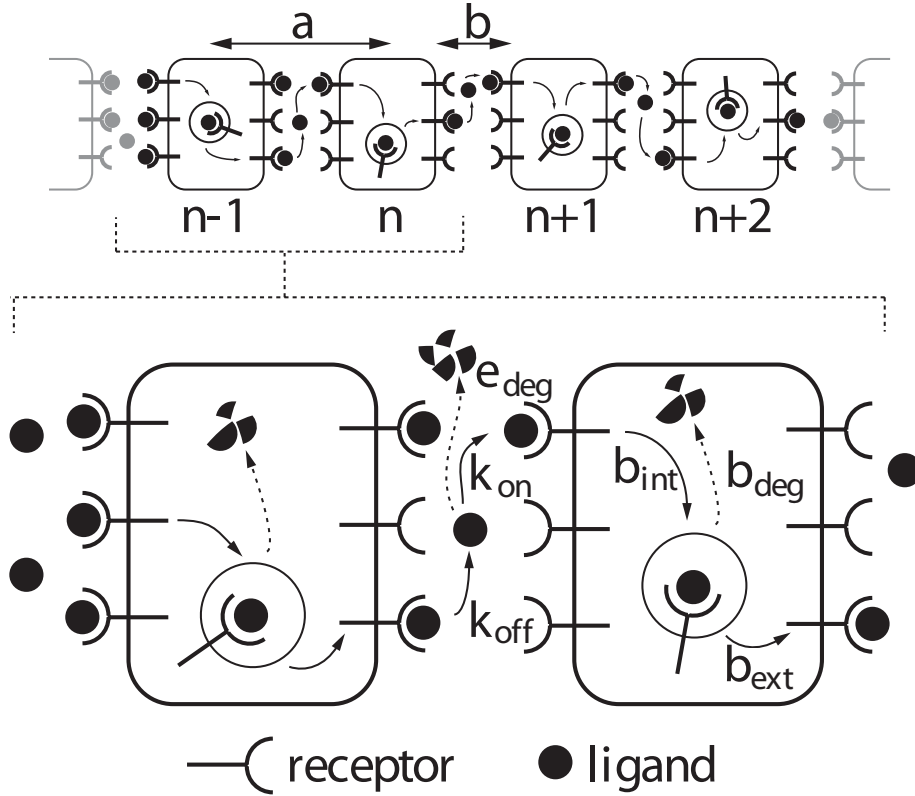


Figure 3.1: Schematic representation of transport by transcytosis in a chain of cells of diameter a indexed by n . The rates of ligand-receptor binding and un-binding, internalization and externalization of ligand-receptor pairs are denoted k_{on} , k_{off} , b_{int} and b_{ext} . Degradation of ligand occurs inside the cells with rate b_{deg} and in the extracellular space with rate e_{deg} . Ligands can also hop directly between neighboring extracellular spaces at a rate p which describes their movement in the extracellular space around the cells by passive diffusion (not shown). Figure modified from [9].

transcytosis. To reflect this generality, we will mostly refer to the transported molecules as “ligands” instead of “morphogens”. In general, ligands are molecules that can bind to a corresponding receptor molecule.

3.1 One dimensional description of morphogen transport

We define our discrete microscopic description of ligand transport by transcytosis and passive extracellular diffusion in this section and derive effective transport equations that are valid on length scales large compared to one cell diameter. Here, we first discuss a one dimensional description which we will generalize to two space dimensions in section 3.2.

3.1.1 Microscopic one dimensional description

A one dimensional model to describe ligand transport is schematically shown in Fig. 3.1. Ligands can bind to and detach from receptors on the cell surface. They exist as free molecules only in the narrow space between cells where they can move by diffusion. Effective long-range transport can be achieved by transport through the cell interior (transcytosis), diffusion around the cells in the surrounding extracellular space, or a combination of both. Transcytosis occurs

when a ligand binds to a receptor, is internalized into a cell and subsequently externalized at a different location of the surface of the same cell. Repeating this process together with ligands being passed from the cell surface to the surface of neighboring cells leads effectively to long range transport. This process can be characterized by rates k_{on} and k_{off} for receptor binding and un-binding of ligands and the rates b_{int} and b_{ext} of internalization and externalization of receptor-ligand complexes. Free ligands can hop directly from one gap between the cells to the adjacent ones at a rate p . This describes their free diffusion in the extracellular space around cells. Also important for gradient formation is the degradation of ligands with rate e_{deg} in the extracellular space and of ligands bound to receptors inside the cell with rate b_{deg} .

If cells possess a polarity and define a direction in the plane in which transport occurs, transcytosis can have a bias and lead to directed transport. Here, we consider the simpler case where cells are apolar in the plane where transport occurs and transport is nondirectional which is probably the case in the wing disk at early stages of development. In section A.2, we discuss the effects of a bias.

In principle, the diffusion of receptor-bound ligands in the cell membrane also leads to transport between different positions on the surface of one cell [56]. Here, we neglect this phenomenon assuming that the time scale of ligand transport over one cell diameter by this process is much larger than those of transport by free extracellular diffusion or transcytosis. In section A.3 of the appendix, we discuss the treatment of diffusion in the cell membranes in our description.

Description with receptor kinetics The kinetics of free receptors and the production and degradation of receptors by the cells has to be taken into account. Free receptors are internalized and externalized with rates f_{int} and f_{ext} respectively. In addition, each cell produces receptors with a rate f_{syn} . Newly produced receptors appear on the cell surface [61]. In experiments, evidence has been obtained that the rate of receptor synthesis depends on the number of free and ligand-bound receptor molecules present in the cell [61, 92] so that f_{syn} is a function of these quantities, see below. Internalized free receptors are degraded with rate f_{deg} .

In one space dimension, we consider a linear chain of cells. We denote the distance between the centers of two neighboring cells by a and the width of the gap between two cells by b . In biologically relevant cases the volume fraction of the extracellular space is much smaller than that of the cells which implies $b \ll a$. The time-dependent concentrations of internal free and ligand-bound receptors are denoted by $R_n^{(i)}$ and $S_n^{(i)}$. $R_n^{(l)}$ and $R_n^{(r)}$ denote the concentrations of free receptors on the left and right cell surfaces respectively, $S_n^{(l)}$ and $S_n^{(r)}$ for the ligand-bound receptors accordingly. Here, n indexes the cells, see Fig. 3.1. Finally, the concentration of free extracellular ligands between cells n and $n + 1$ is denoted by L_n . The kinetics of this microscopic description is given by

$$\begin{aligned}
\partial_t L_n &= k_{\text{off}}(S_n^{(r)} + S_{n+1}^{(l)}) - k_{\text{on}}(R_n^{(r)} + R_{n+1}^{(l)})L_n + \frac{p}{2}(L_{n+1} + L_{n-1} - 2L_n) - e_{\text{deg}}L_n \\
\partial_t R_n^{(r)} &= \frac{f_{\text{syn}}}{2} + k_{\text{off}}S_n^{(r)} - k_{\text{on}}R_n^{(r)}L_n - f_{\text{int}}R_n^{(r)} + \frac{f_{\text{ext}}}{2}R_n^{(i)} \\
\partial_t S_n^{(r)} &= -k_{\text{off}}S_n^{(r)} + k_{\text{on}}R_n^{(r)}L_n - b_{\text{int}}S_n^{(r)} + \frac{b_{\text{ext}}}{2}S_n^{(i)} \\
\partial_t R_n^{(l)} &= \frac{f_{\text{syn}}}{2} + k_{\text{off}}S_n^{(l)} - k_{\text{on}}R_n^{(l)}L_{n-1} - f_{\text{int}}R_n^{(l)} + \frac{f_{\text{ext}}}{2}R_n^{(i)} \\
\partial_t S_n^{(l)} &= -k_{\text{off}}S_n^{(l)} + k_{\text{on}}R_n^{(l)}L_{n-1} - b_{\text{int}}S_n^{(l)} + \frac{b_{\text{ext}}}{2}S_n^{(i)} \\
\partial_t R_n^{(i)} &= -f_{\text{ext}}R_n^{(i)} + f_{\text{int}}(R_n^{(l)} + R_n^{(r)}) - f_{\text{deg}}R_n^{(i)} \\
\partial_t S_n^{(i)} &= -b_{\text{ext}}S_n^{(i)} + b_{\text{int}}(S_n^{(l)} + S_n^{(r)}) - b_{\text{deg}}S_n^{(i)}.
\end{aligned} \tag{3.1}$$

Receptor internalization, externalization, and degradation as well as ligand un-binding are described by first order rate equations, receptor binding by a second order process. Reflecting the non-directionality of transport, the description (3.1) is invariant under space inversion ($x \rightarrow -x$).

The rate of receptor synthesis f_{syn} in (3.1) is a constant. In a more realistic description of the receptor kinetics, the rate of receptor synthesis f_{syn} depends on $R_n^{(l)} + R_n^{(r)}$ and $S_n^{(l)} + S_n^{(r)}$:

$$f_{\text{syn}} = f_{\text{syn}}^0 \left(1 - \frac{R_n^{(l)} + R_n^{(r)} + \psi (S_n^{(l)} + S_n^{(r)})}{R_{\text{max}}} \right), \quad (3.2)$$

where f_{syn}^0 is a basal rate of receptor synthesis and R_{max} is the saturation value of the surface receptor concentration at which the production of new receptors stops. The dimensionless parameter ψ allows for an enhancement, $\psi < 1$, or a reduction, $\psi > 1$, of receptor synthesis caused by the presence of ligands bound to receptors on the cell surface — phenomena known to biologists as receptor “up-regulation” and “down-regulation” respectively [61]. For Dpp in the *Drosophila* wing disk, receptor down-regulation has been observed [92], while up-regulation can occur for other morphogens [16]. Independent of the specific choice of the function f_{syn} , a realistic approach to the biological situation should satisfy $f_{\text{syn}} \rightarrow 0$ for $(R_n^{(l)} + R_n^{(r)} + S_n^{(l)} + S_n^{(r)}) \rightarrow \infty$. This expresses the existence of a negative feedback loop in which the presence of receptors negatively regulates the production of new receptors.

Constant surface receptor approximation We now discuss a simpler situation where the cells maintain the surface receptor number R constant everywhere. This simplification will be useful for the identification of key properties of the transport mechanism. In the description of this situation, the free receptor number on the left and right cell surface in (3.1) are replaced with $R_n^{(l/r)} \rightarrow (R/2 - S_n^{(l/r)})$ and the equations for the kinetics of the free receptor concentrations are obsolete. The equations describing ligand transport in this approximation are thus

$$\begin{aligned} \partial_t L_n &= k_{\text{off}}(S_n^{(r)} + S_{n+1}^{(l)}) - k_{\text{on}}(R - S_n^{(r)} - S_{n+1}^{(l)})L_n + \frac{p}{2}(L_{n+1} + L_{n-1} - 2L_n) - e_{\text{deg}}L_n \\ \partial_t S_n^{(r)} &= -k_{\text{off}}S_n^{(r)} + k_{\text{on}}\left(\frac{R}{2} - S_n^{(r)}\right)L_n - b_{\text{int}}S_n^{(r)} + \frac{1}{2}b_{\text{ext}}S_n^{(i)} \\ \partial_t S_n^{(l)} &= -k_{\text{off}}S_n^{(l)} + k_{\text{on}}\left(\frac{R}{2} - S_n^{(l)}\right)L_{n-1} - b_{\text{int}}S_n^{(l)} + \frac{1}{2}b_{\text{ext}}S_n^{(i)} \\ \partial_t S_n^{(i)} &= -b_{\text{ext}}S_n^{(i)} + b_{\text{int}}(S_n^{(l)} + S_n^{(r)}) - b_{\text{deg}}S_n^{(i)}. \end{aligned} \quad (3.3)$$

Boundaries effects The descriptions (3.1) and (3.3) are valid in the bulk of the lattice. We also have to specify the kinetics at the boundaries of this lattice. To describe the effects of a ligand source located at $n = 0$ in (3.1), we modify the equation for the free ligand:

$$\partial_t L_0 = k_{\text{off}}S_1^{(l)} - k_{\text{on}}R_1^{(l)}L_0 + \frac{p}{2}(L_1 - L_0) - e_{\text{deg}}L_0 + \nu, \quad (3.4)$$

where ν is the rate at which ligands from the source enter the system. At the position $n = N$ where the lattice ends, we have

$$\partial_t L_N = k_{\text{off}}S_N^{(r)} - k_{\text{on}}R_N^{(r)}L_N + \frac{p}{2}(L_{N-1} - L_N) - e_{\text{deg}}L_N, \quad (3.5)$$

which corresponds to a zero flux boundary condition at this edge of the lattice. The equation for $\partial_t L_0$ and $\partial_t L_N$ in the description with the constant surface receptor approximation (3.3) are modified accordingly at the boundaries.

3.1.2 Transport equations in the transcytosis dominated limit

In this section, we derive effective continuous transport equations for ligand transport corresponding to the discrete descriptions (3.1) and (3.3). Such an effective description is of great value because it makes an analytic investigation of the transport phenomenon possible which greatly simplifies the identification of its properties. Here, we focus on the limit in which extracellular diffusion gives a small contribution to the ligand current, i.e. a situation in which the time scale for crossing a length of one cell diameter a by transcytosis is much smaller than that for crossing the same distance by diffusion in the extracellular space around the cells. In section 3.4, we will treat the opposite limit in which extracellular diffusion dominates ligand transport.

Description with receptor kinetics In order to derive effective continuous transport equations for the transport phenomenon defined by (3.1), we introduce the densities $l(t, x)$, $r^{(l/r)}(t, x)$, $r_i(t, x)$, $s^{(l/r)}(t, x)$, and $s_i(t, x)$, such that $x = na$, $L_n(t)/a = l(t, x)$, $R_n^{(l)}(t)/a = r^{(l)}(t, x)$, $R_n^{(r)}(t)/a = r^{(r)}(t, x)$, $R_n^{(i)}/a = r_i(t, x)$, $S_n^{(l)}(t)/a = s^{(l)}(t, x)$, $S_n^{(r)}(t)/a = s^{(r)}(t, x)$, and $S_n^{(i)}/a = s_i(t, x)$. Kinetic equations for these are obtained by replacing the discrete densities $R_n^{(i)}$, $R_n^{(l/r)}$, $S_n^{(i)}$, $S_n^{(l/r)}$, and L_n in (3.1) with the continuous densities r_i , $r^{(l/r)}$, s_i , $s^{(l/r)}$, and l . The spatial separation of the quantities defined on the lattice as indicated in Fig. 3.1 is taken into account by including terms up to second order in a power series expansion in x . Moreover, it is convenient to change to the densities $r_{\pm}(t, x) = r^{(l)}(t, x) \pm r^{(r)}(t, x)$ and $s_{\pm}(t, x) = s^{(l)}(t, x) \pm s^{(r)}(t, x)$ so that r_+ and s_+ measure the total free and ligand bound surface receptor concentrations per cell and r_- and s_- the polarization of these concentrations on the cell surface respectively. This yields the continuous equations

$$\begin{aligned}
\partial_t l &= k_{\text{off}} s_+ - (ak_{\text{on}} r_+ + e_{\text{deg}}) l - \frac{ab^2 k_{\text{on}}}{8} l \partial_x^2 r_+ + \frac{b^2 k_{\text{off}}}{8} \partial_x^2 s_+ + \frac{pa^2}{2} \partial_x^2 l \\
&\quad - \frac{abk_{\text{on}}}{2} l \partial_x r_- + \frac{bk_{\text{off}}}{2} \partial_x s_- \\
\partial_t s_+ &= ak_{\text{on}} l r_+ + b_{\text{ext}} s_i - (b_{\text{int}} + k_{\text{off}}) s_+ + \frac{ab^2 k_{\text{on}}}{8} r_+ \partial_x^2 l + \frac{(a-b)^2 b_{\text{ext}}}{8} \partial_x^2 s_i - \frac{abk_{\text{on}}}{2} r_- \partial_x l \\
\partial_t s_i &= -(b_{\text{ext}} + b_{\text{deg}}) s_i + b_{\text{int}} s_+ + \frac{(a-b)^2 b_{\text{int}}}{8} \partial_x^2 s_+ - \frac{(a-b) b_{\text{int}}}{2} \partial_x s_- \\
\partial_t s_- &= ak_{\text{on}} l r_- - (b_{\text{int}} + k_{\text{off}}) s_- + \frac{ab^2 k_{\text{on}}}{8} r_- \partial_x^2 l - \frac{abk_{\text{on}}}{2} r_+ \partial_x l + \frac{(a-b) b_{\text{ext}}}{2} \partial_x s_i \\
\partial_t r_+ &= \frac{f_{\text{syn}}}{a} + f_{\text{ext}} r_i - f_{\text{int}} r_+ - ak_{\text{on}} l r_+ + k_{\text{off}} s_+ - \frac{(ab^2) k_{\text{on}}}{8} r_+ \partial_x^2 l \\
&\quad + \frac{(a-b)^2 f_{\text{ext}}}{8} \partial_x^2 r_i + \frac{abk_{\text{on}}}{2} r_- \partial_x l \\
\partial_t r_i &= -(f_{\text{ext}} + f_{\text{deg}}) r_i + f_{\text{int}} r_+ + \frac{(a-b)^2 f_{\text{int}}}{8} \partial_x^2 r_+ - \frac{(a-b) f_{\text{int}}}{2} \partial_x r_- \\
\partial_t r_- &= -f_{\text{int}} r_- - ak_{\text{on}} l r_- + k_{\text{off}} s_- - \frac{ab^2 k_{\text{on}}}{8} r_- \partial_x^2 l + \frac{abk_{\text{on}}}{2} r_+ \partial_x l + \frac{(a-b) f_{\text{ext}}}{2} \partial_x r_i. \quad (3.6)
\end{aligned}$$

Here, it is reasonable to neglect higher order terms because the most important contribution to ligand transport on large length scales comes from the second order terms. This is due to the fact that first order terms must not appear in an effective transport equation due to the mirror symmetry of the original description. The next higher order contribution would come from fourth order terms that are insignificant for the long wavelength behavior we are interested in here.

In the absence of degradation and production, there are two conserved quantities in the system, namely the total ligand number and the total receptor number. Indeed, the kinetic

equation for the total ligand density $\lambda = l + s_i + s_+$ that follows from (3.6) can be written as a continuity equation with sink term

$$\partial_t \lambda = -\partial_x j - b_{\text{deg}} s_i - e_{\text{deg}} l. \quad (3.7)$$

Here, the total ligand current is

$$j = \frac{abk_{\text{on}}}{2} l r_- + \frac{(a-b)b_{\text{int}}}{2} s_- - \frac{bk_{\text{off}}}{2} s_- - \frac{ab^2 k_{\text{on}}}{8} (r_+ \partial_x l - l \partial_x r_+) - \frac{(a-b)^2 b_{\text{ext}}}{8} \partial_x s_i - \frac{(a-b)^2 b_{\text{int}} + b^2 k_{\text{off}}}{8} \partial_x s_+ - \frac{pa^2}{2} \partial_x l. \quad (3.8)$$

Note, that the terms involving r_- and s_- appear directly whereas all other terms are proportional to derivatives of r_+ , s_+ , s_i , or l . The kinetics of the total receptor density $\rho = r_i + r_+ + s_i + s_+$ is given by another continuity equation with source and sink terms:

$$\partial_t \rho = -\partial_x j_\rho + \frac{f_{\text{syn}}}{a} - f_{\text{deg}} r_i - b_{\text{deg}} s_i \quad (3.9)$$

with the total receptor current

$$j_\rho = \frac{(a-b)}{2} (f_{\text{int}} r_- + b_{\text{int}} s_-) - \frac{(a-b)^2}{8} (f_{\text{ext}} \partial_x r_i + f_{\text{int}} \partial_x r_+ + b_{\text{ext}} \partial_x s_i + b_{\text{int}} \partial_x s_+). \quad (3.10)$$

The individual terms of the currents j and j_ρ are difficult to interpret. However, it will become clear below that the terms in j_ρ do not give rise to transport over large distances whereas this is the case for the terms in j .

The equations (3.7) and (3.9) have the unpleasant property that they relate the time development of λ and ρ to that of all the individual quantities whose time development is given by the set of coupled partial differential equations (3.6). It would be better if the kinetics of λ and ρ could be described by equations which only involve these two quantities. This can be achieved by making use of a time scale separation.

As we are interested in transport over many cell diameters, we assume that the relaxation time scale τ_a of the kinetics in one cell is much smaller than the time scale τ_L for transport on a large length scale L . In the absence of free diffusion, i.e. $p = 0$, this is given because the time scale for transport over N cells is $\tau_L \gtrsim N\tau_a$ because N cells have to be crossed, $L \approx Na$. For small ligand concentrations we may expect diffusive behavior so that $\tau_L \approx N^2\tau_a$. In either case, the two time scales are separated if N is sufficiently large. In the presence of free diffusion, p must be small for this separation of time scales to endure.

We can exploit $\tau_a \ll \tau_L$ by making an adiabatic approximation in which the system equilibrates infinitely fast locally. This is done by setting the time derivatives in (3.6) to zero and solving the resulting equations for l, r_i, r_+, s_i, s_- . Here, we also assume that the production and degradation terms are small compared to the other rates and only include the leading order terms in a power series expansion in these rates. Formally, this corresponds to setting $b_{\text{deg}} = e_{\text{deg}} = f_{\text{deg}} = f_{\text{syn}} = 0$. To leading order, this yields the relations

$$\begin{aligned} l &= \frac{k_{\text{off}} s_+}{k_{\text{on}} a r_+} \\ s_i &= \frac{b_{\text{int}} s_+}{b_{\text{ext}}} \\ s_- &= \frac{k_{\text{on}} a l r_- - \frac{abk_{\text{on}}}{2} r_+ \partial_x l + \frac{(a-b)b_{\text{ext}}}{2} \partial_x s_i}{b_{\text{int}} + k_{\text{off}}} \\ r_i &= \frac{f_{\text{int}} r_+}{f_{\text{ext}}} \end{aligned}$$

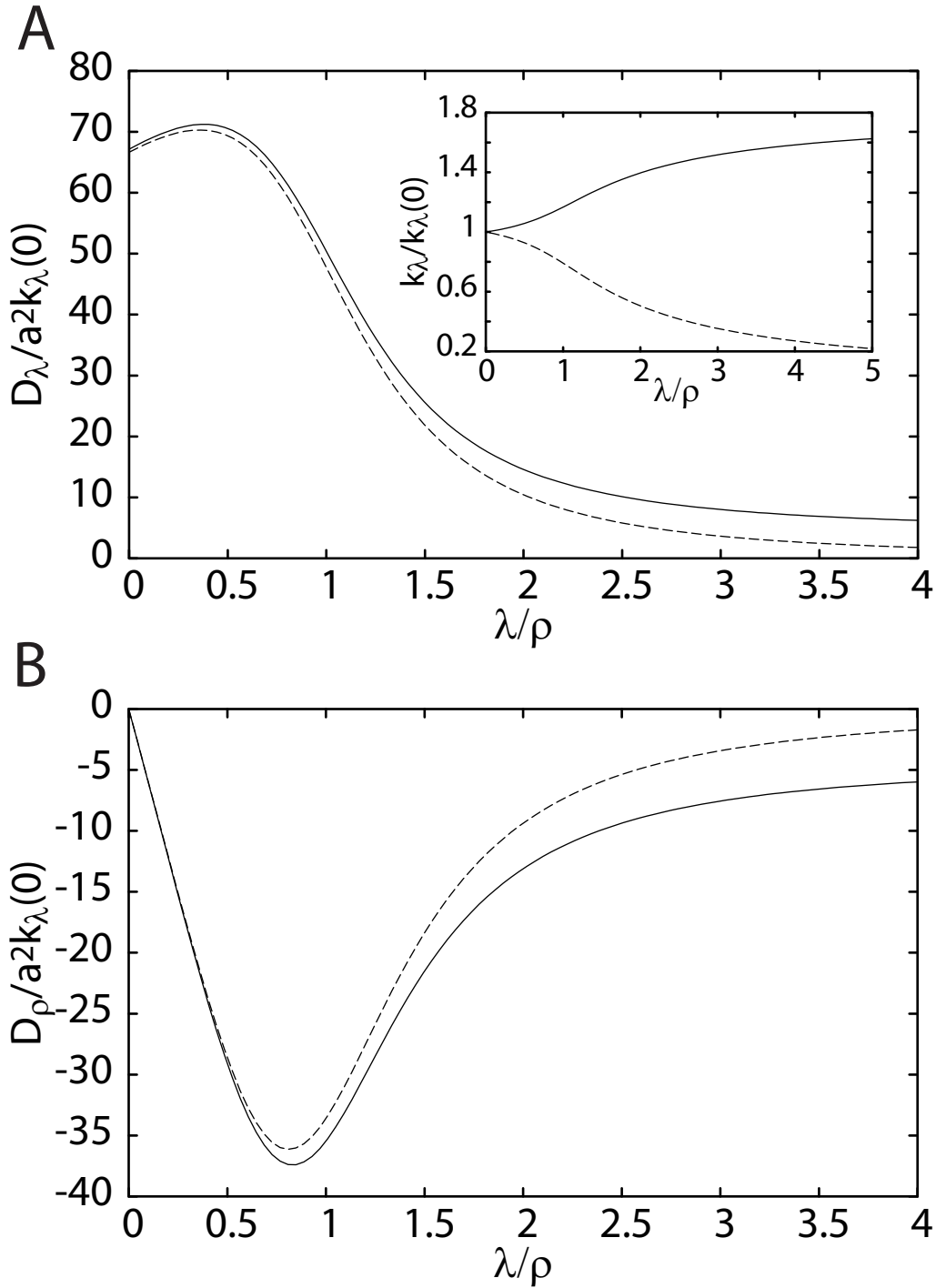


Figure 3.2: Coefficients $D_\lambda(\lambda, \rho)$, $D_\rho(\lambda, \rho)$, and $k_\lambda(\lambda, \rho)$ in the transport equation (3.12) as a function of the dimensionless ratio λ/ρ of the total ligand concentration λ and the total receptor concentration ρ . (A,B) The solid lines show the coefficients D_λ and D_ρ in presence of extracellular diffusion with $p/b_{\text{deg}} = 10/3$. Broken lines show these coefficients with $p = 0$. Inset in A: the solid line shows k_λ with $e_{\text{deg}}/b_{\text{deg}} = 2/3$ and the broken line with $e_{\text{deg}} = 0$. Parameters are: $k_{\text{off}}/b_{\text{deg}} = b_{\text{int}}/b_{\text{deg}} = f_{\text{int}}/b_{\text{deg}} = 1000/3$, $k_{\text{on}}a\rho/b_{\text{deg}} = 8000/3$, $b_{\text{ext}}/b_{\text{deg}} = f_{\text{ext}}/b_{\text{deg}} = 2000/3$.

$$r_- = \frac{k_{\text{off}}s_- + \frac{abk_{\text{on}}}{2}r_+\partial_x l + \frac{(a-b)f_{\text{ext}}}{2}\partial_x r_i}{f_{\text{int}} + k_{\text{on}}al}. \quad (3.11)$$

Note, that we have kept the first order terms for r_- and s_- . This is done to retain all second order terms when inserting (3.11) into (3.8) and (3.10). Using (3.11), one can express l, r_i, r_-, s_i, s_- in terms of r_+ and s_+ and spatial derivatives thereof. Finally, r_+ and s_+ can be expressed in terms of ρ and λ . Mathematically, there are two solutions for this but only one of them satisfies the physical requirement that $s_+ = 0$ for $\lambda = 0$ and $r_+ = 0$ for $\rho = 0$. Thus, we can uniquely express $l, r_i, r_{\pm}, s_i,$ and s_{\pm} in terms of λ and ρ in the adiabatic approximation.

Using these expressions, we can cast (3.7) and (3.9) into two coupled partial differential equations for only two densities λ and ρ :

$$\partial_t \lambda = \partial_x (D_\lambda(\lambda, \rho)\partial_x \lambda + D_\rho(\lambda, \rho)\partial_x \rho) - k_\lambda(\lambda, \rho)\lambda, \quad (3.12)$$

$$\partial_t \rho = \nu_{\text{syn}}(\lambda, \rho) - k_\rho(\lambda, \rho)\rho \quad (3.13)$$

The other quantities can be calculated from $\lambda, \rho,$ and their first spatial derivatives via (3.11). This description of ligand transport is much easier to study than the discrete description (3.1) we started with and will be of great value for the remainder of this work.

The explicit expressions for $D_\lambda(\lambda, \rho), D_\rho(\lambda, \rho), k_\lambda(\lambda, \rho),$ and $k_\rho(\lambda, \rho)$ in (3.12, 3.13) which follow from the derivation just described are rather involved. For $p = 0,$ they can be found in section D.1 of the appendix. For small ligand concentrations, $\lambda = 0,$ these expressions read:

$$\begin{aligned} D_\lambda(0, \rho) &= \frac{a^2 b_{\text{ext}} k_{\text{off}} (2(f_{\text{ext}} + f_{\text{int}})(b_{\text{int}} + k_{\text{off}})p + ab_{\text{int}} f_{\text{ext}} k_{\text{on}} \rho)}{4(b_{\text{int}} + k_{\text{off}})(b_{\text{ext}}(f_{\text{ext}} + f_{\text{int}})k_{\text{off}} + a(b_{\text{ext}} + b_{\text{int}})f_{\text{ext}}k_{\text{on}}\rho)} \\ D_\rho(0, \rho) &= 0 \\ k_\lambda(0, \rho) &= \frac{b_{\text{ext}} e^{\text{deg}} (f_{\text{ext}} + f_{\text{int}}) k_{\text{off}} + ab_{\text{deg}} b_{\text{int}} f_{\text{ext}} k_{\text{on}} \rho}{b_{\text{ext}}(f_{\text{ext}} + f_{\text{int}})k_{\text{off}} + a(b_{\text{ext}} + b_{\text{int}})f_{\text{ext}}k_{\text{on}}\rho} \\ k_\rho(0, \rho) &= \frac{f_{\text{deg}} f_{\text{int}}}{f_{\text{ext}} + f_{\text{int}}}. \end{aligned} \quad (3.14)$$

In Fig. 3.2, the coefficients D_λ, D_ρ and k_λ are displayed as a function of the ligand concentration λ for a typical choice of the parameters.

The receptor production rate in (3.13) following from the discrete description (3.1) is $\nu_{\text{syn}}(\lambda, \rho) = f_{\text{syn}}/a.$ Instead of being constant, it can be a different function of the ligand and receptor concentrations as discussed in section 3.1.1. In correspondence with the more realistic function (3.2) in the discrete case, we choose

$$\nu_{\text{syn}}(\lambda, \rho) = \frac{f_{\text{syn}}^0}{a} \left(1 - \frac{r_+(\lambda, \rho) + \psi s_+(\lambda, \rho)}{r_{\text{max}}} \right), \quad (3.15)$$

so that the receptor production saturates at some maximum total surface receptor concentration r_{max} for $\psi = 1.$ As in (3.2), the dimensionless parameter ψ allows for an enhancement, $\psi < 1,$ or reduction, $\psi > 1,$ of receptor synthesis caused by the presence of ligands bound to receptors on the cell surface.

Constant surface receptor approximation We now discuss the simpler situation described by (3.3) in which the cells maintain the surface receptor number R constant everywhere. In this case, an analogous derivation can be performed and leads to the result that ligand transport on large length scales is described by a single nonlinear diffusion equation:

$$\partial_t \lambda = \partial_x (D(\lambda)\partial_x \lambda) - k(\lambda)\lambda \quad . \quad (3.16)$$

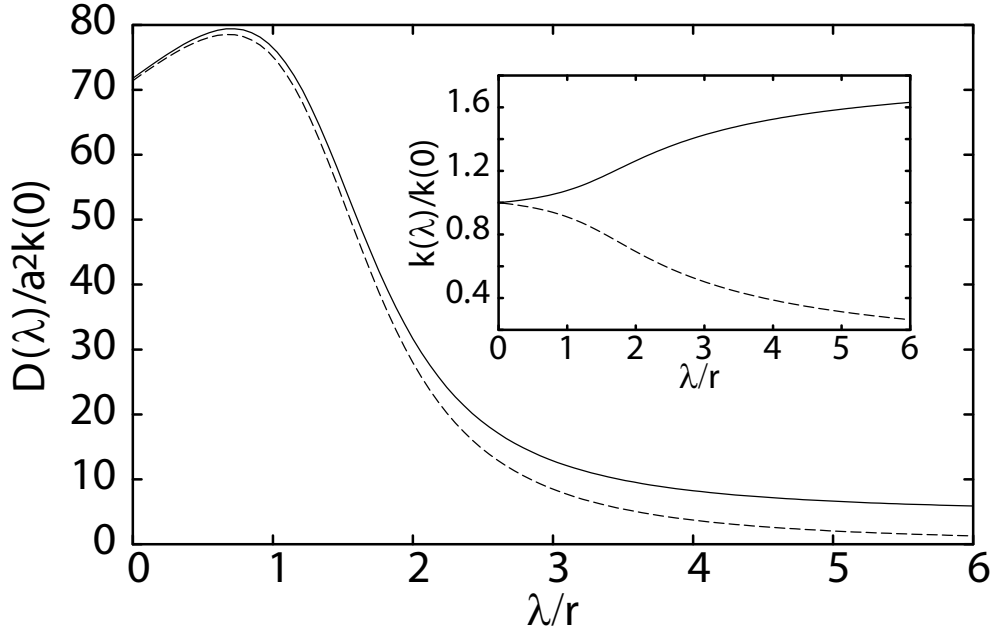


Figure 3.3: Effective diffusion coefficient $D(\lambda)$ in the transport equation for the constant surface receptor approximation (3.16) as a function of the ligand concentration λ/r for $p/b_{\text{deg}} = 10/3$ (solid line) and $p = 0$ (dashed line). Inset: effective degradation rate $k(\lambda)$ as a function of λ/r for $e_{\text{deg}} = 0$ (dashed line) and $e_{\text{deg}}/b_{\text{deg}} = 2/3$ (solid line). The total surface receptor concentration is denoted by r . Parameters as in Fig. 3.2.

Here, the effective diffusion coefficient $D(\lambda)$ in the absence of free diffusion, $p = 0$, and the effective degradation rate $k(\lambda)$ are given by

$$\begin{aligned} D(\lambda) &= \frac{a^2 b_{\text{ext}} b_{\text{int}} k_{\text{off}} a k_{\text{on}} r C_-(\lambda)}{4A(\lambda)(2a k_{\text{on}} r k_{\text{off}} (b_{\text{ext}} + b_{\text{int}}) + b_{\text{int}} C_-(\lambda))} \\ k(\lambda) &= \frac{C_+(\lambda)}{a k_{\text{on}} \lambda} \left(\frac{b_{\text{deg}} b_{\text{int}}}{2b_{\text{ext}} (b_{\text{ext}} + b_{\text{int}})} + \frac{e_{\text{deg}} k_{\text{off}}}{C_-(\lambda)} \right). \end{aligned} \quad (3.17)$$

In these expressions, $r = R/a$ and

$$\begin{aligned} A(\lambda) &= [-4b_{\text{ext}}(b_{\text{ext}} + b_{\text{int}})a^2 k_{\text{on}}^2 r \lambda + (b_{\text{int}} a k_{\text{on}} r + b_{\text{ext}} B_+(\lambda))^2]^{1/2} \\ B_{\pm}(\lambda) &= k_{\text{off}} + a k_{\text{on}} (\lambda \pm r) \\ C_{\pm}(\lambda) &= b_{\text{int}} a k_{\text{on}} r \mp A(\lambda) \pm b_{\text{ext}} B_{\pm}(\lambda). \end{aligned} \quad (3.18)$$

These coefficients $D(\lambda)$ and $k(\lambda)$ are shown as a function of λ in Fig. 3.3. Note, that in general only a appears as a length scale in the explicit expressions of the coefficients which appear in (3.12, 3.13) and (3.16), i.e. the ratio of the cell diameter $a - b$ and the diameter of the gap between cells b is insignificant for transport on large length scales.

Boundary effects So far, we have developed continuous descriptions for the ligand and receptor concentrations in the bulk. In a continuous description, we also need to define boundary conditions which correspond to the treatment of the boundary sites of the lattice in the discrete description defined in (3.4) and (3.5). These boundary conditions can be obtained

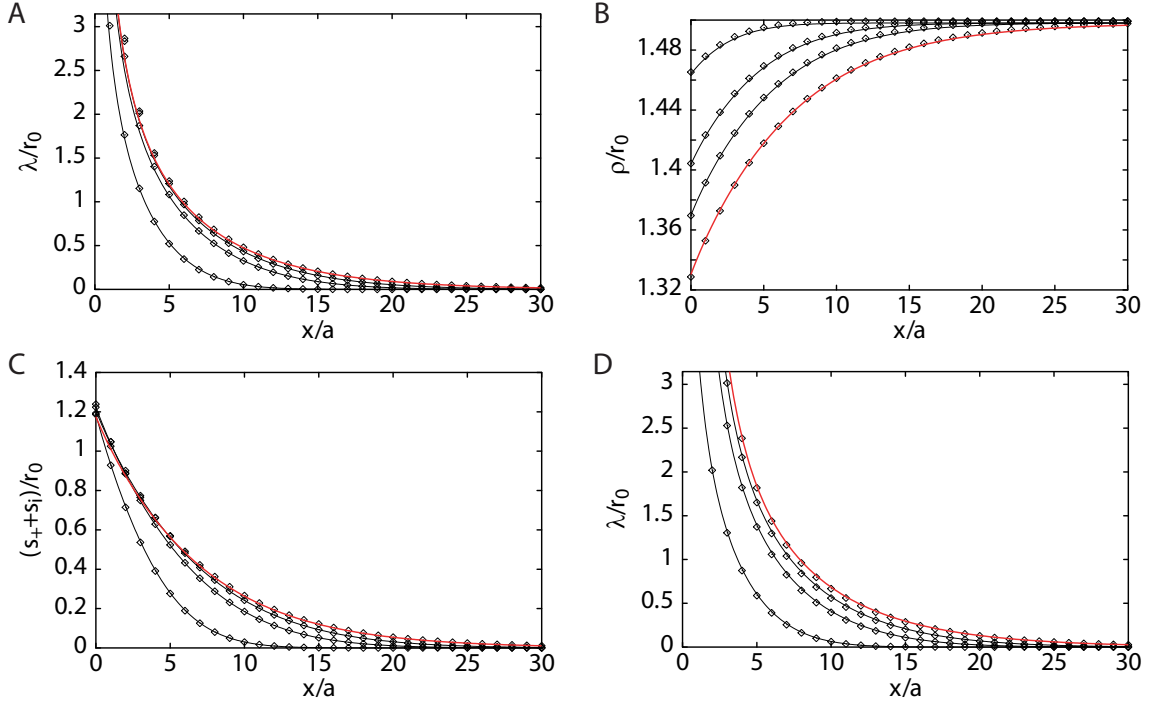


Figure 3.4: Time development of gradient formation in our description of ligand transport. Ligand densities in the presence of a source at $x = 0$ at different times $tb_{\text{deg}} = 0.72, 2.16, 3.6$ during gradient formation (black lines) and in steady state (red lines). Lines indicate solutions to (3.12), while symbols indicate solutions to (3.1) for comparison. (A-C) Time development of the profiles of the total ligand density $\lambda(x)$, the total receptor density $\rho(x)$, and the receptor bound ligand density $s_i(x) + s_+(x)$ in the absence of extracellular diffusion, i.e. for $p = 0$. (D) Like A but with $p/b_{\text{deg}} = 10/3$. All concentrations are normalized to the steady state value of the surface receptor concentration in the absence of ligands r_0 . Initial conditions at $t = 0$: $\lambda(x) = 0$ and $\rho(x) = (1 + f_{\text{int}}/f_{\text{ext}})r_0$. Parameters as in Fig. 3.2 with $\psi = 2$, $j_0/b_{\text{deg}}ar_0 = 175/6$, and $j = 0$ at $x/a = 50$.

from the requirement that the flux of ligands across the boundaries must be the same in the discrete and continuous descriptions. The description of the source (3.4) at $n = 0$ translates to imposing a λ -current $j_0 = -(D_\lambda(\lambda, \rho)\partial_x\lambda + D_\rho(\lambda, \rho)\partial_x\rho) = \nu$ at $x = 0$. The zero flux boundary condition (3.5) simply translates to a vanishing current of λ , i.e. $j = 0$, at these boundaries in the continuous description.

Comparison of discrete and continuous descriptions For several different parameter choices, we have numerically verified that the solutions of (3.12, 3.13) and (3.16) are in good agreement with the corresponding discrete microscopic description on large length scales, see Figures 3.4 and 3.5. For simplicity, we sometimes use the same notation for the quantities appearing in the discrete descriptions and the corresponding ones in the continuous descriptions. In the previous chapter, for example, we denoted the total ligand concentration $L_n + S_n^{(l)} + S_n^{(r)} + S_n^{(i)}$ in the discrete description by λ which was actually defined as the total ligand concentration in the continuous description. This slightly imprecise notation is justified by the good agreement between the continuous and discrete descriptions.

It is important to be aware of the fact that the description via (3.12, 3.13) or (3.16) is inappropriate if p is too large, i.e. if extracellular diffusion contributes significantly to

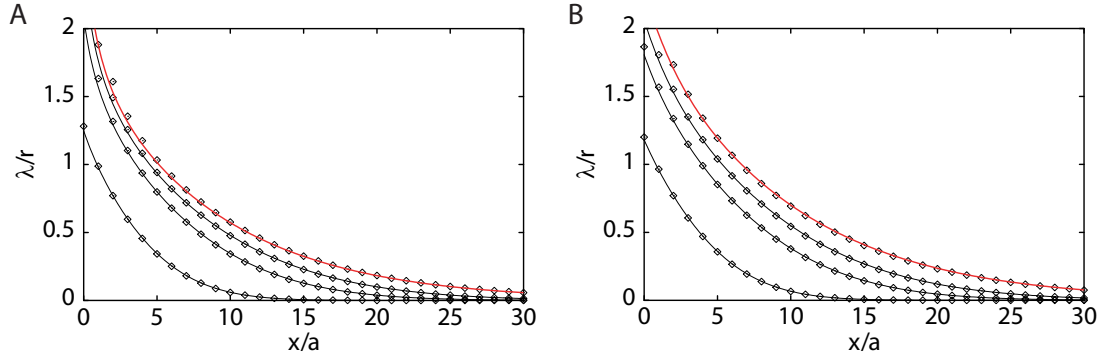


Figure 3.5: Time development of gradient formation in the description of ligand transport with constant surface receptor approximation. Ligand densities $\lambda(x)$ in the presence of a source at $x = 0$ at different times $tb_{\text{deg}} = 0.72, 2.16, 3.6$ during gradient formation (black lines) and in the steady state (red lines). Lines indicate solutions to (3.16), while symbols indicate solutions to (3.3) for comparison. (A) Time development of $\lambda(x)$ in the absence of extracellular diffusion, i.e. for $p = 0$. (B) Like A but with $p/b_{\text{deg}} = 100/3$. Parameters as in Fig. 3.2 with $j_0/b_{\text{deg}}R = 25/3$ and $j = 0$ at $x/a = 50$.

ligand transport, or if the degradation and production rates $b_{\text{deg}}, e_{\text{deg}}, f_{\text{deg}}, f_{\text{syn}}$ are not much smaller than the other rates. This is a consequence of the approximations made in the derivation: the degradation rates were treated as a small perturbation in (3.11) and the adiabatic approximation clearly becomes invalid if p is sufficiently large to make the time scales τ_a and τ_L comparable.

3.2 Two dimensional description of morphogen transport

3.2.1 Microscopic two dimensional description

In this section, we generalize the theoretical description of ligand transport for the constant surface receptor approximation given by (3.3) to two space dimensions. The generalization of the description with receptor kinetics (3.1) is conceptually identical but notationally more cumbersome. One can choose different lattice structures in two dimensions. Obvious possibilities are a square lattice or a triangular lattice in which the cells have the shape of hexagons. One could even use lattices with more than one cell type or irregular lattices. A disordered lattice structure would give the best account of the situation in a developing tissue. For simplicity, we have decided to use a triangular lattice with hexagonal cells in our description, see Fig. 3.6 D for an illustration. This lattice structure is an idealization since it neglects the irregular cell arrangement in a tissue, compare Fig. 3.6 B and D.

It is straightforward to generalize (3.3) to two dimensions. Taking into account that the externalization of the ligand-receptor complexes can occur on all surfaces of the cell with equal probability, the equations for the kinetics on a two dimensional lattice are

$$\begin{aligned} \partial_t L_m &= k_{\text{off}} \sum_{\langle m, (n, j) \rangle} S_{n, j} - \frac{N k_{\text{on}}}{2} \left(\frac{2R}{N} - \sum_{\langle m, (n, j) \rangle} S_{n, j} \right) L_m - e_{\text{deg}} L_m \\ \partial_t S_{n, j} &= \frac{b_{\text{ext}}}{N} S_n^{(i)} - (b_{\text{int}} + k_{\text{off}}) S_{n, j} + \frac{N k_{\text{on}}}{2} \left(\frac{R}{N} - S_{n, j} \right) L_{\langle n, j \rangle} \end{aligned}$$

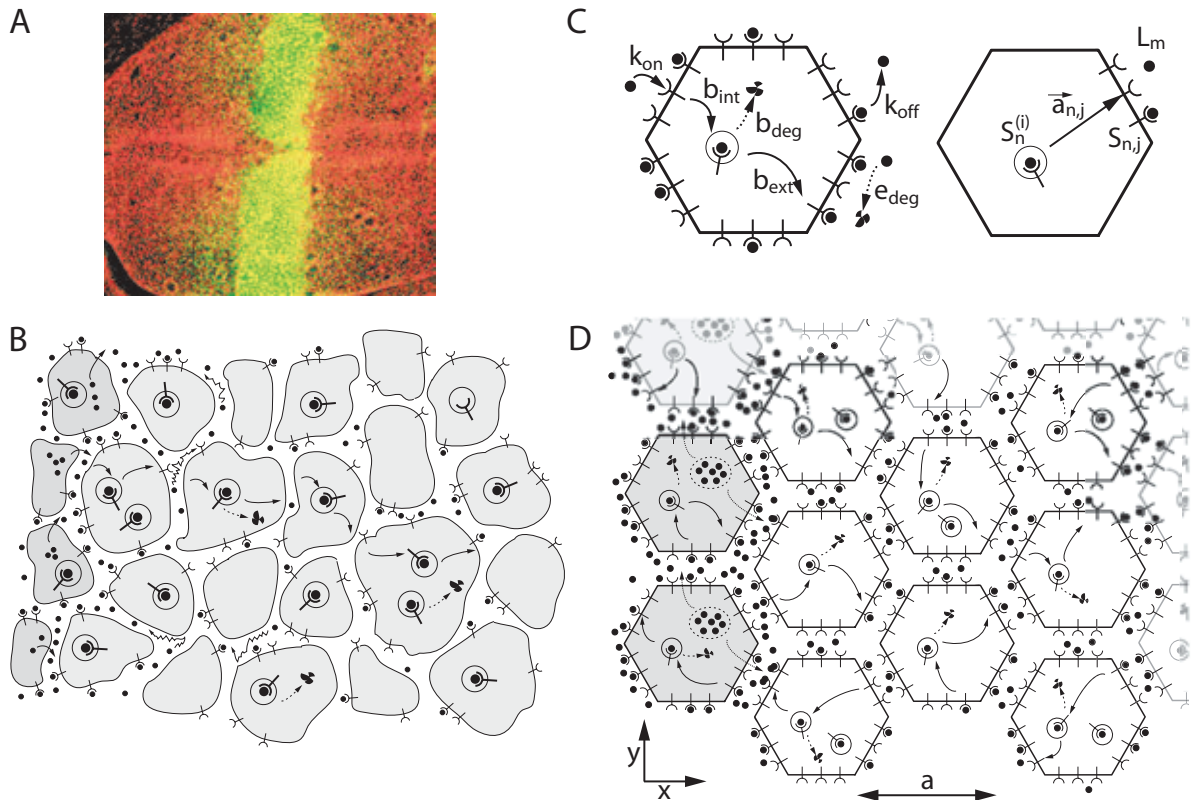


Figure 3.6: Ligand transport in two dimensions. (A) Tissue in the region of the wing disk where the Dpp gradient forms. Cell membranes are labeled in red, the morphogen Dpp is shown in green. (B) Schematic of this tissue. Source cells which produce ligands are shown in darker gray, the cells in the target tissue in light gray. The ligands spread from the source into the target tissue by transcytosis and diffusion in the extracellular space surrounding the cells. (C) The rates for the various processes are denoted as in one dimension, see Fig. 3.1. Receptor bound ligands can be present on the six surfaces of each cell and inside the cells. The concentration of the receptor-bound ligands on surface j of cell n is denoted $S_{n,j}$, that inside cell n is termed $S_n^{(i)}$. Free ligands exist in the gaps between two cell surfaces. Their concentration in gap m is denoted L_m . (D) Triangular lattice structure with hexagonal cells used for the discrete theoretical description of ligand transport in two dimensions. The source cells which are shown in darker gray secrete ligands into the extracellular spaces surrounding them. The cell diameter is a .

$$\partial_t S_n^{(i)} = -b_{\text{ext}} S_n^{(i)} + b_{\text{int}} \sum_{j=1}^N S_{n,j} - b_{\text{deg}} S_n^{(i)}, \quad (3.19)$$

where the $\langle \cdot, \cdot \rangle$ denote adjacent lattice sites, $S_n^{(i)}$ is the internal bound ligand concentration in cell n , $S_{n,j}$ the surface bound ligand concentration on surface j of cell n , L_m the free ligand concentration in extracellular space m , and N denotes the number of surfaces per cell. The free ligand concentration L_m is always defined in the middle between two surfaces of adjacent cells. The sum over $\langle m, (n, j) \rangle$ in (3.19) extends over the values of $S_{n,j}$ on those two surfaces. The notation used here is illustrated in Fig. 3.6 C for a triangular lattice with $N = 6$. At the boundaries of the lattice, the equation for $\partial_t L_m$ in (3.19) is modified analogously to the one dimensional situation, see (3.4, 3.5).

3.2.2 Effective transport equations for transcytosis in two dimensions

In two dimensions, a formal derivation of transport equations for the transcytosis dominated limit starting from the discrete description (3.19) is aggravated by the fact that one has to introduce a two dimensional lattice structure that generally breaks rotational symmetry. However, rotational invariance is to be anticipated in a tissue with disordered cell arrangement because there is no distinguished direction defined on length scales large compared to one cell diameter in such a tissue. The demand of rotational invariance puts constraints on the general form of the transport equation in two dimensions.

Furthermore, in the absence of ligand degradation, the total ligand number is a conserved quantity. This implies that the equation describing the time development of the total ligand concentration λ is a continuity equation. Thus, in the case of the constant total surface receptor approximation, transport in two dimensions is described by a rotationally invariant second order continuity equation for the total ligand concentration λ . The presence of ligand degradation should appear as a sink term in this equation.

If we finally consider that the two dimensional description should in essence reduce to the one dimensional one for boundary and initial conditions that lead to translation invariance in one direction, we obtain the general form

$$\partial_t \lambda = \nabla \cdot (D(\lambda) \nabla \lambda) - k(\lambda) \lambda \quad (3.20)$$

for the transport equation describing transcytosis in two dimensions.

The coefficients $D(\lambda)$ and $k(\lambda)$ in (3.20) depend on the two dimensional cell arrangement and are usually different from those in the one dimensional case (3.17). For a regular lattice like the triangular lattice shown in Fig. 3.6 D, (3.20) is only approximately valid. We have calculated $D(\lambda)$ and $k(\lambda)$ to give a good approximation to the discrete description defined on the triangular lattice structure shown in Fig. 3.6 D. This was done by projecting this lattice structure on a one dimensional lattice. We then proceeded with the derivation as in the one dimensional case described in section 3.1.2. We find the same $k(\lambda)$ as in one dimension, see (3.17). The effective diffusion coefficient $D(\lambda)$ simply changes by a factor of 2/3, i.e. $D^{(2d)}(\lambda) = (2/3)D^{(1d)}(\lambda)$ with $D^{(1d)}(\lambda)$ from (3.17).

As in one dimension, the continuous densities of the quantities corresponding to those defined in the discrete microscopic description can be related to λ via an adiabatic approximation similar to (3.11). While the concentration of receptor-bound ligands on the cell surface $s_+(\vec{x}) = \sum_{j=1}^N S_{n,j}/a^2$, the concentration of internalized receptor-bound ligand $s_i(\vec{x}) = S_n^{(i)}/a^2$, and the free ligand concentration $l(\vec{x}) = L_m/a^2$ are scalars as in the one dimensional case, a vector $\vec{s}(\vec{x}, t) = \sum_{j=1}^N S_{n,j} \vec{a}_j/a^2$ appears in the two dimensional case. Here, the \vec{a}_j define the location of the N surfaces of the cell with respect to its center, see Fig. 3.6 C. The vector

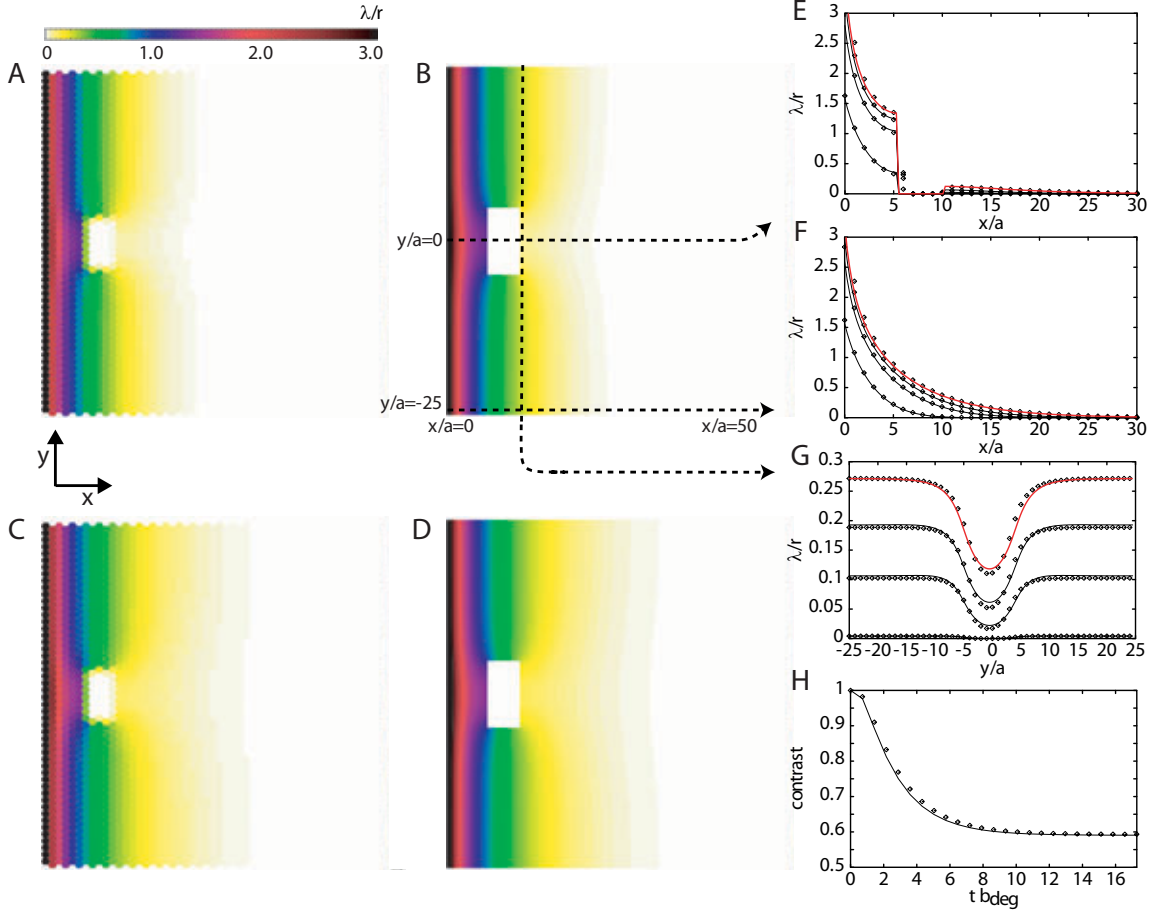


Figure 3.7: Ligand densities $\lambda(\vec{x})$ in two dimensions. The solution to the continuous transport equation (3.20) is compared to that of the discrete description (3.19) in presence of a region which the ligand cannot enter located at $6 \leq x/a \leq 11$ and $-4 \leq y/a \leq 4$. In the discrete description, this is realized by setting b_{int} to zero in the region. In the continuous description, zero flux boundary conditions are imposed on the outlining edge of the region. (A-D) Two dimensional ligand profiles at $t b_{\text{deg}} = 3.6$ (A,B) and at $t b_{\text{deg}} = 17.3$ which is close to the steady state (C,D). These were obtained by solving the discrete (A,C) and continuous description (B,D) respectively. The rectangular region which the ligand cannot enter appears in white. It looks smaller in A and C than in B and D because in the discrete description, ligands can still bind to surface receptors on the cells located at the edge of the region so that $\lambda > 0$ for these cells, see also section F.2 of the appendix. (E-G) Profiles of $\lambda(\vec{x}, t)$ along the slices indicated in B at $t b_{\text{deg}} = 0.72, 2.16, 3.6$ (black lines) and in steady state (red lines). Lines indicate solutions to (3.20), while symbols indicate solutions to (3.19) for comparison. (H) Contrast of the depletion of $\lambda(\vec{x}, t)$ shown in G, see (2.1) for definition. Initial condition: $\lambda(\vec{x}) = 0$. Parameters as in Fig. 3.2 with $p = 0$, $j_0 a / b_{\text{deg}} R = 25/3$ at $x = 0$, $j = 0$ at $y/a = \pm 25$ and at $x/a = 50$.

\vec{s} corresponds to s_- in the one dimensional situation and measures the polarization of the distribution of receptor bound ligands on the cell surface.

By the same considerations as discussed above, the description with receptor kinetics (3.12, 3.13) generalizes to

$$\begin{aligned}\partial_t \lambda &= \nabla \cdot (D_\lambda(\lambda, \rho) \nabla \lambda + D_\rho(\lambda, \rho) \nabla \rho) - k_\lambda(\lambda, \rho) \lambda, \\ \partial_t \rho &= \nu_{\text{syn}}(\lambda, \rho) - k_\rho(\lambda, \rho) \rho,\end{aligned}\tag{3.21}$$

where the coefficients $D_\lambda(\lambda, \rho)$, $D_\rho(\lambda, \rho)$, $k_\lambda(\lambda, \rho)$, and $k_\rho(\lambda, \rho)$ again depend on the lattice structure. We have calculated these coefficients for a triangular lattice structure as outlined above and find $D_\lambda^{(2d)}(\lambda, \rho) = (2/3)D_\lambda^{(1d)}(\lambda, \rho)$ and $D_\rho^{(2d)}(\lambda, \rho) = (2/3)D_\rho^{(1d)}(\lambda, \rho)$, where the expressions for the one dimensional case are shown explicitly in section D.1. The degradation rates k_λ and k_ρ are the same as in the one dimensional situation. Moreover, the rate of receptor synthesis ν_{syn} is the same as in one dimension, see (3.15), except for a factor of $1/a$:

$$\nu_{\text{syn}}(\lambda, \rho) = \frac{f_{\text{syn}}^0}{a^2} \left(1 - \frac{r_+(\lambda, \rho) + \psi s_+(\lambda, \rho)}{r_{\text{max}}} \right).$$

Boundary effects In the absence of ligand degradation, the equations for $\partial_t \lambda$ in (3.20) and (3.21) are continuity equations as in one dimension. Thus, a homogeneous ligand source located at $x < 0$ injecting ligands into the system at rate ν per cell is described by fixing a λ -current $j_0 = \nu/a$ across the boundary line at $x = 0$. The zero flux boundary condition is realized by a vanishing current of λ , i.e. $j = 0$, at the corresponding boundaries in the continuous description.

Comparison of discrete and continuous description We have compared solutions of the continuous equation (3.20) to those of the discrete description for a two dimensional geometry containing a rectangular region which the ligand cannot enter, see Fig. 3.7. The agreement between both descriptions is reasonably good. As in one dimension, the continuous description becomes inappropriate for large degradation rates or a large hopping rate p which describes extracellular diffusion. Moreover, the use of a particular lattice structure in the discrete microscopic description in two dimensions always leads to a small discrepancy in comparison to the continuous description which does not account for the respective lattice anisotropy.

3.3 Analysis of the effective transport equations

Given the effective transport equations for transcytosis found in the previous sections, let us now discuss essential properties of this transport mechanism. Since we have shown that the two dimensional case is closely related to the one dimensional one, we concentrate on the one dimensional situation here and discuss features which are apparent in (3.12, 3.13) and (3.16).

3.3.1 Properties of transcytosis

For small λ , D_λ and k_λ approach finite values. In this limit, (3.12) becomes a linear diffusion equation with degradation. On large length scales, transcytosis is consequently indistinguishable from passive diffusion for small ligand concentrations. For large λ , D_λ and k_λ exhibit the asymptotic behavior $D_\lambda \approx D_0 + c_1(\rho)\lambda^{-2}$, and $k_\lambda \approx e_{\text{deg}} + c_2(\rho)\lambda^{-1}$, with the diffusion constant of the extracellular diffusion $D_0 = pa^2/2$, $c_1(\rho) = ab_{\text{ext}}f_{\text{int}}k_{\text{off}}\rho/4k_{\text{on}}(b_{\text{ext}} + b_{\text{int}})$ and $c_2(\rho) = b_{\text{deg}}b_{\text{int}}\rho/(b_{\text{ext}} + b_{\text{int}})$. Furthermore, $D_\rho \approx -D_0 - c_1(\rho)\lambda^{-2}$ in this limit. A maximum

of D_λ can occur for intermediate values of λ if p is not too large. Similarly, there is a minimum of D_ρ as a function of λ for small p .

In the special case $D_0 = 0$, D_ρ as well as D_λ vanish in the absence of receptors, i.e. for $\rho = 0$, and if either binding or un-binding of ligands from the receptor, internalization or externalization of occupied or free receptors is suppressed, i.e., if either one of the rates k_{on} , k_{off} , b_{int} , b_{ext} , f_{int} , or f_{ext} vanishes. This reflects that in the absence of extracellular diffusion, transport is generated by repeated internalization and externalization of ligand-bound receptors as well as ligands binding to and un-binding from surface receptors. In the limit of fast internalization or fast un-binding, ligand is confined to the cell interior or the extracellular space, respectively, and transport is consequently hampered. Indeed for $D_0 = 0$, $D_\lambda \rightarrow 0$ if $b_{\text{int}} \rightarrow \infty$ or if $k_{\text{off}} \rightarrow \infty$.

The functions $D(\lambda)$ and $k(\lambda)$ appearing in the simplified equation for the constant surface receptor approximation (3.16) have virtually the same properties as just discussed for D_λ and k_λ from (3.12). For example the asymptotic behavior for large λ is essentially the same: $D(\lambda) \approx D_0 + c'_1 \lambda^{-2}$ and $k \approx e_{\text{deg}} + c'_2 \lambda^{-1}$, where the constants are different: $c'_1 = ab_{\text{int}}k_{\text{off}}r/(4k_{\text{on}})$ and $c'_2 = b_{\text{deg}}b_{\text{int}}r/b_{\text{ext}}$.

Comparing (3.13) and (3.9), we see that $j_\rho = 0$. This demonstrates that the terms in (3.10) do not give rise to transport over large distances. They are merely caused by transport within one cell. Thus, the continuous description reflects that receptors are confined to one cell in the discrete description. Interestingly, in (3.12), a coupling term exists with effective coefficient $D_\rho(\lambda, \rho)$ which describes ligand currents induced by gradients of the receptor concentration. This additional term $\propto \partial_x \rho$ gives a contribution to the ligand current that is directed upwards a receptor gradient since $D_\rho \leq 0$. This contribution to the current comes up, because the ligand affinity for a region increases with the receptor concentration in that region. In the limit of small ligand concentrations this term can be interpreted as a drift term since $D_\rho \propto \lambda$ for small λ .

3.3.2 Simple limits

The system (3.12, 3.13) becomes simpler if some of the transport steps are assumed to be much faster than the others, i.e. if the corresponding rates are very large. For example in the limit of very fast binding, $k_{\text{on}} \rightarrow \infty$,

$$\begin{aligned} D_\lambda(\lambda, \rho) &= \frac{-a^2 b_{\text{ext}} b_{\text{int}} f_{\text{ext}} f_{\text{int}} k_{\text{off}} \rho}{B(\lambda, \rho)} \\ D_\rho(\lambda, \rho) &= \frac{a^2 b_{\text{ext}} b_{\text{int}} f_{\text{ext}} f_{\text{int}} k_{\text{off}} \lambda}{B(\lambda, \rho)} \\ k_\lambda(\lambda, \rho) &= \frac{b_{\text{deg}} b_{\text{int}}}{b_{\text{ext}} + b_{\text{int}}} \\ k_\rho(\lambda, \rho) &= \frac{b_{\text{deg}} b_{\text{int}} (f_{\text{ext}} + f_{\text{int}}) \lambda + (b_{\text{ext}} + b_{\text{int}}) f_{\text{deg}} f_{\text{int}} (\rho - \lambda)}{(b_{\text{ext}} + b_{\text{int}}) (f_{\text{ext}} + f_{\text{int}}) \rho}, \end{aligned} \quad (3.22)$$

with

$$\begin{aligned} B(\lambda, \rho) &= 4(b_{\text{int}} f_{\text{ext}} f_{\text{int}} (b_{\text{int}} + k_{\text{off}}) + b_{\text{ext}} (b_{\text{int}} f_{\text{ext}} f_{\text{int}} + f_{\text{ext}} f_{\text{int}} k_{\text{off}} \\ &\quad - b_{\text{int}} (f_{\text{ext}} + f_{\text{int}}) k_{\text{off}})) \lambda - 4(b_{\text{ext}} + b_{\text{int}}) f_{\text{ext}} f_{\text{int}} (b_{\text{int}} + k_{\text{off}}) \rho. \end{aligned}$$

A closer look at this limit is worthwhile because in actual biological systems, it is well possible that the binding step is fast due to the small volume of the gaps between cells. There are no free ligand molecules in this limit, $l = 0$ via (3.11). As all ligands are bound to receptors, free diffusion does not contribute to the current and p does not appear in (3.22). All ligands are

bound to a receptor which imposes the restriction $\lambda \leq \rho$. Many of the properties discussed above for the general case can be read directly from the expressions (3.22). Due to the constraint $\lambda \leq \rho$, however, the statements for the asymptotic behavior for $\lambda \rightarrow \infty$ do not apply anymore. Furthermore, D_λ does no longer exhibit a maximum as a function of λ . It either grows or decreases monotonically depending on the parameter choice.

In principle, one can write down simpler expressions like in (3.22) for many different limits. If several transport steps are much faster than the others, only the ratios of the corresponding parameters enter the simplified description. For example, if the binding and un-binding of the ligand to the receptor is much faster than all other processes the effective diffusion coefficient and degradation rate do not depend on k_{on} and k_{off} individually but only on the ratio $k_{\text{on}}/k_{\text{off}}$. The number of parameters can thus be reduced to obtain the minimal description for a given situation. A trivial example is the situation $k_{\text{on}} \gg k_{\text{off}} \gg b_{\text{ext}} \gg b_{\text{int}}$ in (3.16), for which we obtain the effective diffusion coefficient

$$\lim_{b_{\text{ext}} \rightarrow \infty} \lim_{k_{\text{off}} \rightarrow \infty} \lim_{k_{\text{on}} \rightarrow \infty} D(\lambda) = b_{\text{int}} a^2 / 4,$$

which reflects that the slowest process — in this case the internalization of ligands — limits transport. Note, that the limits taken above do not commute, e.g. $D(\lambda) = 0$ for $k_{\text{off}} \gg k_{\text{on}}$ as pointed out in section 3.3.1.

3.3.3 Analytical steady state solution

It is useful to have an analytical solution of the steady state gradients generated by the transport equations (3.12, 3.13) and (3.16) where the ligand current is $j = -D_\lambda(\lambda, \rho)\partial_x \lambda - D_\rho(\lambda, \rho)\partial_x \rho$ and $j = -D(\lambda)\partial_x \lambda$ respectively. We calculate the steady state solution corresponding to a gradient formed in the half space $x \geq 0$ in the presence of a source which is located at $x = 0$. The effect of the source is captured by a boundary condition on the current $j = j_0 > 0$ at $x = 0$. Here, j_0 is proportional to the rate of ligand secretion from the source cells. Starting from the initial condition $\lambda(x) = 0$ and $\rho(x) = \rho_0$, the ligands spread into the region $x \geq 0$, where they build up a gradient. Here, ρ_0 denotes the equilibrium value of the total receptor concentration in the absence of ligands. The steady state ligand profile $\lambda(x)$ is established after very long times, i.e. for $t \rightarrow \infty$. The typical time scale for the relaxation of the ligand distribution into the steady state can be estimated by linearizing the transport equations about the steady state profile $\lambda(x)$. If j_0 is small so that the ligand concentration λ for $x \geq 0$ is small, (3.16) simplifies to a linear equation $\partial_t \lambda = D(0)\partial_x^2 \lambda - k(0)\lambda$. It can be shown that the time scale of gradient formation is then given by $k(0)^{-1}$. As λ always becomes small sufficiently far away from the source, we expect essentially the same relaxation time for larger currents j_0 .

In the steady state, (3.13) with the condition $\partial_t \rho = 0$ yields a relation $\rho(\lambda)$. This combined with (3.12) leads to the steady state equation

$$\partial_x(D(\lambda)\partial_x \lambda) - k(\lambda)\lambda = 0, \quad (3.23)$$

with $D(\lambda) = D_\lambda(\lambda, \rho(\lambda)) + D_\rho(\lambda, \rho(\lambda))\partial_\lambda \rho(\lambda)$ and $k(\lambda) = k_\lambda(\lambda, \rho(\lambda))$. We assume that the steady state relation $\rho(\lambda)$ is a monotonic function of λ and converges to finite values ρ_∞ for $\lambda \rightarrow \infty$ and ρ_0 for $\lambda \rightarrow 0$. This expresses that each cell only contains a limited number of receptors and is never completely devoid of receptors. It implies that $\partial_\lambda \rho = 0$ for large λ , so that in this limit $D(\lambda) \approx D_\lambda(\lambda, \rho_\infty)$ in (3.23). The steady state equation of the simplified description (3.16) in which the surface receptor concentration is assumed to be constant is an equation of the same general form as (3.23).

In the steady state, the total ligand concentration decreases monotonically with increasing distance from the source. The corresponding distribution $\lambda(x)$ which follows from (3.23) can be determined exactly. It is given by

$$x = - \int_{\lambda(0)}^{\lambda(x)} d\lambda' D(\lambda')/j(\lambda') \quad . \quad (3.24)$$

Here, $j(\lambda)$ is the steady state current:

$$j(\lambda) = \left(2 \int_0^\lambda d\lambda' k(\lambda') D(\lambda') \lambda' \right)^{1/2} \quad . \quad (3.25)$$

For small λ , the ligand profile decays as $\lambda \propto \exp(-x/\xi)$ with $\xi = \sqrt{D(0)/k(0)}$. Furthermore, in the limit of large λ and in the absence of free diffusion $D_0 = 0$, the steady state profile can be formally described by a singularity which occurs at a position $x^* < 0$. The approach to this singularity is characterized by

$$\lambda \sim (x - x^*)^{-1} (-\ln(x - x^*))^{-1/2} \quad . \quad (3.26)$$

This singularity results from the asymptotic behavior of the current j for large $\lambda \gg \lambda_T$:

$$j^2(\lambda) \approx j(\lambda_T)^2 + 2e_{\text{deg}} c_1(\rho_\infty) \ln(\lambda/\lambda_T) + 2c_1(\rho_\infty) c_2(\rho_\infty) (1/\lambda_T - 1/\lambda).$$

Here, λ_T denotes a crossover value beyond which the asymptotic behavior becomes valid. Therefore the current diverges as $j^2 \approx 2c_1(\rho_\infty) e_{\text{deg}} \ln \lambda$. Note, that the limit of vanishing e_{deg} is singular. For $e_{\text{deg}} = 0$, the current reaches for large λ a finite maximal value j_{max} and the steady state profile diverges as $\lambda \approx c_1(\rho_\infty)/(x - x^*) j_{\text{max}}$.

The situation is different if free diffusion in the extracellular space is present. Then, $D(\lambda)$ in (3.23) changes its asymptotic behavior to $D \approx c_1(\rho_\infty)/\lambda^2 + D_0$. For large λ , (3.23) becomes linear and the steady state solution decays exponentially on a length scale $\xi_d = \sqrt{D_0/e_{\text{deg}}}$. This implies that $\lambda(x)$ does not have a formal singularity at a finite x^* .

Note, that the whole discussion of steady states in this section also applies to the simpler description (3.16) in which the surface receptor concentration is assumed to be constant. In section 4.1, we will use these results to discuss the robustness of steady state gradients formed by transcytosis and extracellular diffusion.

3.4 Extracellular diffusion dominated limit and DBTS model

In order to ultimately identify the mechanism of morphogen gradient formation present in a given system, it is important to develop mathematical descriptions of all possibly relevant transport mechanisms so that these can be compared to the available experimental data. As pointed out in section 1.4, extracellular diffusion is widely believed to be the dominant transport mechanisms for some morphogens. For this reason, we discuss the extracellular diffusion dominated limit of the transport phenomenon defined by (3.1) in this section.

It is assumed that extracellular diffusion gives the dominant contribution to the ligand current. We consequently neglect the contribution of transcytosis. This approach is valid if the rates are such that the effective diffusion coefficient resulting from transcytosis $D(\lambda, \rho)|_{\rho=0}$ in (3.12) is much smaller for all values of λ and ρ than the extracellular diffusion constant D_0 . This situation arises if D_0 is large and at least one of the rates k_{on} , k_{off} , b_{int} , and b_{ext} is very small.

The derivation of the continuum limit of (3.1) is straightforward for this situation. Only the equation for the time development of the free ligand concentration contains a linear diffusion term. All other quantities can be described by a coupled set of ordinary differential equations. Together, these constitute a set of reaction-diffusion equations. Such reaction-diffusion systems have been studied extensively in pattern formation [67, 58]. It is also unproblematic to generalize this system to two space dimensions. With the notation used throughout this chapter, the kinetic equations in two dimensions read

$$\begin{aligned}
 \partial_t l &= D_0 \Delta l - k_{\text{on}} a^2 l r_+ + k_{\text{off}} s_+ - e_{\text{deg}} l \\
 \partial_t s_+ &= k_{\text{on}} a^2 l r_+ - (b_{\text{int}} + k_{\text{off}}) s_+ + b_{\text{ext}} s_i \\
 \partial_t s_i &= b_{\text{int}} s_+ - (b_{\text{ext}} + b_{\text{deg}}) s_i \\
 \partial_t r_+ &= \frac{f_{\text{syn}}}{a^2} + k_{\text{off}} s_+ + f_{\text{ext}} r_i - k_{\text{on}} l r_+ - f_{\text{int}} r_+ \\
 \partial_t r_i &= f_{\text{int}} r_+ - (f_{\text{ext}} + f_{\text{deg}}) r_i.
 \end{aligned} \tag{3.27}$$

To obtain agreement with the diffusion, binding, and trafficking model with saturating surface receptor concentration (DBTS model) that was first introduced in [59], we describe the receptor production by the cells in a slightly different way than in (3.27). Newly synthesized receptors appear inside the cells and not on the cell surface. This is done in order to facilitate the comparison to previous results [60], see chapter B of the appendix for details. Moreover, the receptor externalization rates f_{ext} and b_{ext} depend on the total surface receptor concentration $s_+ + r_+$ such that this concentration saturates at a maximal value r_{max} . In section B.3, we discuss the small differences which occur from this treatment of the receptor kinetics compared to the one used above. The corresponding kinetic equations in two dimensions read:

$$\begin{aligned}
 \partial_t l &= D_0 \Delta l - k_{\text{on}} a^2 l r_+ + k_{\text{off}} s_+ - e_{\text{deg}} l \\
 \partial_t s_+ &= k_{\text{on}} a^2 l r_+ - (b_{\text{int}} + k_{\text{off}}) s_+ + b_{\text{ext}}^0 \left(1 - \frac{s_+ + r_+}{r_{\text{max}}} \right) s_i \\
 \partial_t s_i &= b_{\text{int}} s_+ - \left(b_{\text{ext}}^0 \left(1 - \frac{s_+ + r_+}{r_{\text{max}}} \right) + b_{\text{deg}} \right) s_i \\
 \partial_t r_+ &= k_{\text{off}} s_+ + f_{\text{ext}}^0 \left(1 - \frac{s_+ + r_+}{r_{\text{max}}} \right) r_i - k_{\text{on}} l r_+ - f_{\text{int}} r_+ \\
 \partial_t r_i &= \frac{f_{\text{syn}}^0}{a^2} + f_{\text{int}} r_+ - \left(f_{\text{ext}}^0 \left(1 - \frac{s_+ + r_+}{r_{\text{max}}} \right) + f_{\text{deg}} \right) r_i,
 \end{aligned} \tag{3.28}$$

where l again denotes the concentration of free extracellular ligands, s_+ is the concentration of ligand bound receptors on cell surfaces, s_i is the concentration of ligand bound receptors inside cells, and r_+ and r_i are the concentrations of free receptors outside and inside the cell, respectively.

It must be emphasized that a model which is very similar to this limit of our description was first introduced by Lander et al. [60]. Our discrete description (3.1) captures processes that were neglected in the model studied in that work, namely the transport of ligands through the cells by transcytosis. Unfortunately, some technical and conceptual flaws were made in [60] which lead to doubtful conclusions about the role of extracellular diffusion and receptor binding in morphogen transport, see chapter B of the appendix for details. A thorough investigation of the two dimensional ligand profiles obtained from (3.28) was performed in [59]. The main results found in that article are presented in section 2.3 and chapter B of the appendix.

Chapter 4

Robustness and precision of morphogen gradients

In this chapter, we discuss two key properties of morphogen gradients — robustness and precision.

The “robustness” of morphogen gradients quantifies their sensitivity to fluctuations and larger changes of the morphogen secretion rate of the source cells. It has been observed in experiments that over-expression of the morphogen Dpp in the *Drosophila* wing disk does not significantly affect the patterning of the tissue [71]. As target gene expression is directly controlled by the morphogen concentration, a possible explanation for this observation is that the morphogen gradient itself does not change significantly in this situation. In section 4.1, we will use the effective transport equations derived in chapter 3 to investigate this property in our description of morphogen gradient formation.

The shape and functionality of adult structures and tissues often shows only very slight variations between different animals of the same species. As these structures are a result of the processes that occur during the development of the organism, one may expect that the spatial patterns of gene expression in a developing tissue are defined in a reliable and reproducible way. In fact, such reproducibility of accurate gene expression patterns during development has been observed in the *Drosophila* embryo [54]. It could be achieved if the morphogen gradients that control gene expression in the tissue are themselves reliable in specifying concentration thresholds at well-defined positions. We refer to this property of a morphogen gradient as “precision”. In general, the precision of a gradient is reduced by the disorder and noise that is present in a developing tissue. In section 4.2, we will discuss how precise gradient formation can be achieved.

4.1 Robustness of morphogen gradients

We investigate the robustness of steady state morphogen gradients in this section. We have previously discussed most of the results presented in this section in [9]. We start from the one dimensional continuous description of transcytosis (3.12, 3.13) and investigate the effects of extracellular diffusion in section 4.1.2. The results presented here remain valid in the two dimensional case.

Definition of robustness We examine steady state gradients formed in the half space $x \geq 0$ in the presence of a source which is located at $x = 0$. The effect of the source is captured by a boundary condition on the current $j = j_0 > 0$ at $x = 0$. Here, j_0 is proportional to the

rate of ligand secretion from the source cells. We define the robustness \mathcal{R} of the gradient such that \mathcal{R} becomes large if changes of j_0 have little influence on the ligand profile $\lambda(x)$ in the steady state. This implies that the gradient is robust with respect to fluctuations of the ligand secretion rate if \mathcal{R} is large.

This robustness can be quantified by an appropriate response function of the system that measures the sensitivity of the steady state gradient to changes of j_0 . A useful definition for the dimensionless robustness is

$$\mathcal{R}(j_0, \lambda) = a(j_0 \partial_{j_0} x(\lambda))^{-1}, \quad (4.1)$$

where $x(\lambda)$ is the inverse function of the steady state profile $\lambda(x)$. Here, a robustness of $\mathcal{R}(\lambda) = 1$ implies that under a 100% increase of j_0 the position at which the ligand profile attains the fixed value λ is displaced by about one cell diameter a , see Fig. 4.1. Thus for $\mathcal{R}(\lambda) \geq 1$, the shift of the position x where the ligand concentration has the value λ cannot be detected by the cells in the target tissue even under significant changes of j_0 .

4.1.1 Robustness of gradients formed by transcytosis

In order to examine the robustness of gradients, we use the analytical solution (3.24, 3.25) of the corresponding steady states, see section 3.3.3. The general form and the properties of this analytical solution are identical for the description with receptor kinetics (3.12, 3.13) and that in the constant surface receptor approximation (3.16), see section 3.3.3. The discussion of robustness in this section consequently applies to both cases.

In absence of extracellular diffusion, the singular behavior (3.26) of the steady state profile near $x = x^*$ has remarkable consequences for the robustness of gradient formation. Using the robustness \mathcal{R} defined in (4.1), we see from (3.24) that \mathcal{R} is independent of λ . For steady state equations of the general form (3.23), the definition (4.1) can be rewritten as

$$\mathcal{R} = a(j_0 \partial_{j_0} x)^{-1} = a \partial_{\lambda_0} j_0 / D(\lambda_0) = ak(\lambda_0) \lambda_0 / j_0 \quad (4.2)$$

where $\lambda_0 = \lambda(x = 0)$ and (3.24) and (3.25) have been used. The robustness is thus completely determined by the ratio of the effective degradation rate and the ligand current at $x = 0$. High degradation rates and small currents lead to a robust gradient. Using the asymptotic behavior of the steady state profile for $D_0 = 0$, we find that the robustness increases rapidly for large currents j_0 as $\mathcal{R} \sim j_0^{-1} e^{j_0^2/j_c^2}$ with $j_c^2 = 1/2c_1(\rho_\infty)e_{\text{deg}}$. For small j_0 , $\mathcal{R} \simeq a/\xi$ becomes constant. For small e_{deg} , $\mathcal{R} \sim j_0^{-1}$ decreases with increasing j_0 as long as $j_0 < j_{\text{max}}$ and grows rapidly as $\mathcal{R} \sim j_0^{-1} e^{j_0^2/j_c^2}$ for $j_0 > j_{\text{max}}$. In Fig. 4.1, we illustrate this behavior of the robustness of steady state gradients for a small and a large value of j_0 .

4.1.2 Robustness with extracellular diffusion

The situation is different if free diffusion in the extracellular space is present. As discussed in section 3.3.3, the singularity in the steady state solution disappears for $D_0 > 0$. For small D_0 , the robustness approaches a finite value $\mathcal{R}_{\text{max}} = a/\xi_d$ as $j_0 \rightarrow \infty$. Thus, \mathcal{R}_{max} is an upper bound for the robustness that can be achieved. Clearly, a small extracellular diffusion length ξ_d that can be due to a small D_0 or large e_{deg} leads to large robustness. \mathcal{R}_{max} becomes greater than 1 and the cells in the target tissue are thus insensitive to a 100% increase of j_0 if the diffusion length in the extracellular space ξ_d is smaller than the cell diameter a . In Fig. 4.2, $\mathcal{R}(j_0)$ is shown for different values of ξ_d/a and Fig. 4.1 C shows an example for the effect of the presence of extracellular diffusion on the robustness of the gradient. Note, that the continuous description used here is only valid for small D_0 .

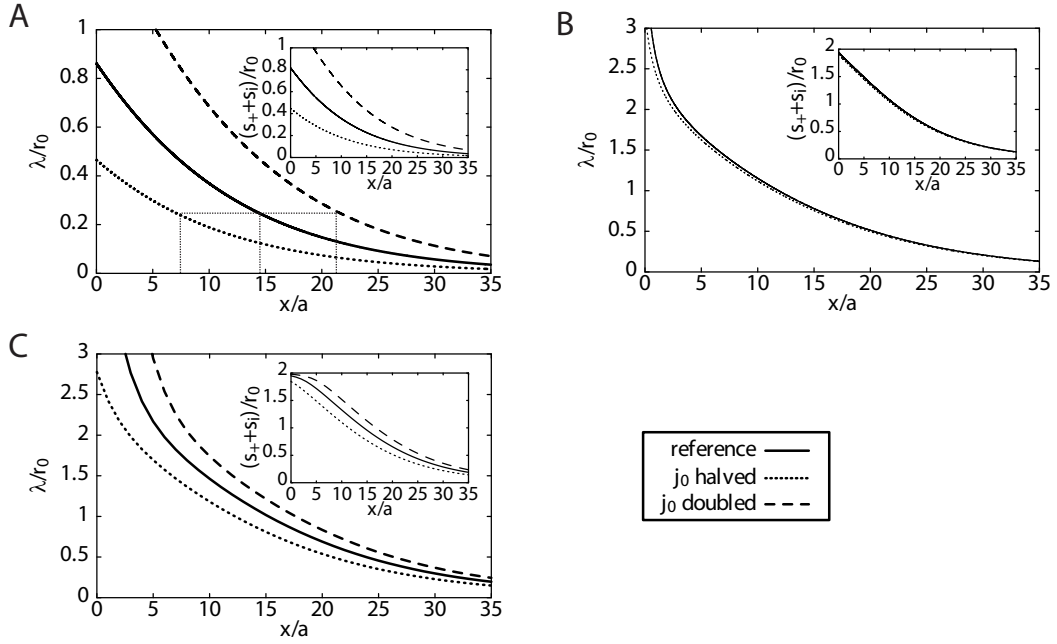


Figure 4.1: Non-robust and robust steady state gradient in our description of morphogen transport with constant surface receptor approximation (3.16). (A) Ligand profiles in the steady state for $D_0 = 0$ and $j_0/b_{\text{deg}}R = 7$ where robustness is small, $\mathcal{R} \approx 0.1$. The profile (solid line) is strongly affected by halving (dotted line) or doubling (dashed line) the ligand current of the reference state. The positions of an arbitrarily chosen concentration threshold are indicated. (B) Ligand profiles in the steady state for $D_0 = 0$ and $j_0/b_{\text{deg}}R = 70$ where robustness is large, $\mathcal{R} \approx 470$. The profile (solid line) is virtually unaffected by halving (dotted line) or doubling (dashed line, covered by the solid line) the ligand current of the reference state. (C) Like B but with extracellular diffusion at rate $D_0/a^2 b_{\text{deg}} = 50$ which reduces robustness to $\mathcal{R} \approx 0.32$. The insets show the respective profiles of the receptor-bound ligand concentration $s_+ + s_i$ which is the biologically relevant quantity. Parameters are $b_{\text{int}}/b_{\text{deg}} = b_{\text{ext}}/b_{\text{deg}} = 3 \times 10^3$, $k_{\text{on}}R/b_{\text{deg}} = 1.1 \times 10^4$, and $k_{\text{off}}/b_{\text{deg}} = 7 \times 10^2$.

For large values of D_0 , we can use the extracellular diffusion dominated limit (3.28). It can be shown that the robustness of steady state gradients is very small in this limit. This is due to the fact that the ligand current in this description is linear. Increasing the ligand current imposed at $x = 0$ actually leads to a reduction of robustness in this limit as has been pointed out in [60]. It can be verified by numerical calculations that modifications to the ligand current imposed at the source boundary have a strong impact on the resulting steady state gradients.

In summary, we find that morphogen gradients can be extremely robust to changes in the morphogen secretion rate of the source cells if transport is dominantly due to transcytosis. The presence of extracellular diffusion reduces this robustness that is completely lost when extracellular diffusion is the dominant transport mechanism.

4.2 Precision of morphogen gradients

In this section, we investigate the precision of steady state morphogen gradients, i.e. the ability of these gradients to specify concentration thresholds at well-defined distances to the

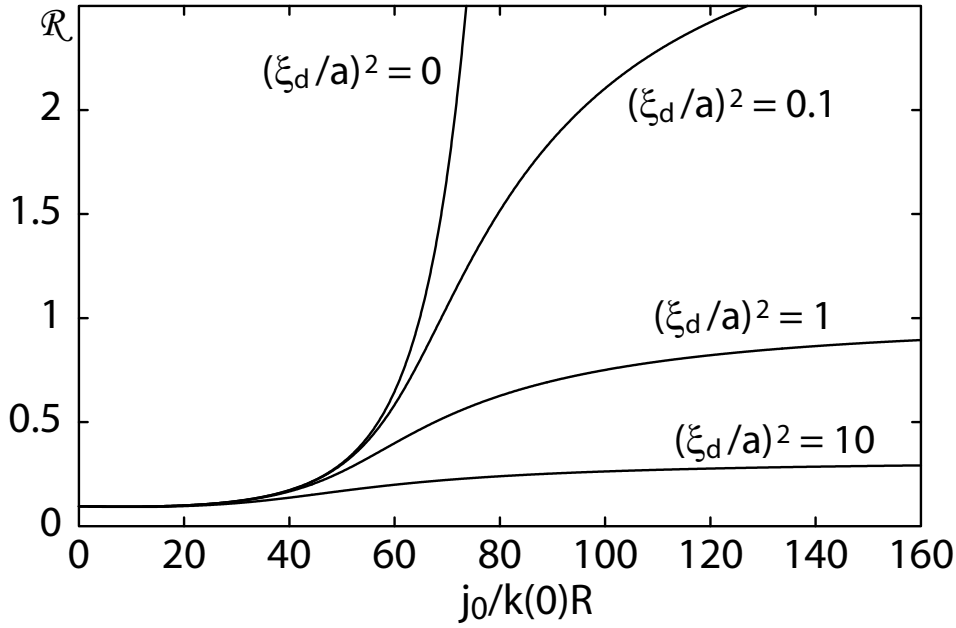


Figure 4.2: Robustness \mathcal{R} of steady state ligand profiles as a function of the ligand current j_0 from the source for different values of the ratio of the diffusion length ξ_d and the cell size a . Our description of morphogen transport with constant surface receptor approximation (3.16) was used to calculate \mathcal{R} . Parameters as in Fig. 4.1. Figure taken from [9].

morphogen source as illustrated in Fig. 1.1. This is generally alleviated by the presence of fluctuations in the system. These affect morphogen transport and degradation and consequently lead to fluctuations of the morphogen concentration profile in the steady state.

One type of fluctuations is due to the finite particle numbers in the system. In the steady state gradients which are reached after long times, these lead to temporal fluctuations about the mean value of the morphogen concentration. For the biological systems we are most interested in here, the morphogen and receptor numbers are anticipated to be relatively large. They are estimated to be at least on the order of several hundred per cell [26]. However, one must keep in mind that in a morphogen gradient far away from the morphogen source, the number of morphogen molecules always becomes small and particle number fluctuations cannot be neglected in general. This, however, is insignificant for the biological situation because experimental data indicate that target gene expression cannot be controlled by less than several hundred receptor-bound morphogens per cell [26, 86]. Thus the part of the gradient far away from the source where the particle numbers in the steady state are very small and strongly fluctuating is not used to determine cell fates. This is why we neglect fluctuations due to the finite particle numbers and assume that another type of fluctuations in the system has a dominant impact.

This different type of fluctuations is caused by the disorder in the system. Disorder emerges because the cells in a tissue are generally not completely identical even if they are all of the same cell type. For example, they exhibit stochastic variations in size and shape. Cell surface proteins are also present in different amounts on the surfaces of different cells. Moreover, the cell division cycles of cells in a tissue are not synchronized. Consequently, different cells in the same tissue are generally in different stages of the cell cycle which may affect their function. Such differences are not restricted to the cells. The extracellular space can have different properties at different locations of the tissue as well. For example, the concentrations of extra-

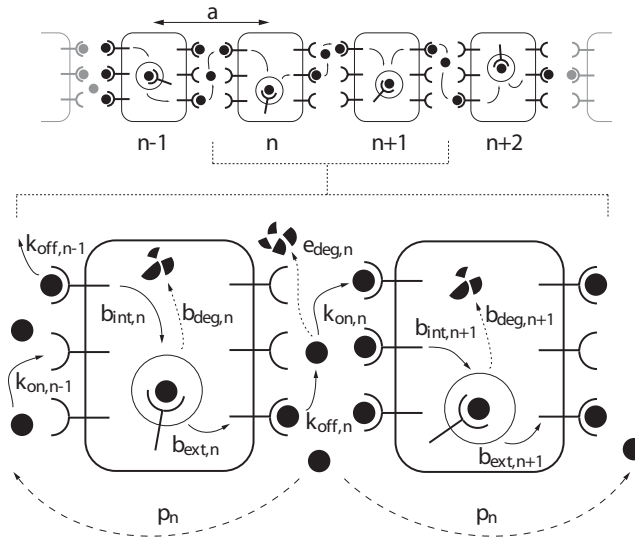


Figure 4.3: Cellular individuality in our one dimensional description of morphogen transport with receptor kinetics (3.1) or with the constant surface receptor approximation (3.3). The rates for the various processes depend on the cell or extracellular space n and are stochastically distributed around a mean value. The rates b_{int} , b_{ext} , b_{deg} , f_{int} , f_{ext} , and f_{deg} depend on the cell number n . We show this only for the rates describing the kinetics of the morphogen-bound receptors. Analogously, the rates k_{on} , k_{off} , p , and e_{deg} depend on the index n of the extracellular space. Here, the hopping rate p describes the extracellular diffusion of the morphogens.

cellular molecules, the extracellular volume fraction, and the actual shape of the extracellular space surrounding the cells depend on the location within a given tissue.

In chapter 5, we will calculate the effects of such disorder on steady state concentration profiles formed in a simple model of morphogen gradient formation by extracellular diffusion. This model is described by a diffusion equation with degradation term for the extracellular morphogen concentration $c(t, \vec{x})$:

$$\partial_t c = \nabla_x \cdot [(D + \eta(\vec{x})) \nabla_x c] - (k + \zeta(\vec{x}))c, \quad (4.3)$$

where the effective diffusion coefficient D and the degradation rate k fluctuate in space. Their spatial fluctuations are captured by the noise terms $\eta(\vec{x})$ and $\zeta(\vec{x})$ respectively. We investigate morphogen gradient formation in the half-space $x > 0$ in different space dimensionalities d . The presence of the morphogen source is described by a current j_0 imposed at the boundary located at $x = 0$. This boundary is a point in $d = 1$, a line in $d = 2$, and a plane in $d = 3$. The current j_0 across this boundary can also fluctuate.

For each different realization of the disorder, the steady state gradient $c(\vec{x})$ following from (4.3) will be different. We consequently study the statistical properties of $c(\vec{x})$ in an ensemble of realizations of the disorder. In chapter 5, we will mathematically define this problem and develop a method for calculating the moments and the normalized standard deviation $\Sigma(x)$ of the morphogen concentration $c(x)$ in steady state as a function of the distance x to the morphogen source. $\Sigma(x)$ is a measure for the relative error of the local morphogen concentration at position x . Due to the symmetries of the problem, all moments of $c(\vec{x})$ depend only on the distance x to the source boundary independent of the space dimensionality.

In section 5.2, we will also calculate the effects of fluctuations in our more detailed description of morphogen transport that was introduced in chapter 3. Here, disorder due to cellular

individuality is introduced by assigning random values to the rates describing the trafficking and degradation of morphogens and receptors in each cell, see Fig. 4.3 for an illustration.

Here, we discuss the origin and the biological relevance of disorder in morphogen gradient formation. As the different noise amplitudes entering our description have not been measured in experiments, we concentrate on generic results that are independent of these values. Interesting points of examination are the role of different space dimensionalities and the impact of fluctuations in the bulk of the system compared to that of fluctuations at the boundary. Moreover, it is important to investigate if the different transport mechanisms have different implications for the precision of morphogen gradient formation.

4.2.1 Microscopic origin of fluctuations

Let us first discuss in more detail how the disorder in the tissue leads to random fluctuations of the parameters entering the theoretical description. In the simple description of morphogen gradient formation by extracellular diffusion (4.3), the effective degradation rate k captures the removal of morphogens from the extracellular space by extracellular degradation and their internalization into cells after binding to cell surface receptors. The spatial fluctuations $\zeta(\vec{x})$ of this degradation rate originate in stochastically different concentrations of extracellular molecules that affect the removal of the morphogen from the extracellular space. These molecules can be extracellular proteases that destroy the morphogen or cell surface molecules like the morphogen receptors.

In (4.3), the passive diffusion of morphogens in the extracellular space is characterized by an effective diffusion coefficient D . This is not a free diffusion coefficient for a particle with the size of a morphogen molecule in a watery liquid because all kinds of interactions with molecules of the extracellular matrix and on cell surfaces that the morphogen can temporarily bind to cause a reduction of the effective diffusion coefficient D . The spatial fluctuations $\eta(\vec{x})$ of this effective extracellular diffusion coefficient have multiple roots. One origin is stochastically different distances over which the morphogens have to diffuse through the extracellular space to cover a distance of one cell diameter a in the tissue. These different lengths of path connecting equidistant points in the extracellular space are a natural result of the disordered cell arrangement in the tissue, see Fig. 4.4 A for an illustration. The spatially varying concentrations of cell surface molecules and extracellular matrix components which the morphogen can bind to are another origin of fluctuations of the extracellular diffusion coefficient. These components can be more abundant at some places of the extracellular space than at others. Hence, the morphogen is typically trapped at these places for a longer time, see Fig. 4.4 B. In summary, fluctuations in the distribution of the different components of the extracellular matrix and the disordered cell arrangement in the tissue which both affect transport are taken into account by a fluctuating effective diffusion coefficient.

The fluctuations of the other parameters than D_0 in the more detailed description of morphogen transport from chapter 3 capture other effects of stochastic cell-to-cell variability in a tissue. Several rates entering this theoretical description effectively describe complicated active processes performed by the intracellular molecular machinery. For example, the internalization of cell surface proteins that is described by a simple rate b_{int} requires several different proteins that have to be produced by the cell. The numbers of these proteins vary from cell to cell due to the randomness in their transcription, translation, and degradation [31]. These differences in the protein numbers lead to different abilities of the cell to internalize proteins from its surface which can be described by different effective rates for this process [80]. This is the origin of the fluctuations of the rates like b_{int} , b_{ext} , b_{deg} , f_{int} , f_{ext} , f_{deg} , and f_{syn} which effectively capture such cellular processes in our theoretical description.

The gene expression in the source cells is also a stochastic process. This stochasticity leads

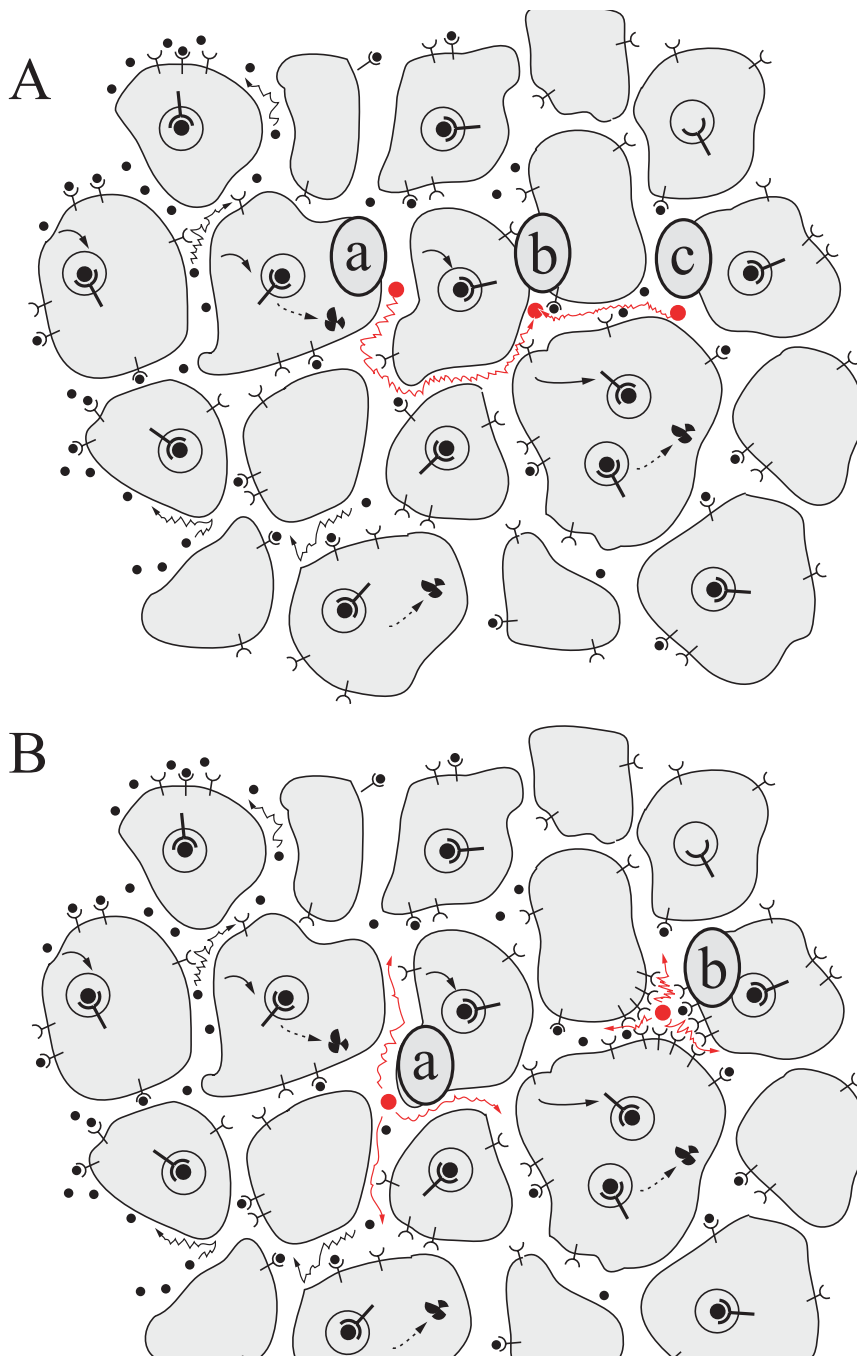


Figure 4.4: Microscopic origin of the space-dependent fluctuations of the effective diffusion coefficient D in the case of transport by extracellular diffusion. (A) It takes longer for the morphogen to diffuse along the curved path which connects points (a) and (b) than along the straight path connecting the equidistant points (b) and (c). In a coarse-grained description, this leads to a reduced hopping rate between points (a) and (b) compared to that between points (b) and (c). This hopping rate is the same for hopping in both directions which corresponds to case A discussed in section 5.1. (B) The morphogen can diffuse away from point (a) faster than from point (b) because extracellular proteins which it can bind to are much more abundant at (b). In a coarse-grained description, this leads to a reduced rate of hopping away from point (b) compared to that for hopping away from point (a) which corresponds to case B discussed in section 5.1.

to variations in the rate ν at which these cells produce new morphogen molecules and secrete them into the extracellular space surrounding them. This is the origin of the fluctuations of the current j_0 imposed at the source boundary which is proportional to ν .

The fluctuations of the rates k_{on} and k_{off} describing binding and un-binding of morphogens to and from cell surface receptors respectively have a different origin. Receptors exist in different conformations and the rates of ligand binding and un-binding depend on these conformations. The receptors can also form complexes with other proteins or among themselves which can affect the ligand affinity. These phenomena are stochastic and consequently cause fluctuations of the effective rates k_{on} and k_{off} . Moreover, the binding of ligands to receptors on the cell surface is usually a diffusion-limited process, so that the fluctuations of the extracellular environment which have an impact on the extracellular diffusion coefficient as discussed above affect the binding rate k_{on} . Finally, spatial fluctuations of the number of extracellular proteases which are involved in extracellular morphogen degradation cause fluctuations of the rate e_{deg} . While the presence of all these fluctuations is beyond doubt, their magnitude in the biological systems we are interested in here has so far not been estimated from experimental data.

4.2.2 Definition of precision

It is useful to define a measure of the precision of a morphogen gradient that quantifies how accurately the position of a concentration threshold in the target tissue is specified. In agreement with the notation used in chapter 5, we denote the average steady state gradient of an ensemble of realizations of the disorder by $c_0(x) = \langle c(x) \rangle$. A dimensionless measure for the precision of the gradient at a given distance x from the source is

$$\mathcal{P}(x) = a \left(\frac{(\partial_x c_0(x))^2}{\langle (c(x) - c_0(x))^2 \rangle} \right)^{1/2}. \quad (4.4)$$

The precision $\mathcal{P}(x)$ becomes large at x if the variance of the morphogen concentration $\langle (c(x) - c_0(x))^2 \rangle$ is small or if the gradient is steep there, i.e. if $(\partial_x c_0(x))^2$ is large. This is illustrated in Fig. 4.5. For $\mathcal{P}(x) = 1$ the uncertainty of the morphogen concentration at x is sufficiently small to define the position of a concentration threshold with an uncertainty of about one cell diameter a . Thus, for $\mathcal{P}(x) \geq 1$, the morphogen gradient can be considered precise at x .

As the steepness of the gradient becomes small and the relative uncertainty of $c(x)$ usually increases for large x , one expects $\mathcal{P}(x)$ to be a monotonically decreasing function for large x . This implies that there is a critical distance x_c from the source boundary such that the gradient is precise for $0 \leq x \leq x_c$. The whole gradient can be called precise if x_c is larger than the distance of the concentration threshold farthest away from the source. The linear decay length of the gradient gives a length scale for this distance. Thus, we call the gradient precise if x_c is larger than this decay length.

In the simple model of morphogen gradient formation by extracellular diffusion (4.3), one can express the precision defined in (4.4) as

$$\mathcal{P}(x) = \frac{ac_0(x)}{\xi_D \langle (c(x) - c_0(x))^2 \rangle^{1/2}} = \frac{a}{\xi_D \Sigma(x)}, \quad (4.5)$$

where $\Sigma(x) = \langle (c(x) - c_0(x))^2 \rangle^{1/2} / c_0(x)$ denotes the normalized standard deviation of $c(x)$ and $\xi_D = \sqrt{D/k}$ is the diffusion length. This reveals an inverse relationship between the precision of morphogen gradients and $\Sigma(x)$ which is the quantity we will calculate throughout chapter 5. Since we have only used $\partial_x c_0(x) = -c_0(x)/\xi_D$, this result also holds in any other situation where $c_0(x)$ decays exponentially. Note, that the simple relation (4.5) between $\mathcal{P}(x)$

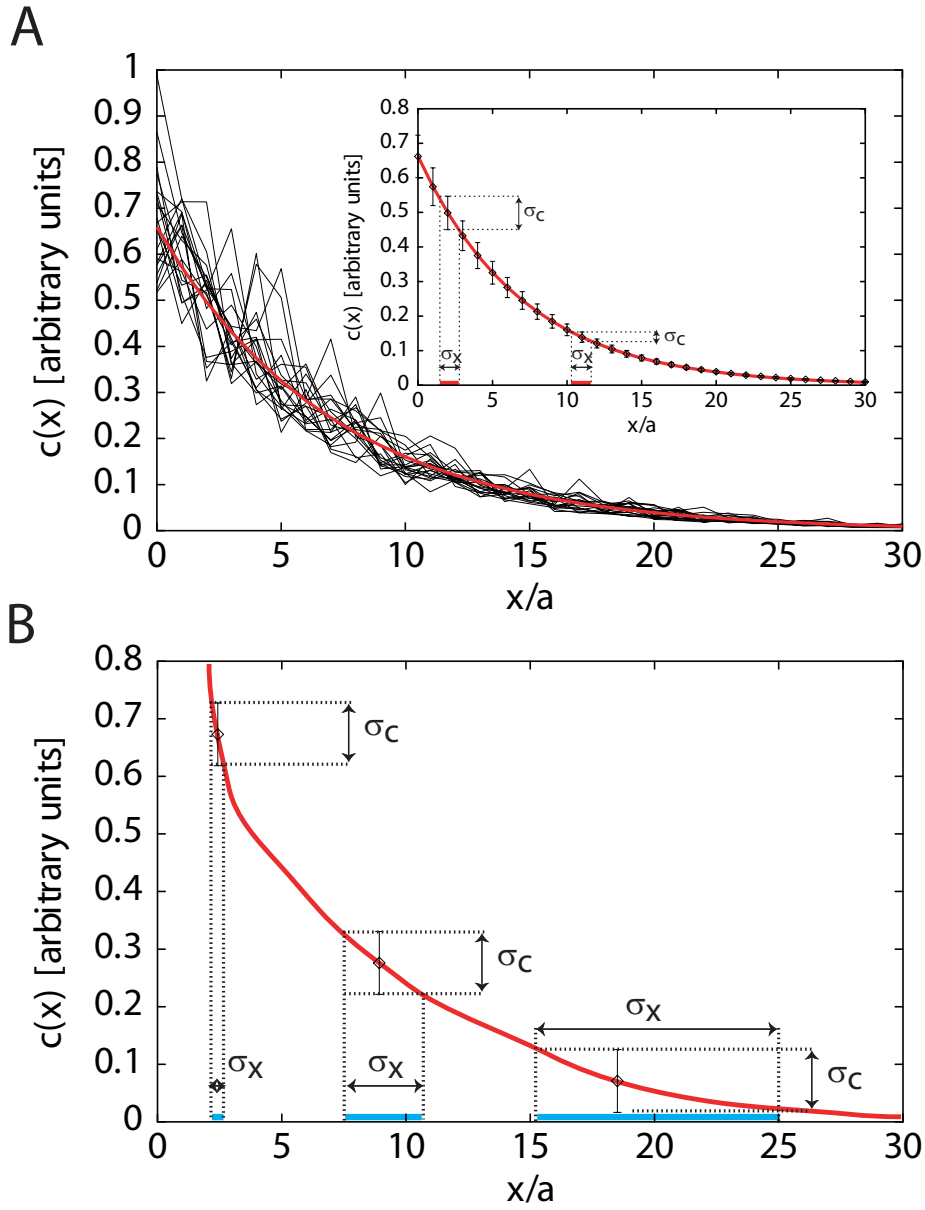


Figure 4.5: Morphogen gradients in a system with disorder. (A) Schematic of steady state gradients $c(x)$ for 20 realizations of the disorder. Each realization of the disorder leads to different fluctuations of $c(x)$ about the mean gradient which is shown in red and coincides with the gradient in the absence of disorder in the schematic. From many such realizations, the standard deviation of $c(x)$ at each position can be calculated. The standard deviation is shown by the error-bars in the inset. (B) The schematic shows a fictive morphogen gradient with the source located at $x = 0$. The local morphogen concentration c at a position x has an uncertainty σ_c that is given by the standard deviation of c . This uncertainty σ_c leads to an uncertainty σ_x of the position where the concentration c is present. As illustrated, the uncertainty σ_x depends on σ_c and the steepness of the gradient at x . This motivates our definition of the precision $\mathcal{P}(x)$ given by (4.4).

and $\Sigma(x)$ does not hold for morphogen gradients $\lambda(x)$ formed by transcytosis. This is due to the nonlinear nature of the transport equations for transcytosis. Equation (4.5) holds only in the linear regime, i.e. in regions where the morphogen concentration λ is small. For large currents j_0 imposed at $x = 0$, the morphogen profile near $x = 0$ is characterized by the singularity (3.26). This implies that the profile $\lambda(x)$ is very steep there and the precision is larger than in the linear case.

In order to achieve a reliable patterning of the target tissue, a precision $\mathcal{P}(x) \geq 1$ over a distance that is on the order of the gradient range is needed. One way to increase the precision $\mathcal{P}(x)$ is to make the gradient steeper. There are limitations to this because having a steep gradient conflicts with having a gradient with morphogen concentrations of the same order of magnitude that extends over a large structure that has to be patterned. Moreover, steepness requires a high effective morphogen degradation rate which implies a high turnover of morphogens. These must be produced consuming the limited resources available. Thus, the precise definition of the position of concentration thresholds in the proximity of the morphogen source is only possible if the fluctuations of the local morphogen concentration are not too strong there.

4.2.3 Effects of disorder on the precision of gradients

In this section, we discuss the implications of the results found in chapter 5 for morphogen gradients in real biological systems.

Role of space dimensionality A fundamental result is that the dimensionality of the space in which the gradient is formed has an enormous impact on the resulting uncertainty of the local morphogen concentration which is measured by the normalized standard deviation $\Sigma(x)$. In the simple description of morphogen gradient formation by extracellular diffusion (4.3), the precision $\mathcal{P}(x)$ is much smaller in one dimension as compared to two dimensions for the same values of the effective diffusion coefficient D , the effective degradation rate k , and the current j_0 imposed at the source boundary at $x = 0$ and the same amplitudes σ_D , σ_k , and σ_{j_0} of the corresponding noise terms. This is true both near the source and asymptotically for large x , see Fig. 4.6 A. Going from two to three dimensions, another strong increase of the precision occurs. A similar effect is observed in the more detailed description of morphogen transport.

This reflects that, in one dimension, a strong fluctuation at a position x_0 strongly affects the steady state concentration profile at all positions $x > x_0$ because all morphogens moving from the source to x have to pass x_0 . In two dimensions this effect is weaker because the morphogens can reach any position \vec{x} on many different paths so that the effects of the fluctuations of D and k are partly averaged out.

The role of the space dimensionality d can be identified by looking at the behavior of $\Sigma(x)$ for large x . We show in chapter 5 that $\Sigma(x)$ increases asymptotically following a power-law $\Sigma(x) \sim x^\phi$ that is characteristic of the space dimensionality d . According to (4.5), the precision decreases correspondingly as $\mathcal{P}(x) \sim x^{-\phi}$. The general formula for the exponent ϕ as a function of the space dimensionality d is

$$\phi = (3 - d)/4$$

for $d < 3$. This shows how the precision rapidly increases with increasing space dimensionality and suggests that $d = 3$, where we find $\Sigma(x) \sim \ln(x)$, is the upper critical dimension beyond which the fluctuations of D and k become irrelevant.

Apart from the fluctuations of D and k , the impact of fluctuations of the current j_0 imposed at the boundary is qualitatively different in two dimensions than in one dimension. While boundary fluctuations in one dimension lead to an increase of $\Sigma(x)^2$ by an additive constant

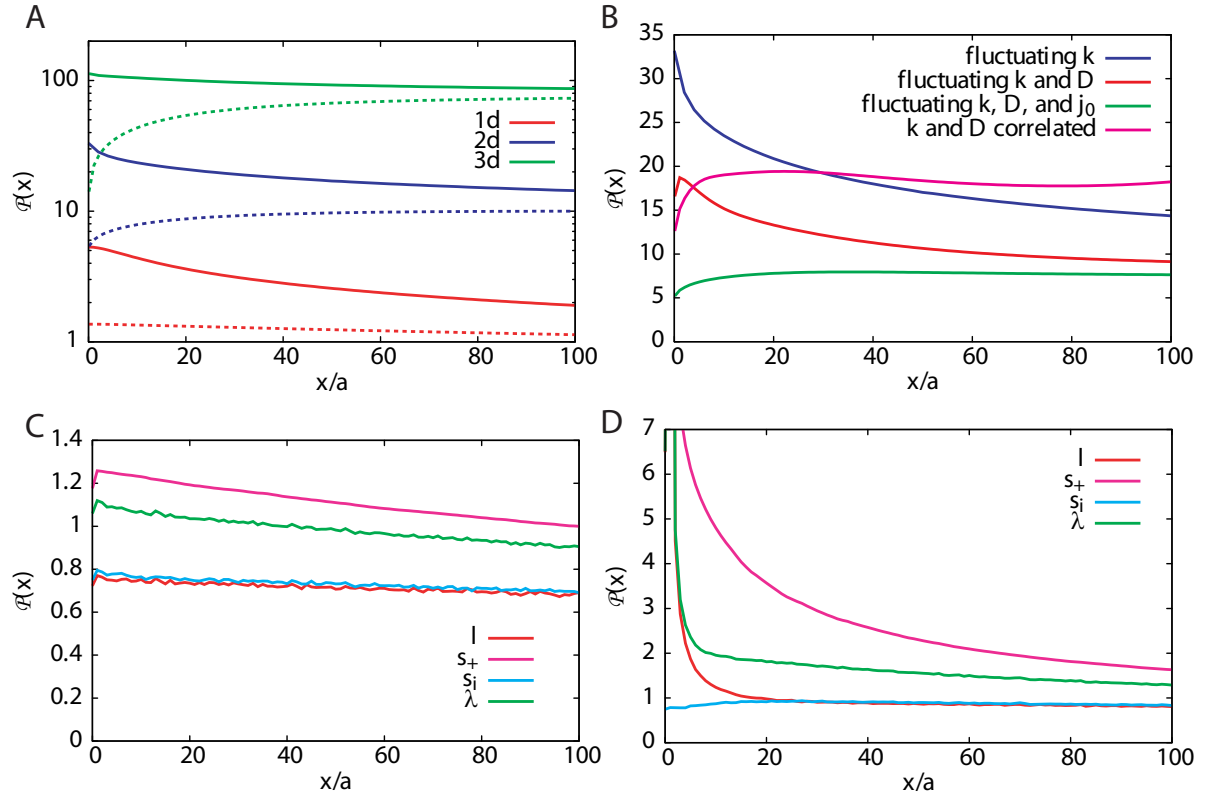


Figure 4.6: (A,B) Precision $\mathcal{P}(x)$ of gradients in the simple description of extracellular diffusion (4.3). Logarithmic plot of $\mathcal{P}(x)$ in one dimension (red lines), in two dimensions (blue lines), and in three dimensions (green lines). For the solid lines, only k is fluctuating and for the broken lines both k and the current j_0 imposed at $x = 0$ are fluctuating. The precision $\mathcal{P}(x)$ was calculated from the analytical results shown in Fig. 5.5 A using (4.5). (B) Precision $\mathcal{P}(x)$ in two dimensions. The blue line shows $\mathcal{P}(x)$ if only k is fluctuating, the red line if both D and k are fluctuating, the magenta line if D and k are fluctuating in a fully correlated way, and the green line if D , k and the current j_0 imposed at the boundary at $x = 0$ are fluctuating. $\mathcal{P}(x)$ was calculated from the analytical results shown in Fig. 5.4 A using (4.5). (C,D) Precision $\mathcal{P}(x)$ of gradients formed in one dimension in the transcytosis dominated limit of our more detailed description of morphogen transport shown in Fig. 4.3 with constant surface receptor approximation. The lines show $\mathcal{P}(x)$ for the gradients of the free extracellular morphogen concentration l (red), the surface receptor-bound morphogen concentration s_+ (magenta), the internalized receptor-bound morphogen concentration s_i (blue), and the total morphogen concentration λ (green). The linear regime in which j_0 is very small is shown in C. The nonlinear regime where j_0 is large and most receptor molecules are occupied near the source at $x = 0$ is shown in D. The precision $\mathcal{P}(x)$ in C and D was calculated from the numerical data shown in Fig. 5.8 C and D. See chapter 5 for details about how the data shown in this figure were calculated.

and thus affect the precision at all distances x from the source, they result in a decreasing contribution to $\Sigma(x)$ that ultimately goes to zero with increasing distance x from the source in two dimensions. This leads to a precision $\mathcal{P}(x)$ that increases with x near the source boundary at $x = 0$, see green line in Fig. 4.6 B. This feature is even more pronounced in three dimensions, i.e. the fluctuations of the boundary current cause an increase of the precision with x that is even faster than in two dimensions, see dashed lines in Fig. 4.6 A.

This behavior is again due to an averaging effect that occurs for $d > 1$. At a position \vec{x} very close to the source, the steady state concentration $c(\vec{x})$ is strongly affected by the fluctuations of the current j_0 across a narrow region of the source boundary near \vec{x} . Farther away from the source, the concentration is affected by a wider part of the source boundary over which the fluctuations of j_0 are effectively averaged. This leads to a reduction of the fluctuations of $c(\vec{x})$ and consequently to an increase of precision.

In summary, we find that if relevant disorder is present in the system, the precision of gradient formation is relatively low in one space dimension. This suggests that the minimal dimension in which precise gradients can be formed is $d = 2$. At least, it appears highly advantageous to pattern tissues via morphogen gradients in geometries that are at least two dimensional. This may seem insignificant in cases like the wing disk, where the adult structure, i.e. the wing of the fly, is itself two dimensional. However, there are formidable examples of developing organisms where patterning first occurs in a two dimensional geometry that is later reduced to an essentially one dimensional one by letting the cells in parts of the tissue die in a programmed way by a process called apoptosis. The formation of digits, i.e. fingers or toes, in the development of the chick and other vertebrates is such an example. First, the pattern of the digits is formed in a two dimensional plate-like tissue. After the correct formation of this pattern, the cells in the tissue between the digits die by apoptosis leaving behind several essentially one dimensional structures [103]. At first glance, apoptosis seems wasteful. Our results concerning the precision of morphogen gradients in different space dimensions are a possible explanation for the ample use of this mechanism in development.

Impact of boundary fluctuations Another interesting issue is the relative importance of fluctuations at the boundary compared to fluctuations in the bulk of the system. For the simple description of morphogen gradient formation (4.3), the fluctuations of the current j_0 across the boundary at $x = 0$ generally reduce the precision $\mathcal{P}(x)$ significantly near the source, see Fig. 4.6 A and B. If the same relative widths for the fluctuations of D , k , and j_0 are used, the fluctuations of j_0 usually give the largest contribution to the uncertainty $\Sigma(x)$ near the source located at $x = 0$. For larger distances x to the source, the bulk fluctuations become dominant. However, in a biological system, the precision of the gradient is only relevant in the proximity of the morphogen source because that is where the concentration thresholds which control cell fate determination are located. Thus, it is important to have a sufficiently high precision of the morphogen concentration in that region. These two considerations combine to the conclusion that in order to achieve the formation of a precise gradient, it is of great importance to reduce the impact of the fluctuations of the ligand current across the source boundary. In the description of extracellular diffusion with disorder (4.3), there is no other way of doing this than to directly reduce the amplitude σ_{j_0} of the fluctuations of the boundary current j_0 . This is due to the linearity of the description.

The situation is different in the transcytosis dominated limit of our more detailed description of morphogen gradient formation. For small currents j_0 across the boundary at $x = 0$, the fluctuations of this current also lead to a strong reduction of the precision of the gradient of the total morphogen concentration $\lambda(x)$ close to the source. However, in the nonlinear regime which is reached by a high value of j_0 , we find a significantly increased precision. This

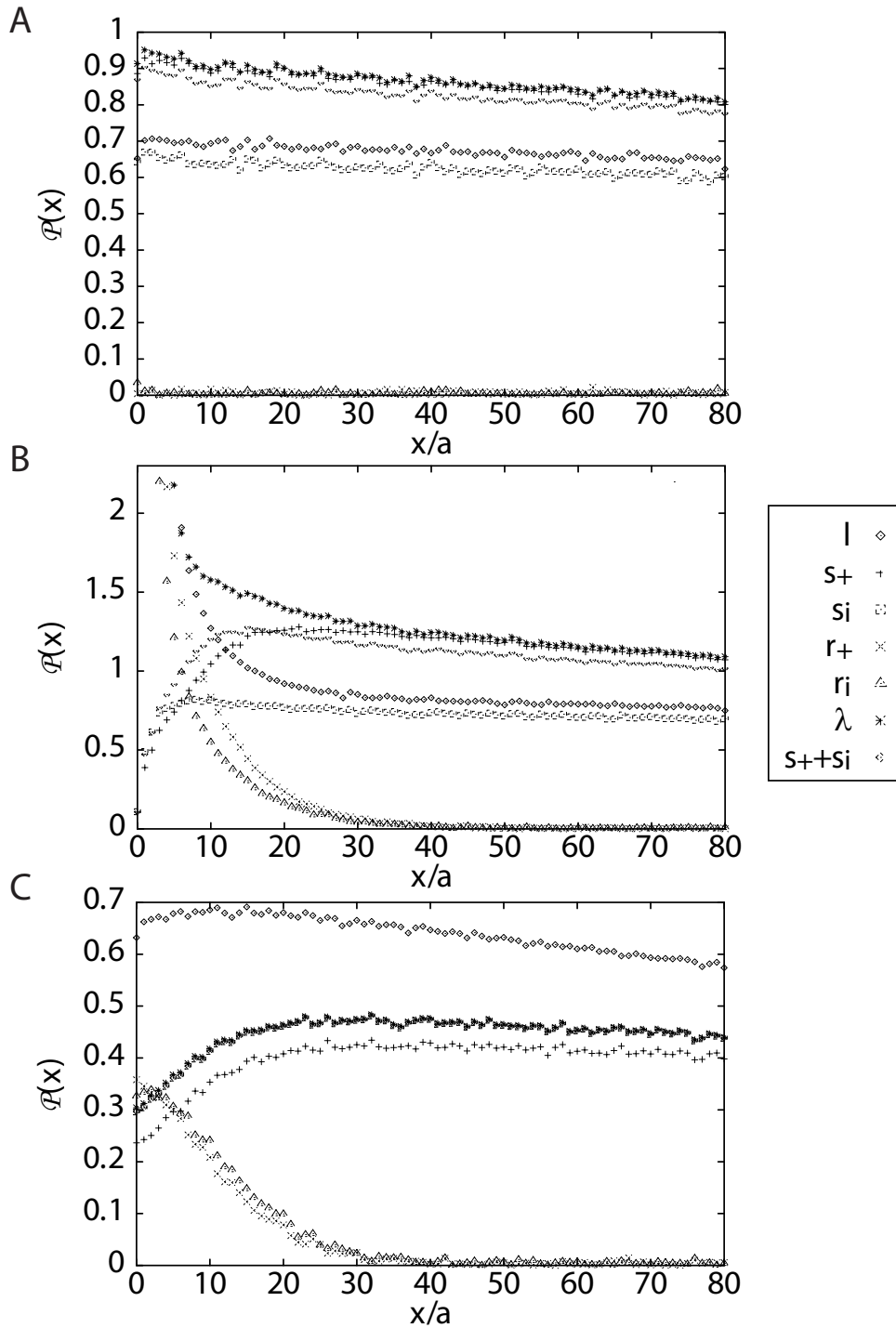


Figure 4.7: Precision of steady state gradients formed in the one dimensional description of morphogen gradient formation with receptor kinetics discussed in section 3.1.1. The precision $\mathcal{P}(x)$ was calculated from the data shown in Fig. 5.6. (A) Precision $\mathcal{P}(x)$ of steady state gradients with parameters in the transcytosis regime with a small morphogen secretion rate $\nu/R_0 b_{\text{deg}} \ll 1$. We show $\mathcal{P}(x)$ for the gradients of the different quantities as indicated in the key. (B) Like A but with a large morphogen secretion rate $\nu/R_0 b_{\text{deg}} = 13.3$. (C) Like A but with parameters in the diffusion regime and $\nu/R_0 b_{\text{deg}} = 207$.

comparison of the precision $\mathcal{P}(x)$ that was obtained from calculations in the linear and the nonlinear regime of transcytosis is shown in Fig. 4.6 C and D for the constant surface receptor approximation and in Fig. 4.7 A and B for the description with receptor kinetics. The increase of precision in the nonlinear regime is mainly due to the robustness of the gradients that are insensitive to comparatively large changes of j_0 in this regime as discussed in section 4.1. This suppression of boundary fluctuations from the source and the increased steepness of the gradient near the source lead to an increase of the precision in the nonlinear regime of transcytosis.

Role of local correlations Studying the simple description of morphogen gradient formation (4.3), we further find that local correlations between the fluctuations of the effective diffusion coefficient D and those of the effective degradation rate k can have a strong impact on the uncertainty $\Sigma(x)$, see section 5.1. A positive correlation leads to a slower asymptotic increase of $\Sigma(x)$ and in fact to a decrease of $\Sigma(x)$ everywhere except for a small region extremely close to the source. Consequently, the precision $\mathcal{P}(x)$ is increased as a result of such correlations, compare the magenta line and the red line in Fig. 4.6 B.

In section 5.2, we show that in the transcytosis dominated limit of our theoretical description of morphogen transport with disorder illustrated in Fig. 4.3, well-defined local correlations between the fluctuations of the effective diffusion coefficient $D(\lambda)$ that characterizes transcytosis and the corresponding effective degradation rate $k(\lambda)$ appear quite naturally. Let us exemplify the origin of such correlations by looking at the internalization rate b_{int} . Suppose that b_{int} is slightly increased in a given cell. This usually leads to faster transport of ligand-receptor complexes from one position on the surface of this cell to another one simply because the internalization step which is part of this transport process occurs faster. Moreover, morphogen degradation is enhanced because the enhanced internalization of the morphogen leads to an increase of the amount of morphogens present inside the cell which is a prerequisite for intracellular degradation. Thus, both the effective diffusion coefficient $D(\lambda)$ characterizing transcytosis and the effective degradation rate $k(\lambda)$ are increased by the fluctuation of the rate b_{int} . This example illustrates how positive correlations between the fluctuations of the effective diffusion coefficient and the effective degradation rate naturally occur in transcytosis.

Fluctuations of the other rates can be demonstrated to have similar effects. In transcytosis, both positive and negative correlations between the resulting fluctuations of the effective diffusion coefficient and the effective degradation rate can occur. As we have discussed above, positive correlations can strongly decrease the uncertainty $\Sigma(x)$ of the local morphogen concentration and thus increase the precision $\mathcal{P}(x)$. The capability of the system to control correlations between the fluctuations that occur is consequently of potential value.

Correlations between the fluctuations of D and k could also be present in a system where a gradient is formed by extracellular diffusion. For example, the presence of a fictive extracellular protein could lead to a reduction of the extracellular degradation rate and could at the same time lead to a decrease of the effective extracellular diffusion coefficient. For example, this protein would have to inhibit a protease that is needed for morphogen degradation and also bind the diffusing morphogen thus obstructing its Brownian motion. However, this is speculative and it appears unlikely that such well-defined correlations between the passive processes occurring in the extracellular space exist in real systems. On the other hand, they are almost inevitable in active transport mechanisms like transcytosis as illustrated by the example discussed above. If morphogen gradient formation has to be precise, this is a potential advantage of active transport processes over passive ones.

Precision of microscopic quantities So far, we have discussed the precision of morphogen gradients without taking into account the individual gradients of the free morphogen concentration l , the surface receptor-bound morphogen concentration s_+ , and the internalized receptor-bound morphogen concentration s_i for which the precision $\mathcal{P}(x)$ can be calculated separately in the more detailed description of morphogen gradient formation with disorder shown Fig. 4.3. In Fig. 4.6 C,D and Fig. 4.7, we see that the gradients of these microscopic quantities usually have a different precision than the gradient of the total morphogen concentration $\lambda(x)$. The biologically relevant gradient is most likely that of the receptor-bound morphogen concentration, see section 1.1.

If morphogen transport is dominated by extracellular diffusion, the uncertainty of this gradient can certainly be higher than that of the free extracellular morphogen gradient because it is accessorially affected by intracellular noise. However, it cannot be lower than that of the free extracellular morphogen gradient because the cells can only attempt to accurately detect the free extracellular morphogen concentration present at the position in the tissue where they are located. There is no way to reduce the uncertainty of the extracellular morphogen concentration in this process as long as we stick to the plausible assumption that intracellular and extracellular fluctuations are uncorrelated. The data for the precision of morphogen gradients formed in the extracellular diffusion dominated regime of our more detailed description of morphogen gradient formation shown in Figures 4.7 C and 5.6 C support this argument: the precision of $l(x)$ is much larger than that of $s_+(x)$ and $s_i(x)$ and the normalized standard deviation of $l(x)$ is smaller.

The situation is different the limit in which transport is dominated by transcytosis. In Fig. 4.7 A and B, we see that the precision of the biologically relevant gradient $s_+(x) + s_i(x)$ can be higher than that of the extracellular morphogen gradient $l(x)$ or the gradients of the other quantities in this limit. This behavior is in contrast to the situation that arises in the extracellular diffusion dominated limit, see Fig. 4.7 C. Comparing Fig. 4.7 A and B, we further see that the precision of the quantities s_+ , s_i , r_+ and r_i is increased at most positions x in the nonlinear regime of transcytosis if compared to the linear one. Interestingly, the precisions of the receptor bound morphogen concentrations $\mathcal{P}_{s_+}(x)$, $\mathcal{P}_{s_i}(x)$, and $\mathcal{P}_{s_++s_i}(x)$ increase as a function of x near the source and rapidly reach a relatively high value.

In summary, we find that morphogen gradient formation by passive extracellular diffusion has some apparent disadvantages in comparison to transcytosis as far as the precision of gradient formation is concerned: the boundary fluctuations cannot be suppressed, well-controlled local correlations which could counteract the effects of fluctuations in the bulk are probably unavailable, and the highest precision is achieved for the gradient of free extracellular morphogens which cannot be directly detected by the cells.

Chapter 5

Gradient formation in disordered systems

In this chapter, we investigate morphogen gradients which are formed in a disordered environment. The origins of disorder and its relevance for morphogen gradient formation in biological systems were explained in section 4.2. Here, we treat the theoretical aspects of this problem in detail.

The disorder in a developing tissue can be characterized by spatiotemporal fluctuations of the properties of the tissue. In a theoretical description of morphogen transport like the one we introduced in chapter 3, the presence of disorder and cell-to-cell variability can be captured by allowing certain parameters of the description to depend on the location in a stochastic manner. In a discrete description like (3.1), it is reasonable to assign random values to the parameters for each cell. These parameters are distributed around a mean value following a certain probability distribution. The mean value of this distribution corresponds to the parameter value in a description that does not account for the disorder in the system like the ones we have discussed in chapter 3.

We assume that the time scale on which the disorder changes is larger than the time scale of relaxation into the steady state and do not deal with temporal fluctuations and the relaxation kinetics. Instead, we focus on the effects of frozen spatial disorder on steady state morphogen gradients. We develop a method for calculating the spatial correlation functions of the morphogen concentration in the steady state. These depend on the distance from the morphogen source in such a frozen disorder scenario. From the two point correlation function, we calculate the variance and finally the normalized standard deviation that measures the relative error of the local morphogen concentration. This is a quantity of immediate relevance for the precision of morphogen gradients as we discussed in chapter 4. We apply the method to two examples: a diffusion model with particle decay that can be regarded as a simple description of morphogen transport by extracellular diffusion and the more detailed description of morphogen transport from chapter 3.

5.1 Diffusion with particle decay

To introduce the problem and the methods we use, a simple class of discrete systems that are capable of gradient formation is studied in this section. We investigate a mean field description of non-interacting decaying particles which are hopping on a lattice. In sections 5.1.1 and 5.1.2, we treat the one dimensional situation and discuss the generalization to higher space dimensions in section 5.1.3.

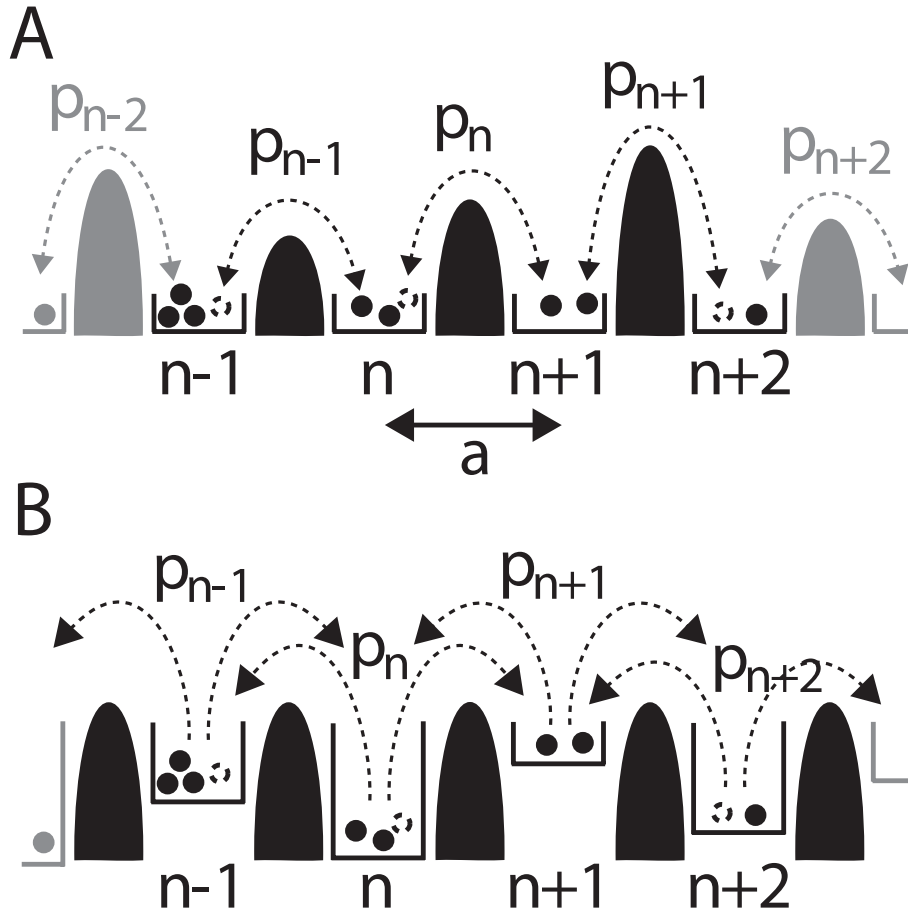


Figure 5.1: Schematic of the hopping model with random barrier heights (A) and random trap depths (B). (A) The hopping rates p_n are the same for hopping over each barrier in both directions. (B) The rates p_n for hopping away from a site n are the same for both directions. In A and B, the particles also decay at a rate k_n which randomly depends on the lattice site (not shown).

5.1.1 Diffusion with frozen disorder

Consider non-interacting, decaying particles which are hopping non-directionally on a semi-infinite one dimensional lattice. The hopping rate and the decay rate depend on the position on the lattice. There are two obvious realizations of this discrete kinetics that conserve the particle number in the absence of degradation, see Fig. 5.1. These are well-known from the study of random lattice systems [2]. The “barrier height” between two lattice sites can depend on the location (case A). Alternatively, the “trap depth” at one site can depend on the location (case B). The problem of morphogen transport in a disordered environment that we are interested in here can be formally described by the same kinetic equations used for these systems although the origin of the fluctuations of the hopping rate is quite different. Usually these hopping rates are determined by an energy landscape in which the particles move. However, in section 4.2, we explained that these models can be viewed as an effective description of morphogen transport by passive diffusion in the extracellular space of a tissue that is coarse-grained on a length scale given by the average cell diameter a , see Fig. 4.4. It is reasonable to use a as a coarse-graining length because the fluctuations of the ligand concentration on this length scale

are those perceived by the cells in the tissue.

The mean field equation in the bulk which describes case A is

$$\partial_t C_n = p_{n-1}(C_{n-1} - C_n) + p_n(C_{n+1} - C_n) - k_n C_n, \quad \text{for } n > 0, \quad (5.1)$$

where C_n denotes the particle number at lattice site n , p_{n-1} is the rate for particle hopping between sites n and $n - 1$ in both directions, and k_n is the rate of particle decay at site n . The lattice begins at site $n = 0$. The treatment of this boundary has to be specified. We investigate both a fixed particle number $C_0 = C_0^0 = \text{const.}$ and a constant influx of particles at a rate ν into the system at $n = 0$. The latter is described by

$$\partial_t C_0 = \nu + p_1(C_1 - C_0) - k_0 C_0. \quad (5.2)$$

The mean field description of case B is

$$\partial_t C_n = p_{n-1}C_{n-1} + p_{n+1}C_{n+1} - 2p_n C_n - k_n C_n, \quad \text{for } n > 0, \quad (5.3)$$

where p_n denotes the rate of hopping away from site n . The corresponding equation for C_0 with an influx of particles at rate ν is

$$\partial_t C_0 = \nu + p_1 C_1 - p_0 C_0 - k_0 C_0. \quad (5.4)$$

In the following, we investigate a frozen disorder configuration of this system in which the p_n are distributed randomly around a mean value p , i.e. $p_n = p + \eta_n$. Here, η_n is a random variable with $\langle \eta_n \rangle = 0$. Moreover, the correlator is assumed to be $\langle \eta_n \eta_j \rangle = \sigma_p^2 \delta_{nj}$. This implies that the values of η_n at different lattice sites are uncorrelated. The k_n are distributed analogously, i.e. $k_n = k + \zeta_n$ with $\langle \zeta_n \rangle = 0$ and $\langle \zeta_n \zeta_j \rangle = \sigma_k^2 \delta_{nj}$. The η_n and ζ_n can be correlated at each lattice site: $\langle \eta_n \zeta_j \rangle = C_{kp} \delta_{nj}$. Note, that in case A this implies that the degradation rate k_n at site n is correlated with the hopping rate to the right p_n . It could also be correlated with the hopping rate to the left p_{n-1} . Only the numerical results presented in the following depend very weakly on this subtle difference. Note, that a correlation with both p_n and p_{n-1} would lead to nonlocal correlations in the system. We do not treat this here and restrict ourselves to the simpler case of local correlations.

In addition to the rates p_n and k_n , the rate of ligand influx into the system ν can be fluctuating, i.e. $\nu = \nu_0 + \chi$ where χ is a random variable with $\langle \chi \rangle = 0$, $\langle \chi^2 \rangle = \sigma_\nu^2$, and $\langle \chi \eta_n \rangle = \langle \chi \zeta_n \rangle = 0$ for all $n \geq 0$. In the case of a fixed concentration at $n = 0$, one can introduce fluctuations at the boundary very similarly: $C_0 = C_0^0 + \tilde{\gamma}$ with a random variable $\tilde{\gamma}$ satisfying $\langle \tilde{\gamma} \rangle = 0$, $\langle \tilde{\gamma}^2 \rangle = \sigma_C^2$, and $\langle \tilde{\gamma} \eta_n \rangle = \langle \tilde{\gamma} \zeta_n \rangle = 0$. The variances σ_p , σ_k , σ_ν , and σ_C of the noise terms η_n , ζ_n , χ , and $\tilde{\gamma}$ are assumed to be small compared to the mean values p , k , ν_0 , and C_0^0 respectively. Our discussion is mostly independent of the specific probability distributions of η_n , ζ_n , χ , and $\tilde{\gamma}$. It is only required that these distributions are tightly localized around their mean value zero.

One can formally derive continuous descriptions of (5.1) and (5.3), see section E.1 of the appendix. The continuum limit of case A is

$$\partial_t c(x, t) = \partial_x (D + \eta(x)) \partial_x c(x, t) - (k + \zeta(x)) c(x, t) \quad (5.5)$$

and that of case B

$$\partial_t c(x, t) = \partial_x^2 (D + \eta(x)) c(x, t) - (k + \zeta(x)) c(x, t). \quad (5.6)$$

Here $x = na$, $c(x, t)|_{x=na} = C_n(t)/a$, and $D = pa^2$ with the lattice constant a . The continuum limit of the noise correlators is $\langle \eta(x) \eta(x') \rangle = \sigma_D^2 a \delta(x - x')$, $\langle \zeta(x) \zeta(x') \rangle = \sigma_k^2 a \delta(x - x')$, and $\langle \eta(x) \zeta(x') \rangle = C_{kD} a \delta(x - x')$ respectively. Here $\sigma_D = \sigma_p a^2$ and $C_{kD} = C_{kp} a^2$.

	Mean value	Fluctuations	Width of distribution
Diffusion coefficient	D	η	σ_D
Degradation rate	k	ζ	σ_k
Current at $x = 0$	j_0	χ	σ_{j_0}
Concentration at $x = 0$	c_0^0	γ	σ_c

Table 5.1: Notation used for the simple diffusion models with disorder in section 5.1.

For $x \rightarrow \infty$, the boundary condition $c(x) = 0$ has to be satisfied. The boundary condition at $x = 0$ that corresponds to fixing the concentration at site $n = 0$ in the discrete descriptions above is $c(0, t) = c_0^0 + \gamma$ with $c_0^0 = C_0^0/a$ and $\gamma = \tilde{\gamma}/a$. The variance of γ is $\langle \gamma^2 \rangle = \sigma_c^2 a \delta(x - x')$ with $\sigma_c = \sigma_C/a$. A fixed particle influx at site $n = 0$ at rate $\nu = \nu_0 + \chi$ corresponds to a fixed current $j_0 + \chi$ at $x = 0$ with $j_0 = \nu_0$. For case A, this imposes the constraint

$$(D + \eta(x)) \partial_x c(x, t) \Big|_{x=0} = -j_0 - \chi \quad (5.7)$$

and in case B we have

$$\partial_x (D + \eta(x)) c(x, t) \Big|_{x=0} = -j_0 - \chi. \quad (5.8)$$

For convenience, the notation used throughout this section is summarized in Table 5.1.

These continuous equations are still a description of the underlying discrete systems, i.e. we do not take the limit $a \rightarrow 0$ here. This implies that the continuum description is only valid on length scales that are large compared to a . Here, we are interested in the behavior of the system on such large length scales. The fluctuations of D and k at different positions x are actually correlated on a length scale a . In the correlators, one should consequently use a discrete delta function like $\delta_a(x) = 1/a$ if $-a/2 < x < a/2$ and $\delta_a(x) = 0$ otherwise. We use the Dirac delta functions in these correlators for mathematical convenience. This is a reasonable approximation on length scales that are much larger than a . For the delta function at $x = 0$ that appears in the noise correlators for $x = x'$, we formally use $\delta(0) = 1/a$ where necessary. Note, that in the formal continuum limit which is obtained for $a \rightarrow 0$, the fluctuations of D and k vanish unless one lets the relative noise amplitudes σ_D/D and σ_k/k diverge.

5.1.2 Effects of the disorder on the steady state

The time development defined by equations (5.1) and (5.3) in the absence of particle decay, i.e. with $k_n = 0$, has been studied extensively in previous work [2]. In fact, the long time behavior of such systems can be solved exactly [2]. Here, however, we investigate a strikingly different problem, namely the formation of steady state profiles in presence of a localized particle source with particle decay throughout the system. The presence of a source located at $x = 0$ breaks the space inversion symmetry. Moreover, even in the steady state, there is a non-vanishing particle current throughout the system because particles constantly enter from the source and decay in the bulk. This implies that detailed balance is violated in the steady state. For the satisfaction of detailed balance, it is required that the net particle current vanishes everywhere. Consequently, we are looking at non-equilibrium steady states. This highlights the qualitative difference to the previously investigated situation without particle production and decay in which the system relaxes into an equilibrium steady state [2].

Let us now investigate the effects of the disorder on the steady state gradients that are reached for $t \rightarrow \infty$. Due to the presence of multiplicative noise in (5.1) and (5.3), the calculation of the steady state solutions in both cases A and B is a nontrivial problem. Using a small noise

approximation, we apply a perturbative approach to calculate the spatial correlation functions of the particle concentration $c(x)$ in steady state. To begin with, we calculate the first order correction of the steady state profile that is due to the presence of the disorder.

Effects of disorder in case A It is assumed that the amplitude of the noise is small, i.e. $\sigma_D/D \ll 1$ and $\sigma_k/k \ll 1$. The smallness is formally expressed by a factor ϵ which is introduced in (5.5):

$$\partial_x(D + \epsilon\eta(x))\partial_x c(x) - (k + \epsilon\zeta(x))c(x) = 0. \quad (5.9)$$

The ansatz

$$c(x) = c_0(x) + \epsilon c_1(x) + \epsilon^2 c_2(x) + \dots$$

combined with (5.9) yields a differential equation with boundary conditions for each order in ϵ . The $O(\epsilon^0)$ -equation is identical to the one without fluctuations, $D\partial_x^2 c_0 - kc_0 = 0$. The $O(\epsilon^1)$ -equation is

$$(D\partial_x^2 - k)c_1(x) = -\partial_x\eta(x)\partial_x c_0(x) + \zeta(x)c_0(x). \quad (5.10)$$

In fact, the equations for all higher order corrections can be obtained by iteration:

$$(D\partial_x^2 - k)c_{j+1}(x) = -\partial_x\eta(x)\partial_x c_j(x) + \zeta(x)c_j(x), \quad j \geq 0. \quad (5.11)$$

The boundary conditions for $c_0(x)$, $c_1(x)$, etc. at $x = 0$ are obtained by requiring that the boundary condition on $c(x)$ is satisfied to each order in ϵ . For a fixed concentration, $c(0) = c_0^0$, this simply implies $c_0(0) = c_0^0$, $c_1(0) = \gamma$, and $c_2(0) = c_3(0) = \dots = 0$. If the current is fixed at $x = 0$, (5.7) has to be satisfied. To $O(\epsilon^0)$, this yields $Dc_0'(0) = -j_0$ where the prime denotes the derivative with respect to x . To $O(\epsilon^1)$, we have

$$c_1'(0) = -D^{-1}(\eta(0)c_0'(0) + \chi) \quad (5.12)$$

and the boundary conditions for all higher order terms are obtained by iteration:

$$c_{j+1}'(0) = -D^{-1}\eta(0)c_j'(0), \quad j \geq 1.$$

For small noise amplitudes, we may assume that the iteration scheme (5.11) converges rapidly. In the following, we will consequently focus on calculating $c_0(x)$ and $c_1(x)$ and neglect higher order corrections. For c_0 , we find the same steady state solution as for the problem without disorder: $c_0(x) = c_0^0 e^{-x/\xi_D}$, where $\xi_D = \sqrt{D/k}$ is the diffusion length and $c_0^0 = j_0/\sqrt{kD}$.

Equation (5.10) can be solved by using a Green's function $G(x, x')$ of the linear operator $(D\partial_x^2 - k)$. The Green's function must satisfy $(D\partial_x^2 - k)G(x, x') = \delta(x - x')$. It is straightforward to calculate the free Green's function $G_0(x, x')$ using Fourier transforms:

$$G_0(x, x') = \frac{-1}{2\sqrt{kD}} e^{-|x-x'|/\xi_D}.$$

Using a mirror image technique, one can construct two different Green's functions which satisfy the boundary condition $G(0, x') = 0$ and $\partial_x G(x, x')|_{x=0} = 0$ respectively. These Green's functions explicitly read

$$G_{\pm}(x, x') = \frac{-1}{2\sqrt{kD}} \left(e^{-|x-x'|/\xi_D} \pm e^{-(x+x')/\xi_D} \right), \quad (5.13)$$

where at the boundary $G_-(0, x') = G_-(x, 0) = 0$ and $\partial_x G_+(x, x')|_{x=0} = \partial_{x'} G_+(x, x')|_{x'=0} = 0$. Note, that the first derivatives of G_+ are not defined at $x = x'$ by (5.13). The first derivative of

$G_0(x, x')$ vanishes because the free Green's function should satisfy $G_0(x, x') = G_0(x', x)$. This implies $\partial_x G_0(x, x') = -\partial_x G_0(x', x)$ which is only satisfied for $x = x'$ if $\partial_x G_0(x, x')|_{x=x'} = 0$. Thus, we formally choose the derivative of the absolute value function $\partial_x |x|_{x=0} = 0$. This corresponds to defining $\Theta(0) = 1/2$ for the Heaviside function at $x = 0$. While this choice will simplify our notation at some points, the results in this section do not depend on it.

Applying the Green's function method, the solution to equation (5.10) is

$$\begin{aligned} c_1^\pm(x) &= -D\gamma\partial_{x'}G_\pm(x, x')\Big|_{x'=0} - G_\pm(x, 0)(\eta(0)c'_0(0) + \chi) \\ &\quad + \int_0^\infty dx' G_\pm(x, x')\left(-\partial_{x'}\eta(x')\partial_{x'}c_0(x') + \zeta(x')c_0(x')\right) \\ &= -D\gamma\partial_{x'}G_\pm(x, x')\Big|_{x'=0} - G_\pm(x, 0)\chi \\ &\quad + \int_0^\infty dx' \left(\eta(x')c'_0(x')\partial_{x'}G_\pm(x, x') + G_\pm(x, x')\zeta(x')c_0(x')\right), \end{aligned} \quad (5.14)$$

where the first terms come from the boundary condition imposed at $x = 0$. We use a condensed notation for both choices of the boundary condition at $x = 0$: c_1^+ denotes the solution for a fixed current and c_1^- the solution for a fixed concentration at $x = 0$. For the choice $G_-(x, x')$, $-D\gamma\partial_{x'}G_-(x, x')|_{x'=0} = \gamma \exp(-x/\xi_D)$, so that the first order correction $c_1^-(x)$ satisfies the required boundary condition. One can easily verify that the condition (5.12) is satisfied for $c_1^+(x)$. Note, that in our notation $\partial_x G_+(x, 0)|_{x=0} = D^{-1} \neq \partial_x G_+(x, x')|_{x=x'=0} = 0$. From (5.14), we can see that $\langle c_1^\pm(x) \rangle = 0$ which implies that in the presence of disorder, the mean value of $c(x)$ is not shifted compared to the solution in the absence of noise. This is valid to first order in perturbation theory. The second and higher order corrections that can be calculated by applying the iteration scheme given in (5.11) and (5.12) lead to a small shift of the mean value of $c(x)$.

In principle, one could calculate all correlation functions $\langle c(x_1)c(x_2)\dots \rangle$ from (5.14) and the corresponding noise correlators $\langle \eta(x_1)\eta(x_2)\dots \rangle$, $\langle \zeta(x_1)\zeta(x_2)\dots \rangle$, et cetera. We exploit (5.14) to calculate the two point correlation function $\langle c(x_1)c(x_2) \rangle$ and from that the second moment of $c(x)$. To first order, the mean is $\langle c(x) \rangle = c_0(x)$ because $c(x) = c_0(x) + c_1(x)$ and $\langle c_1(x) \rangle = 0$. The variance of $c(x)$ is thus $\langle (c(x) - \langle c(x) \rangle)^2 \rangle = \langle c_1(x)^2 \rangle$ for which we obtain using (5.14):

$$\begin{aligned} \langle c_1^\pm(x)^2 \rangle &= D^2 \left(\partial_{x'} G_\pm(x, x') \Big|_{x'=0} \right)^2 \sigma_c^2 + G_\pm(x, 0)^2 \sigma_{j_0}^2 \\ &\quad + \int_0^\infty dx' \int_0^\infty dx'' \left(\sigma_D^2 a \delta(x' - x'') c'_0(x') \partial_{x'} G_\pm(x, x') c'_0(x'') \partial_{x''} G_\pm(x, x'') \right. \\ &\quad + \sigma_k^2 a \delta(x' - x'') G_\pm(x, x') G_\pm(x, x'') c_0(x') c_0(x'') \\ &\quad \left. + 2C_{kD} a \delta(x' - x'') c'_0(x') \partial_{x'} G_\pm(x, x') G_\pm(x, x'') c_0(x'') \right) \\ &= D^2 \left(\partial_{x'} G_\pm(x, x') \Big|_{x'=0} \right)^2 \sigma_c^2 + G_\pm(x, 0)^2 \sigma_{j_0}^2 \\ &\quad + a \int_0^\infty dx' \left(\sigma_D^2 c'_0(x')^2 (\partial_{x'} G_\pm(x, x'))^2 + \sigma_k^2 G_\pm(x, x')^2 c_0(x')^2 \right. \\ &\quad \left. + 2C_{kD} G_\pm(x, x') c_0(x') c'_0(x') \partial_{x'} G_\pm(x, x') \right). \end{aligned} \quad (5.15)$$

Using the explicit expressions for the Green's functions and $c_0(x)$, this integral can be solved and expressed in terms of elementary functions. A dimensionless measure of the relative uncertainty of the concentration at x is the normalized standard deviation

$$\Sigma(x) = \frac{\langle (c(x) - \langle c(x) \rangle)^2 \rangle^{1/2}}{\langle c(x) \rangle} = \frac{\langle c_1(x)^2 \rangle^{1/2}}{c_0(x)}$$

where the last equality holds to first order in perturbation theory. Using (5.15), one obtains for case A

$$\begin{aligned}
\Sigma^\pm(x) &= \left(\Sigma_B^\pm(x)^2 + \Sigma_k^\pm(x)^2 + \Sigma_D^\pm(x)^2 + \Sigma_{kD}^\pm(x)^2 \right)^{1/2}, \text{ with} \\
\Sigma_B^+(x)^2 &= \left(\frac{\sigma_{j_0}}{j_0} \right)^2 \\
\Sigma_B^-(x)^2 &= \left(\frac{\sigma_c}{c_0^0} \right)^2 \\
\Sigma_k^\pm(x)^2 &= \frac{a}{8\xi_D} \left(\frac{\sigma_k}{k} \right)^2 \left(1 \pm 2 \mp e^{-2x/\xi_D} + \frac{2x}{\xi_D} \right) \\
\Sigma_D^\pm(x)^2 &= \frac{a}{8\xi_D} \left(\frac{\sigma_D}{D} \right)^2 \left(1 \mp 2 \pm 3e^{-2x/\xi_D} + \frac{2x}{\xi_D} \right) \\
\Sigma_{kD}^\pm(x) &= \frac{a}{4\xi_D} \frac{C_{kD}}{kD} \left(1 \pm e^{-2x/\xi_D} - \frac{2x}{\xi_D} \right), \tag{5.16}
\end{aligned}$$

where $\Sigma^+(x)$ corresponds to a fixed current and $\Sigma^-(x)$ to a fixed concentration at $x = 0$. This result satisfies $\Sigma^-(0) = \sigma_c/c_0^0$ as it is required for a fixed concentration at $x = 0$ while $\Sigma^+(0) \neq 0$. The asymptotic behavior of $\Sigma^\pm(x)$ for large x is independent of the boundary condition used at $x = 0$:

$$\Sigma^\pm(x)^2 \approx \frac{ax}{4\xi_D^2} \left(\left(\frac{\sigma_k}{k} \right)^2 + \left(\frac{\sigma_D}{D} \right)^2 - \frac{2C_{kD}}{kD} \right). \tag{5.17}$$

We see that the normalized standard deviation of the concentration grows as $\Sigma(x) \sim \sqrt{x}$ for large x . Notably, positive correlations between D and k lead to a reduction of this increase.

We have performed numerical calculations of the discrete description of case A for the two boundary conditions. A large number of steady state gradients was calculated for different realizations of the disorder using a Gaussian distribution for the random variables. From these, the first and second moments of C_n at all lattice sites n were calculated, see Fig. 4.5 A for an illustration and section F.4 of the appendix for more details. The resulting normalized standard deviation is shown in Fig. 5.2 for the different boundary conditions. The good agreement with the results of the perturbative calculation is remarkable. If only D is fluctuating, a decrease of $\Sigma^+(x)$ near the boundary at $x = 0$ is observed. This is at odds with a picture in which the disorder leads to an accumulating loss of precision of the concentration $c(x)$ with increasing distance from the particle source. However, this notion remains valid sufficiently far away from the source. For the degenerate case $2C_{kD}/kD = (\sigma_D/D)^2 + (\sigma_k/k)^2$, the asymptotic behavior given in (5.17) shows that $\Sigma(x)$ becomes constant for large x . The numerical calculations confirm this intriguing result, see Fig. 5.2.

Effects of disorder in case B We apply the same method to case B. Again, $c_0(x)$ is the steady state without noise. The iteration scheme for the calculation of $c_1(x)$ and higher corrections is

$$(D\partial_x^2 - k)c_{j+1}(x) = -\partial_x^2\eta(x)c_j(x) + \zeta(x)c_j(x), \quad j \geq 0. \tag{5.18}$$

For a fixed concentration at $x = 0$, the boundary conditions at $x = 0$ are again $c_0(0) = c_0^0$, $c_1(0) = \gamma$, and $c_2(0) = c_3(0) = \dots = 0$. For a fixed current at $x = 0$, (5.8) has to be satisfied. To $O(\epsilon^0)$, this yields $Dc'_0(0) = -j_0$, to $O(\epsilon^1)$

$$c'_1(0) = -D^{-1} \left(\partial_x\eta(x)c_0(x) \Big|_{x=0} + \chi \right),$$

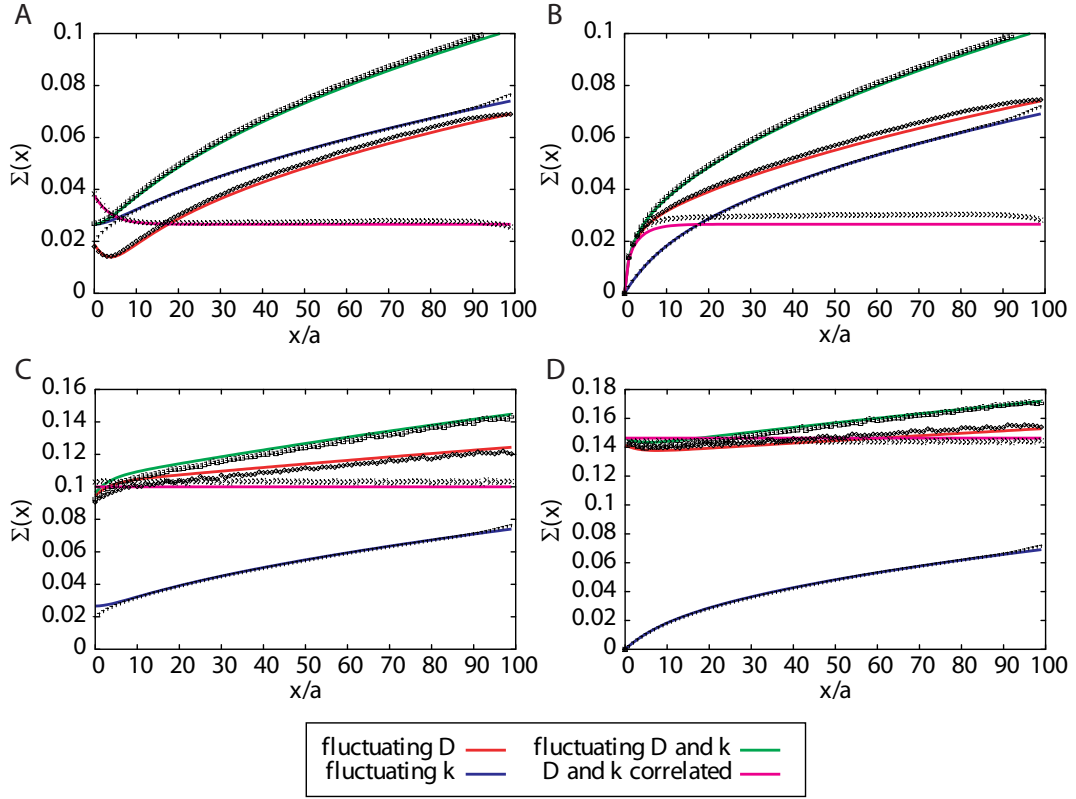


Figure 5.2: Normalized standard deviation $\Sigma(x)$ of the steady state concentration $c(x)$ for the simple diffusion model with disorder in one dimension. The symbols indicate results from numerical calculations in which steady state gradients were calculated for many (typically 100,000) realization of the disorder. The lines show the corresponding analytical results (5.16) and (5.20) for $\Sigma(x)$. The red lines show $\Sigma(x)$ if only D is fluctuating, the blue lines if only k is fluctuating, the green lines if both D and k are fluctuating, and the magenta lines if D and k are fluctuating in a fully correlated way. (A,B) Case A with the current j_0 (A) and the concentration c_0^0 (B) imposed at $x = 0$. (C,D) Case B with the current j_0 (C) and the concentration c_0^0 (D) imposed at $x = 0$. Parameters are $\xi_D/a = \sqrt{50}$, $\sigma_{j_0}/j_0 = \sigma_c/c_0^0 = 0$, $\sigma_D/D = \sigma_k/k = 0.1$. In the fully correlated case $2C_{kD}/kD = (\sigma_D/D)^2 + (\sigma_k/k)^2$ while $C_{kD} = 0$ otherwise. A Gaussian distribution was used for the noise terms in the numerical calculations.

and higher order corrections can be obtained iteratively. With the same Green's functions $G_{\pm}(x, x')$ as defined above, the solution to equation (5.18) for $x \geq 0$ is

$$\begin{aligned} c_1^{\pm}(x) &= -D\gamma\partial_{x'}G_{\pm}(x, x')\Big|_{x'=0} - G_{\pm}(x, 0)\chi - \eta(0)c_0(0)\partial_{x'}G_{\pm}(x, x')\Big|_{x'=0} \\ &\quad - \int_0^{\infty} dx' \left(\eta(x')c_0(x')\partial_{x'}^2G_{\pm}(x, x') - \zeta(x')G_{\pm}(x, x')c_0(x') \right), \end{aligned} \quad (5.19)$$

where we have integrated by parts twice. From (5.19), we calculate the variance

$$\begin{aligned} \langle c_1^{\pm}(x)^2 \rangle &= D^2\sigma_c^2 \left(\partial_{x'}G_{\pm}(x, x')\Big|_{x'=0} \right)^2 + \sigma_{j_0}^2 G_{\pm}(x, 0)^2 \\ &\quad + \sigma_D^2 c_0(0)^2 (\partial_{x'}G_{\pm}(x, x'))^2\Big|_{x'=0} + \sigma_D^2 a c_0(0)^2 (\partial_{x'}G_{\pm}(x, x'))\partial_{x'}^2G_{\pm}(x, x')\Big|_{x'=0} \\ &\quad + a \int_0^{\infty} dx' \left(\sigma_D^2 c_0(x')^2 (\partial_{x'}^2G_{\pm}(x, x'))^2 + \sigma_k^2 G_{\pm}(x, x')^2 c_0(x')^2 \right. \\ &\quad \left. - 2C_{kD}G_{\pm}(x, x')c_0(x')^2\partial_{x'}^2G_{\pm}(x, x') \right), \end{aligned}$$

where we have used $\Theta(0) = 1/2$ which affects the result only at $x = 0$. Using the explicit expressions for $G_{\pm}(x, x')$ the normalized standard deviation for $x > 0$ can be calculated:

$$\begin{aligned} \Sigma^{\pm}(x) &= \left(\Sigma_B^{\pm}(x)^2 + \Sigma_k^{\pm}(x)^2 + \Sigma_D^{\pm}(x)^2 + \Sigma_{kD}^{\pm}(x) \right)^{1/2}, \text{ with} \\ \Sigma_D^{\pm}(x)^2 &= \frac{a}{8\xi_D} \left(\frac{\sigma_D}{D} \right)^2 \left(-7 \pm 2 \mp 9e^{-2x/\xi_D} + \frac{2x}{\xi_D} \right) + \frac{3 \mp 1}{2} \left(\frac{\sigma_D}{D} \right)^2 \\ \Sigma_{kD}^{\pm}(x) &= \frac{a}{4\xi_D} \frac{C_{kD}}{kD} \left(3 \mp 2 \pm 5e^{-2x/\xi_D} - \frac{2x}{\xi_D} \right). \end{aligned} \quad (5.20)$$

Here, $\Sigma_B^{\pm}(x)$ and $\Sigma_k^{\pm}(x)$ are as in (5.16). Note, that $\Sigma_D^-(x)$ is discontinuous at $x = 0$ with $\Sigma_D^-(0) = 0$. The asymptotic behavior of $\Sigma(x)$ for large x is identical to that in case A given by (5.17).

The normalized standard deviation again grows as $\Sigma(x) \sim \sqrt{x}$ for large x . In fact, this is a characteristic behavior for the one dimensional situation: independent of which rates fluctuate and whether the case of random barrier heights or random trap depths is used, the asymptotic \sqrt{x} -behavior that is reminiscent of a random-walk is found.

As for case A, we have performed numerical calculations to verify these results. A comparison of the numerically calculated normalized standard deviation to $\Sigma^+(x)$ and $\Sigma^-(x)$ from (5.20) is shown in Fig. 5.2. The agreement is remarkable. Note that $\Sigma(x)$ is generally much larger for small x in case B than in case A although the same values for the parameters were applied. The shapes of the curves for case A and case B are also very different. Finally, the boundary condition imposed at $x = 0$ has a strong impact on $\Sigma(x)$ near this boundary.

5.1.3 Generalization to two and three space dimensions

Motivated by the fact that morphogen gradient formation often occurs in an essentially two dimensional geometry, we now generalize these calculations to two space dimensions. To simplify the discussion, we restrict our attention to case A.

Disorder in two dimensions The discrete mean field kinetics for the particle number $C_{n,m}$ at site (n, m) in the bulk of a square lattice with sites indexed by $n \in \mathbb{N}_0$ in the x -direction and by $m \in \mathbb{Z}$ in the y -direction reads for $n \geq 1$

$$\partial_t C_{n,m} = p_{n-1 \leftrightarrow n, m} (C_{n-1, m} - C_{n, m}) + p_{n \leftrightarrow n+1, m} (C_{n+1, m} - C_{n, m}) + p_{n, m-1 \leftrightarrow m}$$

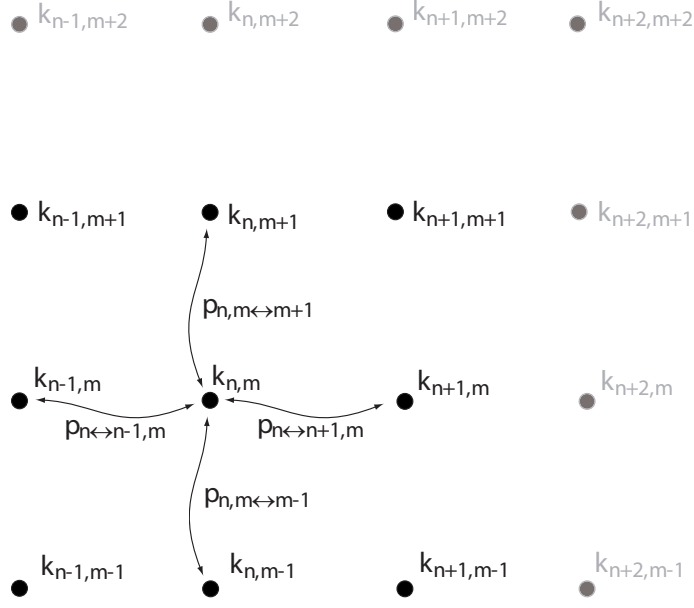


Figure 5.3: Two dimensional hopping model with particle decay for case A. The decay rate of the particles at the lattice site (n, m) is $k_{n,m}$. The hopping rate from that site to site $(n, m + 1)$ and vice versa is $p_{n,m \leftrightarrow m+1}$ and accordingly for hopping in the other directions. For clarity, we only illustrate the hopping to and away from site (n, m) .

$$\times (C_{n,m-1} - C_{n,m}) + p_{n,m \leftrightarrow m+1} (C_{n,m+1} - C_{n,m}) - k_{n,m} C_{n,m}. \quad (5.21)$$

The notation is further clarified in Fig. 5.3. The boundary is located on the line $n = 0$. Either the concentrations at the lattice sites on this boundary are fixed, $C_{0,m} = C_{0,m}^0$, or a constant influx of particles at rate ν_m into the system is imposed there:

$$\begin{aligned} \partial_t C_{0,m} = & \nu_m + p_{0 \leftrightarrow 1, m} (C_{1,m} - C_{0,m}) + p_{0, m-1 \leftrightarrow m} (C_{0, m-1} - C_{0,m}) \\ & + p_{0, m \leftrightarrow m+1} (C_{0, m+1} - C_{0,m}) - k_{0,m} C_{0,m}. \end{aligned} \quad (5.22)$$

For simplicity, we will denote the multi-indices of p by Greek letters in the following. The p_α and $k_{n,m}$ are assumed to be distributed around a mean like in the one dimensional situation: $p_\alpha = p + \eta_\alpha$ with $\langle \eta_\alpha \rangle = 0$, $\langle \eta_\alpha \eta_\beta \rangle = \sigma_p^2 \delta_{\alpha\beta}$, and $k_{n,m} = k + \zeta_{n,m}$ with $\langle \zeta_{n,m} \rangle = 0$, $\langle \zeta_{n,m} \zeta_{i,j} \rangle = \sigma_k^2 \delta_{ni} \delta_{mj}$. Local correlations between p_α and $k_{n,m}$ can be introduced in several ways, e.g. via $\langle \eta_{n \leftrightarrow n+1, m} \zeta_{i,j} \rangle = \langle \eta_{n, m \leftrightarrow m+1} \zeta_{i,j} \rangle = C_{kp} \delta_{ni} \delta_{mj}$ which means that the degradation rate at a site is correlated with the hopping rates to the top and to the right. The details of this choice do not affect our results significantly. The $C_{0,m}^0$ and the ν_m are stochastic variables with $C_{0,m}^0 = C_0^0 + \tilde{\gamma}_m$, $\nu_m = \nu_0 + \tilde{\chi}_m$, where $\langle \tilde{\gamma}_m \rangle = 0$, $\langle \tilde{\chi}_m \rangle = 0$, $\langle \tilde{\gamma}_m \tilde{\gamma}_k \rangle = \sigma_C^2 \delta_{mk}$, and $\langle \tilde{\chi}_m \tilde{\chi}_k \rangle = \sigma_\nu^2 \delta_{mk}$.

The continuum limit is obtained as in the one dimensional case, see section E.1 of the appendix. With $\vec{x} = (x, y)$ and $\nabla = (\partial_x, \partial_y)$, it reads

$$\partial_t c(\vec{x}, t) = \nabla \cdot ((D + \eta(\vec{x})) \nabla c(\vec{x}, t)) - (k + \zeta(\vec{x})) c(\vec{x}, t), \quad (5.23)$$

where $c(\vec{x}, t)|_{x=na, y=ma} = C_{n,m}/a^2$. The boundary conditions translate to $c(0, y) = c_0^0 + \gamma(y)$ with $c_0^0 = C_0^0/a^2$ and $\gamma(y)|_{y=ma} = \tilde{\gamma}_m/a^2$ for a fixed concentration at $x = 0$ and

$$(D + \eta(\vec{x})) \partial_x c(\vec{x}, t) \Big|_{x=0} = -(j_0 + \chi(y)) \quad (5.24)$$

with $j_0 = \nu_0/a$ and $\chi(y)|_{y=ma} = \tilde{\chi}_m/a$ for a fixed current. Finally, the noise correlators are $\langle \eta(\vec{x})\eta(\vec{x}') \rangle = \sigma_D^2 a^2 \delta(\vec{x} - \vec{x}')$, $\langle \zeta(\vec{x})\zeta(\vec{x}') \rangle = \sigma_k^2 a^2 \delta(\vec{x} - \vec{x}')$, $\langle \eta(\vec{x})\zeta(\vec{x}') \rangle = C_{kD} a^2 \delta(\vec{x} - \vec{x}')$, $\langle \gamma(y)\gamma(y') \rangle = \sigma_c^2 a \delta(y - y')$, and $\langle \chi(y)\chi(y') \rangle = \sigma_{j_0}^2 a \delta(y - y')$. Here $\sigma_D = \sigma_p a^2$, $C_{kD} = C_{kp} a^2$, $\sigma_{j_0} = \sigma_\nu/a$, and $\sigma_c = \sigma_C/a^2$.

Effects of the disorder in two dimensions The steady state of (5.23) can be calculated iteratively as in the one dimensional situation. We again calculate $c_0(\vec{x})$ and $c_1(\vec{x})$. Evidently, the unperturbed steady state is the same as for the one dimensional situation, $c_0(\vec{x}) = c_0(x) = c_0^0 \exp(-x/\xi_D)$. The first order correction $c_1(x, y)$ must satisfy $c_1(0, y) = \gamma(y)$ for fixed concentration at $x = 0$ and

$$\partial_x c_1(x, y) \Big|_{x=0} = -D^{-1}(\eta(0, y)c_0'(0) + \chi(y)) \quad (5.25)$$

if the current is fixed at $x = 0$.

The free Green's function for the operator $(D(\partial_x^2 + \partial_y^2) - k)$ satisfying $(D(\partial_x^2 + \partial_y^2) - k)G_0(\vec{x}, \vec{x}') = \delta(\vec{x} - \vec{x}')$ is

$$G_0(\vec{x}, \vec{x}') = \frac{-1}{2\pi D} K_0(|\vec{x} - \vec{x}'|/\xi_D),$$

where K_0 is a modified Bessel function of the second kind [97]. Using a mirror image technique, one can construct Green's functions $G_\pm(\vec{x}, \vec{x}')$ that satisfy $G_-(\vec{x}, \vec{x}')|_{x=0} = 0$ and $\partial_x G_+(\vec{x}, \vec{x}')|_{x=0} = 0$ respectively:

$$G_\pm(x, y, x', y') = G_0(x, y, x', y') \pm G_0(x, y, -x', y'). \quad (5.26)$$

With this, the solution for $c_1(\vec{x})$ is

$$\begin{aligned} c_1^\pm(\vec{x}) &= - \int_{-\infty}^{\infty} dy' \left(D \gamma(y') \partial_{x'} G_\pm(\vec{x}, \vec{x}') \Big|_{x'=0} + (\eta(0, y')c_0'(0) + \chi(y')) G_\pm(x, y, 0, y') \right) \\ &\quad + \int_0^{\infty} dx' \int_{-\infty}^{\infty} dy' G_\pm(\vec{x}, \vec{x}') \left(\zeta(\vec{x}')c_0(x') - \nabla \cdot (\eta(\vec{x}')\nabla c_0(x')) \right) \\ &= - \int_{-\infty}^{\infty} dy' \left(D \gamma(y') \partial_{x'} G_\pm(\vec{x}, \vec{x}') \Big|_{x'=0} + \chi(y') G_\pm(x, y, 0, y') \right) \\ &\quad + \int_0^{\infty} dx' \int_{-\infty}^{\infty} dy' \left(G_\pm(\vec{x}, \vec{x}') \zeta(\vec{x}')c_0(x') + \eta(\vec{x}')c_0'(x') \partial_{x'} G_\pm(\vec{x}, \vec{x}') \right), \end{aligned} \quad (5.27)$$

where $\nabla \cdot (\eta(\vec{x}')\nabla c_0(x')) = \partial_{x'} \eta(\vec{x}') \partial_{x'} c_0(x')$ was used. The first term is due to the respective boundary condition on $c_1(\vec{x})$. As we show in section E.2 of the appendix $\partial_x G_+(x, y, 0, y')|_{x=0} = D^{-1} \delta(y - y')$, so that $c_1^+(\vec{x})$ satisfies (5.25). It can be shown in a very similar way that $c_1^-(\vec{x})|_{x=0} = \gamma(y)$.

To first order, the variance of $c(\vec{x})$ is consequently

$$\begin{aligned} \langle c_1^\pm(\vec{x})^2 \rangle &= a \int_{-\infty}^{\infty} dy' \left(\sigma_c^2 D^2 \left(\partial_{x'} G_\pm(\vec{x}, \vec{x}') \Big|_{x'=0} \right)^2 + \sigma_{j_0}^2 G_\pm(x, y, 0, y')^2 \right) \\ &\quad + a^2 \int_0^{\infty} dx' \int_{-\infty}^{\infty} dy' \left(\sigma_k^2 G_\pm(\vec{x}, \vec{x}')^2 c_0(x')^2 + \sigma_D^2 c_0'(x')^2 (\partial_{x'} G_\pm(\vec{x}, \vec{x}'))^2 \right. \\ &\quad \left. + 2C_{kD} c_0(x') c_0'(x') G_\pm(\vec{x}, \vec{x}') \partial_{x'} G_\pm(\vec{x}, \vec{x}') \right). \end{aligned} \quad (5.28)$$

By symmetry, $\langle c_1(\vec{x})^2 \rangle$ is independent of y . This enables us to numerically evaluate (5.28) as a function of x . It is not possible to express the integral explicitly in terms of elementary functions. However, one can extract the asymptotic behavior for large x . As we show in section E.3.1 of the appendix $\langle c_1(\vec{x})^2 \rangle \sim \exp(-2x/\xi_D) \sqrt{x}$. Consequently, the normalized standard

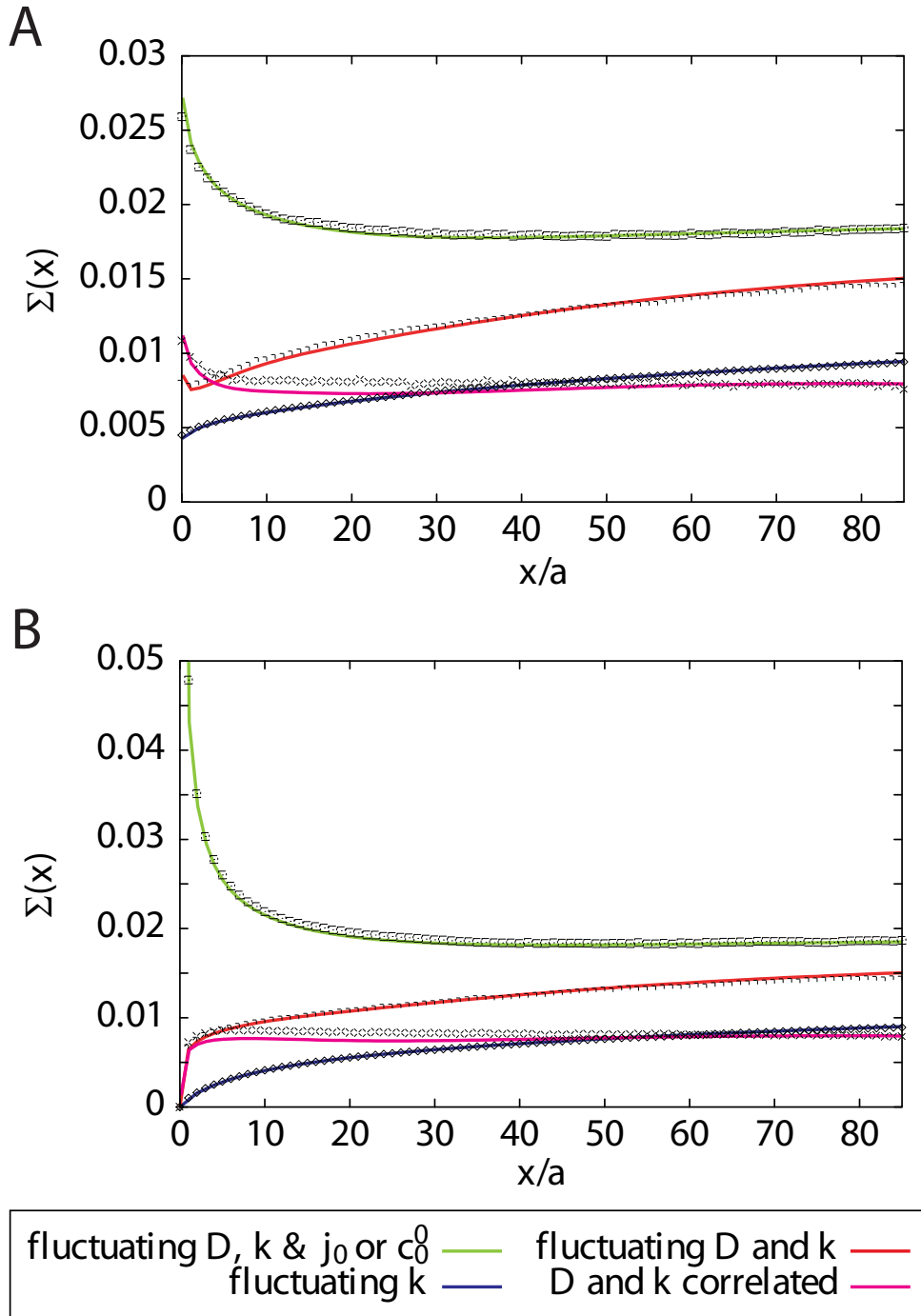


Figure 5.4: Normalized standard deviation $\Sigma(x)$ of the steady state concentration $c(x)$ for the simple diffusion model with disorder in two dimensions. The symbols indicate results from numerical calculations in which steady state gradients were calculated for many (typically 100,000) realizations of the disorder. The lines show the corresponding analytical results for $\Sigma(x)$ that follow from (5.28). The blue lines show $\Sigma(x)$ if only k is fluctuating, the red lines if both D and k are fluctuating, the magenta lines if D and k are fluctuating in a fully correlated way, and the green lines if D , k and the respective quantity imposed at the boundary at $x = 0$ are fluctuating. (A) Normalized standard deviation $\Sigma(x)$ with the current j_0 imposed at $x = 0$. (B) $\Sigma(x)$ with the concentration c_0^0 imposed at $x = 0$. Parameters as in Fig. 5.2 with $\sigma_{j_0}/j_0 = \sigma_c/c_0^0 = 0.1$. A Gaussian distribution was used for the noise terms in the numerical calculations.

Dimensionality	$\Sigma(x) \sim$
1d	$x^{1/2}$
2d	$x^{1/4}$
3d	$\ln(x)$

Table 5.2: Asymptotic behavior of the normalized standard deviation of the concentration $c(x)$ in steady state for different space dimensionalities.

deviation grows asymptotically as $\Sigma(x) = \sqrt{\langle c_1(\vec{x})^2 \rangle} / c_0(x) \sim x^{1/4}$. Note, that the fluctuations of the current or concentration imposed on the boundary line $x = 0$ have a more subtle effect on the normalized standard deviation than in one dimension where they lead to an additional constant in $\Sigma(x)^2$.

Again, we have performed numerical calculations to verify these results. A comparison of the numerically calculated normalized standard deviation to the analytic result following from (5.28) is shown in Fig. 5.4.

Effects of the disorder in three dimensions Naturally, one can calculate the normalized standard deviation in three dimensions as well. As the procedure remains the same, we discuss this only briefly for case A here. We are interested in the steady state solution of (5.23) with $\vec{x} = (x, y, z)$ and $\nabla = (\partial_x, \partial_y, \partial_z)$ in the half-space $x \geq 0$. Either the concentration or the current is imposed on the boundary plane $x = 0$, i.e. $c(\vec{x})|_{x=0} = c_0^0 + \gamma(y, z)$ or $\partial_x c(\vec{x})|_{x=0} = -D^{-1}(j_0 + \chi(y, z))$.

We calculate the free Green's function $G_0(\vec{x}, \vec{x}')$ of the operator $(D\Delta - k)$ in three dimensions in section E.2 of the appendix. Using G_0 , the Green's functions for the two boundary conditions at $x = 0$ can again be constructed:

$$G_{\pm}(\vec{x}, \vec{x}') = \frac{-1}{4\pi D} \left(\frac{e^{-r/\xi_D}}{r} \pm \frac{e^{-r_m/\xi_D}}{r_m} \right), \quad (5.29)$$

with $r = ((x - x')^2 + (y - y')^2 + (z - z')^2)^{1/2}$ and $r_m = ((x + x')^2 + (y - y')^2 + (z - z')^2)^{1/2}$. The result for the variance of $c(\vec{x})$ to first order in perturbation theory is

$$\begin{aligned} \langle c_{\pm}^2(\vec{x}) \rangle &= a^2 \int_{-\infty}^{\infty} dy' \int_{-\infty}^{\infty} dz' \left(\sigma_c^2 D^2 (\partial_{x'} G_{\pm}(\vec{x}, \vec{x}'))^2 + \sigma_{j_0}^2 G_{\pm}(\vec{x}, \vec{x}')^2 \right) \Big|_{x'=0} \\ &+ a^3 \int_0^{\infty} dx' \int_{-\infty}^{\infty} dy' \int_{-\infty}^{\infty} dz' \left(\sigma_k^2 G_{\pm}(\vec{x}, \vec{x}')^2 c_0(x')^2 + \sigma_D^2 c_0'(x')^2 (\partial_{x'} G_{\pm}(\vec{x}, \vec{x}'))^2 \right. \\ &\left. + 2C_{kD} c_0(x') c_0'(x') G_{\pm}(\vec{x}, \vec{x}') (\partial_{x'} G_{\pm}(\vec{x}, \vec{x}')) \right). \end{aligned} \quad (5.30)$$

We have integrated (5.30) numerically. The resulting normalized standard deviation $\Sigma(x)$ is shown in Fig. 5.5 A for a fixed current at the boundary. Asymptotically, $\Sigma(x) \sim \ln(x)$ as we show in section E.3.2 of the appendix.

Role of space dimensionality The results for the different dimensions are compared to each other for the same choice of parameters D , k , j_0 , σ_D , σ_k , C_{kD} , and σ_{j_0} in Fig. 5.5 and Table 5.2. It can be seen that the fluctuating rates lead to a severely slower asymptotic increase of the normalized standard deviation with increasing dimensionality of the space. The general formula for the exponent ϕ in the asymptotic behavior of $\Sigma(x) \sim x^{-\phi}$ as a function of the space dimensionality d is

$$\phi = (3 - d)/4$$

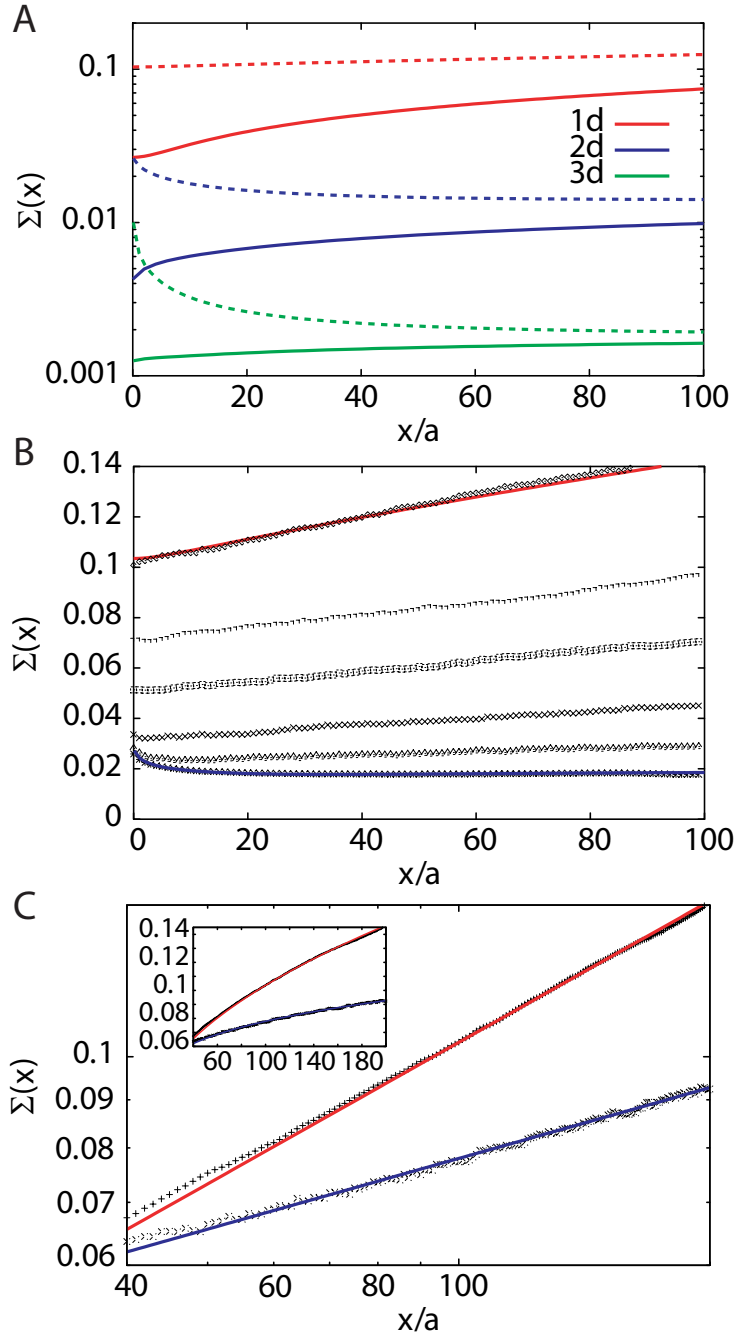


Figure 5.5: Normalized standard deviation $\Sigma(x)$ for the simple diffusion model with disorder for different space dimensionalities. All calculations were done for case A with j_0 imposed at $x = 0$. (A) Logarithmic plot of $\Sigma(x)$ in one dimension (red lines), in two dimensions (blue lines), and in three dimensions (green lines). For the solid lines, only k is fluctuating and for the broken lines both k and j_0 are fluctuating. Shown are the analytical results for $\Sigma(x)$ given by (5.16), (5.28), and (5.30) for the different space dimensionalities respectively. (B) Normalized standard deviation $\Sigma(x)$ in two space dimensions with zero flux boundary conditions imposed at $y = \pm W/2a$ for different values of W/a . The symbols show the numerical results for $W/a = 1$, $W/a = 2$, $W/a = 5$, $W/a = 10$, $W/a = 25$, and $W/a = 50$ from top to bottom. The analytic results for the one dimensional case (red line) and the two dimensional case (blue line) are shown for comparison. In these calculations, k , D , and j_0 are fluctuating. (C) Double-logarithmic plot of the $\Sigma(x)$ for large x in one and two dimensions. In these calculations, k and D are fluctuating. Numerical results are shown by crosses (one dimension) and open symbols (two dimensions). In two dimensions, $\Sigma(x)$ was multiplied by a factor of five. For comparison, functions proportional to $x^{1/2}$ and $x^{1/4}$ are shown in red and blue respectively. The inset shows the same data using linear axes. Parameters as in Fig. 5.2 with $\sigma_{j_0}/j_0 = 0.1$ and $C_{kD} = 0$.

for $d < 3$. It appears that $d = 3$ is the upper critical dimension beyond which the fluctuations of D and k become irrelevant.

It is of great value to use the behavior of $\Sigma(x)$ for large x to identify the fundamental influence of the space dimensionality on the accumulation of the uncertainty of the morphogen concentration with increasing distance to the source. However, the space dimensionality d also has a strong effect on $\Sigma(x)$ near the source boundary at $x = 0$. In Fig. 5.5, it can be seen that $\Sigma(x)$ near $x = 0$ strongly decreases with increasing space dimensionality as well.

The effect of the fluctuating ligand current j_0 across the boundary at $x = 0$ is of particular interest. In one dimension it leads to the trivial addition of a constant to $\Sigma(x)^2$ that consequently causes an increase of $\Sigma(x)$ at all distances x from the source. In two and three dimensions it gives a contribution to $\Sigma(x)$ that decays with increasing x where this decay becomes faster with increasing space dimensionality, see Fig 5.5 A. For identical values of the relative noise strengths σ_D/D , σ_k/k , and σ_{j_0}/j_0 , we see that the fluctuations of j_0 give a large contribution to $\Sigma(x)$ near the source in all dimensions. All these observations regarding the effects of the fluctuations of the boundary condition at $x = 0$ remain qualitatively unaltered if the ligand concentration c_0^0 instead of the current j_0 is imposed at the boundary at $x = 0$.

One may argue that real biological systems are always three dimensional and, strictly speaking, that is true. However, in the theory we deal with systems that extend infinitely in all directions. If, in a two dimensional geometry, side boundaries with zero flux boundary conditions are introduced at $y = \pm W/2$, so that the region in which the gradient forms is constrained to a stripe of width W , the disordered system is more accurately described using a one dimensional description for small values of W . This is illustrated in Fig. 5.5 B, where we show $\Sigma(x)$ in two dimensions for different values of W . With decreasing W , the shape of $\Sigma(x)$ undergoes a transition from the two dimensional to the one dimensional behavior. This is also the justification for using a two dimensional geometry instead of a three dimensional one when dealing with gradient formation in a narrow sheet containing one cell layer.

Note, that the results found in this section are very general. They do not depend on the choice of the parameters D and k because the non-dimensionalization via $t \rightarrow t/k$ and $x \rightarrow \xi_D x$ of equations (5.5) and (5.6) leads to equations in which only the noise terms depend on selectable parameters. The only parameters determining the results are thus the relative noise strengths σ_D/D , σ_k/k , σ_{j_0}/j_0 or σ_c/c_0 , and the ratio of the diffusion length and the lattice constant ξ_D/a . This feature makes an unbiased comparison of the different space dimensionalities possible.

5.2 Detailed description of morphogen transport with disorder

In this section, we discuss the effects of disorder in the more detailed theoretical description of morphogen gradient formation discussed in chapter 3. We focus on steady state gradients formed by transcytosis. A reasonable approach to describing the disorder due to cell-to-cell variability in the discrete description of morphogen transport (3.1) is to assume that the rates entering the microscopic description are slightly different in different cells and extracellular spaces. While we discussed the origins of this disorder in section 4.2, we focus on the mathematical treatment here.

5.2.1 One dimensional description with receptor kinetics

We assume in the discrete description (3.1) where the receptor production rate is given by (3.2) that all the parameters $\alpha \in \mathcal{M}$ with $\mathcal{M} = \{b_{\text{int}}, b_{\text{ext}}, b_{\text{deg}}, k_{\text{on}}, k_{\text{off}}, e_{\text{deg}}, f_{\text{int}}, f_{\text{ext}}, f_{\text{deg}}, f_{\text{syn}}^0, R_{\text{max}}, p\}$ depend on the lattice site. The α_n are distributed around a mean, $\alpha_n = \alpha^0 + \eta_{\alpha,n}$, with

$\langle \eta_{\alpha,n} \eta_{\beta,k} \rangle = \sigma_\alpha^2 \delta_{nk} \delta_{\alpha\beta}$. This implies that different parameters are uncorrelated which we assume for simplicity. In the one dimensional description we further assume that $b_{\text{int},n}$, $b_{\text{ext},n}$, $b_{\text{deg},n}$, $f_{\text{int},n}$, $f_{\text{ext},n}$, $f_{\text{deg},n}$, $f_{\text{syn},n}^0$, and $R_{\text{max},n}$ are defined at the same location as $S_n^{(i)}$, inside the cell, and that $k_{\text{on},n}$, $k_{\text{off},n}$, $e_{\text{deg},n}$, and p_n are defined at the same location as L_n , in the gap between two cells, see Fig. 4.3 for an illustration. We use case B discussed above to describe the fluctuations of the extracellular diffusion coefficient. In the transcytosis dominated limit, it is possible to derive an effective transport equation for transcytosis with disorder by treating the space-dependent rates in the same way as the concentrations in the derivation shown in section 3.1.2. This treatment is valid if the noise amplitudes are small, i.e. $\sigma_\alpha \ll \alpha^0$ for $\alpha \in \mathcal{M}$. It results in a different transport equation:

$$\begin{aligned} \partial_t \lambda &= \partial_x \left(D_\lambda(\lambda, \rho) \partial_x \lambda + D_\rho(\lambda, \rho) \partial_x \rho + \sum_{\alpha \in \mathcal{M}} F_\alpha(\lambda, \rho) \partial_x \alpha \right) - k_\lambda(\lambda, \rho) \lambda \\ \partial_t \rho &= \nu_{\text{syn}}(\lambda, \rho) - k_\rho(\lambda, \rho) \rho, \end{aligned} \quad (5.31)$$

where the expressions of D_λ , D_ρ , k_λ , ν_{syn} , and k_ρ are the same as in the description without disorder (3.12, 3.13) as shown in (D.1). However, they implicitly depend on x through the x -dependent parameters $\alpha(x)$, with $\alpha \in \mathcal{M}$. Compared to the transport equation for λ without disorder (3.12), additional terms appear in the ligand current in (5.31) that involve functions F_α . Explicit expressions of the F_α for all parameters $\alpha \in \mathcal{M}$ follow from the derivation of (5.31). The F_α are identical to zero for $\alpha \in \{b_{\text{deg}}, e_{\text{deg}}, f_{\text{deg}}, f_{\text{syn}}, R_{\text{max}}\}$. General properties for all the other F_α are $F_\alpha \propto \lambda$ for small and $F_\alpha \sim \lambda^{-3}$ for large λ .

The continuum limit of the noise correlators is $\langle \eta_\alpha(x) \eta_\beta(x') \rangle = \sigma_\alpha^2 a \delta(x - x') \delta_{\alpha\beta}$. For a fixed current j_0 of ligands into the system at $x = 0$, the boundary condition

$$\left(D_\lambda(\lambda, \rho) \partial_x \lambda + D_\rho(\lambda, \rho) \partial_x \rho + \sum_{\alpha \in \mathcal{M}} F_\alpha(\lambda, \rho) \partial_x \alpha \right) \Big|_{x=0} = -j_0 - \chi \quad (5.32)$$

has to be satisfied. Here, χ is a stochastic variable describing the fluctuations of j_0 .

There are several striking differences between this problem and the simple diffusion model with disorder discussed in section 5.1.2. Firstly, the differential equations describing transcytosis in a disordered system are nonlinear. Secondly, well-defined correlations between the effective diffusion coefficient and the effective degradation rate arise in general because both depend on the rates describing transcytosis. For example, a fluctuation of the internalization rate b_{int} at a position x leads to a correlated modification of both D_λ and k at x . Thirdly, we see that additional terms in the ligand current, namely the F_α , appear that are important for the results even in the linear regime of small ligand concentrations. Consequently, it is worthwhile to investigate the effects of disorder on the steady state gradients formed by transcytosis. The differences in comparison to the simple diffusion model from section 5.1.2 are of particular interest.

Using our discrete description of morphogen transport with disorder, we have numerically calculated the normalized standard deviation $\Sigma(x)$ for a parameter choice in the transcytosis regime and one in the diffusion regime. The results are shown in Fig. 5.6. We support these numerical data by analytical results in the next section.

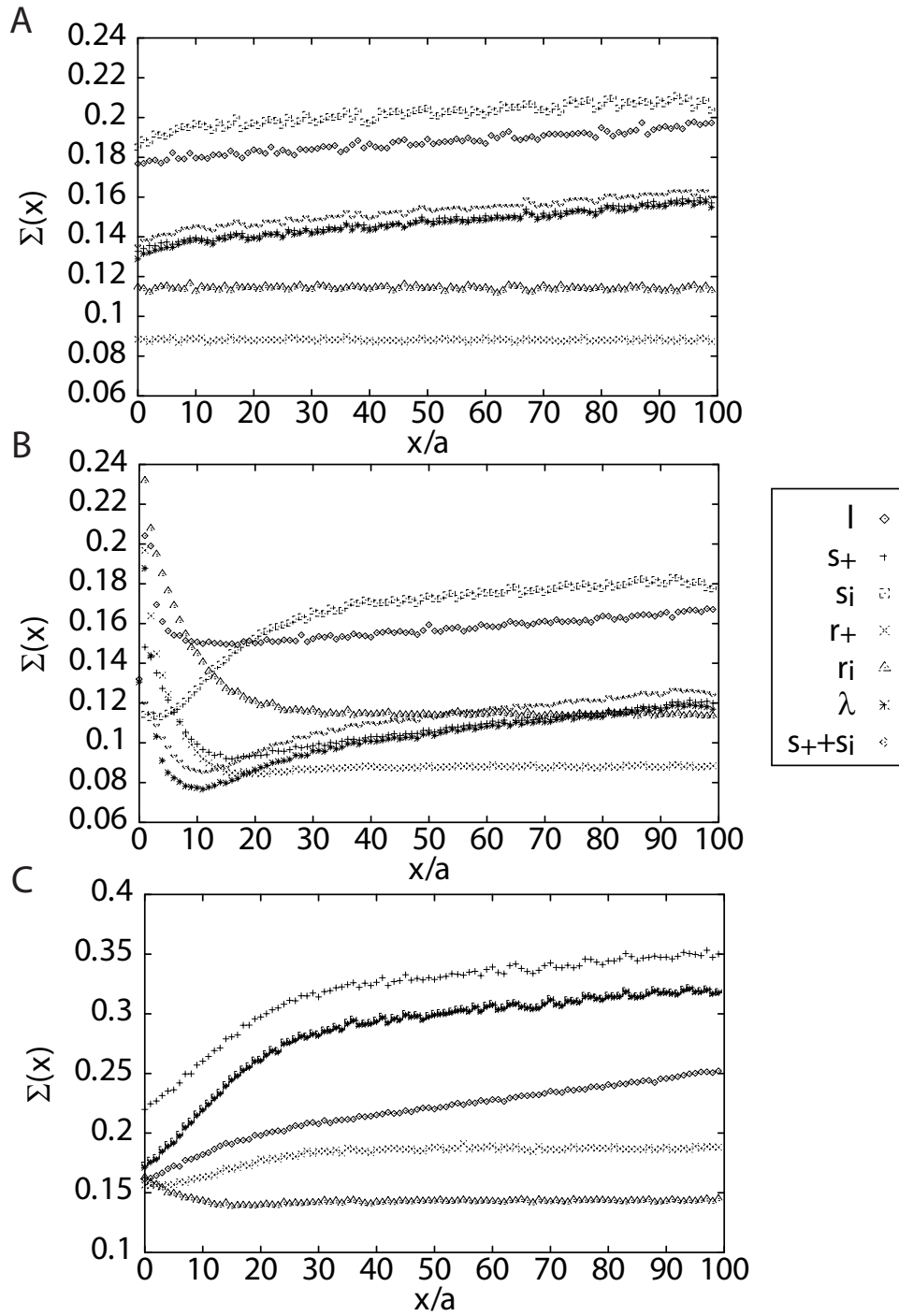


Figure 5.6: Normalized standard deviation $\Sigma(x)$ for morphogen gradients formed in one dimension. $\Sigma(x)$ was numerically calculated using the one dimensional description of morphogen transport with receptor kinetics (3.1). (A,B) $\Sigma(x)$ for the different quantities l , $s+$, s_i , $r+$, r_i , and λ as shown in the key for parameters in the transcytosis regime with $\nu/R_0 b_{\text{deg}} \ll 1$ (A) and $\nu/R_0 b_{\text{deg}} = 13.3$ (B) which leads to a steady state that is strongly affected by the nonlinearity of the description. (C) Like A and B but with parameters in the diffusion regime and $\nu/R_0 b_{\text{deg}} = 207$. Parameters are as shown in Table 2.1 with $k_{\text{on}} R_0 = 20 \text{min}^{-1}$ in the transcytosis and $k_{\text{on}} R_0 = 2.4 \text{min}^{-1}$ in the diffusion regime. R_0 denotes the steady state concentration of surface receptors in the absence of ligand. In the calculations, all parameters $\alpha \in \mathcal{M}$ of the description are fluctuating with $\sigma_\alpha/\alpha^0 = 0.1$. A Gaussian distribution was used for the noise terms.

5.2.2 One dimensional description with constant surface receptor approximation

For the sake of simplicity, we restrict the discussion to the case of the constant surface receptor approximation in the following. Here, (5.31) reduces to

$$\partial_t \lambda = \partial_x \left(D(\lambda) \partial_x \lambda + \sum_{\alpha \in \mathcal{M}_c} F_\alpha(\lambda) \partial_x \alpha \right) - k(\lambda) \lambda, \quad (5.33)$$

where $\mathcal{M}_c = \{b_{\text{int}}, b_{\text{ext}}, k_{\text{on}}, k_{\text{off}}\}$ and the explicit expressions for $D(\lambda)$ and $k(\lambda)$ are the same as in (3.16) with space-dependent parameters $\alpha(x)$ for $\alpha \in \mathcal{M}_c$. Explicit expressions for the functions $F_\alpha(\lambda)$ are given in (D.2) in the appendix. The behavior of these functions $F_\alpha(\lambda)$ for large and small λ is identical to that of the $F_\alpha(\lambda, \rho)$ which appear in (5.31) as discussed in the previous section. Note, that we have kept the constant total surface receptor concentration R as a non-fluctuating parameter. The boundary condition (5.32) at $x = 0$ simplifies to

$$\left(D(\lambda) \partial_x \lambda + \sum_{\alpha \in \mathcal{M}_c} F_\alpha(\lambda) \partial_x \alpha \right) \Big|_{x=0} = -j_0 - \chi. \quad (5.34)$$

Assuming that the noise amplitudes are small, i.e. $\sigma_\alpha \ll \alpha^0$ for all $\alpha \in \mathcal{M}_c$, one can perturbatively solve this nonlinear equation as for the simple diffusion models discussed in section 5.1. To do that, we decompose $\alpha(x) = \alpha^0 + \epsilon \eta_\alpha(x)$ and expand the coefficients

$$\begin{aligned} D(\lambda) &= D^0(\lambda) + \epsilon \sum_{\alpha \in \mathcal{M}_c} (\partial_\alpha D^0(\lambda)) \eta_\alpha(x) + O(\epsilon^2) \\ k(\lambda) &= k^0(\lambda) + \epsilon \sum_{\alpha \in \mathcal{M}_c} (\partial_\alpha k^0(\lambda)) \eta_\alpha(x) + O(\epsilon^2) \\ F_\alpha(\lambda) &= F_\alpha^0(\lambda) + O(\epsilon), \end{aligned} \quad (5.35)$$

where we have introduced the short notation $D^0(\lambda) = D(\lambda)|_{\eta_\alpha=0}$ for all $\alpha \in \mathcal{M}$ and accordingly for $k^0(\lambda)$ and $F_\alpha^0(\lambda)$. Note, that $D^0(\lambda)$ and $k^0(\lambda)$ are exactly the same functions as $D(\lambda)$ and $k(\lambda)$ in (3.16) respectively. Using this, we obtain the steady state equation

$$\partial_x D^0(\lambda) \partial_x \lambda - k^0(\lambda) \lambda + \epsilon \sum_{\alpha \in \mathcal{M}_c} [\partial_x (\partial_\alpha D^0(\lambda) \eta_\alpha(x) \partial_x \lambda + F_\alpha^0(\lambda) \partial_x \eta_\alpha(x)) - \partial_\alpha k^0(\lambda) \eta_\alpha(x) \lambda] = 0. \quad (5.36)$$

The ansatz $\lambda(x) = \lambda_0(x) + \epsilon \lambda_1(x) + \epsilon^2 \lambda_2(x) + \dots$ yields the equation without disorder (3.16) for $\lambda_0(x)$. The solution for λ_0 is the same as in the absence of disorder which is given by (3.24) and (3.25). To $O(\epsilon^1)$, we obtain the equation for $\lambda_1(x)$:

$$\begin{aligned} &\partial_x D^0(\lambda_0) \partial_x \lambda_1 - k^0(\lambda_0) \lambda_1 + \partial_x D^{0'}(\lambda_0) (\partial_x \lambda_0) \lambda_1 - k^{0'}(\lambda_0) \lambda_0 \lambda_1 \\ &= - \sum_{\alpha \in \mathcal{M}_c} [\partial_x (\partial_\alpha D^0(\lambda_0) \eta_\alpha(x) \partial_x \lambda_0 + F_\alpha^0(\lambda_0) \partial_x \eta_\alpha(x)) - \partial_\alpha k^0(\lambda_0) \eta_\alpha(x) \lambda_0], \end{aligned} \quad (5.37)$$

where $D^{0'}(\lambda_0) = \partial_\lambda D^0(\lambda)|_{\lambda=\lambda_0(x)}$ and accordingly for $k^{0'}(\lambda_0)$. At $x = 0$, λ_1 must satisfy the boundary condition

$$\left(D^0(\lambda_0) \partial_x + D^{0'}(\lambda_0) \lambda_0' \right) \lambda_1 \Big|_{x=0} = - \left[\chi + \sum_{\alpha \in \mathcal{M}_c} (F_\alpha^0(\lambda_0(0)) \eta_\alpha'(0) + \partial_\alpha D^0(\lambda_0(0)) \eta_\alpha(0) \lambda_0'(0)) \right].$$

Note, that the linear operator $\mathcal{L}(x) = \partial_x D^0(\lambda_0) \partial_x - k^0(\lambda_0) + \partial_x D^{0'}(\lambda_0) (\partial_x \lambda_0) - k^{0'}(\lambda_0) \lambda_0$ acting on λ_1 on the left side of (5.37) is x -dependent through $\lambda_0(x)$ which makes an analytical calculation of its Green's function impossible. Using the condition $\mathcal{L}(x) G_+(x, x') = \delta(x - x')$ with $\partial_x G_+(x, x')|_{x=0} = 0$, one could numerically calculate the Green's function $G_+(x, x')$ and use the Green's function method as above to calculate the variance $\langle \lambda_1(x)^2 \rangle$.

Linear regime In order to obtain analytical results, we now study the steady state of (5.33) for small λ . In this case, we can approximate (5.36) as

$$D^0(0)\partial_x^2\lambda - k^0(0)\lambda + \epsilon \sum_{\alpha \in \mathcal{M}_c} [\partial_x (\partial_\alpha D^0(0)\eta_\alpha \partial_x \lambda + F_\alpha^{0'}(0)\lambda \partial_x \eta_\alpha) - \partial_\alpha k^0(0)\eta_\alpha \lambda] = 0,$$

where we have kept the leading order term $F_\alpha^{0'}(0)\lambda = (\partial_\lambda F_\alpha^0(\lambda)|_{\lambda=0})\lambda$. In this linear approximation, the Green's function $G_+(x, x')$ can be calculated analytically because the linear operator acting on λ_1 is no longer x -dependent as it was in (5.36). In fact, the operator $(D^0(0)\partial_x^2 - k^0(0))$ and the corresponding Green's function $G_+(x, x')$ are the same as for the simple diffusion model with disorder in 5.1.2 if we identify $D = D^0(0)$ and $k = k^0(0)$.

Applying the perturbative approach as above, we find $\lambda_0(x) = \lambda_0^0 \exp(-x/\xi)$ with $\xi = (D^0(0)/k^0(0))^{1/2}$ and $\lambda_0^0 = j_0(D^0(0)k^0(0))^{-1/2}$. The equation for $\lambda_1(x)$ reads

$$\begin{aligned} & (D^0(0)\partial_x^2 - k^0(0)) \lambda_1 \\ &= - \sum_{\alpha \in \mathcal{M}_c} [\partial_x (\partial_\alpha D^0(0)\eta_\alpha(x) \partial_x \lambda_0 + F_\alpha^{0'}(0)\lambda_0(x) \partial_x \eta_\alpha(x)) - \partial_\alpha k^0(0)\eta_\alpha(x)\lambda_0(x)], \end{aligned}$$

and for the boundary condition of λ_1 at $x = 0$, we find:

$$\lambda_1'(0) = -D^0(0)^{-1} \left(\chi + \sum_{\alpha \in \mathcal{M}_c} (F_\alpha^{0'}(0)\lambda_0(0)\eta_\alpha'(0) + \partial_\alpha D^0(0)\eta_\alpha(0)\lambda_0'(0)) \right). \quad (5.38)$$

Consequently, the solution $\lambda_1(x)$ for $x \geq 0$ reads

$$\begin{aligned} \lambda_1(x) &= -G_+(x, 0)\chi + \sum_{\alpha \in \mathcal{M}_c} \int_0^\infty dx' \eta_\alpha(x') \left(\partial_\alpha D^0(0) (\partial_{x'} \lambda_0(x')) \partial_{x'} G_+(x, x') \right. \\ &\quad \left. + G_+(x, x') \partial_\alpha k^0(0)\lambda_0(x') - F_\alpha^{0'}(0)\partial_{x'} \lambda_0(x') \partial_{x'} G_+(x, x') \right), \end{aligned} \quad (5.39)$$

where we have integrated by parts twice and made use of $\partial_{x'} G_+(x, x')|_{x'=0} = 0$. From (5.39), the variance $\langle \lambda_1(x)^2 \rangle$ can be calculated:

$$\begin{aligned} \langle \lambda_1(x)^2 \rangle &= \sigma_{j_0}^2 G_+(x, 0)^2 + a \sum_{\alpha \in \mathcal{M}_c} \int_0^\infty dx' \sigma_\alpha^2 \left(\partial_\alpha D^0(0) (\partial_{x'} \lambda_0(x')) \partial_{x'} G_+(x, x') \right. \\ &\quad \left. + G_+(x, x') \partial_\alpha k^0(0)\lambda_0(x') - F_\alpha^{0'}(0)\partial_{x'} \lambda_0(x') \partial_{x'} G_+(x, x') \right)^2, \end{aligned} \quad (5.40)$$

where we have used $\langle \eta_\alpha(x)\eta_\beta(x') \rangle = \sigma_\alpha^2 a \delta(x-x')\delta_{\alpha\beta}$. Note, that the integral in (5.40) depends on $\partial_{x'} G_+(x, x')|_{x'=x}$ the value of which was discussed in section 5.1.2. We can now calculate the normalized standard deviation $\Sigma_\lambda(x) = \sqrt{\langle \lambda_1(x)^2 \rangle} / \lambda_0(x)$ from (5.40). The explicit result is shown in (D.3) in the appendix. For large x , the asymptotic behavior of Σ_λ is

$$\Sigma_\lambda(x)^2 \approx \sum_{\alpha \in \mathcal{M}_c} \frac{\sigma_\alpha^2 a}{4D^0(0)^3 k^0(0)} (D^0(0)\partial_\alpha k^0(0) - k^0(0)\partial_\alpha D^0(0))^2 x,$$

i.e. we find the \sqrt{x} -increase for large x as for the simple diffusion model. This asymptotic behavior is also valid for the nonlinear problem (5.37).

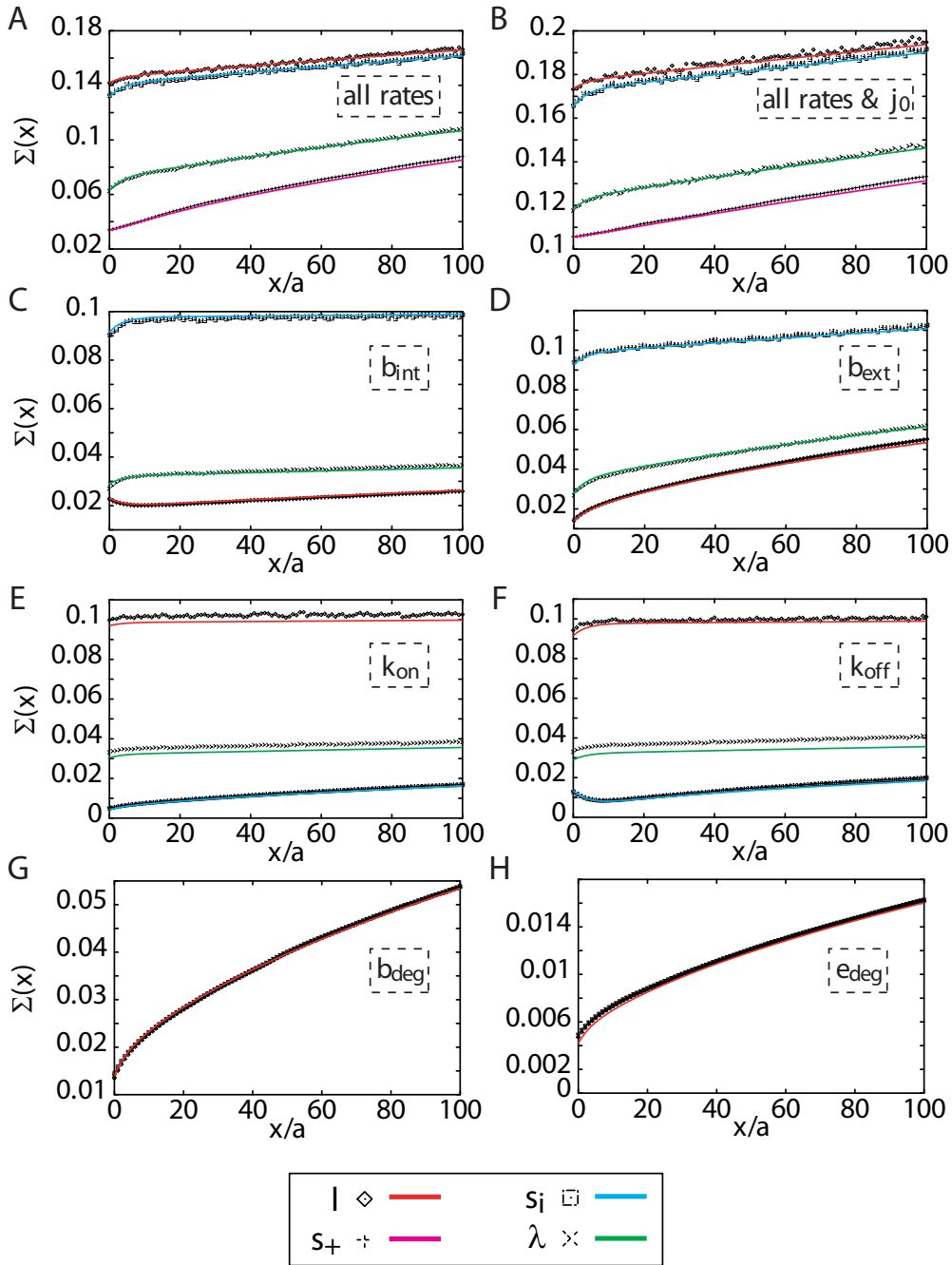


Figure 5.7: Normalized standard deviation $\Sigma(x)$ for morphogen gradients formed by transcytosis in one dimension. $\Sigma(x)$ for the different quantities l , s_+ , s_i , and λ was calculated numerically using the one dimensional description of morphogen transport with constant surface receptor approximation (3.3) with disorder, see main text. The results are shown by symbols and compared to the corresponding analytical results following from (5.40) and (5.41) which are shown by lines. The morphogen production rate $\nu/Rb_{\text{deg}} \ll 1$ for all calculations so that the linear approximation is valid. (A) Normalized standard deviation $\Sigma(x)$ if the rates b_{int} , b_{ext} , k_{on} , k_{off} , b_{deg} , and e_{deg} are all fluctuating. (B) Like A but with the current at the boundary j_0 also fluctuating. (C-H) $\Sigma(x)$ if only b_{int} (C), only b_{ext} (D), only k_{on} (E), only k_{off} (F), only b_{deg} (G), and only e_{deg} is fluctuating (E) respectively. In C-F, the magenta lines are covered by the red lines (C and D) or the blue lines (E and F). In G and H, all lines are on top of each other. Parameters are $b_{\text{int}}^0 = b_{\text{ext}}^0 = k_{\text{on}}^0 R = k_{\text{off}}^0$ with $b_{\text{int}}^0/b_{\text{deg}}^0 = 600$, $e_{\text{deg}}^0/b_{\text{deg}}^0 = 0.3$, $p^0 = 0$, and $\sigma_{j_0}/j_0 = \sigma_\alpha/\alpha^0 = 0.1$ for all $\alpha \in \mathcal{M}_c$.

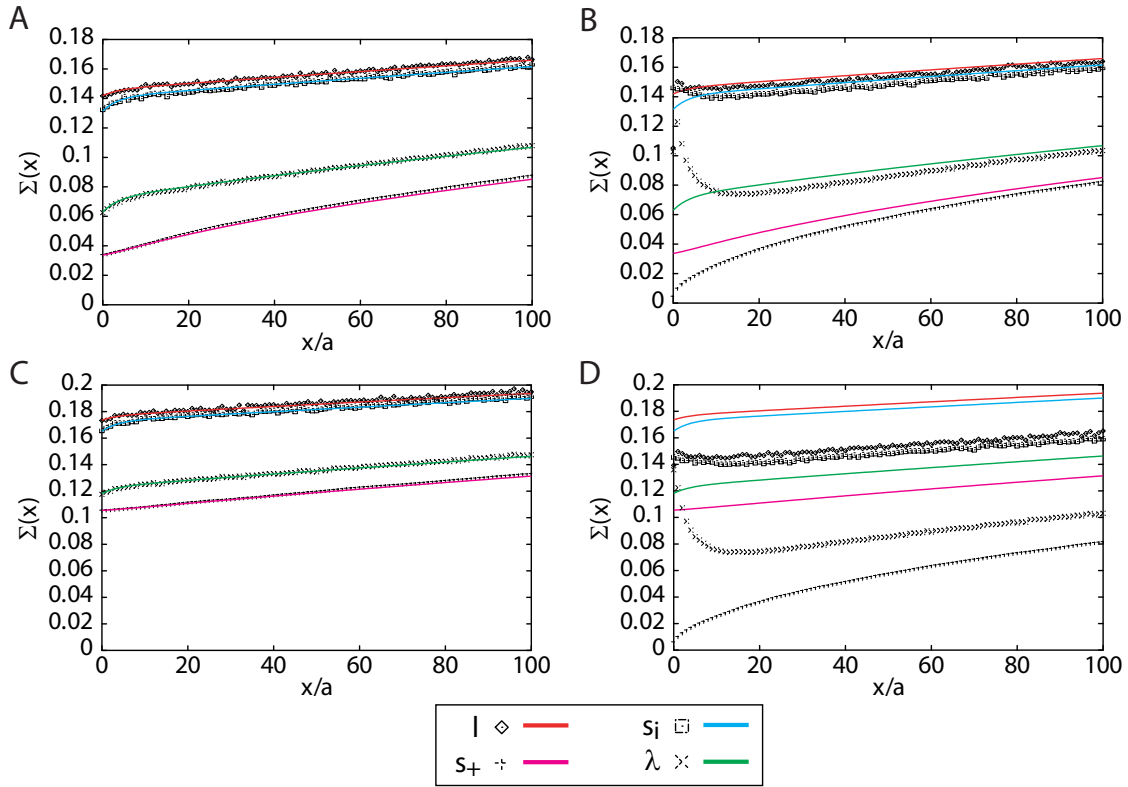


Figure 5.8: Impact of fluctuations of the current at the boundary on the normalized standard deviation $\Sigma(x)$ for morphogen gradients formed by transcytosis in one dimension in the linear and in the nonlinear regime. The symbols show $\Sigma(x)$ for the different quantities l , s_+ , s_i , and λ calculated numerically using the one dimensional description of morphogen transport with constant surface receptor approximation (3.3) with disorder. The analytical results for the linear regime following from (5.40) and (5.41) are shown by lines. (A,B) Normalized standard deviation $\Sigma(x)$ if the rates b_{int} , b_{ext} , k_{on} , k_{off} , b_{deg} , and e_{deg} are all fluctuating for $\nu/Rb_{\text{deg}} \ll 1$ which is in the linear regime (A) and for $\nu/Rb_{\text{deg}} = 40$ which is in the nonlinear regime (B). (C,D) Like A,B but with the current at the boundary j_0 also fluctuating. Parameters as in Fig. 5.7.

5.2.3 Fluctuations of microscopic quantities

We can further use the result for the variance of the total ligand concentration λ to calculate the variances of the microscopic quantities in the description of transcytosis, i.e. the free ligand concentration $l(x)$, the surface bound ligand concentration $s_+(x)$, and the internal bound ligand concentration $s_i(x)$ separately. These are related to each other via the adiabatic approximation (3.11). For the quantity $q \in \{l, s_+, s_i\}$, we denote the first order correction of $q(x)$ by $q_1(x)$. For small λ , the relations $q(\lambda)$ which follow from the adiabatic approximation (3.11) can be approximated as $q(\lambda) \approx (\partial_\lambda q|_{\lambda=0})\lambda = q^{0'}\lambda$. The first order correction $q_1(x)$ is then

$$q_1(x) = q^{0'}\lambda_1(x) + \sum_{\alpha \in \mathcal{M}_c} (\partial_\alpha q^{0'})\lambda_0(x)\eta_\alpha(x),$$

which leads to the variance

$$\langle q_1(x)^2 \rangle = (q^{0'})^2 \langle \lambda_1(x)^2 \rangle + \sum_{\alpha \in \mathcal{M}_c} (\sigma_\alpha^2 (\partial_\alpha q^{0'})^2 \lambda_0(x)^2 + 2q^{0'} (\partial_\alpha q^{0'}) \lambda_0(x) \langle \lambda_1(x) \eta_\alpha(x) \rangle). \quad (5.41)$$

The variance of all $q \in \{l, s_+, s_i\}$ can be calculated using (5.41) and (5.39).

We have again performed numerical calculations to verify these results. For each situation, between 20,000 and 100,000 steady state gradients were calculated for different realizations of the disorder using Gaussian distributions for the random variables. It is straightforward to calculate the normalized standard deviation from these. A comparison of the numerically calculated normalized standard deviation to the analytic result following from (5.40) and (5.41) is shown in Fig. 5.7. We also show numerical results in the nonlinear regime in Fig. 5.8. We see that in the nonlinear regime, the uncertainty of λ caused by the fluctuations of the current at the boundary are strongly reduced. Moreover, the shape of the curves $\Sigma_q(x)$ is affected differently for the different quantities q in the proximity of the source boundary.

5.2.4 Two dimensional description

In principle, one can generalize the analytical treatment to the two dimensional situation. For the description of transcytosis with disorder in the constant surface receptor approximation, the same symmetry considerations as used in section 3.2.2 can be applied to derive the general form of the two dimensional equation from (5.33). The result is

$$\partial_t \lambda = \nabla \cdot \left(D(\lambda) \nabla \lambda + \sum_{\alpha \in \mathcal{M}_c} F_\alpha(\lambda) \nabla \alpha \right) - k(\lambda) \lambda,$$

where the coefficient functions $D(\lambda)$, $k(\lambda)$, and $F_\alpha(\lambda)$ have to be calculated for the two dimensional lattice structure used.

In Fig. 5.9, we show the results of numerical calculations based on the discrete two dimensional description on a triangular lattice as defined in section 3.2.2. The disorder is introduced analogously to the one dimensional case. These calculations were done in the linear regime where λ is small and most receptors are unoccupied. As in the case of the simple diffusion models, we find that the uncertainty of λ is smaller in two dimensions than in one dimension for the same parameter choice and increases more slowly with increasing x . Asymptotically, the normalized standard deviation $\Sigma(x)$ grows again as $x^{1/4}$.

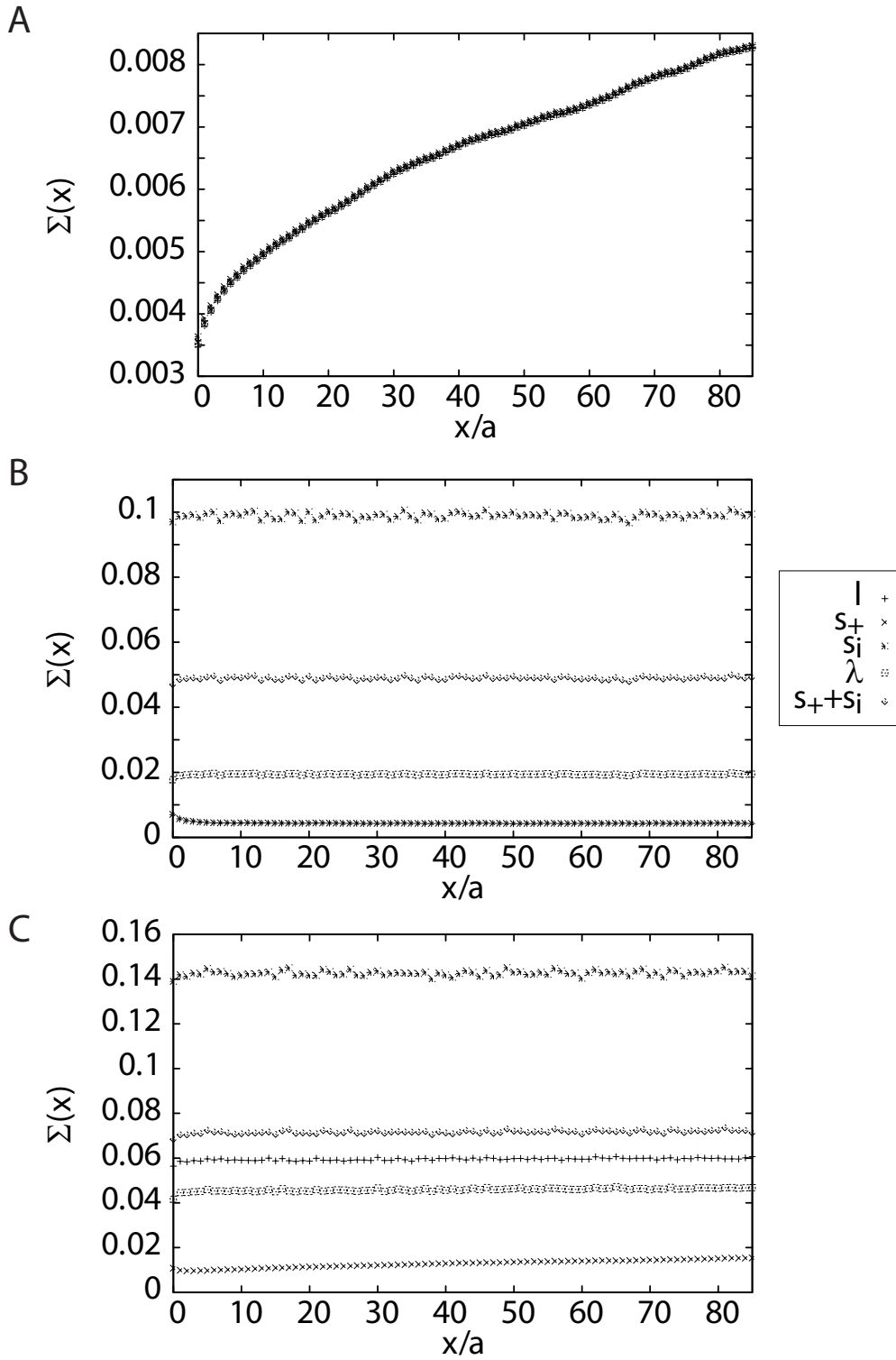


Figure 5.9: Normalized standard deviation of gradients formed by transcytosis in two dimensions. $\Sigma(x)$ for the different quantities l , s_+ , s_i , λ and $s_+ + s_i$ was calculated numerically using the two dimensional description of morphogen transport with constant surface receptor approximation (3.19) with disorder, see main text. The morphogen production rate $\nu/Rb_{\text{deg}} \ll 1$ for all calculations. (A-C) Normalized standard deviation $\Sigma(x)$ if only the degradation rate b_{deg} is fluctuating (A), if only the internalization rate b_{int} is fluctuating (B), and if the rates b_{int} , b_{ext} , k_{on} , k_{off} , b_{deg} , and e_{deg} are all fluctuating (C). Note the slower increase of $\Sigma(x)$ with increasing x in comparison to the one dimensional case shown in Fig. 5.7. Parameters as in Fig. 5.7.

Chapter 6

Summary and outlook

In this work, we theoretically investigated morphogen transport and gradient formation by extracellular diffusion and transcytosis. The most important results of this investigation were presented in chapters 2 and 4. In chapter 2, we related a theoretical description of morphogen transport which we have developed to experimental data for the morphogen Dpp which acts in the *Drosophila* wing disk. In chapter 4, the implications of a detailed theoretical analysis for the robustness and precision of steady state morphogen gradients were presented and discussed.

Comparison to experiments on Dpp in the *Drosophila* wing disk In section 2.2, we introduced key experiments that were performed to study the impact of endocytosis on the transport of the morphogen Dpp in the wing disk. In the “shibire rescue assay”, endocytosis is blocked in all cells of the target tissue but not in the source cells while in the “shibire clone assay”, endocytosis is only blocked in a relatively small patch of mutant cells in the target tissue. In the shibire rescue assay, the concentration of Dpp is strongly reduced in the target tissue after several hours and in the shibire clone assay, a depletion of Dpp is observed in and behind the patch of mutant cells, see Fig. 1.4. The outcome of both experiments suggests a role of endocytosis in Dpp transport [34, 33] but, due to the complexity of the system, commonsense is insufficient to draw serious conclusions from the data [60, 59].

In order to address the unsolved question how morphogens like Dpp are transported in developing tissues, we performed a quantitative comparison of results obtained from our theoretical description of morphogen transport to these experimental data. Two different parameter sets were used in this comparison: one for which transport is dominated by passive diffusion in the extracellular space and another one for which morphogen transport is dominantly due to transcytosis. In the latter case, the extracellular diffusion coefficient D_0 is very small which can occur if the morphogen molecules bind to the cell membranes, cell surface molecules, and extracellular matrix components. This can strongly reduce their ability to move rapidly through the extracellular space. Since the parameters entering our description have so far not been measured in experiments, we chose their values within plausible limits and in order to get the best possible agreement with the experimental data.

For the parameter set that leads to transport dominantly due to transcytosis, the results obtained from calculations which correspond to the experimental setups mentioned above are in semi-quantitative agreement with the observations that were made in the experiments, see Fig. 2.4 and 2.6. We further showed that a parameter set for which extracellular diffusion dominates morphogen transport leads to results that are inconsistent with some of the experimental data. Most notably, we found a strong accumulation of cell surface receptors and extracellular morphogens in cells in which endocytosis is blocked in the numerical calculations, see Fig. 2.9 and 2.10, while no such accumulation of comparable magnitude could be observed

in experiments [59]. Some of our results are at odds with previous theoretical findings on Dpp gradient formation by extracellular diffusion [60]. The origins of this discrepancy are due to technical and conceptual shortcomings in [60] that are carefully discussed in [59] and chapter B of the appendix.

Theoretical description of morphogen transport In section 3.1.1, we presented a microscopic description of morphogen transport in which cells are discrete entities. This description captures key processes like the diffusion of morphogens in the extracellular space, binding and un-binding of the morphogens to and from receptor molecules that are located on the cell surfaces, internalization of these receptor-ligand complexes into the cell and their subsequent externalization, see Fig. 3.1. Moreover, the production and intracellular trafficking of receptor molecules by the cells is included in the description. We were able to show that this microscopic description is well approximated by a set of two nonlinear transport equations (3.12, 3.13) for the total morphogen concentration and the total receptor concentration if transport is dominated by transcytosis, see section 3.1.2. The effective diffusion coefficient that characterizes morphogen transport by transcytosis in these equations is concentration dependent. In the different limit in which transport is dominated by extracellular diffusion, the microscopic description is well approximated by a set of nonlinear reaction-diffusion equations, see section 3.4.

Robustness of morphogen gradients In the limit of our description in which morphogen transport is dominated by transcytosis, we were able to analytically calculate the steady state solution which corresponds to the morphogen gradient in biological systems. Investigating this analytic solution, we uncovered a remarkable property of morphogen gradients formed by transcytosis. If the ligand current j_0 imposed at the source boundary which is proportional to the morphogen secretion rate of the morphogen source cells is sufficiently large, these gradients are insensitive to relatively large changes of this secretion rate. In fact, the secretion rate can be increased by 100% and more without significantly changing the distance x to the source at which a certain concentration of the morphogen is present. This robustness of the gradients is independent of the specific values of the parameters entering the description. It is rather due to a characteristic asymptotic power-law behavior of the concentration-dependence of the effective diffusion coefficient which characterizes morphogen transport by transcytosis. This nonlinearity results from the effects of receptor saturation at high morphogen concentrations and leads to a formal singularity (3.26) of the morphogen concentration in steady state. This singularity constitutes the origin of the observed robustness, see section 4.1. We further demonstrated that the presence of extracellular diffusion reduces the robustness that is ultimately lost if the typical length over which a morphogen molecule can move through the extracellular space by diffusion exceeds one cell diameter, see Fig. 4.1 and 4.2.

Robustness is important for the reliable patterning of tissues by morphogen gradients during development. In the case of Dpp in the wing disk, indications for the type of robustness we studied here were indeed observed in experiments [71]. Different mechanisms that lead to robustness were previously discussed for other morphogens and different systems [28, 29]. It was shown that if transport is dominated by extracellular diffusion, a nonlinear extracellular ligand degradation rate can increase robustness [29]. However, there is no direct experimental evidence for such behavior in the case of Dpp, which is why we have kept the extracellular degradation term linear in our theoretical description.

Precision of morphogen gradients In section 4.2, we discussed the precision with which morphogen gradients can define concentration thresholds at a given distance to the morphogen

source in the target tissue. In the absence of other potential mechanisms to accurately pattern the developing tissue in a well-defined way, a high precision of the morphogen gradient is needed. In biological systems, morphogen molecule number fluctuations and the disorder due to the cell-to-cell variability affect morphogen gradient formation and reduce precision. In this work, we assumed that the disorder has a dominant impact and neglected effects due to the finite morphogen molecule numbers.

In a simple model of morphogen gradient formation by extracellular diffusion (4.3), the disorder in the system can be captured by a spatially fluctuating effective diffusion coefficient and degradation rate. Here the fluctuations of the diffusion coefficient are due to fluctuations of the properties of the extracellular space. For example, the concentration of extracellular matrix components which the morphogens can bind to may fluctuate as a function of the position in the tissue, see Fig. 4.4 B. Moreover, the disordered cell arrangement leads to fluctuation of the effective diffusion coefficient, see Fig. 4.4 A. Similarly, fluctuations of the effective degradation rate are due to fluctuations in the concentrations of molecules like extracellular proteases that play a role in morphogen degradation. In this simple model, we were able to analytically calculate how the uncertainty of the local morphogen concentration in the steady state gradient behaves as a function of the distance to the morphogen source. This uncertainty or imprecision is measured by the normalized standard deviation $\Sigma(x)$ of the morphogen concentration at x . The imprecision usually increases with increasing distance to the source. It was shown that the precision increases drastically with increasing space dimensionality of the system in which the gradient is formed, see Fig. 5.5. For large x , the uncertainty of the concentration increases in a way that is characteristic of the space dimensionality d of the system: $\Sigma(x) \sim x^\phi$ with $\phi = (3 - d)/4$ for $d < 3$. We have identified $d = 3$ as the upper critical dimension beyond which the fluctuations in the system become irrelevant. We also demonstrated that correlations between the fluctuations of the effective diffusion coefficient and those of the effective degradation rate can strongly increase the precision of the gradient, see Fig. 4.6 B. Moreover, we found that fluctuations of the morphogen secretion rate of the source cells usually contribute strongly to the imprecision of the gradient in the proximity of the morphogen source.

Furthermore, we numerically investigated the effects of disorder in our detailed description of morphogen transport. Here, the disorder is due to cell-to-cell variability and captured by fluctuations of the parameters entering the description. For the same relative amplitude of the fluctuations of these parameters, the biologically relevant gradient of receptor-bound morphogens has a higher precision at most positions if transport is dominated by transcytosis than if it is dominated by extracellular diffusion, see Fig. 4.7. While this result may depend on our particular parameter choice, we were able to identify several potential causes of this behavior. Firstly, the robustness of morphogen gradients formed by transcytosis leads to a reduced impact of fluctuations of the morphogen secretion rate of the source cells on the imprecision of the gradient. Secondly, well-defined correlations between the fluctuations of the effective diffusion coefficient characterizing transcytosis and those of the corresponding effective degradation rate arise because the fluctuations of the microscopic parameters describing transcytosis affect both. We argued that for transcytosis and probably also for other active transport processes such correlations occur quite naturally while they are less likely to occur if morphogens are transported by passive diffusion. This implies that active mechanisms can in principle form more precise gradients than passive ones. In addition, we found that for morphogen gradients formed by passive diffusion unlike for those formed by transcytosis, the gradient of the free extracellular morphogen concentration has the highest precision. A high precision of this gradient is useless because the cells do not directly detect the free extracellular morphogen concentration. Only the concentration of morphogens that are bound to a receptor can determine the cell fate.

Discussion While we focused on transcytosis and extracellular diffusion in this work, other mechanisms of cell-to-cell ligand transport can be effectively described by equations (3.12, 3.13) or (3.16) with coefficients whose functional form must be derived from a detailed microscopic description of the transport mechanism using the method exemplified in chapter 3. An example for this is given by the “glypican model” of morphogen transport introduced in section 1.4. We derive an effective transport equation for this model in section A.3 of the appendix.

While our theoretical description of morphogen transport captures the processes that are widely believed to be most relevant in biological systems like the wing disk, it is important to keep in mind that we highly simplified these processes and neglected several additional aspects that could play a role. For example, we disregarded a possible contribution to ligand transport that could result from the diffusion of receptor-bound ligands in the cell membrane. Moreover, we did not account for cell divisions and tissue growth in our description. This is justified because in the case of Dpp, gradient formation occurs on a time scale of eight hours that is shorter than the time scales during which the tissue grows significantly. However, in a more sophisticated description that includes cell divisions, one could study the role of morphogen gradients in the regulation of tissue size. This is an interesting topic because Dpp is known to play a role in growth regulation [40].

More importantly, the presence of different receptor types which is quite common for signaling molecules of the TGF- β superfamily like Dpp was neglected in our description. These receptors can form dimers or other complexes and, in general, the affinity of the ligand is different for these different receptor types and complexes. The trafficking of receptors inside the cell is also more involved than in our description in which it is effectively captured by a few effective parameters. Among other things, only a component of the receptor complex with low ligand affinity could be externalized or the ligand could be separated from the receptor during intracellular trafficking.

In fact, such processes might explain why the rate k_{off} of ligand un-binding from the receptor which we need in the transcytosis regime to obtain results that are consistent with the time scales of gradient formation observed in experiments is significantly larger than values of k_{off} which are typically measured for TGF- β receptors [106], see Table 2.1. It has also been argued, that endocytosis would be too slow to explain the formation of morphogen gradients by transcytosis on the time scales that are observed in experiments [60]. However, the corresponding rate b_{int} has so far not been measured in the wing disk and the value of b_{int} that is needed in the transcytosis regime to obtain gradient formation over 30 cell diameters within eight hours as observed in the experiments is only one order of magnitude larger than values that have been measured in cultures of cancer cells [61], see Table 2.1. These may have quite different properties than the much smaller cells in the wing disk which might perform endo- and exocytosis faster.

These concerns show that to identify the mechanism by which morphogens are transported, it is of great importance to quantitatively measure the time scales on which the individual microscopic processes entering our description occur. From these, the effective rates used in our theoretical description could be estimated even if the underlying microscopic processes are more complicated. While such measurements may have appeared almost impossible a short time ago, new experimental tools like the photo-activatable green fluorescent protein (PA-GFP) whose fluorescence can be “switched on” as desired by irradiation with a laser beam of 405nm wavelength [79] and two photon microscopy that allows for an activation of intracellular PA-GFP in only one cell or even exclusively in a small region of the extracellular space [20] seem to open the door for these quantitative experiments that might be accomplished within the next few years [78].

To conclude the criticism of the simplifying assumptions made in our theoretical investi-

gation, let us come to the description with disorder. Investigating the precision of morphogen gradients, we have neglected time-dependent disorder due to cell-to-cell variability and possible effects due to the finite morphogen and receptor molecule numbers in our description. Moreover, in the analysis of transcytosis with cell-to-cell variability in section 5.2, we have disregarded possible correlations between the fluctuations of the individual parameters describing the intracellular trafficking. Although it is reasonable to disregard these aspects for simplicity, one could study time-dependent disorder by introducing temporal fluctuations of the rates in the respective microscopic description of morphogen transport. The effects of finite molecule numbers could be studied in a stochastic description based on master equations.

Outlook The analysis of the theoretical description of morphogen transport that was developed in this work lead to several predictions that can be tested in experiments. While some of these require detailed knowledge about the values of the parameters entering the description, several others are independent of these values and rely only on fundamental aspects of the underlying transport mechanisms.

Firstly, one can experimentally test if the GFP-Dpp gradient in the wing disk is robust to changes of the GFP-Dpp secretion rate in the source cells as predicted. While indications for such robustness have been found in previous work [71], it has so far not been observed directly for the morphogen gradient. It is possible to breed *Drosophila* flies that do not express endogenous Dpp but only GFP-Dpp under the control of a thermo-sensitive gene expression system. Keeping these flies at different temperatures at which the production rate and presumably also the secretion rate of GFP-Dpp is different, one could measure the resulting steady state GFP-Dpp gradients. If transcytosis is the dominant transport mechanism, the range of the observed GFP-Dpp gradient should increase going from low to intermediate temperatures where relatively little GFP-Dpp is secreted. Increasing the temperature further so that GFP-Dpp secretion becomes stronger and stronger, the observed change of the GFP-Dpp gradient should decrease until only a small change should be observed when the robust regime is reached. If transport is dominated by extracellular diffusion, this robustness should not be observed unless other mechanisms are at work [29]. Such other mechanisms that lead to robustness even if transport is due to extracellular diffusion could possibly be identified if changes in the receptor profiles were observed [29].

Secondly, the effective diffusion coefficient of GFP-Dpp can be measured in FRAP experiments, see section 2.5. One could photo-bleach GFP in stripes at different distances to the GFP-Dpp source at which the concentrations of GFP-Dpp are different and calculate the apparent diffusion coefficient from the observed recovery. This way, a concentration-dependence of the effective diffusion coefficient could be uncovered. If transport is dominated by transcytosis, our theoretical analysis showed that the effective diffusion coefficient depends on the morphogen concentration and becomes small for large concentrations, see Fig. 3.2. In contrast, one would expect to find an increase of the apparent diffusion coefficient with the morphogen concentration if transport is dominated by extracellular diffusion because for increasing concentrations, the cell surface receptors and other extracellular molecules that the morphogens can bind to, are increasingly occupied so that free morphogen diffusion in the extracellular space is less obstructed. Thus, the identification of a concentration-dependence of the apparent diffusion coefficient can give indications about the underlying transport mechanism.

Furthermore, several results concerning the precision of morphogen gradients could be investigated in experiments. Quantifying the concentration gradients of these molecules via fluorescent labels in many different animals at the same developmental stage under identical conditions, an average concentration gradient and its variance as a function of the distance x to the morphogen source could be calculated. Here, it would be important to average out

fluctuations that occur on a length scale that is smaller than one cell diameter when quantifying the concentration. The normalized standard deviation $\Sigma(x)$ of the morphogen concentration at x could then be calculated from these measurements. In fact, such a measurement was performed for the morphogen Bicoid that acts in the *Drosophila* embryo [54] but unfortunately, the data was not analyzed in a way that would allow for a comparison to our theoretical predictions. To apply our results for gradient formation in disordered systems, one would also have to verify that the fluctuations of the morphogen concentration are due to the disorder and do not result from temporal fluctuations of the morphogen molecule numbers. A possible way of doing this would be to measure these molecule numbers. This way, one could verify that they are relatively large in the region of interest.

According to the results discussed in chapter 5, $\Sigma(x)$ usually increases with increasing distance to the morphogen source. At a larger distance to the source, this increase should follow a power-law characteristic of the dimensionality of the system in which the gradient is formed. However, this behavior may be hard to observe due to the fluctuations of the background fluorescence and finite molecule number effects in the experiments. These may cover the fluctuations of the morphogen concentration caused by the disorder as the morphogen concentration is relatively small far away from the source. In two and three dimensional systems, a decrease of $\Sigma(x)$ with increasing x near the source would be an indication for relatively strong fluctuations of the morphogen secretion rate of the source cells, see Fig. 5.3. Using specific antibody staining protocols, $\Sigma(x)$ could possibly also be measured separately for the gradient of the free morphogen concentration in the extracellular space. If the imprecision of this extracellular morphogen gradient is smaller than that of the total gradient, that would be an indication that extracellular diffusion contributes strongly to transport while a larger uncertainty of the extracellular gradient would suggest that other transport mechanisms like transcytosis dominate, see section 4.2.

In principle, the uncertainty $\Sigma(x)$ could be measured for gradients of several different morphogens that are formed by different mechanisms. This way, one could test the general prediction that the precision of morphogen gradients increases with increasing dimensionality of the structure in which these gradients are formed. While all experiments suggested here are in principle feasible, one must keep in mind that unpredictable technical problems and the limited accuracy of the resulting data could aggravate the test of some of our predictions.

In order to fully exploit the growing possibilities of performing quantitative experiments on morphogen transport and gradient formation, a comparison to a detailed theoretical description of the underlying processes is necessary. Overall, this work demonstrated that theory can help in understanding the implications of experimental data and lead to the suggestion of new experiments in which predictions of the theoretical analysis can be tested.

Appendix A

Generalizations of the description of morphogen transport

In this chapter, we present generalizations of our description of morphogen transport. Firstly, we derive a description for two distinguishable ligand species. Secondly, we investigate the effects of a directional bias. Thirdly, we discuss the effects of diffusion in the cell membrane.

A.1 Two ligand species in the theoretical description of morphogen transport

In this section, we derive the transport equations for a scenario in which two ligand species that can bind to the same receptor are present. This is not merely of academic interest since, in the most important experiments, morphogens are tagged by a fluorescent protein. Often, both tagged and un-tagged (endogenous) morphogens are present in the tissue at the same time. In a typical experimental setup, the un-tagged species is produced at the source and initially distributed in a steady state gradient. The production of the tagged species is switched on at $t = 0$. Afterwards, it begins to partly oust the other species, see also section 2.2. This is a powerful setup for studying gradient formation. However, to avoid a possible misinterpretation of the experimental data caused by effects due to the presence of two different ligand species, a thorough theoretical description must include both ligand species.

Fusing a fluorescent protein to the ligand does not strongly effect its properties. Thus, it can be assumed that the kinetics for both species is described by the same set of parameters. However, the initial and boundary conditions can generally differ for the two species. We denote the quantities involving the un-tagged ligand by an asterisk. It is straightforward to generalize the discrete one dimensional description (3.1) to this situation:

$$\begin{aligned}\partial_t L_n &= k_{\text{off}}(S_n^{(r)} + S_{n+1}^{(l)}) - k_{\text{on}}(R_n^{(r)} + R_{n+1}^{(l)})L_n - e_{\text{deg}}L_n + \frac{p}{2}(L_{n+1} + L_{n-1} - 2L_n) \\ \partial_t L_n^* &= k_{\text{off}}(S_n^{*(r)} + S_{n+1}^{*(l)}) - k_{\text{on}}(R_n^{(r)} + R_{n+1}^{(l)})L_n^* - e_{\text{deg}}L_n^* + \frac{p}{2}(L_{n+1}^* + L_{n-1}^* - 2L_n^*) \\ \partial_t R_n^{(r)} &= \frac{1}{2}f_{\text{syn}} + k_{\text{off}}(S_n^{(r)} + S_n^{*(r)}) - k_{\text{on}}R_n^{(r)}(L_n + L_n^*) - f_{\text{int}}R_n^{(r)} + \frac{1}{2}f_{\text{ext}}R_n^{(i)} \\ \partial_t S_n^{(r)} &= -k_{\text{off}}S_n^{(r)} + k_{\text{on}}R_n^{(r)}L_n - b_{\text{int}}S_n^{(r)} + \frac{1}{2}b_{\text{ext}}S_n^{(i)} \\ \partial_t S_n^{*(r)} &= -k_{\text{off}}S_n^{*(r)} + k_{\text{on}}R_n^{(r)}L_n^* - b_{\text{int}}S_n^{*(r)} + \frac{1}{2}b_{\text{ext}}S_n^{*(i)} \\ \partial_t R_n^{(l)} &= \frac{1}{2}f_{\text{syn}} + k_{\text{off}}(S_n^{(l)} + S_n^{*(l)}) - k_{\text{on}}R_n^{(l)}(L_{n-1} + L_{n-1}^*) - f_{\text{int}}R_n^{(l)} + \frac{1}{2}f_{\text{ext}}R_n^{(i)} \\ \partial_t S_n^{(l)} &= -k_{\text{off}}S_n^{(l)} + k_{\text{on}}R_n^{(l)}L_{n-1} - b_{\text{int}}S_n^{(l)} + \frac{1}{2}b_{\text{ext}}S_n^{(i)}\end{aligned}$$

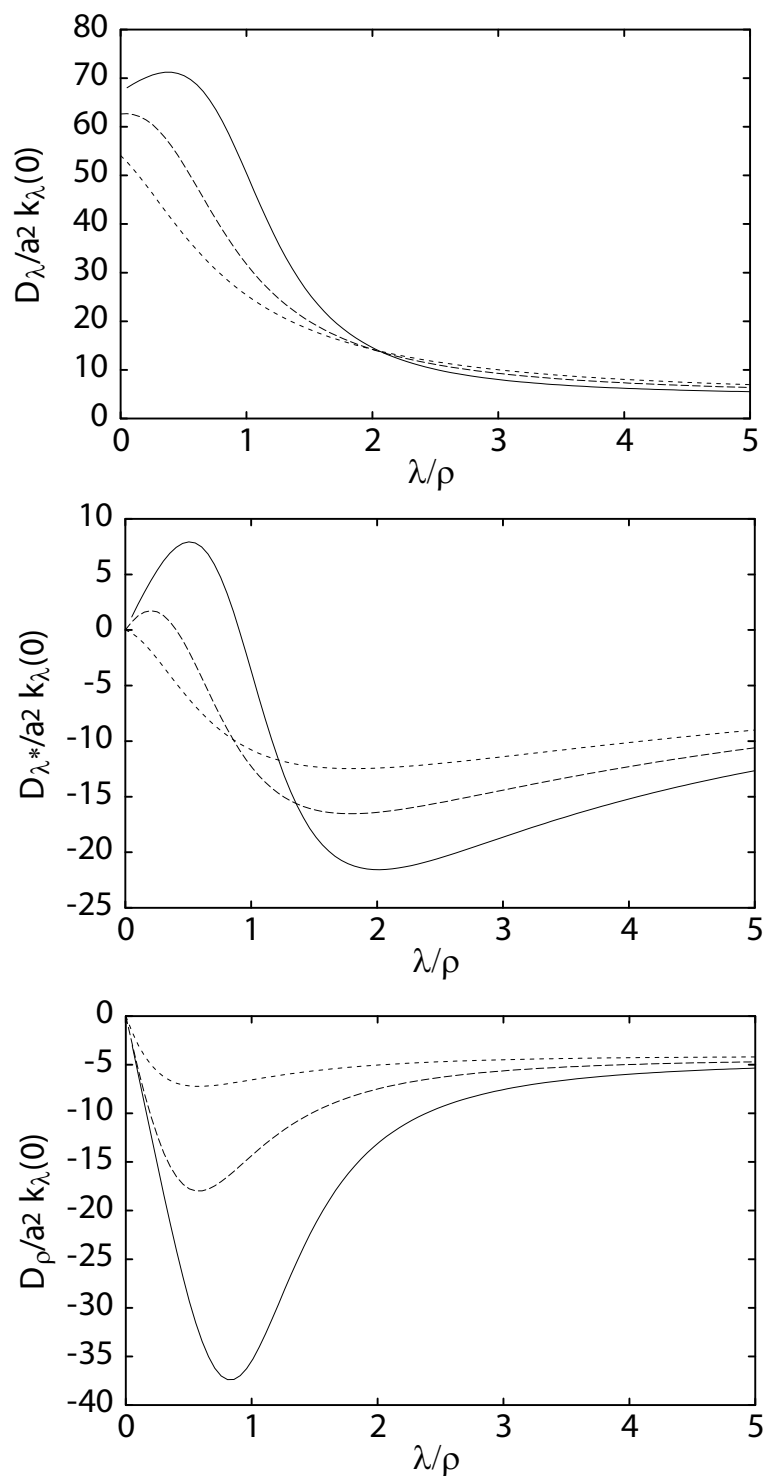


Figure A.1: Coefficients D_λ , D_{λ^*} , and D_ρ in the transport equations (A.5) for two ligand species as a function of the ratio λ/ρ of the total ligand concentration of one species λ and the total receptor concentration ρ . The coefficients are shown for different values of the total concentration of the other ligand species λ^* : for the solid lines $\lambda^* = 0$, for the dashed lines $\lambda^*/\rho = 0.5$, and for the dotted lines $\lambda^*/\rho = 1$. Parameters as in Fig. 3.2.

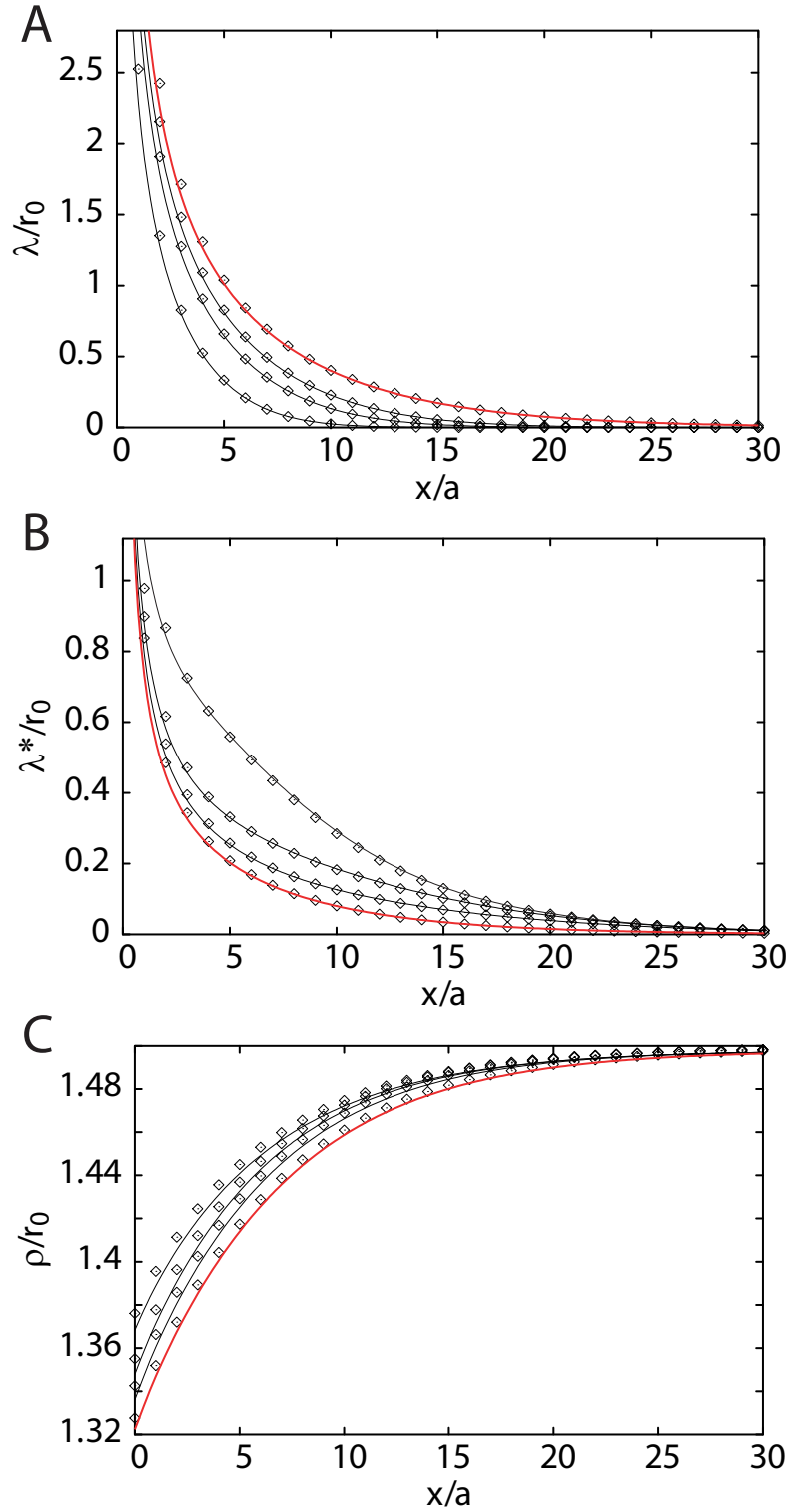


Figure A.2: Time development of gradient formation with two different ligand species. Ligand densities in the presence of a source at $x = 0$ at different times $tb_{\text{deg}} = 0.72, 2.16, 3.6$ during gradient formation (black lines) and in steady state (red lines). Lines indicate solutions to (A.5), while symbols indicate solutions to (A.1) for comparison. (A-C) Time development of the profiles of the total concentration of the first ligand species $\lambda(x)$ (A), the total concentration of the second ligand species $\lambda^*(x)$ (B), and the total receptor concentration $\rho(x)$ (C). All concentrations are normalized to the steady state value of the surface receptor concentration in the absence of ligands r_0 . Initial condition: steady state profile of λ^* and ρ with $j_0^*/b_{\text{deg}}ar_0 = 35/6$ and $\lambda = 0$. At $t = 0$, the current of ligands of the first species is raised from 0 to $j_0/b_{\text{deg}}ar_0 = 175/6$. Parameters as in Fig. 3.2 with $D_0 = 0$, $\psi = 2$, and $j = 0$ at $x/a = 50$.

$$\begin{aligned}
\partial_t S_n^{*(l)} &= -k_{\text{off}} S_n^{*(l)} + k_{\text{on}} R_n^{(l)} L_{n-1}^* - b_{\text{int}} S_n^{*(l)} + \frac{1}{2} b_{\text{ext}} S_n^{*(i)} \\
\partial_t R_n^{(i)} &= -f_{\text{ext}} R_n^{(i)} + f_{\text{int}} (R_n^{(l)} + R_n^{(r)}) - f_{\text{deg}} R_n^{(i)} \\
\partial_t S_n^{(i)} &= -b_{\text{ext}} S_n^{(i)} + b_{\text{int}} (S_n^{(l)} + S_n^{(r)}) - b_{\text{deg}} S_n^{(i)} \\
\partial_t S_n^{*(i)} &= -b_{\text{ext}} S_n^{*(i)} + b_{\text{int}} (S_n^{*(l)} + S_n^{*(r)}) - b_{\text{deg}} S_n^{*(i)}
\end{aligned} \tag{A.1}$$

One goes to the continuous description as demonstrated in section 3.1.2 and finds two separate continuity equations for the two ligand species:

$$\begin{aligned}
\partial_t \lambda &= -\partial_x j - b_{\text{deg}} s_i - e_{\text{deg}} l, \text{ with } \lambda = l + s_+ + s_i \\
\partial_t \lambda^* &= -\partial_x j^* - b_{\text{deg}} s_i^* - e_{\text{deg}} l^*, \text{ with } \lambda^* = l^* + s_+^* + s_i^*.
\end{aligned} \tag{A.2}$$

For j and j^* the same expressions as in (3.8) are obtained. The continuity equation for the total receptor concentration $\rho = r_i + r_+ + s_i + s_+ + s_i^* + s_+^*$ reads

$$\partial_t \rho = -\partial_x j \rho + \frac{f_{\text{syn}}}{a} - f_{\text{deg}} r_i - b_{\text{deg}} (s_i + s_i^*) \tag{A.3}$$

with the current

$$\begin{aligned}
j_\rho &= \frac{(a-b)}{2} (f_{\text{int}} r_- + b_{\text{int}} (s_- + s_-^*)) \\
&\quad - \frac{(a-b)^2}{8} (f_{\text{ext}} \partial_x r_i - f_{\text{int}} \partial_x r_+ - b_{\text{ext}} \partial_x (s_i + s_i^*) - b_{\text{int}} \partial_x (s_+ + s_+^*)).
\end{aligned}$$

The adiabatic approximation for l , s_i , s_- , and r_i is the same as above (3.11) and accordingly for l^* , s_i^* , s_-^* . But

$$r_- = \frac{k_{\text{off}} (s_- + s_-^*) + \frac{ab}{2} k_{\text{on}} r_+ \partial_x (l + l^*) + \frac{a-b}{2} f_{\text{ext}} \partial_x r_i}{f_{\text{int}} + k_{\text{on}} a (l + l^*)}. \tag{A.4}$$

Exploiting these relations and (A.2,A.3), one obtains the system of transport equations

$$\begin{aligned}
\partial_t \lambda &= \partial_x (D_\lambda (\lambda, \lambda^*, \rho) \partial_x \lambda + D_\rho (\lambda, \lambda^*, \rho) \partial_x \rho + D_{\lambda^*} (\lambda, \lambda^*, \rho) \partial_x \lambda^*) - k_\lambda (\lambda + \lambda^*, \rho) \lambda, \\
\partial_t \lambda^* &= \partial_x (D_\lambda (\lambda^*, \lambda, \rho) \partial_x \lambda^* + D_\rho (\lambda^*, \lambda, \rho) \partial_x \rho + D_{\lambda^*} (\lambda^*, \lambda, \rho) \partial_x \lambda) - k_\lambda (\lambda + \lambda^*, \rho) \lambda^*, \\
\partial_t \rho &= \nu_{\text{syn}} (\lambda, \lambda^*, \rho) - k_\rho (\lambda + \lambda^*, \rho) \rho.
\end{aligned} \tag{A.5}$$

The explicit expressions for the coefficient functions are rather involved. The rate of receptor synthesis is

$$\nu_{\text{syn}} (\lambda, \lambda^*, \rho) = \frac{f_{\text{syn}}^0}{a} \left(1 - \frac{r_+ (\lambda, \lambda^*, \rho) + \psi (s_+ (\lambda, \lambda^*, \rho) + s_+^* (\lambda, \lambda^*, \rho))}{r_{\text{max}}} \right).$$

We only mention some key properties of the remaining functions. $D_\lambda (\lambda, \lambda^*, \rho)$ and $D_\rho (\lambda, \lambda^*, \rho)$ have essentially the same properties as discussed above for only one ligand species. There is a contribution to currents of one ligand species that is driven by gradients of the other species. The corresponding coefficient $D_{\lambda^*} (\lambda, \lambda^*, \rho)$ can be positive or negative depending on the concentrations. For $\lambda = 0$, $D_{\lambda^*} = 0$ in (A.5) as required for the conservation of λ . The dependence of D_{λ^*} on λ and λ^* is shown in Fig. A.1.

We now briefly discuss the steady state solution of (A.5). At $x = 0$, boundary conditions for both ligand species have to be imposed. We restrict ourselves to imposing the currents j_0 and j_0^* . In general, the ligand source produces different amounts of the two species, hence $j_0 \neq j_0^*$. The steady state for $\lambda_{\text{tot}} = \lambda + \lambda^*$ is the same as calculated above (3.24) for one

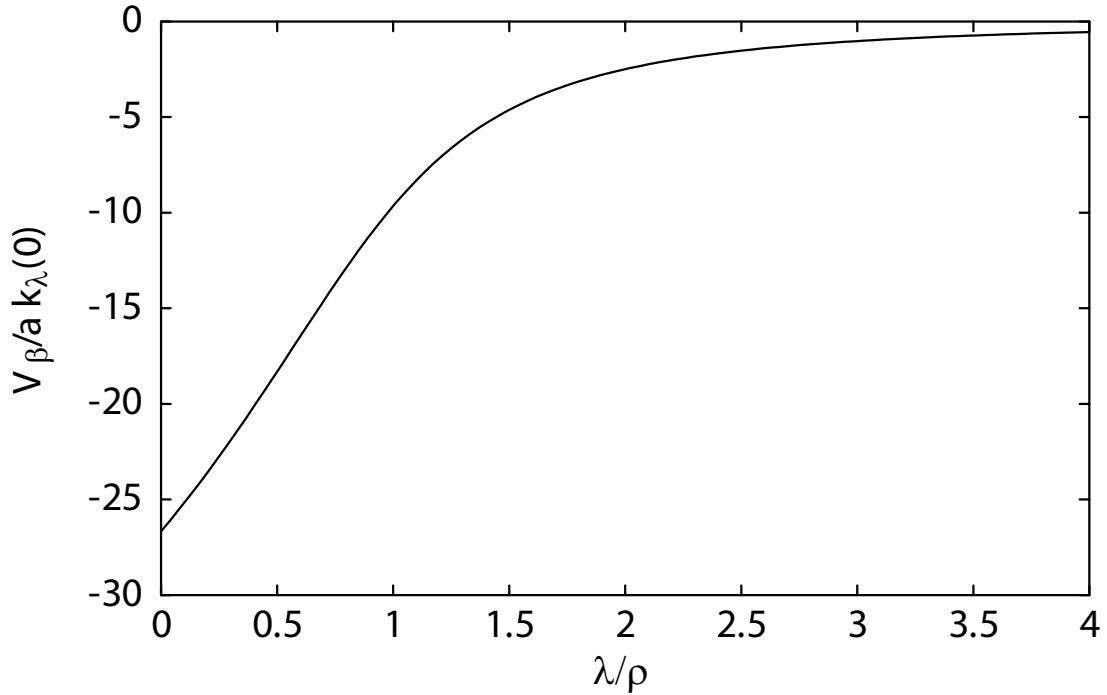


Figure A.3: The drift coefficient V_{β} from (A.9) as a function of λ/ρ for $\beta = .1$. Parameters as in Fig. 3.2.

ligand species with the current $j_{0,\text{tot}} = j_0 + j_0^*$ imposed at $x = 0$. The distributions for the individual species are obtained via $\lambda(x) = \lambda_{\text{tot}}(x)j_0/(j_0 + j_0^*)$ and $\lambda^*(x) = \lambda_{\text{tot}}(x)j_0^*/(j_0 + j_0^*)$. The properties of the steady state as discussed in section 4.1, most notably its robustness, consequently remain unaltered.

The presence of two different ligand species can affect the time development of the system. We have performed numerical calculations for the scenario outlined above: initially, one of the species is present in a steady state distribution and the production of the other species is started at $t = 0$. Fig. A.2 shows the time development for both species. Again, the results from solving the continuous description (A.5) are compared to the solutions of the discrete one (A.1). Because of our specific parameter choice, the initially present ligand species generates a receptor gradient in the opposite direction as compared to the ligand gradient. Due to the term $\propto \partial_x \rho$ in the equation for $\partial_t \lambda$ in (A.5), this situation can help the other species to be transported away from the source rapidly.

Finally, the transport equations (A.5) can be generalized to the two dimensional situation using the same arguments as in section 3.2.

A.2 Directional bias in the theoretical description of transcytosis

In this section, we study the effects of a bias in the description of transcytosis. Although experiments on the morphogen Dpp in the *Drosophila* wing disk have indicated that the macroscopic transport by transcytosis is non-directional on length scales that are larger than one cell diameter, it is conceivable that this is different in other situations where transcytosis is at work. A small bias may also have gone unnoticed in the experiments. We generalize the discrete

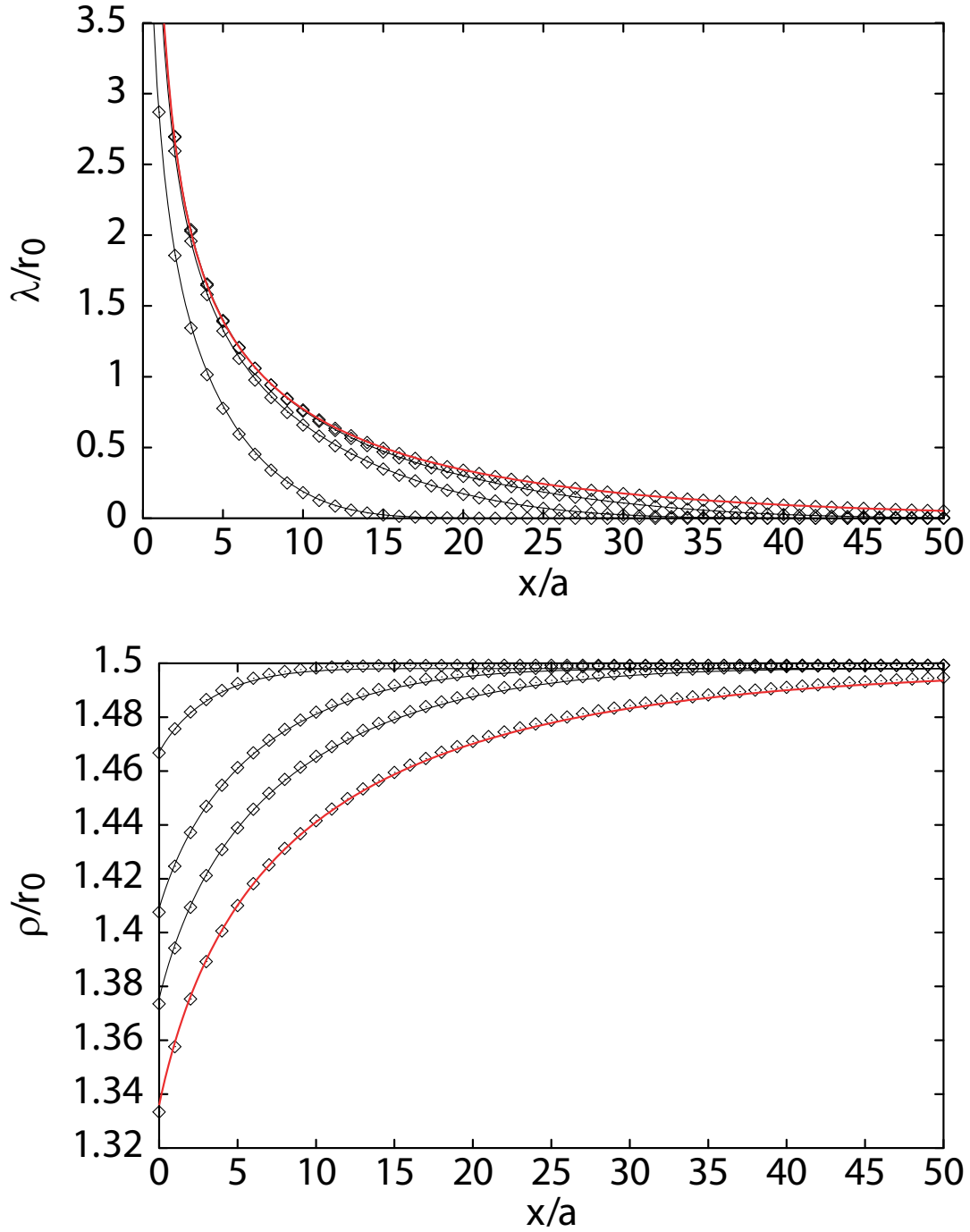


Figure A.4: Time development of gradient formation with directional bias. Profiles of the total ligand concentration $\lambda(x)$ and the total receptor concentration $\rho(x)$ in the presence of a source at $x = 0$ at different times $tb_{\text{deg}} = 0.72, 2.16, 3.6$ during gradient formation (black lines) and in steady state (red lines). Lines indicate solutions to (A.8), while symbols indicate solutions to (A.6) for comparison. All concentrations are normalized to the steady state value of the surface receptor concentration in the absence of ligands r_0 . Initial condition: $\lambda(x) = 0$ and $\rho(x) = (1 + f_{\text{int}}/f_{\text{ext}})r_0$. Parameters as in Fig. 3.2 with $\beta = .1$, $D_0 = 0$, $\psi = 2$, $j_0/b_{\text{deg}}ar_0 = 175/6$, and $j = 0$ at $x/a = 100$.

description (3.1) by allowing receptor-bound ligand molecules to be preferentially externalized to either the left or the right surface. We introduce a dimensionless parameter β measuring this bias. For $\beta = -1/2$, all the receptor-bound ligand is externalized on the left surface, for $\beta = 1/2$ on the right surface, and for $\beta = 0$, we recover the unbiased description. The underlying assumption of this description is that the cells have some means to distinguish between different directions in the tissue and can sort ligand-bound receptors preferentially in one direction. The kinetic equations of the discrete description with bias read:

$$\begin{aligned}\partial_t S_n^{(r)} &= -k_{\text{off}} S_n^{(r)} + k_{\text{on}} R_n^{(r)} L_n - b_{\text{int}} S_n^{(r)} + b_{\text{ext}}(1/2 + \beta) S_n^{(i)} \\ \partial_t S_n^{(l)} &= -k_{\text{off}} S_n^{(l)} + k_{\text{on}} R_n^{(l)} L_{n-1} - b_{\text{int}} S_n^{(l)} + b_{\text{ext}}(1/2 - \beta) S_n^{(i)},\end{aligned}\quad (\text{A.6})$$

with the kinetics for the remaining quantities as in (3.1). This implies that the externalization of the free receptors remains unbiased. We proceed as before to derive the continuous equations. The adiabatic approximation changes to

$$s_- = \frac{k_{\text{on}} a l r_- - 2\beta b_{\text{ext}} s_i - a b k_{\text{on}} / 2 r_+ \partial_x l + (a - b) b_{\text{ext}} / 2 \partial_x s_i}{b_{\text{int}} + k_{\text{off}}}\quad (\text{A.7})$$

with the other relations as in (3.11). Finally, the transport equations (3.12, 3.13) generalize to

$$\begin{aligned}\partial_t \lambda &= \partial_x (D_\lambda(\lambda, \rho) \partial_x \lambda + D_\rho(\lambda, \rho) \partial_x \rho + V_\beta(\lambda, \rho) \lambda) - k_\lambda(\lambda, \rho) \lambda, \\ \partial_t \rho &= \nu_{\text{syn}}(\lambda, \rho) - k_\rho(\lambda, \rho) \rho,\end{aligned}\quad (\text{A.8})$$

with the new drift term

$$\begin{aligned}V_\beta(\lambda, \rho) &= (-2a^2 \beta b_{\text{ext}} b_{\text{int}} f_{\text{ext}} f_{\text{int}} k_{\text{off}} k_{\text{on}} \rho) (b_{\text{ext}} (f_{\text{int}} (b_{\text{int}} + k_{\text{off}}) + a b_{\text{int}} k_{\text{on}} \lambda) ((f_{\text{ext}} + f_{\text{int}}) k_{\text{off}} \\ &\quad + a f_{\text{ext}} k_{\text{on}} \lambda) + a b_{\text{ext}} f_{\text{ext}} k_{\text{on}} (f_{\text{int}} (b_{\text{int}} + k_{\text{off}}) - a b_{\text{int}} k_{\text{on}} \lambda) \rho \\ &\quad + (f_{\text{int}} (b_{\text{int}} + k_{\text{off}}) + a b_{\text{int}} k_{\text{on}} \lambda) A(\lambda, \rho) + a b_{\text{int}} f_{\text{ext}} k_{\text{on}} (f_{\text{int}} k_{\text{off}} (\lambda + \rho) \\ &\quad + b_{\text{int}} (a k_{\text{on}} \lambda (\lambda - \rho) + f_{\text{int}} (\lambda + \rho))))^{-1},\end{aligned}\quad (\text{A.9})$$

where $A(\lambda, \rho)$ is defined in (D.1). The other coefficients appearing in (A.8) remain as in the unbiased case. We will briefly discuss some essential properties of V_β . Firstly, $V_\beta = 0$ for $\beta = 0$ and the unbiased case is recovered. Moreover, V_β vanishes if either ρ , k_{on} , k_{off} , b_{int} , b_{ext} , f_{int} , or f_{ext} is zero and also for $b_{\text{int}} \rightarrow \infty$ or $k_{\text{off}} \rightarrow \infty$. The explanation for the breakdown of transport in these cases were discussed in section 3.3.1 and remain unaltered in the presence of a bias. The drift is independent of the extracellular diffusion as p does not appear in the explicit expression for V_β . For small λ , V_β adopts a finite value. In the limit of large λ , V_β vanishes as $V_\beta \approx c_3(\rho) \lambda^{-2}$, with $c_3(\rho) = -\beta b_{\text{ext}} f_{\text{int}} k_{\text{off}} \rho / [(b_{\text{ext}} + b_{\text{int}}) k_{\text{on}}]$. The fact that V_β goes to zero as $\lambda \rightarrow \infty$ again reflects that transport is mediated by a limited number of receptors. V_β converges to the value $-a \beta b_{\text{ext}} b_{\text{int}} k_{\text{off}} / [(b_{\text{ext}} + b_{\text{int}}) (b_{\text{int}} + k_{\text{off}})]$ for $\rho \rightarrow \infty$. It is a monotonic function of λ and ρ . For $\beta > 0$, V_β increases as a function of λ , for $\beta < 0$ it decreases. In Fig. A.3, we show V_β as a function of λ for $\beta = .1$, i.e. a bias that leads to preferential transport to the right. We have numerically verified that the continuous description (A.8) and the original microscopic description with bias (A.6) are in good agreement on large length scales, see Fig. A.4.

Note, that the steady state solution of (A.8) cannot be obtained analytically as for the unbiased case. It is consequently not possible to strictly analyze the robustness of the steady state solution as in section 4.1. As V_β goes to zero for large ligand densities λ with the same power law as D_λ and D_ρ , one may expect similar robustness properties as in the case $\beta = 0$ for large currents j_0 imposed at $x = 0$. Indeed, numerical calculations of the steady state gradients based on (A.8) show that the robustness endures.

In Fig. A.4, we compare the time development of gradient formation with a bias to the unbiased case. As may have been anticipated, even a small bias can strongly affect the time

development and steady state profile of the concentration gradient. For a bias that leads to preferential transport away from the source, the ligand fills the regions away from the source more rapidly and the steady state gradient range is extended.

A.3 Diffusion on the cell surface: the glypican model

In this work, we have focused on transcytosis and free extracellular diffusion as mechanisms of ligand transport. The transport equations we have presented in chapter 3 and the methods used to derive them are, however, applicable to other cell-to-cell transport mechanisms than transcytosis. As an example, consider a transport mechanism recently suggested for the morphogens Hedgehog and Dpp in the *Drosophila* wing disk [47, 7]. The ligand binds to a so called glypican molecule on the cell surface. This complex then diffuses on the cell surface. The ligand can also detach from the glypican it occupies and, after diffusing over a short distance in the extracellular space, it can attach to a new one that could be located on the surface of a different cell, see Fig. 1.5.

We can describe this mechanism on the same lattice structure as used above for transcytosis, see Fig. 3.1. The glypicans play the role of receptors. Note, however, that many ligands can bind to one glypican. For simplicity, we focus on the transport phenomenon and do not include ligand degradation or production and degradation of glypican molecules in our description. Furthermore, the glypican concentration is assumed to be constant on the cell surface. The description is similar to that of transcytosis with the constant surface receptor approximation (3.3). But instead of the internalization and externalization of receptor-ligand complexes as in transcytosis, dislocation of the ligand-glypican complexes in one cell is due to diffusion on the cell surface and ligand hopping from one glypican to another one on the surface of the same cell. Both effects are effectively captured in the discrete one dimensional description by hopping at a rate h between the left and right surface of each cell. Thus, a coarse-grained discrete description of this mechanism reads

$$\begin{aligned}\partial_t L_n &= k_{\text{off}}(S_n^{(r)} + S_{n+1}^{(l)}) - k_{\text{on}}(N_{\text{bs}}G - S_n^{(r)} - S_{n+1}^{(l)})L_n \\ \partial_t S_n^{(r)} &= -k_{\text{off}}S_n^{(r)} + k_{\text{on}}\left(N_{\text{bs}}G/2 - S_n^{(r)}\right)L_n + h(S_n^{(l)} - S_n^{(r)}) \\ \partial_t S_n^{(l)} &= -k_{\text{off}}S_n^{(l)} + k_{\text{on}}\left(N_{\text{bs}}G/2 - S_n^{(l)}\right)L_{n-1} + h(S_n^{(r)} - S_n^{(l)}),\end{aligned}$$

where G is the glypican number per cell and N_{bs} is the number of ligand binding sites per glypican. L_n denotes the number of free ligands in extracellular space n and $S_n^{(l/r)}$ are the numbers of glypican bound ligands on the left and right cell surface respectively. Moreover, k_{on} and k_{off} are the rates for forward and reverse ligand binding to the binding sites on the glypicans.

Using the same method as in section 3.1.2, we obtain the effective transport equation $\partial_t \lambda = \partial_x(D_{\text{glyp}}(\lambda)\partial_x \lambda)$ where λ is the total ligand concentration and

$$\begin{aligned}D_{\text{glyp}}(\lambda) &= \frac{a^3 g h k_{\text{off}} k_{\text{on}} N_{\text{bs}} (A(\lambda) - k_{\text{off}} + a k_{\text{on}} (-\lambda + g N_{\text{bs}}))}{4A(\lambda) (A(\lambda)h - h(k_{\text{off}} + a k_{\text{on}}\lambda) + a g (h + k_{\text{off}}) k_{\text{on}} N_{\text{bs}})}, \text{ with} \\ A(\lambda) &= \left[-4a^2 g k_{\text{on}}^2 \lambda + (k_{\text{off}} + a k_{\text{on}} (g + \lambda))^2\right]^{1/2}.\end{aligned}\tag{A.10}$$

Here, $g = G/a$. $D_{\text{glyp}}(\lambda)$ has properties that are very similar to those of the effective diffusion coefficient of the transcytosis model. It exhibits a maximum for sufficiently large k_{on} and decays like $D_{\text{glyp}} \sim \lambda^{-2}$ for large λ . Hence, upon inclusion of ligand degradation in the description, gradient formation by this mechanism exhibits similar robustness properties as transcytosis.

Appendix B

The diffusion, binding, and trafficking (DBT) model of morphogen transport

A theoretical description of morphogen transport that is very similar to our description in the extracellular diffusion dominated limit (3.28) has been studied by Lander et al. [60]. The model studied in that work is given by:

$$\begin{aligned}\partial_t l &= D_0 \Delta l - k_{\text{on}} a^2 l r_+ + k_{\text{off}} s_+ \\ \partial_t s_+ &= k_{\text{on}} a^2 l r_+ - (b_{\text{int}} + k_{\text{off}}) s_+ + b_{\text{ext}} s_i \\ \partial_t s_i &= b_{\text{int}} s_+ - (b_{\text{ext}} + b_{\text{deg}}) s_i \\ \partial_t r_+ &= k_{\text{off}} s_+ + f_{\text{ext}} r_i - k_{\text{on}} l r_+ - f_{\text{int}} r_+ \\ \partial_t r_i &= f_{\text{syn}}/a^2 + f_{\text{int}} r_+ - (f_{\text{ext}} + f_{\text{deg}}) r_i,\end{aligned}\tag{B.1}$$

where we have modified the notation used in [60] to agree with the one used throughout this thesis. We will refer to this model as the “diffusion, binding, and trafficking” (DBT) model [59].

In this chapter, we compare numerical results obtained from this DBT model to our description of morphogen transport in the extracellular diffusion dominated limit (3.28) and to the results published in [60]. Moreover, we demonstrate that the different receptor kinetics used for the numerical calculations in the diffusion regime and the negligence of the presence of endogenous Dpp used throughout section 2.3 does not significantly affect the results presented there. The contents of this chapter are largely coincident with those of [59].

B.1 Comparison of the results corresponding to the shibire clone assay

It has been claimed that the DBT model leads to the formation of a transient shadow in a one dimensional calculation corresponding to the shibire clone experiment discussed in section 2.2.3 if the internalization rates b_{int} and f_{int} are reduced by a factor of ten in the clone region. We repeated this calculation in two dimensions and were unable to reproduce these results, see Fig. B.2. Puzzled by the disagreement of our data compared to published results, we tried to reproduce the one dimensional calculation exactly as described in [60]. Even then, we did not obtain the same results, see Fig. B.1. This is due to conceptual and technical weaknesses in the calculations in [60] which we will now discuss in detail.

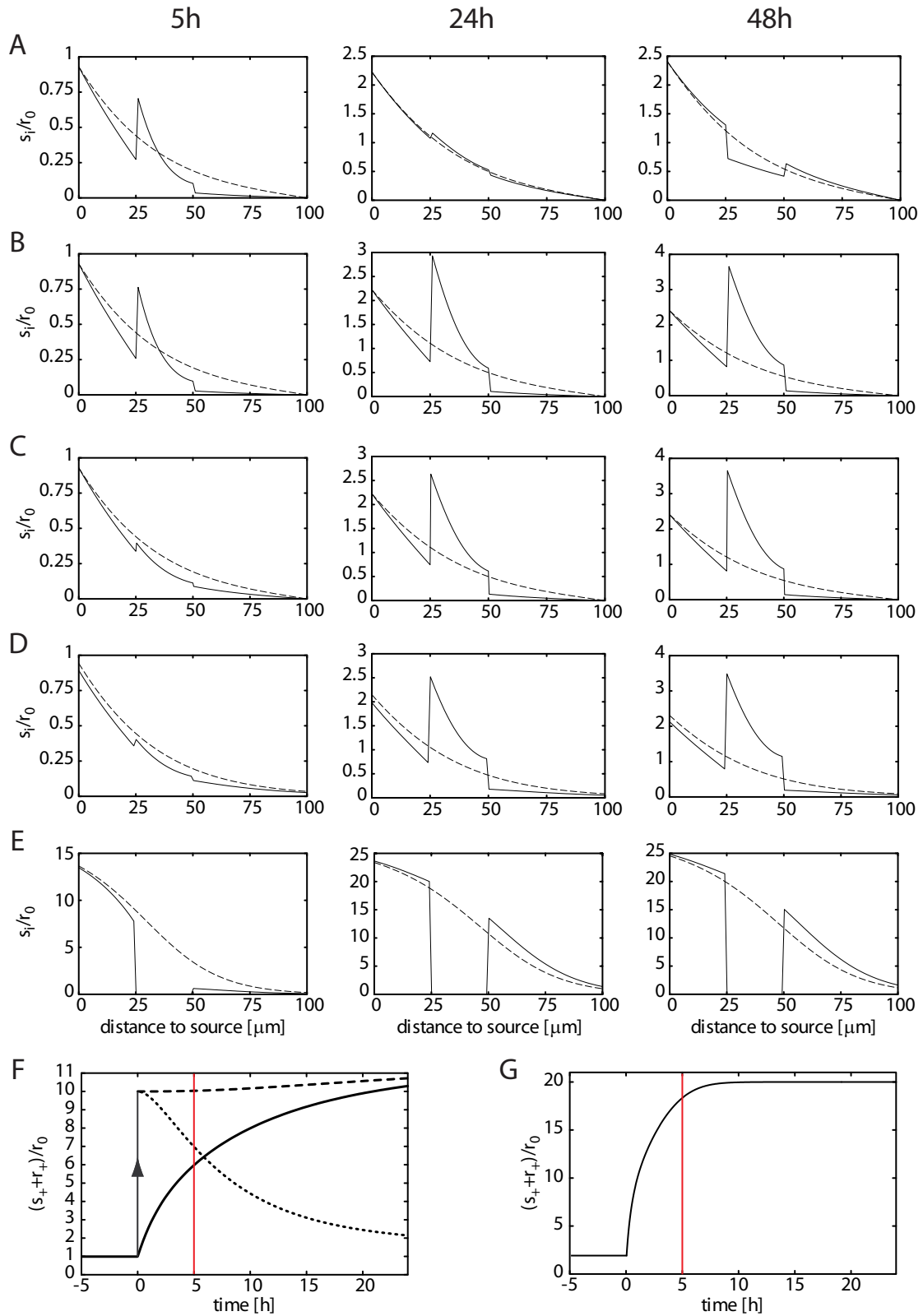


Figure B.1: Concentrations of internal bound ligand s_i in the presence of a shibire clone calculated in the DBT model (B.1) and in our description of morphogen transport in the diffusion regime (3.28).

(Caption of Fig. B.1 continued) (A) Replication of the one dimensional calculations of Lander et al.[60] for the DBT model. Profiles of internal bound ligand s_i at 5 hours, 24 hours, and 48 hours obtained for the same parameters as in [60] (see Table 2.1) with fixed concentration at the boundaries and an AOI size of $L_x = 100\mu\text{m}$. The endocytic block in the clone is described by a tenfold reduction of receptor internalization rates $b_{\text{int}}, f_{\text{int}}$. In addition, at time $t = 0$, the surface receptor concentration was suddenly increased by a factor of ten inside the clone as described in [60]. Note, that in order to replicate the results shown in Fig. 7 of [60], the receptor production rate f_{syn} had also to be reduced by a factor of ten. After five hours the ligand concentration is reduced behind the clone as compared to the results of the same calculation in the absence of a clone (dashed line). This corresponds to a shadow in the experiments. At 24 hours, the shadow is weak. This is not a steady state situation since after 48 hours, an accumulation of ligand behind the clone and depletion in the clone occur. (B) One dimensional calculation as described in A, but with correct receptor production rate f_{syn} in the clone region (not reduced by a factor of ten). A shadow builds up which increases in time and persists. (C) One dimensional calculation as in B (i.e. with corrected f_{syn}), but further corrected with surface receptor concentration in the clone region which increases gradually according to the DBT model. (D) Distribution of internal bound ligand in a two dimensional calculation for the DBT model with an AOI of size $200\mu\text{m} \times 200\mu\text{m}$ at 5 hours, 24 hours, and 48 hours along a section through the clone in x -direction as in Fig. B.2 C (solid line) and Fig. B.2 D (dashed line). Note that the one dimensional and two dimensional calculations generate similar profiles for the geometry of AOI and clone size chosen (compare C and D). Note also that in both cases there is a shadow that persists in the steady state. (E) Ligand distributions as described in D, but obtained from our description of morphogen transport in the diffusion regime for zero internalization rates. A shadow is present at 5 hours and has disappeared at 24 hours. There is no internal bound ligand inside the clone. In A-E, the clone extends from $x = 25\mu\text{m}$ to $x = 50\mu\text{m}$. (F) Total surface receptor concentration $s_+ + r_+$ in the center of the clone. The dotted line corresponds to the calculation shown in A, the dashed line to B, and the solid line to the calculation shown in D (a similar profile corresponds to C). (G) Total surface receptor concentration, $s_+ + r_+$, in the center of the clone for the calculation shown in E. All concentrations are normalized to $r_0 = f_{\text{syn}}f_{\text{ext}}/f_{\text{deg}}f_{\text{int}}$. Figure modified from [59].

Geometry and boundary conditions The geometry and boundary conditions discussed here differ from those introduced in [60]. There, the one dimensional case is considered exclusively, i.e. the concentrations of ligands and receptors are independent of y , even in the presence of a clone. At the boundaries at $x = 0$ and $x = 100\mu\text{m}$, Lander et al. imposed the ligand concentrations. In particular, at $x = 100\mu\text{m}$, the concentration was fixed to $l = 0$ which implies that all ligands that reach $x = 100\mu\text{m}$ are instantaneously degraded. Such a Dpp sink does not exist in the wing disk. This sink has a significant influence on the shape of the gradient obtained in the calculations of Lander et al. with AOI size $L_x = 100\mu\text{m}$, while the difference becomes insignificant for $L_x = 200\mu\text{m}$ (see Fig. B.3).

At $x = 0$, the boundary conditions imposed by Lander et al. are also problematic. These boundary conditions imply that at $x = 0\mu\text{m}$, the ligand concentration is imposed by the secreting cells but is unaffected by the exchange of ligands between secreting and non-secreting cells via diffusion. We refer to the boundary conditions imposing the ligand concentration and the ligand current as “concentration boundary conditions” and “current boundary conditions”, respectively.

We also performed one dimensional calculations in the presence of a clone (Fig. B.1). In these calculations, the clone region is represented by an interval on the x -axis. We find that a one dimensional description can generate ligand profiles which qualitatively correspond to the profiles in the x -direction of a two dimensional calculation (Fig. B.2), if the extension of

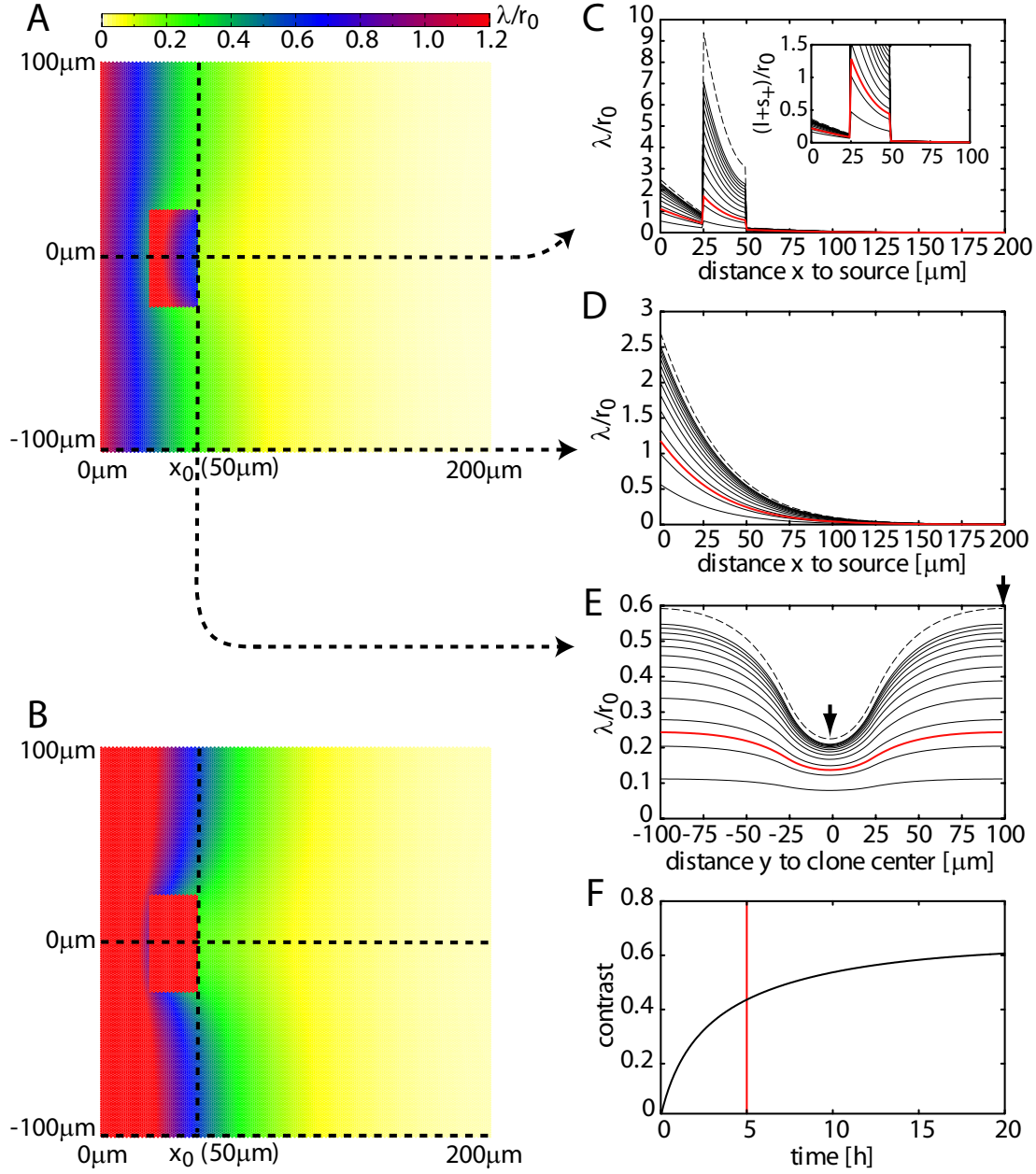


Figure B.2: Gradients in the DBT model describing a tissue with shibire clone. Kinetics of the total ligand distribution λ in the DBT model in an AOI of size $200\mu\text{m} \times 200\mu\text{m}$. The AOI contains a rectangular region, inside which the internalization rates b_{int} and f_{int} are reduced by a factor of ten after $t = 0$. This region covers the intervals $25\mu\text{m} \leq x \leq 50\mu\text{m}$ and $-25\mu\text{m} \leq y \leq 25\mu\text{m}$ and describes the effects of a temperature shift on a shibire clone. (A) Distribution of the total ligand concentration λ at $t = 5\text{h}$. (B) Distribution of λ in steady state. (C-E) Total ligand concentration along the dashed lines indicated in A,B. Solid black lines are separated by two hours. The red line represents the distributions after five hours, the time when the observations were made in the experiments discussed in [34]; the dashed lines represent the steady state distributions. The inset in C displays the profile of total extracellular ligand $l + s_+$. (F) Contrast of the shadow as a function of time. The contrast c is defined as in (2.1). Note, that the contrast still increases after five hours and that the shadow persists. Results in A-F were obtained by solving Equations B.1 with parameter values of Lander et al. as given in Table 2.1 and with the boundary conditions $j_x = 0$ at $x = 200\mu\text{m}$, $j_x = \nu d/2a^2$ at $x = 0$, and $j_y = 0$ at $y = \pm 100\mu\text{m}$. Initial conditions $l = s_+ = s_i = 0$, $r_+ = r_0$, and $r_i = r_0 f_{\text{int}}/f_{\text{ext}}$. All concentrations are normalized to $r_0 = f_{\text{syn}} f_{\text{ext}}/a^2 f_{\text{deg}} f_{\text{int}}$. Figure modified from [59].

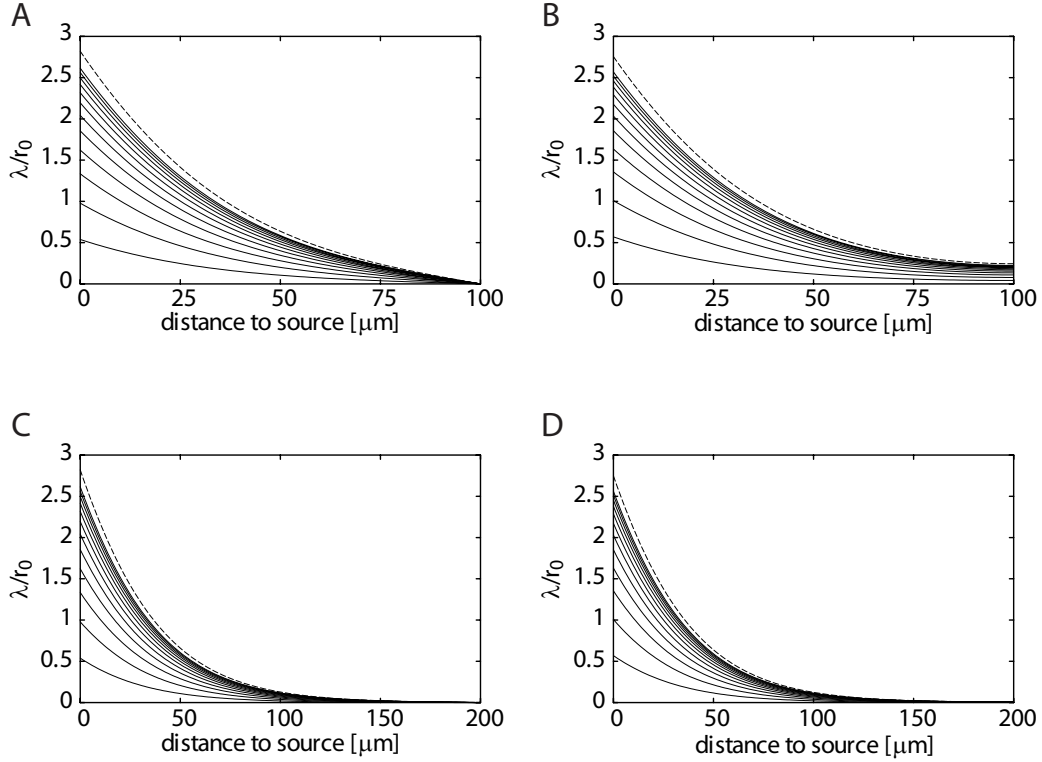


Figure B.3: Morphogen gradients in the DBT model for different boundary conditions and AOI sizes. Total ligand concentration λ as a function of the distance x from the source calculated in the DBT model for different times. Solid curves are separated by intervals of 2h. The dashed curve indicates the respective steady state. (A) Equations (B.1) were solved with concentration boundary conditions as in [60], i.e., $l = 0$ at $x = L_x$ as well as $\partial_t l = \bar{\nu} - k_{\text{on}} l r_+ + k_{\text{off}} s_+$ at $x = 0$, where $\bar{\nu}/r_0 = 8 \cdot 10^{-5} \text{ s}^{-1}$. (B) Equations (B.1) were solved with current boundary conditions, i.e., $j_x = \nu d/2a^2$ for $x = 0$ and $j_x = 0$ at $x = L_x$. In both cases $L_x = 100 \mu\text{m}$. Note, that the ligand concentrations differ significantly close to the distal boundary. (C) Calculation as in A (concentration boundary conditions), but for $L_x = 200 \mu\text{m}$. (D) Calculation as in B (current boundary conditions), but for $L_x = 200 \mu\text{m}$. Note that for this size, the ligand profiles do not depend on boundary conditions. Parameters are chosen as in [60], see Table 2.1. The value of ν for current boundary conditions has been chosen such that $j_x(x = 0)$ equals the ligand current at $x = 0$ in the steady state for concentration boundary conditions with $L_x = 200 \mu\text{m}$. The initial conditions were $l = s_+ = s_i = 0$, $r_+ = r_0$, and $r_i = r_0 f_{\text{int}}/f_{\text{ext}}$ for all x . Note that the total ligand concentration has been displayed in ordinates normalized to $r_0 = f_{\text{syn}} f_{\text{ext}}/a^2 f_{\text{deg}} f_{\text{int}}$ which is a constant that corresponds to the steady state surface receptor concentration in the absence of ligand. Figure modified from [59].

the clone in the y -direction is larger than the distance over which the gradient forms (compare Fig. B.1 C and D). For the present choice of parameters and an extension of the clone of $50\mu\text{m}$ in y -direction, this criterion is satisfied. The contrast c of shadows in the two dimensional geometry can be determined approximately in a one dimensional calculation by taking the difference of the concentration behind the clone and the concentration at the same position in a calculation without a clone. In general, however, a two dimensional description is required to describe the effects of the clone.

Receptor kinetics inside the clone region Our results show that the DBT model generates permanent shadows behind the clone, while the DBTS model that corresponds to our description of morphogen transport in the diffusion regime is able to generate transient shadows similar to those observed in the experiments in [34]. This finding differs from the results of [60] who argued that the DBT model generates transient shadows. In their one dimensional calculations of the DBT model, like in ours, endocytosis block is modeled by a tenfold reduction of the internalization rates at $t = 0$. However, in their study, the receptor concentrations in the clone are simultaneously and abruptly set to the steady state values corresponding to the reduced internalization rates. The latter is not in agreement with the experimental situation and is not justified by the DBT model. In fact, this corresponds to an immediate tenfold increase of the surface receptor concentration within the clone at the time of the temperature shift (see dashed line in Fig. B.1 F). This is different from what is expected to happen in the experiment according to the DBT model: as the internalization rates in the clone are reduced in an abrupt fashion at $t = 0$, the concentration of surface receptors only gradually increases (Fig. B.1 F; solid line). We have performed the same calculations as described in Lander et al. but with corrected initial conditions for the receptor concentration (Fig. B.1 C). This one dimensional calculation qualitatively leads to the same result as already discussed in two dimensions: a shadow develops which at hours is weak and becomes more pronounced after long times (compare Fig. B.1 C and D).

In order to understand how Lander et al. came to the conclusion that transient shadows occur in the DBT model, we have repeated their calculations. Using the parameter values and system size, the boundary conditions, and the initial conditions chosen in their article, we obtain ligand profiles, which differ from those published in their work (Fig. B.1 B). Note that here the initial surface receptor concentration in the clone is set to a tenfold larger value as compared to the remaining tissue. This also results in a persistent shadow in the steady state identical to the situation where the surface receptor level increases gradually (compare Fig. B.1 B and C). In summary, there are no transient shadows in either calculation.

The fact that these calculations lead to ligand profiles that differ from those published in [60] points to a technical problem in their calculations. Repeating the calculations of Lander et al., we noticed that their results could only be reproduced if the receptor production rate inside the clone was reduced by a factor of ten at $t = 0$ as compared to the one outside the clone. The results of our calculations with this additional change in the clone are displayed in Fig. B.1 A. They coincide with the results published in [60], see Fig. 7 therein. Apparently, in their calculations the receptor production rate in the clone was reduced by a factor of ten. As a result, the surface receptor concentration in the clone after undergoing an initial step-wise increase, relaxes in their calculations to a steady state value which is similar to the steady state in the tissue outside the clone (Fig. B.1 F, dotted line). In summary, in the case of Lander et al., the shadow appears because of the sudden step-wise increase of the surface receptor level; the shadow disappears at 24 hours because the receptor production rate is reduced and the surface receptor level therefore relaxes to approximately the same steady state as outside the clone.

Our results emphasize the facts that the number of dimensions considered (in particular in the presence of mutant clone), the size of the AOI, the boundary conditions, and the initial conditions (most notably the levels of surface receptor in the clone at the beginning of the experiment) are of key importance.

B.2 Description of two ligand species in the DBT model

In the experiments described in section 2.2, the kinetics of GFP-Dpp occurs on a background of endogenous Dpp, that presumably is in a stationary state. In order to describe the fluorescence intensity of GFP-Dpp, one should therefore in principle distinguish the concentrations l , s_+ and s_i of non-fluorescent ligand from their GFP-tagged counterparts l^* , s_+^* and s_i^* , which are observed. This leads to a straightforward generalization of (B.1):

$$\begin{aligned}
\partial_t l &= D_0 \Delta l - k_{\text{on}} a^2 l r_+ + k_{\text{off}} s_+ \\
\partial_t l^* &= D_0 \Delta l^* - k_{\text{on}} a^2 l^* r_+ + k_{\text{off}} s_+^* \\
\partial_t s_+ &= k_{\text{on}} a^2 l r_+ - (k_{\text{off}} + b_{\text{int}}) s_+ + b_{\text{ext}} s_i \\
\partial_t s_+^* &= k_{\text{on}} a^2 l^* r_+ - (k_{\text{off}} + b_{\text{int}}) s_+^* + b_{\text{ext}} s_i^* \\
\partial_t s_i &= b_{\text{int}} s_+ - (b_{\text{ext}} + b_{\text{deg}}) s_i \\
\partial_t s_i^* &= b_{\text{int}} s_+^* - (b_{\text{ext}} + b_{\text{deg}}) s_i^* \\
\partial_t r_+ &= k_{\text{off}} (s_+ + s_+^*) + f_{\text{ext}} r_i - k_{\text{on}} (l + l^*) r_+ - f_{\text{int}} r_+ \\
\partial_t r_i &= f_{\text{syn}} / a^2 + f_{\text{int}} r_+ - (f_{\text{ext}} + f_{\text{deg}}) r_i
\end{aligned} \tag{B.2}$$

Furthermore, we introduce the production rate ν^* of GFP-Dpp. The levels of expression of GFP-Dpp are about five times higher than those of the endogenous Dpp [40].

Figure B.4 shows that the profiles of GFP-Dpp in the presence of endogenous Dpp obtained from (B.2) are very similar to the profiles obtained with the DBT model, (B.1). Here, the secretion rate ν^* of GFP-Dpp is seven times that of the secretion rate ν of endogenous Dpp. Note, that for the parameter values given in Table 2.1, this result is independent of the ratio of the production rates ν and ν^* of endogenous Dpp and GFP-Dpp, respectively, as long as the total Dpp production rate, $\nu + \nu^*$, is constant. This is a consequence of the fraction of ligand bound surface receptors being low.

The situation is slightly different in our description of morphogen transport in the diffusion regime because the occupancy of surface receptors is not very low. In particular, if we describe the experimental situation of a shibire clone in the receiving tissue using our description of morphogen transport in the diffusion regime (3.28) with the parameters values given in Table 2.1, the maximal concentration of surface receptors R_{max} has to be increased in order to obtain shadows of the same contrast as in the case without endogenous Dpp.

B.3 Receptor production in the diffusion regime

In the DBT model (B.1) and in our description of morphogen transport in the diffusion regime (3.28), the receptor production rate f_{syn} appears in the equation for the distribution r_i of free internal receptors. This reflects the appearance of newly formed receptor molecules in endosomes inside the cells. The conventional biosynthetic pathway, however, does not involve endosomal structures [1]. Instead newly produced receptors appear directly on the cell surface. This can be incorporated into the DBT model like in our description of morphogen transport in the diffusion regime by modifying the kinetic equations for the distributions of free internal and free surface receptors. In our description (3.28) the equations describing the kinetics of

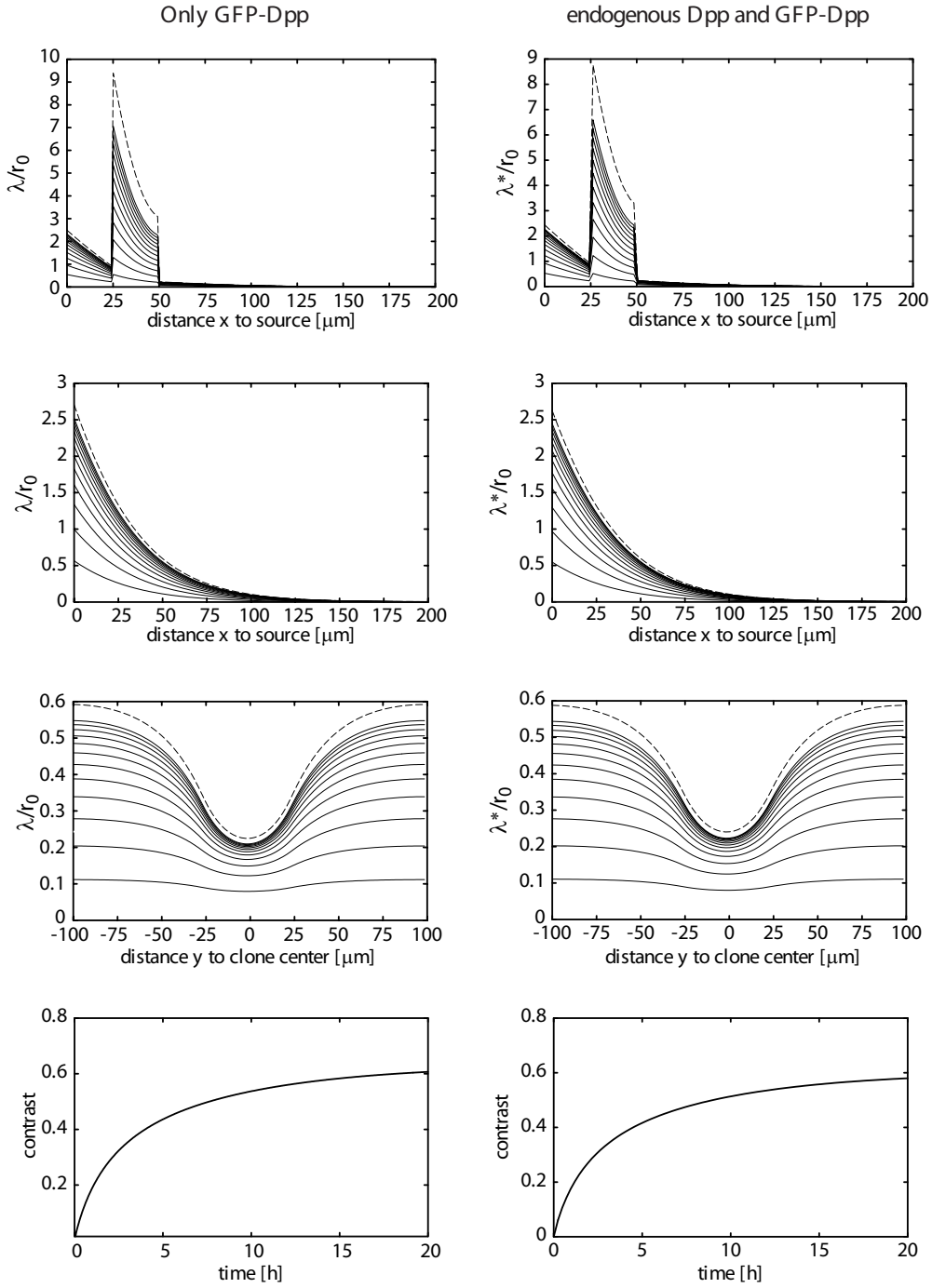


Figure B.4: Competition of GFP-Dpp with endogenous Dpp. Total GFP-Dpp profiles λ^* obtained from a two dimensional calculation of the DBT model in which endogenous Dpp and GFP-Dpp were treated separately according to (B.2) compared to those obtained from the calculation shown in Fig. B.2. The same geometry and parameters as depicted in Fig. B.2 were applied. The production rate of GFP-Dpp was chosen seven times larger than that of endogenous Dpp. All concentrations are normalized to $r_0 = f_{\text{syn}}f_{\text{ext}}/a^2f_{\text{deg}}f_{\text{int}}$. Figure modified from [59].

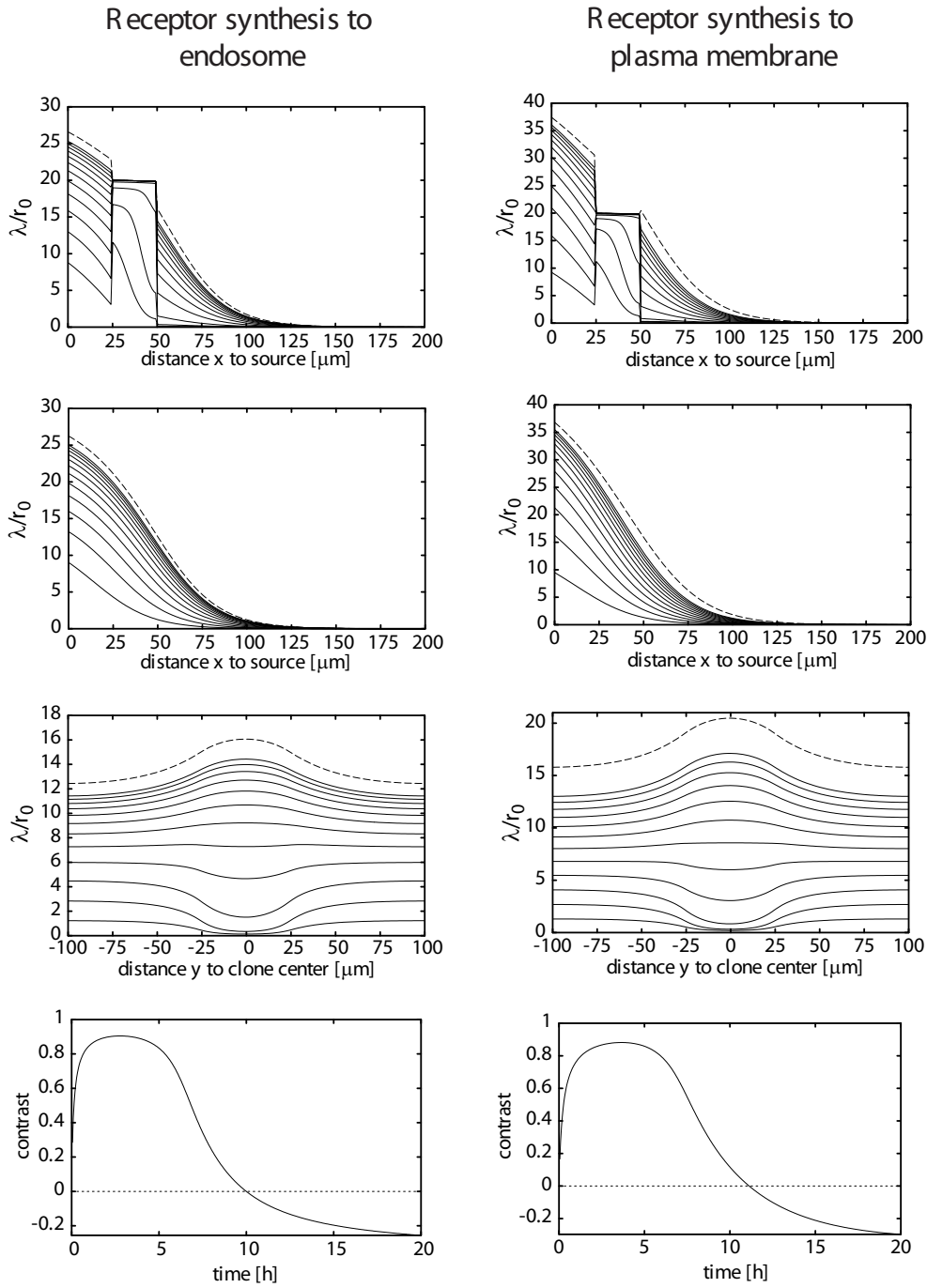


Figure B.5: Receptor synthesis in our description of morphogen transport in the diffusion regime. Total ligand profiles obtained from a two dimensional calculation with receptor synthesis directed to the plasma membrane according to (B.3) compared to those obtained from the calculation shown in Fig. 2.10. For the calculation shown on the right, the rate of receptor synthesis f_{syn}^0 was modified just like f_{ext} and b_{ext} to obtain cell surface receptor saturation. Note, that $r_0 = f_{\text{syn}}^0 (1 + f_{\text{ext}}/f_{\text{deg}})/a^2 f_{\text{int}}$ in the calculation on the right. Otherwise the same parameters as for the calculation shown in Fig. 2.10 were used. The initial conditions for the calculation on the right were $l = s_+ = s_i = 0$, $r_+ = r_0$, and $r_i = f_{\text{int}} r_0 / (f_{\text{deg}} + f_{\text{ext}})$. Figure modified from [59].

r_+ and r_i are replaced by

$$\begin{aligned}\partial_t r_+ &= \frac{f_{\text{syn}}^0}{a^2} \left(1 - \frac{s_+ + r_+}{r_{\text{max}}}\right) + k_{\text{off}} s_+ + f_{\text{ext}}^0 \left(1 - \frac{s_+ + r_+}{r_{\text{max}}}\right) r_i - k_{\text{on}} a^2 l r_+ - f_{\text{int}} r_+ \\ \partial_t r_i &= f_{\text{int}} r_+ - \left(f_{\text{ext}}^0 \left(1 - \frac{s_+ + r_+}{r_{\text{max}}}\right) + f_{\text{deg}}\right) r_i \quad .\end{aligned}\tag{B.3}$$

Note, that this corresponds to the same description of receptor synthesis we used for the transcytosis limit of our description of morphogen transport as discussed in section 3.1.2.

Numerical solutions of the modified models show only a minor effect of this change on the kinetics, see Fig. B.5.

Appendix C

Indirect assays on Dpp in the wing disk

A number of experiments with flies carrying mutations that affect the intracellular trafficking were performed. In these experiments, the Dpp gradient could not be observed directly using fluorescent labels for technical reasons [34]. Instead, the expression patterns of the target genes were analyzed. As target gene expression is controlled by the morphogen concentration, see section 1.1, a possible explanation for an altered range of target gene expression is that the morphogen gradient itself has changed its range accordingly. Alternatively, the change in gene expression could be due to cell autonomous effects of the mutation on the intracellular signal transduction mechanism. Since we do not know which one of these two explanations is correct, these experiments give only indirect information on morphogen transport and gradient formation. In this section, we nevertheless investigate the effects of these mutations on the morphogen gradient.

Experimental data The modifications studied in these experiments involve Rab proteins that affect the intracellular trafficking pathways. Only the cells outside of the source in the posterior compartment of the wing disk are subject to the mutation. The specific mutations studied are called DRab5S43N, and DRab7Q67L. Moreover, the effects of DRab5 over-expression (DRab5 OE) were investigated. These modifications affect the intracellular trafficking in that they impair endocytosis (DRab5S43N), enhance endocytosis (DRab5 OE), and enhance intracellular degradation (DRab7Q67L) respectively. The magnitude of these effects has so far not been quantified in experiments.

In the DRab5S43N experiment, a reduced range of the expression of the Dpp target gene Spalt (sal) was observed, compare Fig. C.1 G and H. It was further found that DRab5 over-expression leads to an enhanced range of sal expression and that expression of DRab7Q67L again results in a reduced range of sal expression, compare Fig. C.1 G to I and J.

Calculation in the transcytosis regime We have numerically calculated steady state gradients corresponding to these experiments using our theoretical description of morphogen transport in the transcytosis regime. We mimic the effect of DRab5S43N by reducing the internalization rates b_{int} and f_{int} to 10% of their wild-type values shown in Table 2.1. The resulting steady state gradients of receptor-bound morphogens and internalized morphogens for this situation are compared to the respective wild-type gradients in Fig. C.1 A and B. The gradient of internalized morphogens is clearly reduced. The gradient of receptor-bound morphogens changes its shape in a more complicated way: the positions of lower concentration

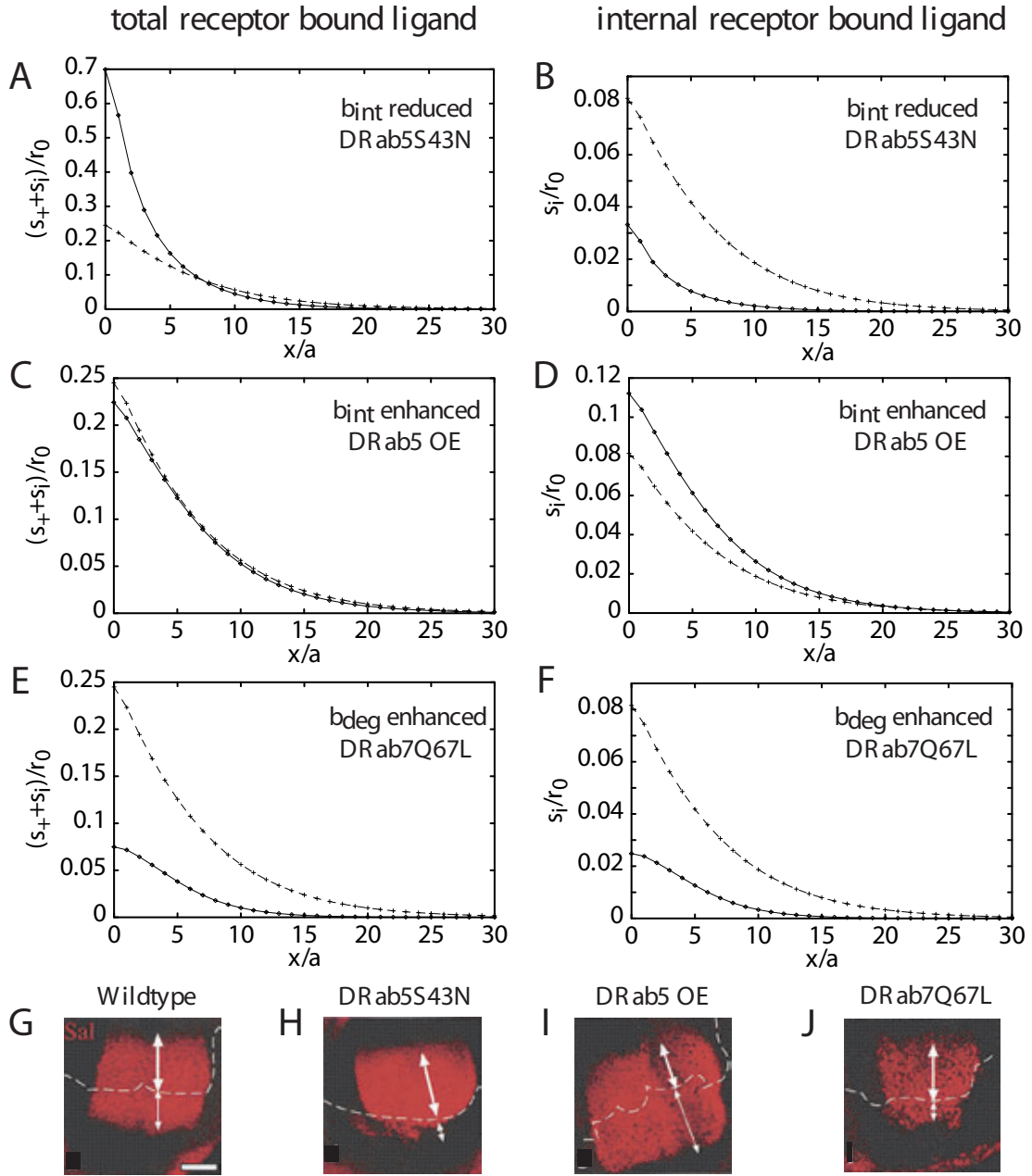


Figure C.1: Steady state profiles corresponding to the Rab experiments obtained from calculations based on our theoretical description of morphogen transport in the transcytosis regime. (A,B) Steady state gradients of the receptor-bound ligand $s_+ + s_i$ (solid line in A) and the internal receptor bound ligand s_i (solid line in B) from a calculation in which b_{int} and f_{int} were reduced to 10% of their wild-type values to mimic the effects of the DRab5S43N mutation. The respective wild-type gradients calculated as in Fig. 2.3 are shown by the broken lines. The concentrations are normalized to the steady state cell surface receptor concentration in the absence of ligands r_0 . (C,D) As in A,B but for a calculation in which b_{int} and f_{int} were increased by a factor of two to mimic the effect of Rab5 over-expression. (E,F) As in A,B but for a calculation in which b_{deg} was increased by a factor of five to mimic the effects of the DRab7Q67L mutation. (G-J) Experimental data showing the expression domain of the sal gene in red (taken from [34]). The modifications of the Rab proteins are present in the region below the white broken line that indicates the boundary between the anterior and the posterior compartment of the wing disk.

thresholds are shifted closer to the source whereas those of higher thresholds are shifted farther away.

To address the DRab5 OE experiment, we have numerically calculated the steady state gradient using rates b_{int} and f_{int} that are increased outside of the source region by an arbitrarily chosen factor of two. The resulting steady state profiles of receptor-bound morphogens and internalized morphogens are shown in Fig. C.1 C and D. Compared to the wild-type situation the range of internalized morphogens is clearly enhanced whereas the gradient of receptor-bound morphogens is hardly affected.

To compare the results of the DRab7Q67L experiment to our theoretical description, a steady state was calculated with the rate b_{deg} increased by an arbitrarily chosen factor of five. The resulting steady state profiles of receptor-bound morphogens and internalized morphogens are shown in Fig. C.1 E and F. Both gradients extend over a strongly reduced range in comparison to the respective wild type gradients.

Note, that the changes of the gradients which result from the calculation corresponding to the DRab5S43N and DRab5 OE experiments depend on the parameter choice since the effective diffusion coefficient derived in 3.1.2 can both increase or decrease if b_{int} is increased depending on the values of the other rates. Moreover, the qualitative change of the effective ligand degradation rate under modifications of b_{int} depends on the ratio $e_{\text{deg}}/b_{\text{deg}}$. One could try to find a fine-tuned parameter set in which the range of the gradient of receptor-bound morphogens obtained from the calculations would better agree to the range of sal expression observed in these experiments. But this would be of little value since it is not clear anyway if the receptor-bound morphogen number on the cell surface, inside the cell in the endosome, or the sum of both is the quantity that controls signal transduction inside the cell [41].

The interpretation that the modifications of the Rab proteins affect the morphogen gradient itself and not only the intracellular signal transduction mechanisms is consistent with the results obtained from numerical calculations based on our theoretical description of transcytosis if we assume that gene expression is controlled by the number of receptor-bound morphogens inside the cell. We would like to emphasize once more that due to the indirect nature of these experiments, the results discussed in this section are far less relevant for the investigation of morphogen transport than those discussed in sections 2.2.2 and 2.2.3.

Appendix D

Explicit expressions for coefficients

Here, we show the explicit expressions for the coefficient functions that appear in the transport equation (3.12, 3.13) and (5.33). Some of the calculations to derive these functions were performed using Mathematica [100].

D.1 Coefficients in the transport equations (3.12, 3.13)

The following are the explicit expressions for the coefficients in the one dimensional description of morphogen transport (3.12, 3.13) in the absence of extracellular diffusion, i.e. $p = 0$.

$$\begin{aligned}
D_\lambda(\lambda, \rho) &= -a^3 b_{\text{ext}} b_{\text{int}} (b_{\text{ext}} + b_{\text{int}}) f_{\text{ext}}^2 f_{\text{int}} k_{\text{off}} k_{\text{on}} \rho [-2b_{\text{int}} (b_{\text{ext}} (f_{\text{ext}} + f_{\text{int}}) k_{\text{off}} \\
&\quad + a(b_{\text{ext}} + b_{\text{int}}) f_{\text{ext}} k_{\text{on}} \lambda)^2 + 2A(\lambda, \rho) (-b_{\text{int}} f_{\text{ext}} (2f_{\text{int}} (b_{\text{int}} + k_{\text{off}}) + ab_{\text{int}} k_{\text{on}} \lambda)) \\
&\quad + b_{\text{ext}} (-2f_{\text{ext}} f_{\text{int}} k_{\text{off}} + b_{\text{int}} (f_{\text{int}} k_{\text{off}} + f_{\text{ext}} (-2f_{\text{int}} + k_{\text{off}} - ak_{\text{on}} \lambda)))] \\
&\quad + 2ab_{\text{int}} (b_{\text{ext}} + b_{\text{int}}) f_{\text{ext}} k_{\text{on}} (A(\lambda, \rho) - 2b_{\text{ext}} (f_{\text{ext}} + f_{\text{int}}) k_{\text{off}} \\
&\quad + 2a(b_{\text{ext}} + b_{\text{int}}) f_{\text{ext}} k_{\text{on}} \lambda) \rho - 2a^2 b_{\text{int}} (b_{\text{ext}} + b_{\text{int}})^2 f_{\text{ext}}^2 k_{\text{on}}^2 \rho^2]^{-1} \\
D_\rho(\lambda, \rho) &= a^4 b_{\text{ext}} b_{\text{int}} (b_{\text{ext}} + b_{\text{int}}) f_{\text{ext}}^2 f_{\text{int}} k_{\text{off}} k_{\text{on}}^2 \lambda \rho [2((-f_{\text{int}} (b_{\text{int}} + k_{\text{off}})) - ab_{\text{int}} k_{\text{on}} \lambda) \\
&\quad (b_{\text{ext}} (f_{\text{ext}} + f_{\text{int}}) k_{\text{off}} + a(b_{\text{ext}} + b_{\text{int}}) f_{\text{ext}} k_{\text{on}} \lambda) (A(\lambda, \rho) \\
&\quad + b_{\text{ext}} (f_{\text{ext}} + f_{\text{int}}) k_{\text{off}} + a(b_{\text{ext}} + b_{\text{int}}) f_{\text{ext}} k_{\text{on}} \lambda) \\
&\quad + a(b_{\text{ext}} + b_{\text{int}}) f_{\text{ext}} k_{\text{on}} (-A(\lambda, \rho) f_{\text{int}} (b_{\text{int}} + k_{\text{off}})) + aA(\lambda, \rho) b_{\text{int}} k_{\text{on}} \lambda \\
&\quad + 2(f_{\text{int}} (b_{\text{int}} + k_{\text{off}}) + ab_{\text{int}} k_{\text{on}} \lambda) (-b_{\text{ext}} (f_{\text{ext}} + f_{\text{int}}) k_{\text{off}}) \\
&\quad + a(b_{\text{ext}} + b_{\text{int}}) f_{\text{ext}} k_{\text{on}} \lambda) \rho - a^2 (b_{\text{ext}} + b_{\text{int}})^2 f_{\text{ext}}^2 k_{\text{on}}^2 \\
&\quad \times (f_{\text{int}} (b_{\text{int}} + k_{\text{off}}) + ab_{\text{int}} k_{\text{on}} \lambda) \rho^2]^{-1} \\
k_\lambda(\lambda, \rho) &= [b_{\text{deg}} b_{\text{int}} (ab_{\text{int}} f_{\text{ext}} k_{\text{on}} (\lambda + \rho) - A(\lambda, \rho) + b_{\text{ext}} (f_{\text{int}} k_{\text{off}} \\
&\quad + f_{\text{ext}} (k_{\text{off}} + ak_{\text{on}} (\lambda + \rho))))] [2a(b_{\text{ext}} + b_{\text{int}})^2 f_{\text{ext}} k_{\text{on}} \lambda]^{-1} \\
k_\rho(\lambda, \rho) &= [(-((b_{\text{ext}} + b_{\text{int}}) f_{\text{deg}} f_{\text{int}}) + b_{\text{deg}} b_{\text{int}} (f_{\text{ext}} + f_{\text{int}})) (-A(\lambda, \rho) \\
&\quad + b_{\text{ext}} (f_{\text{ext}} + f_{\text{int}}) k_{\text{off}} + a(b_{\text{ext}} + b_{\text{int}}) f_{\text{ext}} k_{\text{on}} \lambda) \\
&\quad + a(b_{\text{ext}} + b_{\text{int}}) f_{\text{ext}} ((b_{\text{ext}} + b_{\text{int}}) f_{\text{deg}} f_{\text{int}} + b_{\text{deg}} b_{\text{int}} (f_{\text{ext}} + f_{\text{int}})) k_{\text{on}} \rho] \\
&\quad \times [2a(b_{\text{ext}} + b_{\text{int}})^2 f_{\text{ext}} (f_{\text{ext}} + f_{\text{int}}) k_{\text{on}} \rho]^{-1}, \text{ with} \\
A(\lambda, \rho) &= [(b_{\text{ext}} (f_{\text{int}} k_{\text{off}} + f_{\text{ext}} (k_{\text{off}} + ak_{\text{on}} (\lambda - \rho))) + ab_{\text{int}} f_{\text{ext}} k_{\text{on}} (\lambda - \rho))^2 \\
&\quad + 4ab_{\text{ext}} (b_{\text{ext}} + b_{\text{int}}) f_{\text{ext}} (f_{\text{ext}} + f_{\text{int}}) k_{\text{off}} k_{\text{on}} \rho]^{1/2}
\end{aligned} \tag{D.1}$$

D.2 Explicit expressions for the $F_\alpha(\lambda)$ in (5.33)

With $A(\lambda)$ as in (3.18) and $D(\lambda)$ as in (3.17), we find for the functions $F_\alpha(\lambda)$ appearing in (5.33) in the absence of extracellular diffusion, i.e. for $p = 0$:

$$\begin{aligned}
F_{b_{\text{int}}}(\lambda)/D(\lambda) &= \frac{A(\lambda) - b_{\text{ext}}k_{\text{off}} - ak_{\text{on}}(b_{\text{int}}r + b_{\text{ext}}(\lambda + r))}{2ab_{\text{ext}}(b_{\text{ext}} + b_{\text{int}})k_{\text{on}}} \\
F_{k_{\text{on}}}(\lambda)/D(\lambda) &= \frac{A(\lambda) - b_{\text{ext}}k_{\text{off}} - ak_{\text{on}}(b_{\text{int}}r + b_{\text{ext}}(r - \lambda))}{2ab_{\text{ext}}k_{\text{on}}^2} \\
F_{b_{\text{ext}}}(\lambda)/F_{b_{\text{int}}}(\lambda) &= -b_{\text{int}}/b_{\text{ext}} \\
F_{k_{\text{off}}}(\lambda)/F_{k_{\text{on}}}(\lambda) &= -k_{\text{on}}/k_{\text{off}}.
\end{aligned} \tag{D.2}$$

Moreover, for $p > 0$, we find

$$F_p(\lambda) = \frac{a(A(\lambda) - b_{\text{ext}}k_{\text{off}} + ak_{\text{on}}(b_{\text{ext}}\lambda - (b_{\text{ext}} + b_{\text{int}})r))}{4b_{\text{ext}}k_{\text{on}}}.$$

D.3 Normalized standard deviation for transcytosis

The explicit result for the normalized standard deviation $\Sigma_\lambda(x)$ of the total ligand concentration in our theoretical description of transcytosis with disorder which follows from (5.40) is

$$\begin{aligned}
\Sigma_\lambda(x)^2 &= \sum_{\alpha \in \mathcal{M}_c} \frac{\sigma_\alpha^2}{8k^0(0)^2\xi^4} \left[8F_\alpha^{0'}(0)^2 + 2ax (\partial_\alpha k^0(0) - \partial_\alpha D^0(0)/\xi^2)^2 \xi^2 \right. \\
&\quad + \frac{a}{\xi} e^{-2x/\xi} \left(-\xi^2 \partial_\alpha k^0(0) + 3\partial_\alpha D^0(0) + 6F_\alpha^{0'}(0) \right) \left(\xi^2 \partial_\alpha k^0(0) + \partial_\alpha D^0(0) - 2F_\alpha^{0'}(0) \right) \\
&\quad \left. - \frac{a}{\xi} \left(4F_\alpha^{0'}(0)^2 + (\partial_\alpha D^0(0) - 3\xi^2 \partial_\alpha k^0(0)) (\xi^2 \partial_\alpha k^0(0) + \partial_\alpha D^0(0)) \right) \right], \tag{D.3}
\end{aligned}$$

where $\xi = \sqrt{D^0(0)/k^0(0)}$.

Appendix E

Supplementary analytic calculations

E.1 Derivation of continuous equations for the diffusion model with disorder

We demonstrate the derivation of the continuous equations describing the simple diffusion model with disorder from chapter 5.1. We restrict ourselves to the one dimensional situation here. The derivation is analogous in two dimensions. For case A, the discrete description in the bulk is (5.1)

$$\partial_t C_n = p_{n-1}(C_{n-1} - C_n) + p_n(C_{n+1} - C_n) - k_n C_n.$$

The continuous equation is obtained by replacing the C_n , p_n , and k_n with smooth functions $c(x)$, $p(x)$, and $k(x)$ and making a power series expansion to second order in x . For this, the C_n and k_n are put on the sites of a lattice with lattice constant a and the p_n on the bonds connecting these sites, see Fig. 5.1. This yields

$$\begin{aligned} \partial_t c(x) &= \left(p(x) - \frac{a}{2}p'(x)\right) \left(-ac'(x) + \frac{a^2}{2}c''(x)\right) + \left(p(x) + \frac{a}{2}p'(x)\right) \\ &\quad \times \left(ac'(x) + \frac{a^2}{2}c''(x)\right) - kc(x) + O(3) \\ &= p(x)a^2c''(x) + a^2p'(x)c'(x) - kc(x) + O(3) \\ &= \partial_x p(x)a^2\partial_x c(x) - kc(x) + O(3) = \partial_x D(x)\partial_x c(x) - kc(x) + O(3), \end{aligned}$$

where $D(x) = p(x)a^2$. For case B, the discrete description in the bulk is (5.3)

$$\partial_t C_n = p_{n-1}C_{n-1} + p_{n+1}C_{n+1} - 2p_n C_n - k_n C_n.$$

Proceeding as for case A, we find

$$\begin{aligned} \partial_t c(x) &= -2p(x)c(x) + \left(p(x) + ap'(x) + \frac{a^2}{2}p''(x)\right) \left(c(x) + ac'(x) + \frac{a^2}{2}c''(x)\right) \\ &\quad + \left(p(x) - ap'(x) + \frac{a^2}{2}p''(x)\right) \left(c(x) - ac'(x) + \frac{a^2}{2}c''(x)\right) - kc(x) + O(3) \\ &= a^2p''(x)c(x) + a^2pc''(x) + 2a^2p'(x)c'(x) - kc(x) + O(3) \\ &= \partial_x^2 p(x)a^2c(x) - kc(x) + O(3) = \partial_x^2 D(x)c(x) - kc(x) + O(3). \end{aligned}$$

E.2 Green's functions of $D\Delta - k$

E.2.1 Derivation of Green's function in three dimensions

Here, we exemplarily show how the free Green's function $G_0(\vec{x}, \vec{x}')$ of the operator $(D\Delta - k)$ in three dimensions can be calculated using Fourier transforms. The calculations in one and

two dimensions are similar. The equation to solve is

$$(D\Delta - k)G_0(\vec{x}, \vec{x}') = \delta(\vec{x}, \vec{x}'),$$

with $G_0(\vec{x}, \vec{x}') \rightarrow 0$ for $|\vec{x} - \vec{x}'| \rightarrow \infty$. Doing a Fourier transform $\vec{x} \rightarrow \vec{q}$ yields

$$-(Dq^2 + k)\tilde{G}_0(\vec{q}, \vec{x}') = (2\pi)^{-3/2}e^{i\vec{q}\cdot\vec{x}'},$$

with $q = |\vec{q}|$. We can identify

$$\tilde{G}_0(\vec{q}, \vec{x}') = \frac{-(2\pi)^{-3/2}e^{i\vec{q}\cdot\vec{x}'}}{Dq^2 + k}.$$

Finally, we apply the inverse Fourier transform

$$\begin{aligned} G_0(\vec{x}, \vec{x}') &= (2\pi)^{-3/2} \int_{-\infty}^{\infty} d^3q \tilde{G}_0(\vec{q}, \vec{x}') e^{-i\vec{q}\cdot\vec{x}} \\ &= 2\pi(2\pi)^{-3/2} \int_0^\pi d\theta \int_0^\infty dq \frac{-(2\pi)^{-3/2}e^{iq|\vec{x}'-\vec{x}|\cos\theta} q^2 \sin\theta}{Dq^2 + k} \\ &= \frac{-e^{-\sqrt{k/D}|\vec{x}-\vec{x}'|}}{4\pi D|\vec{x}-\vec{x}'|}, \end{aligned}$$

where we have introduced spherical coordinates in which θ denotes the angle between \vec{q} and $\vec{x}' - \vec{x}$.

E.2.2 Properties at the boundary in two dimensions

The Green's function $G_+(x, y, x', y') = G_0(x, y, x', y') + G_0(x, y, -x', y')$ defined in (5.26) in section 5.1.3 where $G_0(\vec{x}, \vec{x}') = -K_0(|\vec{x} - \vec{x}'|/\xi_D)/2\pi D$ satisfies

$$\partial_x G_+(x, y, 0, y') \Big|_{x=0} = \delta(y - y').$$

This can be seen as follows. Firstly,

$$\partial_x G_+(x, y, 0, y') = \frac{1}{\pi\xi_D} \frac{K_1(\sqrt{x^2 + (y - y')^2}/\xi_D)x}{\sqrt{x^2 + (y - y')^2}},$$

with the modified Bessel function of the second kind K_1 [97]. For $y \neq y'$, this vanishes if $x = 0$. For $y \approx y'$, we can write

$$\partial_x G_+(x, y, 0, y') \Big|_{x=0} = \lim_{\epsilon \searrow 0} \partial_x G_+(x, y, 0, y') \Big|_{x=\epsilon} = \lim_{\epsilon \searrow 0} \frac{1}{\pi} \frac{\epsilon}{\epsilon^2 + (y - y')^2} = \delta(y - y'),$$

where it was used that $K_1(z) \approx z^{-1}$ for $z \ll 1$.

E.3 Asymptotic behavior of the normalized standard deviation

E.3.1 Two dimensions

For the simple diffusion model with disorder in two dimensions discussed in section 5.1.3, the normalized standard deviation $\Sigma(x)$ of the steady state concentration $c(x)$ grows as $x^{1/4}$ for large x . For simplicity, we only show this for fluctuating k here. We can use the free Green's

function because for large x the effect of the boundary condition imposed at $x = 0$ is negligible, $G_{\pm}(\vec{x}, \vec{x}') \approx G_0(\vec{x}, \vec{x}')$. Using (5.28), we have

$$\begin{aligned}\Sigma(x)^2 &= \frac{\langle c_1(\vec{x})^2 \rangle}{c_0(x)^2} \\ &= \left(\frac{\sigma_k a c_0^0}{2\pi D c_0(x)} \right)^2 \int_0^\infty dx' \int_{-\infty}^\infty dy' e^{-2x'/\xi_D} K_0 \left(\sqrt{(x-x')^2 + (y-y')^2} / \xi_D \right)^2 \\ &= \left(\frac{\sigma_k a}{2\pi D} \right)^2 e^{2x/\xi_D} \int_{-\infty}^x dx' \int_{-\infty}^\infty dy' e^{-2(x-x')/\xi_D} K_0 \left(\sqrt{x'^2 + y'^2} / \xi_D \right)^2 \\ &= \left(\frac{\sigma_k a}{2\pi D} \right)^2 \left(\int_{-\infty}^L dx' + \int_L^x dx' \right) \int_{-\infty}^\infty dy' e^{2x'/\xi_D} K_0 (r/\xi_D)^2,\end{aligned}$$

where $1 \ll L < x$, $\xi_D = \sqrt{D/k}$, and $r = \sqrt{x'^2 + y'^2}$. The first integral gives an additive constant and for the second integral, we can apply the asymptotic expansion $K_0(z) \approx \sqrt{\pi/2} e^{-z} z^{-1/2}$ for large z . This yields

$$\begin{aligned}\Sigma(x)^2 &\sim \int_L^x dx' \int_{-\infty}^\infty dy' \frac{e^{-2(r-x')/\xi_D}}{r} = \int_{-\pi/2}^{\pi/2} d\phi \int_{L/\cos\phi}^{x/\cos\phi} dr e^{-2r(1-\cos\phi)/\xi_D} \\ &= \int_{-\pi/2}^{\pi/2} d\phi \int_L^x dr e^{-2r(\sec\phi-1)/\xi_D} \sec\phi \\ &= 2 \int_L^x dr \int_1^\infty dw \frac{e^{-2r(w-1)/\xi_D}}{\sqrt{w^2-1}} = 2 \int_L^x dr e^{2r/\xi_D} K_0(2r/\xi_D) \\ &\sim \int_L^x dr r^{-1/2} \sim x^{1/2},\end{aligned}$$

where we have substituted $\phi = \text{arcsec } w$ and used the asymptotic expansion of K_0 again.

E.3.2 Three dimensions

In three dimensions, the normalized standard deviation $\Sigma(x)$ of the steady state concentration $c(x)$ grows as $\ln x$ for large x . For simplicity, we only show this for fluctuating k here. We use the free Green's function because for large x the effect of the boundary condition imposed at $x = 0$ is negligible, $G_{\pm}(\vec{x}, \vec{x}') \approx G_0(\vec{x}, \vec{x}')$. Using (5.30), we have

$$\begin{aligned}\Sigma(x)^2 &= \frac{\langle c_1(\vec{x})^2 \rangle}{c_0(x)^2} \\ &= a^3 \left(\frac{\sigma_k c_0^0}{4\pi D c_0(x)} \right)^2 \int_0^\infty dx' \int_{-\infty}^\infty dy' \int_{-\infty}^\infty dz' e^{-2x'/\xi_D} \frac{e^{-2|\vec{x}-\vec{x}'|/\xi_D}}{|\vec{x}-\vec{x}'|^2} \\ &= a^3 \left(\frac{\sigma_k}{4\pi D} \right)^2 e^{2x/\xi_D} \int_{-\infty}^x dx' \int_{-\infty}^\infty dy' \int_{-\infty}^\infty dz' e^{-2(x-x')/\xi_D} \frac{e^{-2r/\xi_D}}{r^2} \\ &= a^3 \left(\frac{\sigma_k}{4\pi D} \right)^2 \int_{-\infty}^x dx' \int_{-\infty}^\infty dy' \int_{-\infty}^\infty dz' \frac{e^{-2(r-x')/\xi_D}}{r^2} \\ &= a^3 \left(\frac{\sigma_k}{4\pi D} \right)^2 \left(\int_{-\infty}^L dx' + \int_L^x dx' \right) \int_{-\infty}^\infty dy' \int_{-\infty}^\infty dz' \frac{e^{-2(r-x')/\xi_D}}{r^2}\end{aligned}$$

where $1 \ll L < x$, $\xi_D = \sqrt{D/k}$, and $r = \sqrt{x'^2 + y'^2 + z'^2}$. The first integral gives an additive constant, so we have

$$\Sigma(x)^2 \sim \int_L^x dx' \int_{-\infty}^\infty dy' \int_{-\infty}^\infty dz' \frac{e^{-2(r-x')/\xi_D}}{r^2}$$

$$\begin{aligned}
&= 2\pi \int_0^{\pi/2} d\theta \sin \theta \int_{L/\cos \theta}^{x/\cos \theta} dr e^{-2r(1-\cos \theta)/\xi_D} \\
&= 2\pi \int_0^{\pi/2} d\theta \tan \theta \int_L^x dr e^{-2r(\sec \theta - 1)/\xi_D} \\
&= 2\pi \int_L^x dr \int_1^\infty dw \frac{e^{-2r(w-1)/\xi_D}}{w} \\
&= 2\pi \int_L^x dr e^{2r/\xi_D} \Gamma(0, 2r/\xi_D) \sim \ln(x),
\end{aligned}$$

where we have substituted $\theta = \text{arcsec } w$ and $\Gamma(0, z) = \int_z^\infty dt e^{-t} t^{-1}$ is the incomplete gamma function which has the asymptotic behavior $\Gamma(0, z) \sim e^{-z} z^{-1}$ for large z [97].

Appendix F

Numerical methods

F.1 Kinetic equations of the extracellular diffusion dominated limit

We numerically solved the kinetic equations of the extracellular diffusion dominated limit (3.28) and the DBT model (B.1) by using the Euler discretization forward in time. In the forward Euler scheme, the partial derivatives in space and time of a function f are approximated by

$$\begin{aligned}\partial_x f(x, t) &= \frac{f(x + \Delta x, t) - f(x, t)}{\Delta x} \\ \partial_t f(x, t) &= \frac{f(x, t + \Delta t) - f(x, t)}{\Delta t} .\end{aligned}$$

We now explicitly describe the discretization scheme.

One dimension Consider a system that is homogenous in the y -direction. Then only the kinetics in the x -direction has to be determined and we are left with a one dimensional system. In order to describe the area of interest (AOI), we introduce a one dimensional lattice of size L with the sites being separated by a distance Δx . The ligand and receptor distributions are sampled on the sites. We define $l_n = l(n\Delta x, t)$, where $n = 0, \dots, N = L/\Delta x$, and correspondingly $s_{+,n}$, $s_{i,n}$, $r_{+,n}$, and $r_{i,n}$. Primed quantities denote the distributions at time $t + \Delta t$, e.g., $l'_n = l(n\Delta x, t + \Delta t)$. In the bulk, i.e., for $n = 1, \dots, N - 1$, the discretization of the kinetic equations of the DBT model (B.1) is then given by

$$\begin{aligned}l'_n &= l_n + \Delta t \left[\frac{j_n - j_{n+1}}{\Delta x} - k_{\text{on}} l_n r_{+,n} + k_{\text{off}} s_{+,n} \right] \\ s'_{+,n} &= s_{+,n} + \Delta t [k_{\text{on}} l_n r_{+,n} - (b_{\text{int}} + k_{\text{off}}) s_{+,n} + b_{\text{ext}}] s_{i,n} \\ s'_{i,n} &= s_{i,n} + \Delta t [b_{\text{int}} s_{+,n} - (b_{\text{ext}} + b_{\text{deg}}) s_{i,n}] \\ r'_{+,n} &= r_{+,n} + \Delta t [k_{\text{off}} s_{+,n} + f_{\text{ext}} r_{i,n} - k_{\text{on}} l_n r_{+,n} - f_{\text{int}}] r_{+,n} \\ r'_{i,n} &= r_{i,n} + \Delta t [w + f_{\text{int}} r_{+,n} - (f_{\text{ext}} + f_{\text{deg}}) r_{i,n}] .\end{aligned}\tag{F.1}$$

Here,

$$j_n = -\frac{D_0}{\Delta x} (l_n - l_{n-1}) .$$

The equations of our theoretical description of morphogen transport in the diffusion dominated limit (3.28) are discretized analogously.

Two dimensions In the two dimensional case, the AOI is represented by a triangular lattice with lattice constant Δ . The sites can then be indexed by two indices m and n , where $m = 0, \dots, N_x = L_x/\sqrt{3}\Delta$ and $n = 0, \dots, N_y = 2L_y/\Delta$. Explicitly,

$$l_{m,n} = \begin{cases} l(m\sqrt{3}\Delta, \frac{n}{2}\Delta) & \text{for } n \text{ even} \\ l((m + \frac{1}{2})\sqrt{3}\Delta, \frac{n}{2}\Delta) & \text{for } n \text{ odd} \end{cases} \quad (\text{F.2})$$

and correspondingly for the other densities. The terms in (F.1) describing ligand binding to and un-binding from receptors are readily modified to this situation. The current from site (m', n') to site (m, n) is proportional to $-(l_{m',n'} - l_{m,n})/\Delta$ and the discretization of the diffusion term reads

$$\frac{2D_0}{3\Delta^2} \sum_{\text{n.n.}} (l_{m',n'} - l_{m,n}) \quad . \quad (\text{F.3})$$

Here, the sum over the sites (m', n') extends over all nearest neighbors of the site (m, n) .

F.2 Discrete description of transcytosis

We numerically integrated the kinetic equations of the discrete description of morphogen transport (3.1, 3.3, A.1) and their corresponding generalizations to two dimensions like (3.19) by using the Euler discretization forward in time that was introduced in F.1. In the figures showing the time development calculated using the discrete one dimensional description of morphogen transport, the total ligand concentration at the position of cell n was calculated as $L_n + S_n^{(l)} + S_n^{(r)} + S_n^{(i)}$, the extracellular ligand concentration as $L_n + S_n^{(l)} + S_n^{(r)}$, and the total receptor concentration as $S_n^{(l)} + S_n^{(r)} + S_n^{(i)} + R_n^{(l)} + R_n^{(r)} + R_n^{(i)}$. In two dimensions, the total ligand concentration at the position of one cell was calculated accordingly by summing up the receptor-bound ligand concentrations inside this cell and on its surfaces and one half of the free ligand concentration in the surrounding extracellular space.

F.3 Effective transport equation for transcytosis

The effective transport equations in the transcytosis limit (3.12, 3.13) and (3.16) were solved using the Euler discretization forward in time, see section F.1. The discretization of the ligand current that involves a concentration dependent diffusion coefficient $D(\lambda)$ is not straightforward. We explain our discretization of (3.16). The treatment of (3.12, 3.13) is analogous. We introduce a one dimensional lattice with N sites that are separated by a distance Δx . The ligand concentration λ is sampled on the sites of this lattice. We define $\lambda_n = \lambda(n\Delta x, t)$, where $n = 0, \dots, N$. Let us denote the total ligand concentration on site n at time $t + \Delta t$ by λ'_n , i.e. $\lambda'_n = \lambda_n(t + \Delta t)$, while λ_n denotes $\lambda_n(t)$. The discretization of (3.16) is then given by

$$\lambda'_n = \lambda_n + \Delta t \left(\frac{j_n - j_{n+1}}{\Delta x} - k(\lambda_n)\lambda_n \right),$$

where the ligand current j_n between sites n and $n - 1$ is calculated as

$$j_n = -\frac{D(\lambda_n) + D(\lambda_{n-1})}{2\Delta x} (\lambda_n - \lambda_{n-1}).$$

The effective transport equation in two dimensions (3.20) was solved analogously using a square lattice.

F.4 Ensemble averages for frozen disorder

In the descriptions of morphogen transport with disorder discussed in chapter 5, different realizations of the disorder were generated by numerically calculating random numbers for the corresponding noise terms. A Gaussian distribution was used for these random numbers. Specifically, the random number generator for Gaussian deviates discussed in [82] was used. The steady states were calculated by letting the kinetics of the system given by the corresponding equations evolve for a long time. These kinetic equations were again solved using the Euler discretization forward in time, see section F.1. It was made sure that the system had evolved sufficiently long so that it was very close to its steady state at the end of the numerical calculation by demanding that the relative change of the concentration C_n at each lattice site had become very small, i.e. $|(C'_n - C_n)/\Delta t C_n| < \epsilon$, where $\epsilon = 10^{-15}$ was typically used. It was also verified that a longer evolution of the system did not change the resulting normalized standard deviation $\Sigma(x)$. This way typically 20,000 to 100,000 steady states for different realizations of the disorder were calculated.

The integrals that appear in the analytical results (5.28) and (5.30) for the variance of the concentration $c(x)$ in two and three dimensions were numerically integrated using Mathematica [100].

Bibliography

- [1] B. Alberts, D. Bray, J. Lewis, M. Raff, K. Roberts, and J.D. Watson. *Molecular Biology of the Cell*. Garland Publisher (New York), 1994.
- [2] S. Alexander, J. Bernasconi, W. R. Schneider, and R. Orbach. Excitation dynamics in random one-dimensional systems. *Reviews of Modern Physics*, 53(2):175–198, 1981.
- [3] U. Alon, M. G. Surette, N. Barkai, and S. Leibler. Robustness in bacterial chemotaxis. *Nature*, 397(6715):168–171, 1999.
- [4] D. Axelrod, D. E. Koppel, J. Schlessinger, E. Elson, and W. W. Webb. Mobility measurement by analysis of fluorescence photobleaching recovery kinetics. *Biophysical Journal*, 16:1055–1069, 1976.
- [5] K. Basler and G. Struhl. Compartment boundaries and the control of *Drosophila* limb pattern by Hedgehog protein. *Nature*, 368(6468):208–214, 1994.
- [6] A. Bejsovec and E. Wieschaus. Signaling activities of the *Drosophila* wingless gene are separately mutable and appear to be transduced at the cell-surface. *Genetics*, 139(1):309–320, 1995.
- [7] T. Y. Belenkaya, C. Han, D. Yan, R. J. Opoka, M. Khodoun, and X. Lin. *Drosophila* Dpp morphogen movement is independent of dynamin-mediated endocytosis but regulated by the glypican members of heparan sulfate proteoglycans. *Cell*, 119:231–244, 2004.
- [8] R. P. Bhalerao and M. J. Bennett. The case for morphogens in plants. *Nature Cell Biology*, 5(11):939–943, 2003.
- [9] T. Bollenbach, K. Kruse, P. Pantazis, M. González-Gaitán, and F. Jülicher. Robust formation of morphogen gradients. *Physical Review Letters*, 94:018103, 2005.
- [10] J. P. Bouchaud and A. Georges. Anomalous diffusion in disordered media - statistical mechanisms, models and physical applications. *Physics Reports-Review Section of Physics Letters*, 195(4-5):127–293, 1990.
- [11] A. H. Brand and N. Perrimon. Targeted gene expression as a means of altering cell fates and generating dominant phenotypes. *Development*, 118:401–415, 1993.
- [12] J. Briscoe, Y. Chen, T. M. Jessell, and G. Struhl. A hedgehog-insensitive form of patched provides evidence for direct long-range morphogen activity of Sonic hedgehog in the neural tube. *Molecular Cell*, 7(6):1279–1291, 2001.
- [13] A. Casali and G. Struhl. Reading the Hedgehog morphogen gradient by measuring the ratio of bound to unbound Patched protein. *Nature*, 431(7004):76–80, 2004.

- [14] M. S. Chen, R. A. Obar, C. C. Schroeder, T. W. Austin, C. A. Poodry, S. C. Wadsworth, and R. B. Vallee. Multiple forms of dynamin are encoded by shibire, a *Drosophila* gene involved in endocytosis. *Nature*, 351(6327):583–586, 1991.
- [15] Y. Chen and A. F. Schier. The zebrafish Nodal signal Squint functions as a morphogen. *Nature*, 411(6837):607–610, 2001.
- [16] Y. Chen and G. Struhl. Dual roles for patched in sequestering and transducing Hedgehog. *Cell*, 87:553–563, 1996.
- [17] L. Chu, H. S. Wiley, and D. A. Lauffenburger. Endocytic relay as a potential means for enhancing ligand transport through cellular tissue matrices: Analysis and possible implications for drug delivery. *Tissue Engineering*, 2:17–38, 1996.
- [18] F. Crick. Diffusion in embryogenesis. *Nature*, 225(5231):420, 1970.
- [19] M. C. Cross and P. C. Hohenberg. Pattern-formation outside of equilibrium. *Reviews of Modern Physics*, 65(3):851–1112, 1993. Part 2.
- [20] W. Denk, J. H. Strickler, and W. W. Webb. Two-photon laser scanning fluorescence microscopy. *Science*, 248:73–76, 1990.
- [21] R. Dosch, V. Gawantka, H. Delius, C. Blumenstock, and C. Niehrs. Bmp-4 acts as a morphogen in dorsoventral mesoderm patterning in *Xenopus*. *Development*, 124(12):2325–2334, 1997.
- [22] W. Driever and C. Nüsslein-Volhard. The Bicoid protein determines position in the *Drosophila* embryo in a concentration-dependent manner. *Cell*, 54(1):95–104, 1988.
- [23] W. Driever and C. Nüsslein-Volhard. A gradient of Bicoid protein in *Drosophila* embryos. *Cell*, 54(1):83–93, 1988.
- [24] W. Driever and C. Nüsslein-Volhard. The Bicoid protein is a positive regulator of Hunchback transcription in the early *Drosophila* embryo. *Nature*, 337(6203):138–143, 1989.
- [25] W. Driever, G. Thoma, and C. Nüsslein-Volhard. Determination of spatial domains of zygotic gene-expression in the *Drosophila* embryo by the affinity of binding-sites for the Bicoid morphogen. *Nature*, 340(6232):363–367, 1989.
- [26] S. Dyson and J. B. Gurdon. The interpretation of position in a morphogen gradient as revealed by occupancy of activin receptors. *Cell*, 93(4):557–568, 1998.
- [27] A. Eldar and N. Barkai. Interpreting clone-mediated perturbations of morphogen profiles. *Developmental Biology*, 278(1):203–207, 2005.
- [28] A. Eldar, R. Dorfman, D. Weiss, H. Ashe, B. Z. Shilo, and N. Barkai. Robustness of the BMP morphogen gradient in *Drosophila* embryonic patterning. *Nature*, 419(6904):304–308, 2002.
- [29] A. Eldar, D. Rosin, B. Z. Shilo, and N. Barkai. Self-enhanced ligand degradation underlies robustness of morphogen gradients. *Developmental Cell*, 5(4):635–646, 2003.
- [30] M. B. Elowitz and S. Leibler. A synthetic oscillatory network of transcriptional regulators. *Nature*, 403(6767):335–338, 2000.

- [31] M. B. Elowitz, A. J. Levine, E. D. Siggia, and Swain P. S. Stochastic gene expression in a single cell. *Science*, 297(5584):1183–1186, 2002.
- [32] J. England and J. Cardy. Morphogen gradient from a noisy source. *Physical Review Letters*, 94:078101, 2005.
- [33] E. V. Entchev and M. A. González-Gaitán. Morphogen gradient formation and vesicular trafficking. *Traffic*, 3(2):98–109, 2002.
- [34] E. V. Entchev, A. Schwabedissen, and M. González-Gaitán. Gradient formation of the TGF- β homolog Dpp. *Cell*, 103(6):981–991, 2000.
- [35] A. Ephrussi and D. St Johnston. Seeing is believing: The Bicoid morphogen gradient matures. *Cell*, 116(2):143–152, 2004.
- [36] E. L. Ferguson and K. V. Anderson. Decapentaplegic acts as a morphogen to organize dorsal-ventral pattern in the *Drosophila* embryo. *Cell*, 71(3):451–461, 1992.
- [37] E. L. Ferguson and K. V. Anderson. Localized enhancement and repression of the activity of the TGF- β family member, decapentaplegic, is necessary for dorsal-ventral pattern-formation in the *Drosophila* embryo. *Development*, 114(3):583–597, 1992.
- [38] A. Gierer and H. Meinhard. Theory of biological pattern formation. *Kybernetik*, 12(1):30–39, 1972.
- [39] F. Gonzalez, L. Swales, A. Bejsovec, H. Skaer, and A. M. Arias. Secretion and movement of Wingless protein in the epidermis of the *Drosophila* embryo. *Mechanisms of Development*, 35(1):43–54, 1991.
- [40] M. González-Gaitán. personal communication.
- [41] M. González-Gaitán. Signal dispersal and transduction through the endocytic pathway. *Nature Reviews Molecular Cell Biology*, 4:213–224, 2003.
- [42] D. Gonze, J. Halloy, and A. Goldbeter. Robustness of circadian rhythms with respect to molecular noise. *Proceedings of the National Academy of Sciences of the United States of America*, 99(2):673–678, 2002.
- [43] V. Greco, M. Hannus, and S. Eaton. Argosomes: A potential vehicle for the spread of morphogens through epithelia. *Cell*, 106(5):633–645, 2001.
- [44] J. Green. Morphogen gradients, positional information, and *Xenopus*: Interplay of theory and experiment. *Developmental Dynamics*, 225:392–408, 2002.
- [45] J. B. Gurdon and P. Y. Bourillot. Morphogen gradient interpretation. *Nature*, 413(6858):797–803, 2001.
- [46] J. B. Gurdon, P. Harger, A. Mitchell, and P. Lemaire. Activin signaling and response to a morphogen gradient. *Nature*, 371(6497):487–492, 1994.
- [47] C. Han, T. Y. Belenkaya, B. Wang, and X. H. Lin. *Drosophila* glypicans control the cell-to-cell movement of Hedgehog by a dynamin-independent process. *Development*, 131(3):601–611, 2004.

- [48] C. Han, Y. Dong, T. Y. Belenkaya, and X. Lin. *Drosophila glypicans Dally and Dally-like shape the extracellular Wingless morphogen gradient in the wing disc. Development*, 132(4):667–679, 2005.
- [49] J. Hasty, D. McMillen, F. Isaacs, and J. J. Collins. Computational studies of gene regulatory networks: In numero molecular biology. *Nature Reviews Genetics*, 2(4):268–279, 2001.
- [50] S. Havlin and D. Benavraham. Diffusion in disordered media. *Advances in Physics*, 36(6):695–798, 1987.
- [51] L. I. Held. *Imaginal discs: the genetic and cellular logic of pattern formation*. Cambridge University Press, 2002.
- [52] J. J. Herbst, L. K. Opresko, B. J. Walsh, D. A. Lauffenburger, and H. S. Wiley. Regulation of postendocytic trafficking of the epidermal growth-factor receptor through endosomal retention. *Journal of Biological Chemistry*, 269(17):12865–12873, 1994.
- [53] T. Hofer, H. Nathansen, M. Lohning, A. Radbruch, and R. Heinrich. GATA-3 transcriptional imprinting in Th2 lymphocytes: A mathematical model. *Proceedings of the National Academy of Sciences of the United States of America*, 99(14):9364–9368, 2002.
- [54] B. Houchmandzadeh, E. Wieschaus, and S. Leibler. Establishment of developmental precision and proportions in the early drosophila embryo. *Nature*, 415(6873):798–802, 2002.
- [55] S. Huang, G. Eichler, Y. Ber-Yam, and D. E. Ingber. Cell fates as high-dimensional attractor states of a complex gene regulatory network. *Physical Review Letters*, 94:128701, 2005.
- [56] M. Kerszberg and L. Wolpert. Mechanisms for positional signaling by morphogen transport: a theoretical study. *Journal of Theoretical Biology*, 191(1):103–114, 1998.
- [57] H. Kitano. Biological robustness. *Nature Reviews Genetics*, 5:826–837, 2004.
- [58] A. J. Koch and H. Meinhardt. Biological pattern-formation - from basic mechanisms to complex structures. *Reviews of Modern Physics*, 66(4):1481–1507, 1994.
- [59] K. Kruse, P. Pantazis, T. Bollenbach, F. Jülicher, and M. González-Gaitán. Dpp gradient formation by dynamin-dependent endocytosis: receptor trafficking and the diffusion model. *Development*, 131(19):4843, 2004.
- [60] A. D. Lander, Q. Nie, and F. Y. M. Wan. Do morphogen gradients arise by diffusion? *Developmental Cell*, 2(6):785–796, 2002.
- [61] D. A. Lauffenburger and J. J. Lindermann. *Receptors: models for binding, trafficking, and signaling*. Oxford University Press, 1993.
- [62] T. Lecuit, W. J. Brook, M. Ng, M. Calleja, H. Sun, and S. M. Cohen. Two distinct mechanisms for long-range patterning by decapentaplegic in the *Drosophila* wing. *Nature*, 381(6581):387–393, 1996.
- [63] T. Lecuit and S. M. Cohen. Dpp receptor levels contribute to shaping the Dpp morphogen gradient in the *Drosophila* wing imaginal disc. *Development*, 125(24):4901–4907, 1998.

- [64] A. Martinez Arias. Wnts as morphogens? the view from the wing of drosophila. *Nature Reviews Molecular Cell Biology*, 4:321–325, 2003.
- [65] A. Martinez Arias and A. Stewart. *Molecular Principles of Animal Development*. Oxford University Press, 2002.
- [66] J. Massague. TGF- β signal transduction. *Annual Review of Biochemistry*, 67:753–791, 1998.
- [67] H. Meinhardt. *Models of biological pattern formation*. Academic Press, London, 1982.
- [68] M. M. Moline, C. Southern, and A. Bejsovec. Directionality of Wingless protein transport influences epidermal patterning in the Drosophila embryo. *Development*, 126(19):4375–4384, 1999.
- [69] T. H. Morgan. Regeneration in *Allolobophora foetida*. *Roux's Arch Dev. Biol.*, 5:570–586, 1897.
- [70] T. H. Morgan. *Regeneration*. Macmillan (New York), 1901.
- [71] S. Morimura, L. Maves, Y. Chen, and F.M. Hoffmann. Decapentaplegic overexpression affects Drosophila wing and leg imaginal disc development and wingless expression. *Dev. Biol.*, 177:136, 1996.
- [72] B. Müller, B. Hartmann, G. Pyrowolakis, M. Affolter, and K. Basler. Conversion of an extracellular Dpp/BMP morphogen gradient into an inverse transcriptional gradient. *Cell*, 113(2):221–233, 2003.
- [73] D. Nellen, R. Burke, G. Struhl, and K. Basler. Direct and long-range action of a Dpp gradient. *Cell*, 85:357–368, 1996.
- [74] C. Nüsslein-Volhard. Gradients that organize embryo development. *Scientific American*, 275(2):54–61, 1996.
- [75] E. M. Ozbudak, M. Thattai, H. N. Lim, B. I. Shraiman, and A. van Oudenaarden. Multistability in the lactose utilization network of *Escherichia coli*. *Nature*, 427(6976):737–740, 2004.
- [76] K. J. Painter, P. K. Maini, and H. G. Othmer. Stripe formation in juvenile *Pomacanthus* explained by a generalized Turing mechanism with chemotaxis. *Proceedings of the National Academy of Sciences of the United States of America*, 96(10):5549–5554, 1999.
- [77] P. Pantazis. in preparation.
- [78] P. Pantazis. *Role of endocytic trafficking during Dpp gradient formation*. PhD thesis, Technische Universität Dresden, 2005.
- [79] G. H. Patterson and J. Lippincott-Schwartz. A photoactivatable GFP for selective photolabeling of proteins and cells. *Science*, 297:1873–1877, 2002.
- [80] J. Paulsson. Summing up the noise in gene networks. *Nature*, 427:415–418, 2004.
- [81] S. Pfeiffer, C. Alexandre, M. Calleja, and J. P. Vincent. The progeny of wingless-expressing cells deliver the signal at a distance in Drosophila embryos. *Current Biology*, 10(6):321–324, 2000.

- [82] W. H. Press, S. A. Teukolsky, W. T. Vetterling, and B. P. Flannery. *Numerical Recipes in C*. Cambridge University Press, 1992.
- [83] F. A. Ramirez-Weber and T. B. Kornberg. Cytonemes: Cellular processes that project to the principal signaling center in *Drosophila* imaginal discs. *Cell*, 97(5):599–607, 1999.
- [84] R. P. Ray and K. A. Wharton. Context-dependent relationships between the BMPs *gbb* and *dpp* during development of the *Drosophila* wing imaginal disk. *Development*, 128(20):3913–3925, 2001.
- [85] R. D. Riddle, R. L. Johnson, E. Laufer, and C. Tabin. Sonic-Hedgehog mediates the polarizing activity of the ZPA. *Cell*, 75(7):1401–1416, 1993.
- [86] K. Shimizu and J. B. Gurdon. A quantitative analysis of signal transduction from activin receptor to nucleus and its relevance to morphogen gradient interpretation. *Proceedings of the National Academy of Sciences of the United States of America*, 96(12):6791–6796, 1999.
- [87] F. A. Spencer, F. M. Hoffmann, and W. M. Gelbart. Decapentaplegic - a gene-complex affecting morphogenesis in *Drosophila-melanogaster*. *Cell*, 28(3):451–461, 1982.
- [88] C. Starbuck and D. A. Lauffenburger. Mathematical-model for the effects of epidermal growth-factor receptor trafficking dynamics on fibroblast proliferation responses. *Biotechnology Progress*, 8(2):132–143, 1992.
- [89] M. Strigini and S. M. Cohen. Wingless gradient formation in the *Drosophila* wing. *Current Biology*, 10(6):293–300, 2000.
- [90] T. Tabata. Genetics of morphogen gradients. *Nature Reviews Genetics*, 2(8):620–630, 2001.
- [91] T. Tabata and Y. Takei. Morphogens, their identification and regulation. *Development*, 131(4):703–712, 2004.
- [92] A. A. Teleman and S. M. Cohen. *Dpp* gradient formation in the *Drosophila* wing imaginal disc. *Cell*, 103(6):971–80, 2000.
- [93] A. A. Teleman, M. Strigini, and S. M. Cohen. Shaping morphogen gradients. *Cell*, 105(5):559–562, 2001.
- [94] A. M. Turing. The chemical basis of morphogenesis. *Philosophical Transactions of the Royal Society of London Series B-Biological Sciences*, 237(641):37–72, 1952.
- [95] J. J. Tyson, K. Chen, and B. Novak. Network dynamics and cell physiology. *Nature Reviews Molecular Cell Biology*, 2(12):908–916, 2001.
- [96] J. P. Vincent and L. Dubois. Morphogen transport along epithelia, and integrated trafficking problem. *Developmental Cell*, 3(5):615–623, 2002.
- [97] E. Weisstein. Mathworld. <http://mathworld.wolfram.com/>. Wolfram Research, Inc.
- [98] K. A. Wharton, R. P. Ray, and W. M. Gelbart. An activity gradient of decapentaplegic is necessary for the specification of dorsal pattern elements in the *Drosophila* embryo. *Development*, 117(2):807–822, 1993.
- [99] T. Williams and C. Kelley. Gnuplot version 4.0. <http://www.gnuplot.info/>, 2004.

- [100] S. Wolfram. *Mathematica 5.1*. Wolfram Research, Inc., 1988-2004.
- [101] L. Wolpert. Positional information and spatial pattern of cellular differentiation. *Journal of Theoretical Biology*, 25(1):1, 1969.
- [102] L. Wolpert. Do we understand development? *Science*, 266:571–572, 1994.
- [103] L. Wolpert. *Principles of Development*. Oxford University Press, 2002.
- [104] W. Xiong and J. E. Ferrell. A positive-feedback-based bistable 'memory module' that governs a cell fate decision. *Nature*, 426(6965):460–465, 2003.
- [105] M. Zecca, K. Basler, and G. Struhl. Direct and long-range action of a wingless morphogen gradient. *Cell*, 87(5):833–844, 1996.
- [106] M. Zerial. personal communication.
- [107] A. J. Zhu and M. P. Scott. Incredible journey: how do developmental signals travel through tissue? *Genes & Development*, 18(24):2985–2997, 2004.

Versicherung

Hiermit versichere ich, daß ich die vorliegende Arbeit ohne unzulässige Hilfe Dritter und ohne Benutzung anderer als der angegebenen Hilfsmittel angefertigt habe; die aus fremden Quellen direkt oder indirekt übernommenen Gedanken sind als solche kenntlich gemacht. Die Arbeit wurde bisher weder im Inland noch im Ausland in gleicher oder ähnlicher Form einer anderen Prüfungsbehörde vorgelegt. Die vorgelegte Arbeit wurde vom 1.11.2002 bis 20.4.2005 unter der Aufsicht von Prof. Dr. Frank Jülicher am Max-Planck-Institut für Physik komplexer Systeme in Dresden durchgeführt.

Ich versichere, daß ich bisher keine erfolglosen Promotionsverfahren unternommen habe. Ich erkenne die Promotionsordnung der Fakultät Mathematik und Naturwissenschaften der Technischen Universität Dresden an.

Dresden, den 21.4.2005, Tobias Bollenbach